Analysis and simulation of electromagnetic transients in HVAC cable transmission grids

da Silva, Filipe Miguel Faria

Publication date:
2011

Document Version
Publisher's PDF, also known as Version of record

Citation for published version (APA):
da Silva, F. M. F. (2011). *Analysis and simulation of electromagnetic transients in HVAC cable transmission grids*. Institut for Energiteknik, Aalborg Universitet.

Analysis and simulation of electromagnetic transients in HVAC cable transmission grids

Filipe Miguel Faria da Silva

Dissertation submitted to the Faculty of Engineering, Science and Medicine
at Aalborg University
in partial fulfilment of the requirements for the degree of
Doctor of Philosophy in Electrical Engineering

Preface

This thesis is submitted to the Faculty of Engineering, Science and Medicine at Aalborg University in the partial fulfilment of the requirements for the PhD degree in Electrical Engineering. The research was conducted at the Department of Energy Technology for Energinet.dk, of which I was hired as an employee for the entire project.

The project has been followed full time by Associated Professor Claus Leth Bak (Department of Energy Technology) and by Dr. Wojciech Wiechowski (Energinet.dk) later replaced by Eng. Per Balle Holst (Energinet.dk).

Energinet.dk has fully funded the research leading to this thesis "Analysis and simulation of electromagnetic transients in HVAC cable transmission grids", including travelling expenses for participation in international conferences and working groups, renting of laboratory equipment used in the measurements and acquisition of different software.

In the summer of 2010 I spent three months at The Manitoba HVDC Research Centre in Winnipeg, Canada, as a guest researcher. During this period I focused on the analysis of system with large amounts of underground cables, which are more likely to have numerical instabilities.

The knowledge gained while working on this project resulted in the supervision of five master projects, the teaching of three master level courses and one PhD/industrial course on the field of electromagnetic transients. The research resulted also in the submission of eleven papers, of which seven were published, whereas the remaining are currently being reviewed. More are planned for submission after the thesis defence.

This thesis is divided in nine chapters plus references and fifteen appendices. A list of all authored and co-authored publications written by the author and related with this research project are presented at the end of the thesis. Literature references are shown as [j], where j is the number of the literature in the reference list. References to figures and tables are shown as Figure C.F or Table C.F and references to equations are shown as Equation (F), where C is the chapter number and F indicates the figure, table or equation number.

Acknowledgments

I owe gratitude to many people that helped me in various ways during my work. In particular, I would like to thank to:

- My supervisors, Claus Leth Bak, Wojciech Wiechowski and Per Balle Holst for all their support and comments during the project period, and for all the fruitful discussions.

- Claus Leth Bak, Wojciech Wiechowski, Per Balle Holst, Unnur Stella Guðmundsdóttir, Martin Randrup, Thomas Kjærsgaard Sørensen, Henny K. Nielsen, Vladislav Akhmatov, Sebastian Dollerup, Thomas Kvarts and Jakob Kessel for their contributions during status meetings throughout the entire project period.

- Wojciech Wiechowski and Unnur Stella Guðmundsdóttir for their help with carrying out the field measurements.

- Christian Flytkjær Jensen for all his help with the English-Danish translations.

- Unnur Stella Guðmundsdóttir, Christian Flytkjær Jensen, Elif Inan, Weihao Hu and Lukasz Kocewiak for giving a good atmosphere to the office.

- Everyone at the Planning and Transmission Departments at Energinet.dk for their hospitality and support.

- All the people at the Manitoba HVDC Research Centre for their hospitality and support. I would especially like to thank to Dr. Jeewantha Da Silva for his help with the cable modelling, Juan Carlos for his help with transformers and shunt reactors, Kimberly Laing for all her help with the logistics and for having a huge patience, and to Paul Wilson for let me stay with the Centre for three very prolific months.

- All the people at the CIGRE WG C4.502 for the numerous discussions during the WG meetings.

- My closest friends during the last three years: Aida, Ondrej, Mahdi, Daniela and Eva for their friendship and good times.

- My parents and siblings for all the support and believe.

Filipe Miguel Faria da Silva, July 2011, Aalborg

Abstract

On the 4th of November 2008, Denmark's Government decided that in order to reduce the visual pollution caused by Overhead Lines (OHL), all transmission lines with a voltage level equal and below 150 kV must be undergrounded gradually within the next 20 years. Additionally, all new 400 kV lines will be built as cable lines (with some exceptions).

The replacement of OHL by underground cables is estimated to cost 16 to 17 billion Danish kroner (roughly 2.2 billion euros). However, estimations made by the Danish TSO (Energinet.dk) indicate that 5-6% of this amount can be save by doing a methodically preparation and study of the different phenomena associated to the operation and installation of long underground cables.

Moreover, Denmark is the first country in the world undergrounding most of its transmission network. As a result, several technical barriers and challenges associated to the use of an undergrounded transmission grid must first be dealt with. For that purpose, several research and development projects were initiated by the Danish TSO, among them this PhD thesis.

The main objective of this PhD is to study electromagnetic transient phenomena. Thereto, the thesis is divided into two main parts:

- Description of the different electromagnetic phenomena likely to occur in transmission grids with a large amount of HVAC cables and respective countermeasures;
- Guidelines for the proper simulation of those phenomena when using EMTP software, more specifically PSCAD/EMTDC, and methods to optimize the simulations;

The study and understanding of such complex electromagnetic phenomena requires both the use of realistic electrical grids and a trust in the cable model accuracy. Thus, a simulation network based on the Transmission Grid of West Denmark as planned for 2030 has been used as simulation base case to identify the dimensioning transient phenomena and find the right countermeasures for an undergrounded transmission network.

In order to ensure that the transient studies are made on a proper model basis, the frequency dependent phasor model in PSCAD/EMTDC has been verified by measurements on a 100 km, 58 km of land cable plus 42 km of submarine cable, 165 kV cable, which is connecting an offshore wind farm to the Danish transmission network.

The 2030 West Denmark Grid has two voltage levels, 165 kV and 400 kV. The 165 kV level will be all cables, whereas the 400 kV level will mostly be cables. This network provides the necessary complexity for the electromagnetic studies.

The accuracy of cable simulation models has been addressed by several authors prior to this thesis. However, the validations were normally made for short cables, whereas in this thesis are analysed cables with dozens of km length. Furthermore, during the first year of the thesis, was given the opportunity to access to a 100 km cable prior to its commissioning and perform measurements.

The thesis shows the measurement's results and demonstrates that the land cable model is accurate, yet the same is not true for the used submarine cable model. However, in the studies made in this thesis, only land cables are used, which were demonstrated to be accurate.

It is desired that all the electromagnetic transient phenomena have a theoretical description and to be demonstrated by means of simulations and if possible measurements.

The first phenomenon to be analysed is the energisation of cables in all its different variants: Ideal energisation of a cable connected to a voltage source, energisation of a cable and a shunt reactor together, energisation in weak grids and energisation of cables in parallel. The studies demonstrated that the waveform associated to a cable energisation depends mainly on four different factors: The cable length and its electrical parameters, the switching instant, the grid short-circuit power at the node and the connection of equipment like shunt-reactors or transformers to the cable.

The ideal energisation of a cable was been explained several decades ago. However, the energisation of a cable and a shunt reactor together posts a more interesting study, as shunt reactors are only connected directly to a cable when the cable is long enough, a situation that is not very common at the present. Depending on the compensation level and switching instant the current through the cable circuit breaker may not cross zero, which is an unacceptable situation as it becomes impossible to open the circuit breaker in case of necessity.

In the thesis, several countermeasures that can be used to avoid the zero-missing phenomenon are proposed. Among them should be pointed out the use of a pre-insertion resistor, to which is provided a formula that can be used to calculate the precise value of the pre-insertion resistor.

The energisation of a cable in a weak grid poses an interesting challenge, because of the high overvoltages associated to the phenomenon. The phenomenon is unlikely to occur in European countries where the transmission networks have normally high short-circuit power levels. However, the phenomenon has to be taken into account in the event of a black-start operation.

Another interesting analysis is the one make on the energisation of cables in parallel, an operation that can result in high inrush-currents. This energisation will be the norm in Denmark both to the TSO and to the several distribution companies. An IEEE standard analyses this phenomenon and provides formulas that can be used in the estimation of the worst case scenario. However, the formulas do not always provide accurate results. A detailed and long mathematical analysis resulted in new formulas that can replace with higher accuracy the standard formulas.

The de-energisation of a cable is another transient phenomenon that needs to be investigated. This operation strongly resembles the de-energisation of a capacitor bank and can be analysed using similar methods. However, the de-energisation of a cable and shunt reactor together shows a radical different behaviour. The waveform is no longer a decaying DC but a decaying AC oscillating at resonance frequency or frequencies if mutual coupling is present. The mutual coupling between the shunt reactor phases may lead to an overvoltage in one or more phases, which should be taken into account for the estimation of the TRV.

A restrike of the CB during the cable de-energisation can result in large overvoltages that can in theory go up to a maximum of 3 pu. The overvoltages are even larger in hybrid cable-OHL lines, because of voltage magnifications in the cable/OHL join point. This phenomenon was also used to demonstrate the importance of the modelling depth and the modelling of the cross-bonded sections into the results.

The transient peak overvoltage is influenced by the size of the modelling area around the switched line. Thus, one has to be sure that the modelling area is large enough to provide accurate results. However, the simulation of HVAC cables in EMTP-type software is very time consuming and the simulation of a cable energisation in a cable-based grid can easily last several minutes or even dozen of minutes for a mesh grid.

As a result, an optimization method that can be used to minimise the number of components in the simulation model and still provide accurate results would be very useful. The thesis proposes a method that can be used to estimate the minimum modelling depth, i.e., which lines should be included in the model. The method requires the grid layout, which can be obtained from a PSS/E file or equivalent, and the transient peak time, which normally does not depend on the neighbour network and can be estimated by simply simulating the cable connected to an ideal voltage source. The method can also be used to specify the cables that should have a precise modelling of the correspondent cross-bond sections.

The method is implemented in Matlab and can be run before starting to design the system.

In summary, the application of the method minimises both the number of lines in the model and the number of cross-bond sections, reducing the simulation running time whereas continuing to provide accurate results.

The previous method indicates how much of the grid to model only if no resonance is associated to the transient phenomenon. However, the carrying out of a frequency scan at the switch-on node prior to the EMTP simulation can both predict the existence of a resonance phenomenon and the frequencies excited during the transient, if a resonance is present.

It is again demonstrated that the modelling depth influences the results and it is concluded that a mix of frequency-dependent models and lumped-parameter models present the best accuracy/simulation time relation.

It is also shown, both by means of simulations and mathematical analysis, how the type of used bonding, both-ends or cross-bond, may alter both the resonance frequencies and respective magnitudes.

To finish, in this thesis a systematic method is proposed, which can be used for simulating electromagnetic transients in cable-based grids. The method suggests guidelines that can be used for a methodical step-by-step simulation of electromagnetic transients, in function of the grid and cable characteristics.

Dansk Resumé

Den 4. november 2008 besluttede den danske regering at den visuelle forurening foretaget af luftledninger skulle reduceres. Dette gøres ved gradvist i løbet af de kommende 20 år at kabelægge alle transmissionslinjer med et spændings niveau lig med og under 150 kV. Ydermere vil alle nybyggede 400 kV linjer konstrueres som kabellinjer (med nogle undtagelser).
Udskiftningen af luftledningerne med kabler har en estimeret pris på 16-17 milliarder kroner. Foreløbige udregninger foretaget af den danske transmissions systems operatør Energinet.dk indikerer at 5-6 % af dette beløb kan spares ved at udføre studier of forskellige fænomener relateret til idriftsættelse og installation af lange kabelstrækninger. Ydermere da Danmark er det først land i verden, der planlægger en kabellægning af det meste af transmissionsnettet må løsninger på talrige tekniske problemer udvikles inden kabellægningen igangsættes. For at afklare disse problemstillinger er flere forskningsprojekter blevet startet af Energinet.dk, imellem dem dette PhD-projekt.

Hovedformålene med PhD-projekt er at studere elektromagnetiske transienter i kabelnetværk. Afhandlingen er delt i to hoveddele:
- En beskrivelse af forskellige elektromagnetiske fænomener, der forventeligt kan opstå i transmissionsnet med en stor mængde HVAC kabler og kablernes respektive modparter.
- Retningslinjer for rigtig simulering af disse fænomener ved brug af EMTP software, mere specifik PSCAD/EMTP, og metoder til at optimere disse simuleringer.

Studierne og forståelsen af sådanne komplekse elektromagnetiske fænomener kræver både brug af virkelige elektriske transmissionsnetværk samt kabelmodeller, der giver resultater, der kan stoles på. Derfor er en del af vest Danmarks transmissionsnet, som det er planlægt i 2030, blevet brugt som simuleringsmodel til at identificere de dimensionerende transiente fænomener og til at finde de rigtige modforanstaltninger.
For at sikre at de transiente studier, der fortages i afhandlingen er pålidelige er den ' frekvensafhængige fase model' tilgængelig i PSCAD/EMTP verificeret mod målinger foretaget på et 100 km, 165 kV kabel bestående af en landkabel- samt en søkabeldel. Dette kabel forbinder en dansk vindmølle park til transmissionsnettet.
Det danske 2030 netværk har to spændingsniveauer, 165 kV og 400 kV. 165 kV niveauet vil blive et rent kabelnetværk, hvor 400 kV niveauet vil hovedsageligt være kabel, men udvalgte strækninger vil installeres som luftledninger. Nettets kompleksitet vil være passende for de nødvendige elektromagnetiske studier foretaget i denne afhandling.
De tilgængelige kabelmodellers godhed har været undersøgt af flere forfattere før denne afhandling. Disse verificeringer var dog altid baseret på korte kabelstrækninger. Under projektets første år var der mulighed for at tilgå og udføre målinger på et 100 km kabel før dette kabel blev idriftsat. Afhandlingen præsenterer disse målinger og viser at landkablemodellen er præcis, hvor det samme ikke gør sig gældende for søkablemodellen. Systemerne der simuleres i denne afhandling indeholder dog kun landkabler og disse simuleres som nævnt med høj præcision.

Det er ønskeligt at alle elektromagnetiske transiente fænomener kan forklares med en passende teori og at disse kan vises ved simulering og hvis muligt med målinger.

Det første fænomen der studeres er spændingssætning af kabler i forskellige varianter: ideel spændingssætning gennem en ideel spændingskilde, spændingssætning af et kabel og en kompenseringsreaktor sammen, spændingssætning i svage netværk og spændingssætning af parallelle kabler. Studierne viser at dem bølgeform, der er sammenhængende med en spændingssætning af et kabel afhænger af fire forskellige faktorer: Kablets længde og dens elektriske parametre, tidspunktet, hvor kablet spændingssættes, netværkets kortslutningsniveau og tilsluttet udstyr som kompenseringsreaktorer og transformere.
Teorien bag den ideelle spændingssætning blev forklaret flere årtier siden. Spændingssætningen af en kabelstrækning samt en kompenseringsreaktor udgører et mere interessant studie da kompenseringsreaktoren ofte tilsluttes direkte til kablet, hvis kablet er af en vis længde - en situation der har været sjælden indtil nu. Afhængig af kompenseringsgraden og øjeblikket for spændingssætningen vil strømmen gennem afbryderen ikke krydse nul, hvilket gør en afbrydelse umulig.
I denne afhandling præsenteres flere modforanstaltning, der kan benyttes til at undgå fasestrømmens manglende nulgennemgang. Af disse fremhæves brugen af indkoblingsmodstande, hvor der er udviklet en beregningsmetode, der kan benyttes til at bestemme modstandens værdi.
Spændingssætningen af kabler i svage netværk udfører en interessant udfordring pga. de overspændinger, der er forbundet med denne type kobling. Disse overspændinger vil dog sjældent fremkomme i europæiske lande, da kortslutningsniveauet ofte er højt i disse lande. Fænomenet skal dog undersøges pga. muligheden for opstart efter et dødt net.
Et andet interessant studie er spændingssætningen af kabler i parallel - en operation, der kan medføre høje indkoblingsstrømme. Sådanne indkoblinger vil være normen i Danmark både hos TSOen og hos flere transmissionsselskaber. En IEEE standard analysere dette fænomen og foreslår formler, der kan bruges til at beregne de værste tilfælde. Disse formler er dog ikke altid tilstrækkelige. En ny detaljeret analyse resulterer i nye formler, der med høj nøjagtighed kan erstatte standard formlerne.

Udkobling af et kabel er et andet transient fænomen, der undersøges. Denne koblingstype minder om udkobling af en kondensatorbank og kan derfor analyseres med lignende metoder. Udkoblingen af et kabel og en kompenseringsreaktor sammen viser dog et radikal andet forløb. Bølgeformen er ikke længere en aftagende DC spænding, men en aftagende DC spænding med en overlejret AC oscillation ved systemets resonansfrekvens eller frekvenser, hvis der er gensidig kobling. Den gensidige kobling i kompenseringsreaktoren kan lede til overspændingen i en eller flere faser. Dette må tages i betragtning for estimeringen af TVR.

En gentænding i afbryderen under kabeludkobling kan resultere i høje overspændinger, der i teorien kan nå 3 pu. Overspændingerne er endnu større i hybrid kabel-luftledning linjer pga. spændingen niveaus forstærkning ved kabel/luftledning overgangen. Dette fænomen bliver ligeledes brugt til at vise vigtigheden af modeldybden og modeldannelsen af krydskoblingerne på kabelstrækningerne.

Den simulerede transiente overspænding påvirkes af størrelsen af det modellerede område omkring den koblede linje. Derfor skal det sikres at området medtaget i modellen er stort nok til at give troværdige resultater. Simuleringstiden for et kabelsystem i et EMTP-software er ofte meget tidskrævende og simuleringen af spændingssætning af kabler i kabelnetværk kan vare fra få til adskillige minutter i et maskenetværk.
Som et resultat af dette vil en optimeringsmetode, der minimerer antallet af komponenter i modellen samtidig med at en høj nøjagtighed beholdes være ønskelig. Afhandlingen præsenterer en metode, der kan benyttes til at estimere modeldybden, betydende hvilke linjer der skal medtages i modellen. Meto-

den benytter netværksopsætningen, der kan fremskaffes fra en PSS/E fil eller lignende og tiden for den højeste transient peak. Sidst nævnte er ikke afhænger af det omkringliggende netværk og kan estimeres ved en simpel simulering af kablet koblet til en idel kilde. Metoden kan også benyttes til at fastligge, hvilke kabelstrækninger der skal modeldannes præcist med hensyn til krydskobling.
Metoden implementeres i MATALB og kan køres før designfasen af systemet startes.
For at opsamle på forgående afsnit minimeres både antallet af linjer i modellen og antallet af sektioner, der modelleres med krydskoblinger. Dette reducerer simuleringstiden men fastholder en høj nøjagtighed.

Den førnævnte metode indikerer, hvor meget af nettet der kan medtages i modellen i det tilfælde, hvor resonans ikke opstår i de transiente simuleringer. I tilfælde af resonans kan det forudsiges ved at lave et frekvens scan ved det knudepunkt, hvor spændingssætningen forekommer før EMTP simuleringen foretages. Frekvensscannet kan ikke kun forudsige om, der eksisterer resonanspunkter, men også de frekvenser, der eksisteres under transientforløbet
Det vises igen, at modeldybden påvirker resultaterne og det er konkluderet at en blanding af frekvensafhængige modeller og modeller med koncentrerede parametre giver den bedste nøjagtighed/simulerings hastigheds sammenhæng. Det vises også, ved brug af både simuleringer og matematisk analyse, hvordan krydskoblingstypen påvirker frekvensspektrummet.

Afslutningsvis foreslås, der i afhandlingen, en systematisk metode der kan benyttes til at simulere elektromagnetiske fænomener i kabelbaserede netværk. Metoden foreslår retningslinjer der kan benyttes til en metodisk step by step simulering af elektromagnetiske transienter som funktion af nettets og kablernes karakteristika.

1. Introduction

The focus of this thesis is to gain an understanding of the different transient phenomena associated with the use of long HVAC cables. More precisely, the focus is to accurately describe each transient phenomenon, in providing the necessary guidelines for the performance of proper simulations and in presenting respective countermeasures that can be used in real systems, as for example the future Danish electricity transmission network.

1.1 Background

For more than a century, overhead lines have been the most commonly used technology for transmitting electrical energy at all voltage levels [1], notable exceptions being the crossing of water zones, densely populated areas and areas of relevant natural beauty, where underground cables are typically used [2].
On the 4th of November 2008, the Danish Government took a decision that will completely change Denmark's Electrical Power Transmission System. On that day, it was decided that the entire grid with a voltage below or equal to 150 kV has to be undergrounded, i.e. the existing overhead lines (OHL) have to be substituted by underground cables. On the same date it was also decided to underground all new 400 kV connections [3], [4].
The experience with underground cables at transmission level, which in Denmark means a maximum voltage level equal or superior to 145 kV in Eastern Denmark and 170 kV in Western Denmark, is rather limited because of the low percentage of installed cables. A quantification of this problem can be seen in Figure 1.1, where the percentage of used cables in the world (data from December 2006 [5]) is shown for different voltage levels. It should be also emphasised that where transmission levels are of concern, less than half of these cables are of the XLPE (cross-lined polyethylene) type [5], resulting, when compared with OHL, in reduced practical experience with the use of XLPE HVAC underground cables at transmission levels.

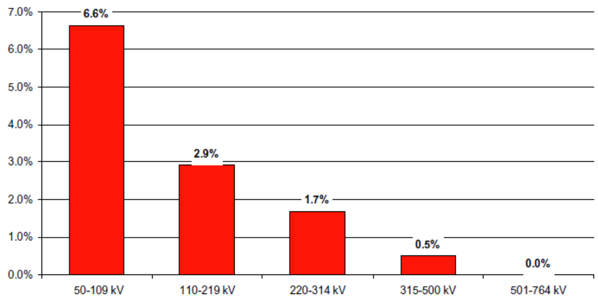

Figure 1.1 - Percentage of the total circuit length that is undergrounded [5]

Due to changes planned in Denmark's transmission system and a lack of experience with long HVAC cables, the Danish TSO, Energinet.dk, decided to research switching operations in HVAC cables, in order to study the undesirable overvoltages generated by a switching operation and the differences from the more familiar OHL switching.

1.2 Insulation co-ordination studies

The impact of a cable in a power grid must be assessed for both normal and fault operations [1], being typical the performance of insulation co-ordination studies when installing a cable [6]. Some examples of insulation co-ordination studies previously performed on behalf of the Danish TSO in connection with the installation of HVAC cables are found in [7], [8] and [9].
General recommendations on how to perform an insulation co-ordination study when installing a HVAC cable can be consulted in [6] and [10]. Reference [6] recommends the development of guidelines for both the modelling of HVAC cables and the interpretation of the simulation results. Similar recommendations plus a number of guidelines are provided in [11].

There are a large number of phenomena associated with a cable connection/disconnection that may result in overvoltages [6], but the type of studies carried out should depend on the cable and network characteristics, as some phenomena are likely to happen only under specific conditions.
The simulation of cable energisation is normally always performed as it may result in temporary overvoltage and/or slow-front overvoltages [9], [12]. Examples of phenomena that may occur during cable energisation are:

- Switching overvoltage, of which magnitude and duration are associated with the switching instant and cable length. This phenomenon is well documented and examples are shown in [9], [11], [13], [14] and [15], with the physical basic explanation being given in [16] and [17].
- Due to the interaction between a cable and a transformer, resonance overvoltages are also associated with a cable energisation. Energisations of cables are especially dangerous when the transformer inrush current matches the system resonance frequency [14], [18], [19] and [20].
- Depending on the reactive power compensation level and the switching instant, the current flowing into the circuit breaker may not have zero crossing for some time after the switching instant, making it impossible to open the circuit breaker without risking to damage it. This phenomenon goes by the name of zero-missing and is explained in [9], [21] and [22].
- The energisation of cables in parallel with an already energised cable may result in high-frequency inrush currents [23], [24], a phenomenon similar to the energisation of capacitor banks in parallel.

Besides the occurrence of unwanted situations associated with the energisation of a cable, there are undesirable phenomena during a cable disconnection. Typically, a cable de-energisation is unlikely to originate any substantial overvoltage, but it may represent a serious risk to the system if a restrike in the circuit breaker occurs. A cable has a large capacitance making its disconnection similar to the disconnection of a capacitor bank [27]. This phenomenon is very well documented for capacitor banks in [25], [26], [27] and [28], which also provide some information about cable lines.

The test protocol for circuit breakers installed in capacitor banks or cables and their restrike probability is available in [29]. In this situation it becomes important to know the Transient Recovery Voltage (TRV), which may change if a shunt reactor is connected to the cable or if the circuit breaker opens to clear a fault condition.

The consequences of a restrike in a hybrid cable-OHL line are not well documented. The most similar situation is the study of lightning strokes in hybrid cable-OHL lines as presented in [31] and [32]. It should be noticed that the restrike overvoltage of a hybrid line may be larger than the theoretical maximum of 3 pu defined in [10].

In some cable lines a shunt reactor is directly connected to the cable, being disconnected together with the cable. Due to the shunt reactor mutual inductance it is possible to have a light overvoltage in the moments following the de-energisation [33]. This overvoltage is typically low and should not by itself represent a risk to the system.

Guidelines for the performance of insulation co-ordination studies are found in IEC 60071.

Reference [12] provides a computation and modelling guide for insulation co-ordination studies. With regard to the modelling of cables, the standard is, however, somewhat outdated. The standard states that cable phase domain models are not popular and it goes as far as not to recommend the use of phase domain models. However, this does not reflect current practice as this model is currently the most accurate model available [34], [35]. Also, the standard does not consider the necessary corrections to the permittivity of the insulation due to the semiconductive layers, as demonstrated in [36] and [37].

It is also recommended in [12] to do an accurate representation of the cross-bonding points. The more cross-bonded sections are included into the model, the more accurate the simulation should be, but for some phenomena it is not necessary to have such a high level of detail, which will only result in longer and more laborious simulations.

The shunt reactor model recommended in [12], which consist only of an inductor with saturation, does not make any reference to mutual inductances, which have to be considered when the impact of some phenomena is to be assessed; one example is shown in [33].

Another recommendation from [12] that should be analysed is the depth of modelling necessary when representing the network. The standard recommends to model two-substations deep when doing a line energisation/re-energisation/fault application, but no special consideration is made for a cable-based network, which is electrically different from a OHL-based network, most notably the large capacitance and lower resonance frequencies of cable-based networks [38].

1.3 Problem formulation

The steady-state and transients results of a pure-cable grid or hybrid cable-OHL grid are substantially different from those typically obtained in pure-OHL grids. Therefore, in order to be able to perform accurate and efficient insulation co-ordination studies in HV cable based grids, specific guidelines should be provided.

The following goals have been set in order to fulfil the thesis objectives:

- to carry out theoretical descriptions of the main transient phenomena associated with HVAC cables, both for a stand-alone cable and cables integrated in a cable based transmission system;
- to perform field measurements in order to verify the different phenomena, validate the models and increase the knowledge about measurements' protocol;
- to study specific countermeasures for the various undesirable phenomena. The countermeasures should always be validated by the use of accurate simulations;
- to adapt and study the application and feasibility of the different countermeasures in complex transmission systems;
- to verify the existence of the different phenomena and the efficiency of the respective countermeasures, by performing simulations in the planned West Denmark Transmission System;
- analyse the current IEC Insulation Co-ordination guide [12] and suggest possible improvements;

The overall aim of the project is to provide guidelines to be used in future insulation co-ordination studies when planning the installation of HVAC cables in a transmission system with different levels of HVAC cables implementation.

1.4 Thesis outline

The thesis is divided into eight chapters. To give an overview of the thesis, a short outline is presented below:

I - Introduction

The first chapter provides an introduction to the thesis and gives an overview of the current knowledge within the field of the thesis subject. The introduction also provides a summary of the main transient phenomena on HVAC cables and outlines what is missing in the existing standards.

II - Description of predominant undergrounded transmission systems

This chapter provides a brief description of the main equipment present when installing HVAC cables, the different cable models available for the simulation of a cable transient and the main transient phenomena.

III - Implementation of the future HV grid in Jutland

Denmark's 132 kV and 150 kV grid is expected to be undergrounded by 2030. This chapter describes the system for West Danish grid as it is currently being planned by the Danish TSO and local transmission companies, and its implementation in PSCAD/EMTDC.

The conversation from PSS/E to PSCAD/EMTDC is validated by comparisons done with the PSS/E files used by the Danish TSO planning department, at steady-state conditions. The cable model is validated in the following chapter.

This chapter also describes the implementation of a pure-OHL system, equivalent to the planned 2030 system, which is used to compare the differences between having a predominantly undergrounded network and an OHL-based network.

IV - Field Measurements - Horns Rev 2 Cable

This chapter briefly describes full-scale measurements performed on a 170 kV cable connecting the Horns Rev 2 offshore wind farm to the transmission grid, where the cable energisation and de-energisation has been measured at the system voltage. The purpose of the measurements is to validate the simulation model, demonstrate some of the expected phenomena and increase the knowledge of measurements protocol.

V - Main transients and countermeasures affecting an HV cable system

The transient phenomena likely to affect a cable line are described in detail in this chapter. All the phenomena are simulated in PSCAD/EMTDC and mathematically demonstrated. Some of the phenomena are compared with measurements performed on Horns Rev 2 cable line.

The phenomena are first explained in simple systems designed specifically for the demonstration of each phenomena and are afterwards, if possible, shown for the Denmark's transmission system.

Whenever possible, countermeasures to the different phenomena are given. The countermeasures are always validated by means of software simulations and mathematical derivations.

VI - Insulation co-ordination studies

An insulation co-ordination study is a long, complex work that is more fluent if good guidelines and recommendations are available. The present IEC computational guide for insulation co-ordination [12] dates back to 2004 and misses some important aspects related with HVAC cables that have become more relevant in recent years. With the exception of lightning phenomenon no special distinctions are made between cables and OHLs, and no specific guidelines are provided for cable-based networks. Therefore, some specific phenomena and simulation details associated with a cable transient are not referred to in the standard.

This chapter provides guidelines that can be used for doing insulation co-ordination studies in an HV cable-based network. It also provides simplifications and information about the modelling detail that should be used when simulating the different phenomena.

VII - Harmonic studies on cable-based grids

A frequency spectrum calculated for a given point of a cable-based network differs from a frequency spectrum of an equivalent OHL-based network calculated for the same point.

This chapter analyses the frequency spectrum for a cable network and demonstrates how the spectrum can provide information about the energisation transient.

The chapter also analyses different modelling approaches that can be used when acquiring the frequency spectrum throughout EMTP simulations and the importance of the bonding in the results.

VIII - Systematic method for the simulation of switching transients

The chapter presents a systematic method that can be used for performing switching transient studies in a cable-based network.

IX - Conclusions

A conclusion stating the main achievements and contributions to the scientific field of the thesis concludes the thesis. A brief summary of all chapters is made and future work identified.

2. Description of predominant undergrounded transmission systems

2.1 Historical evolution

The invention of cable technology can be dated as far back as 1830, and the first underground cable installation 50 years later in 1880, in Berlin [39]. The reason for this temporal hiatus was the need to find a dielectric material capable of withstanding the conductor's heat and the strong electric field. This was only achieved with Ferranti's invention in 1880 of a multi-layer dielectric using lapped paper tapes, which was able to fulfil the necessary requirements. This technology was later improved by Emanueli in 1917, by impregnating the paper dielectric with low-viscosity insulating oil under permanent pressure. This improved the cable's thermal stability and made it possible for the first time to use cables for voltages higher than 100 kV [39].

The next big step forward in power cable technology occurred in the 1960s with the introduction of cross-linked polyethylene (XLPE) as dielectric, which allowed for higher operational temperatures (around 90ºC). Another common cable technology is high pressure gas-filled (HPGF) pipe type cable, which typically uses SF_6. These cables have relativity short lengths (<3000 m) and are not as common as XLPE cables. In this technology, the conductor consists of a rigid aluminium tube inside of an aluminium pipe, the space between the conductor and the pipe being filled with pressurised SF_6 gas. In order to increase the electric strength of the gas, the gas is used under a pressure of 3-5 bar [40].

The basic design of an HV/EHV cable remained unchanged during the last century. The main cable components are: the conductor, the insulation and the metallic screen (see Figure 2.1).

The conductor is typically made of copper or aluminium, and its main function is to carry the electrical current. The size of the conductor is determined by the current flowing through it, the cross-section being proportional to the current, and also by the dielectric used, at present mainly XLPE.

The insulation is one of the most important cable components. Its function is to ensure that there is no electrical connection between the conductor and the cable sheath. Therefore, the insulation must be capable of withstanding the cable's electric field [40] for steady-state and transient conditions.

The metallic screen/sheath's main function is to nullify the electric field outside of the cable, provide a return path for the charging current and to conduct fault currents to the earth. Other advantages of using metal screens are mechanical protection of the cable against accidental contact and minimization of proximity effect. The size of metallic screen depends of the value of the zero-sequence short-circuit currents that must be drained by the cable [44].

The use of semiconductive layers between the conductor and the insulation, and between the insulation and the metal sheath aims to ensure a cylindrical electric field and to avoid the formation of gaps or voids between the conductor/screen/metal sheath [45], preventing the occurrence of partial discharges.

Jackets or armours are added when the cable is installed in tougher environments for mechanical protection. Figure 2.1 shows a typical XLPE cable.

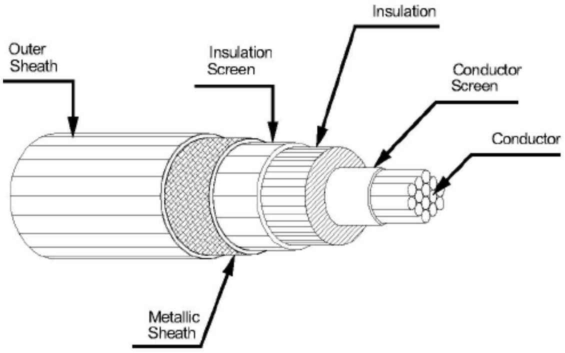

Figure 2.1 – A typical XLPE Cable [41]

New technologies using High Temperature Superconductors (HTS) are currently under development, most notably by the *American Superconductor Corporation, Southwire, NKT Cables* and *Nexans*. The main advantages of this technology are lower transmission losses when compared to traditional cables (1% instead of 5-8%) and its ability to transport up to 10 times as much power for the same thickness of copper (Figure 2.2) [42], [43].
The first demonstration projects were carried out in North America, in 2002 in Detroit and in 2005 in Ohio [42], but the high costs of this technology make it commercially unviable at present.

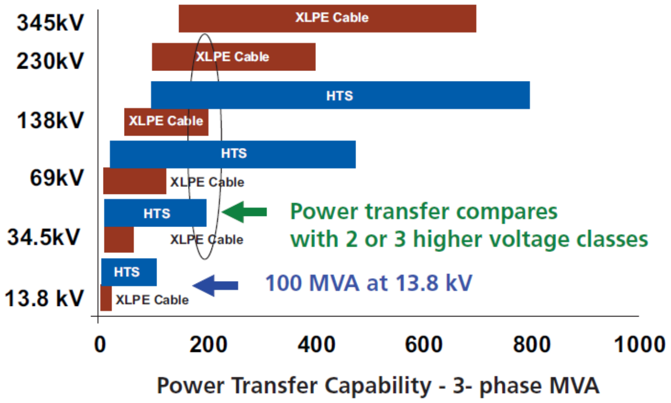

Figure 2.2 - Comparison of transfer power when comparing HTS technology with XLPE [43]

2.2 Shunt reactors

A cable capacitance is 10-20 times higher than the capacitance of an equivalent OHL [46]. Such high capacitance results in high generation of reactive power by the cable, which has to be consumed in order to ensure that the voltage does not increase.
The consumption of this reactive power is achieved by using shunt reactors, which are defined as an inductive reactance whose purpose is to draw inductive current from the system [48].
Shunt reactors are available in different construction designs. Figure 2.3 shows one of the possible configurations, a five-leg shunt reactor, where the three phases are mounted in the same core on different legs

[47]. To prevent the shunt reactor from going into saturation, the reactor is equipped with air gaps in the legs of the iron core.

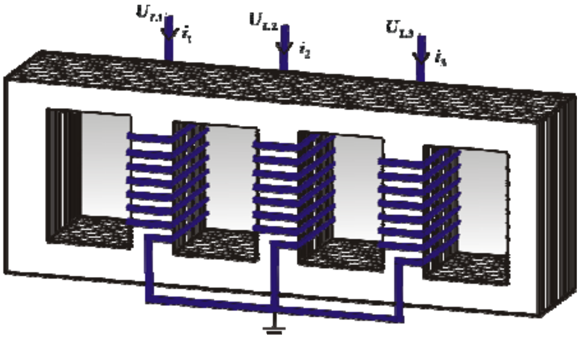

Figure 2.3 - Sketch of a five-leg shunt reactor [47]

The modelling of a shunt reactor is typically done by an inductor in series with a resistor. This modelling is very often accurate enough, but it will be demonstrated in this thesis that for some phenomena it is necessary to also model the mutual inductance between the shunt reactor phases and the shunt reactor saturation in order to achieve an accurate simulation.

The location of the shunt reactor(s) is of most importance both for steady-state, because of the maximum power transmission capability of the line and the Ferranti effect, and for transients, because of the interaction between the shunt reactor and the cable during the transient.

Figure 2.4 shows the loading of an open cable for different reactive power compensation schemes. The best location for the shunt reactor is in the middle of the cable as the current flows from the shunt reactor into both directions. As an example, the installation of the shunt reactor in one of the cable ends would result in two times the amount of reactive current flowing in the cable, and the installation of one shunt reactor in each of the cable ends would have the same effect as the installation of one shunt reactor in the middle of the cable [18].

In the same way, the reactive current flowing in the cable is reduced when using more shunt reactors distributed along the cable.

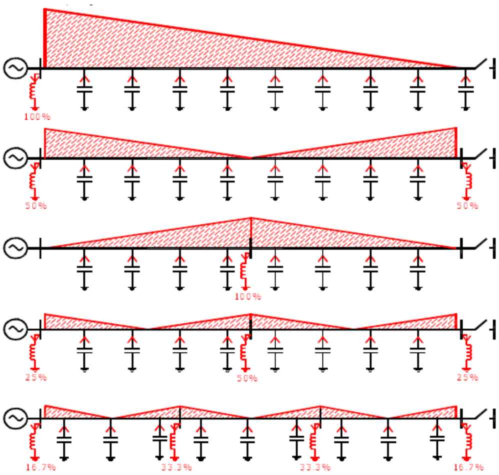

Figure 2.4 - Loading of an open cable for different reactive power compensation schemes [18]

2.3 Cable modelling

The modelling of a line, either a cable or an overhead line, can be obtained by applying the Kirchhoff's laws to the circuit shown in Figure 2.5. By doing this, (1) and (2) are obtained.

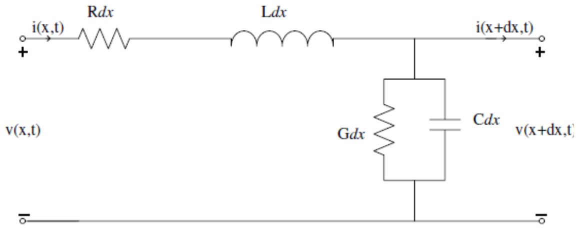

Figure 2.5 - Equivalent single-phase circuit of a length dx cable

$$v(x,t) - v(x+dx,dt) = Rdx \cdot i\left(x,t\right) + Ldx\frac{di\left(x,t\right)}{dt} \tag{1}$$

$$i\left(x,t\right) - i\left(x+dx,t\right) = Gdx \cdot v\left(x+dx,t\right) + Cdx\frac{dv\left(x+dx,t\right)}{dt} \tag{2}$$

The equations (1) and (2) can be simplified to respectively (3) and (4).

$$-\frac{\partial V\left(x,\omega\right)}{\partial x} = \left(R\left(\omega\right) + j\omega L\left(\omega\right)\right) \cdot I\left(x,\omega\right) \tag{3}$$

$$-\frac{\partial I\left(x,\omega\right)}{\partial x} = \left(G\left(\omega\right) + j\omega C\left(\omega\right)\right) \cdot V\left(x,\omega\right) \tag{4}$$

By defining the cable characteristic impedance (5) and propagation constant (6), (7) and (8) can be obtained from (3) and (4), respectively. These two equations can be written, for a defined frequency, in a matricial form as shown in (9) [51].

$$Z_0\left(\omega\right) = \sqrt{\frac{R\left(\omega\right) + j\omega L\left(\omega\right)}{G\left(\omega\right) + j\omega C\left(\omega\right)}} \tag{5}$$

$$\gamma\left(\omega\right) = \sqrt{\left(R\left(\omega\right) + j\omega L\left(\omega\right)\right) \cdot \left(G\left(\omega\right) + j\omega C\left(\omega\right)\right)} \tag{6}$$

$$V\left(x\right) = V_S \cosh\left(\gamma x\right) - Z_0 I_S \sinh\left(\gamma x\right) \tag{7}$$

$$I\left(x\right) = -\frac{V_S}{Z_0}\sinh\left(\gamma x\right) + I_S \cosh\left(\gamma x\right) \tag{8}$$

$$\begin{bmatrix} V_R \\ I_R \end{bmatrix} = \begin{bmatrix} \cosh(\gamma l) & -Z_0 \sinh(\gamma l) \\ -\dfrac{\sinh(\gamma l)}{Z_0} & \cosh(\gamma l) \end{bmatrix} \cdot \begin{bmatrix} V_S \\ I_S \end{bmatrix} \tag{9}$$

These equations do not consider the current flowing in the screen and are only accurate for steady-state conditions [51].

The types of cable models most commonly used are divided into two categories:
- Lumped parameter models: Nominal and exact pi-models
- Distributed parameter models/travelling wave models: Bergeron and frequency-dependent models

2.3.1 *Nominal pi-model*

The nominal pi-model is one of the simplest representations that can be done of a cable line. It includes the cable's total inductance, capacitance, resistance and conductance (usually not considered) modelled as lumped parameters. Figure 2.6 shows a typical nominal pi-model.

However, the use of this model is only acceptable for short distances as the errors become more noticeable when the cable length increases [52]. The error can be minimized by dividing the nominal pi-section into several shorter pi-sections.

Another problem of using nominal pi-models is that they do not provide an accurate cable frequency spectrum, and at higher frequencies they can indicate resonance frequencies that are not real [52].

This model is too inaccurate to be used for performing transient simulations. It should only be used for doing simple studies or performing auxiliary mathematic calculations.

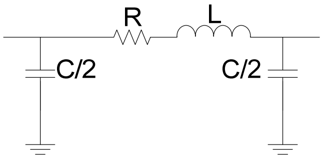

Figure 2.6 - Typical nominal pi-model

2.3.2 *Exact pi-model*

The exact pi-model, sometimes also called the equivalent pi-model, is a more advanced version of the nominal pi-model that considers the distributed nature of the impedance and admittance.

The impedance (Z) and the admittance (Y) of the nominal pi-model are multiplied by the first two terms of differential equations describing the wave propagation along the line, as shown in (10).

$$
\begin{aligned}
Z^{'} &= Z \cdot \frac{\sinh\left(\gamma l\right)}{\gamma l} \\
\frac{Y^{'}}{2} &= \frac{Y}{2} \cdot \frac{\tanh\left(\frac{\gamma l}{2}\right)}{\frac{\gamma l}{2}}
\end{aligned}
\tag{10}
$$

This model is accurate when used in the frequency domain for a single frequency and is normally used to validate other models [11].

2.3.3 *Bergeron model*

The Bergeron model is a constant-frequency model based on travelling wave theory [54]. The cable is considered to be lossless and its distributed resistance is added as a series lumped resistance.
Typically, the model is divided into two sections, it can be divided in more sections, but the differences in the results are minor [54]. The lumped resistance is inserted in each of the sections, ¼ at each end and ½ in the middle section. Figure 2.7 shows the Bergeron model for a cable line.

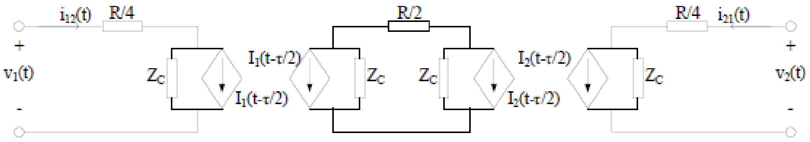

Figure 2.7 - Bergeron model for a cable line [54]

This model is a constant-frequency model and its use is only recommended for the cases when only one frequency is considered [55] (e.g. steady-state analysis).

2.3.4 *Frequency-dependent models*

As the name indicates, frequency-dependent (FD) models are models that have frequency-dependent cable parameters [54]. This is achieved by using the cable's propagation and admittance matrices.
When compared with the previous models, the use of the frequency domain increases the results accuracy. In FD-models all calculations are performed in the frequency domain and the solutions converted to time domain by the using transformations such as Fourier-transform or Z-transform [56].
An outline of the historical evolution of the different FD-models is available in [56], where it is shown that decades of research lead to the FD phase-model [34]. The FD-model is the most accurate model available at present for the modelling of cables [35].

2.3.5 Designing the cable in a EMTP software

A simulation is only as good as the model used. A cable model cannot represent all the details and layers of the cables, thus making it necessary to utilize simplifications and apply corrections to the model.
The most common corrections are described in the following pages. For a practical example of the described corrections, please refer to section 4.5.1.

Conductor resistivity

Most of the EMTP software cannot model segmented and stranded conductors, as it only allows the modelling of solid and hollow conductors, which due to skin effect are not used for cables with large cross-sectional areas. Figure 2.8 shows the different type of conductors quoted in the previous sentence.
Consequently, it becomes necessary to correct the conductor resistivity when modelling a segmented or stranded conductor, which are the two types normally used at transmission levels.

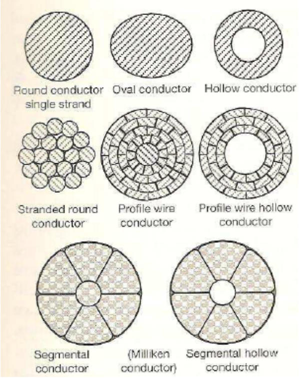

Figure 2.8 - Conductor types for HV cables [39]

A conductor's DC resistance is calculated as shown in (11), where *l* is the conductor length, *ρ* the material's electrical resistivity and *A* the conductor's cross-sectional area.

$$R_{DC} = l\frac{\rho}{A} \quad [\Omega] \tag{11}$$

The cross-section of a segmented conductor as given in the datasheet is not equal to $\pi.r^2$, where *r* is the conductor radius. This difference is used to correct the resistivity as shown in (12), where *ρ* is the material's resistivity and ρ' the corrected resistivity.

$$R_{DC} = l\frac{\rho}{A} = l\frac{\rho'}{\pi r^2} \Leftrightarrow \rho' = \rho\frac{\pi r^2}{A} \tag{12}$$

Insulation permittivity and thickness

Modelling a cables' semiconductive layers by means of EMTP software is normally not possible. However, it is shown in [36] and [37] that these layers should be considered when simulating a transient, as they have influence in the waveform.

The semiconductive layers are included in the model by changing two of the insulation parameters and assuming that the capacitance between the conductor and screen is constant [36]:

- The semiconductive layers are considered as belonging to the insulation, and the insulation thickness is increased by the thickness of the semiconductive layers;
- The insulation permittivity increases as shown in (13), where ε is the insulation permittivity, r_1 the conductor's outer radius, r_2 the screen's inner radius, a the insulation's inner radius and b the insulation's outer radius;

$$\varepsilon' = \varepsilon \frac{\ln\left(\frac{r_2}{r_1}\right)}{\ln\left(\frac{b}{a}\right)} \tag{13}$$

Screen resistivity

The screen of a cable is made of copper wires and/or a lead sheath; for environmental reasons the lead sheath is sometimes substituted by laminated aluminium [60]. Thus, the screen is not a solid conductor and similar to the central conductor its resistivity should be corrected.

The copper resistivity is corrected as shown in (14), where A_S is the screen's cross sectional area, r_2 the screen's inner radius and r_3 the screen's outer radius calculated as shown in (15), where n is the number of wires in the screen.

$$\rho'_{Cu} = \rho_{Cu} \frac{\pi\left(r_3^2 - r_2^2\right)}{A_S} \tag{14}$$

$$r_3 = r_2 + 2 \cdot \sqrt{\frac{A_S}{n\pi}} \tag{15}$$

When the screen consists of copper wires and aluminium sheath, the screen resistivity is corrected as shown in (16), where A_{Cu} is the copper wires area and A_{Al} the aluminium foil area [62].

$$\rho'_S = \rho'_{Cu} \frac{A_{Cu}}{A_{Cu} + A_{Al}} + \rho_{Al} \frac{A_{Al}}{A_{Cu} + A_{Al}} \tag{16}$$

Fitting parameters

The frequency domain equations for cable parameters cannot be directly simulated in the time domain, making it necessary to fit these functions to the time domain by means of transfer equations [63].
One of the main problems of cable fitting is that it does not guarantee the passivity of the cable, i.e. it does not guarantee that the cable does not generate any active power. Depending on the simulation conditions, these passivity violations may originate incorrect and unstable simulations [64].
Designing a cable in PSCAD/EMTDC requires the user to set a number of calculation parameters. By default these parameters have the values shown in Figure 2.9, and a correct choice of these values may mean the difference between a stable or unstable simulation.

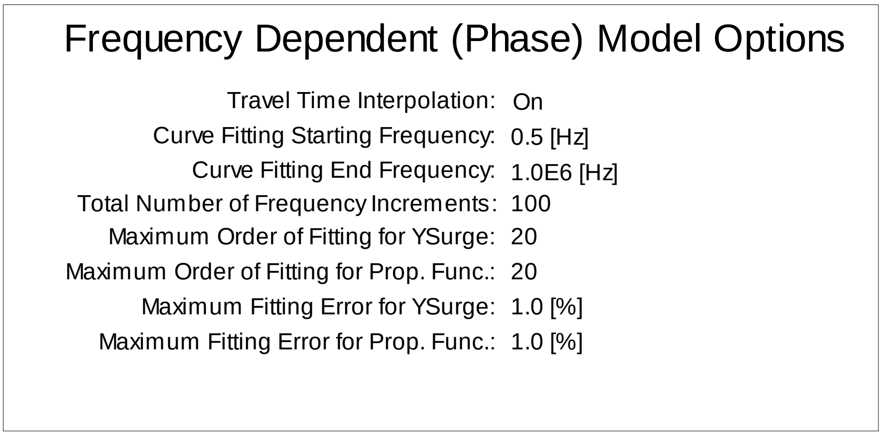

Frequency Dependent (Phase) Model Options

Travel Time Interpolation: On
Curve Fitting Starting Frequency: 0.5 [Hz]
Curve Fitting End Frequency: 1.0E6 [Hz]
Total Number of Frequency Increments: 100
Maximum Order of Fitting for YSurge: 20
Maximum Order of Fitting for Prop. Func.: 20
Maximum Fitting Error for YSurge: 1.0 [%]
Maximum Fitting Error for Prop. Func.: 1.0 [%]

Figure 2.9 - Default options when using frequency dependent phase models in PSCAD/EMTDC

The choice of these values is very often an empirical decision, and according to the Manitoba HVDC Research Centre, the developers of PSCAD/EMTDC, the default values are suitable for most of the simulations. Nevertheless, many users noticed that for the more complex simulations these parameters have to be changed in order to unsure a stable simulation.
The guidelines below suggest changes that should be made in these values in order to avoid unstable simulations.

- Travel time Interpolation: If the cable end is reached between time steps, the wave travelling time is interpolated, reducing the error. Should be always on.
- Maximum Order of Fitting for YSurge: The user should verify that the number of poles used in the Fitting function is not equal to the defined number. If equal, the number of poles should be increased, in order to assure that the error is inferior to the desired one.
- Maximum Fitting Error for YSurge and Prop. Func.: Last parameters to be changed. If the function is unstable or the number of poles insufficient, the error can be increased.
- Max. Order per Delay Grp. for Prop. Func.: The user should verify that the number of poles used in the Fitting function is not equal to the defined number. If equal, the number of poles should be increased, in order to assure that the error is inferior to the desired one.

The choice of the time step is also important for a good simulation. A too large time step can either result in unstable or inaccurate simulations. A common rule of thumb is to select a time step that is 10 times smaller than the smallest wave travelling time in the system [61].
If the system has small cable sections, this leads to very long simulation times. This situation can be minimised through simplifications in the simulation model, as explained later in this thesis.

2.4 Transients phenomena

Chapter 1 briefly mentioned several phenomena associated with the use of HVAC cables. A summary and brief description of the different phenomena is provided in the following pages. At the end of the section, a table summarizes the main risks that each phenomenon poses to the system.

2.4.1 Cable Energisation - Switching Overvoltage

A cable energisation may originate a transitory overvoltage, whose amplitude depends on the moment in which the cable is connected. If the circuit breaker is closed when the voltage at its terminals is zero, the overvoltage is minimum, ideally zero, but if the connection is made for a peak voltage, the overvoltage is maximum [17].
The reason for this difference is the charging of the cable's capacitance and the energy oscillation between the cable's capacitance and inductance. To better understand this phenomenon it will be explained using a simple LC series circuit, as the one shown in Figure 2.10, whose simulation plot is shown in Figure 2.11.

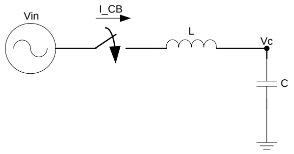

Figure 2.10 - LC Circuit

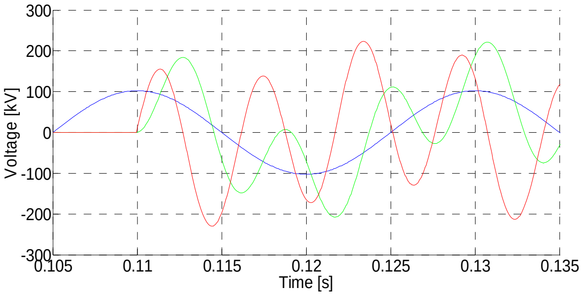

Figure 2.11 - Voltages and current (current not at scale) for Figure 2.10 circuit when connected at peak voltage. Blue: Vin, Green: Vc, Red: I_CB

In this system, both capacitor and inductor are initially discharged, but as the voltage in the capacitor (*Vc*) has to be continuous when the circuit breaker closes for a voltage value that is not zero, the capacitor has to be charged through the inductor, initiating a transient. After a short moment, the voltage in the capacitor is equal to the source voltage, but at that instant the current in the inductor is at peak value (see Figure 2.11) and by energy conservation it can not become zero immediately. Thus, the voltage in the capacitor continues to increase, exceeding the source voltage, while the current decreases to zero, when the current crosses zero, *Vc* reaches a peak value and the capacitor starts to discharge [16].

As the voltage source is sinusoidal, *Vc* matches the source voltage at different points, for each transient cycle at system resonant frequency. Thus, the amplitude of *Vc* is different for each cycle, as the reference voltage for the capacitor terminals, is constantly changing.

A cable consists of distributed capacitance, inductance and resistance. Thus, a cable's energisation waveform is initially similar to the energisation of a LC circuit, but with damping due to the resistance. Figure 2.12 shows the voltage and current during the energisation of a 60 km, three single-core 400 kV cable, where the voltage behaviour previously described can be observed.

The voltage waveform depends on the connections instant, i.e. the voltage difference at the circuit breaker terminals in the closing moment, the cable length, the shunt compensation and the short-circuit power level [13].

Because of the fast damping, the overvoltage is less than 2 pu at the first peak, assuming that the source voltage is 1 pu and the short-circuit power infinite (the short circuit power level influence is explained in a later section).

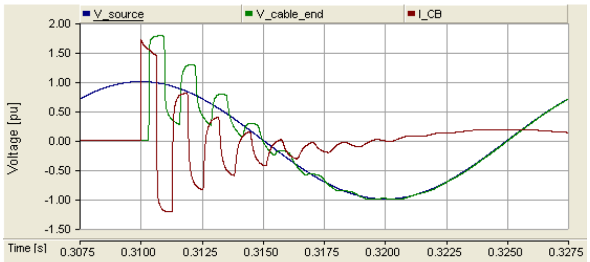

Figure 2.12 - Voltages and current (current not at scale) in a cable energised at peak voltage. Blue: Source Voltage; Green: Voltage in the cable receiving end; Red: Current into the cable

2.4.2 Cable Energisation - Zero-missing phenomenon

Zero-missing can occur when compensating for more than 50% of reactive power of a cable using shunt reactors and is characterized by having a current not crossing zero point during several cycles after energizing the cable+reactor system, which may be hazardous to the system.

An example of this is a fault in the cable during its energisation. If zero-missing is present, it may be impossible to open the poles of a circuit breaker (CB) in the healthy phases without risking damaging the CB [21].

When a shunt reactor is energised, both an AC and a decaying DC current component appear. The decay of the DC current component may take several seconds to disappear depending on the cable and shunt reactor resistances, and its initial value depends both on the voltage value in the shunt reactor's terminals and the reactive power compensation level, by other words the shunt reactor inductance.

The AC current component has a phase difference of almost 90° to the voltage. Due to energy conservation the current in a shunt reactor must be continuous, therefore the DC current has a value equal to that of the AC current in the connection moment, with an opposite sign. So, if the shunt reactor is energized when the voltage is zero the DC component will be at its maximum, with a value which in theory is equal to the peak value of the AC current component.

While the shunt reactor is inductive, the cable is mostly capacitive. Therefore, the AC current component in the cable is capacitive and is approximately in phase opposition to the AC current component in the shunt reactor. The current in the CB is the sum of these currents, and as they are in phase opposition there is an annulment and the resultant current in the CB may become dominated by the decaying DC component of the reactors.

Using the circuit on Figure 2.13 to explain the phenomenon, the AC current in the shunt reactor is given by (17) and in the CB by (18):

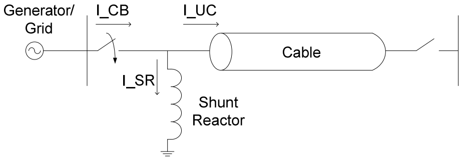

Figure 2.13 - Single-line diagram of a system with cable, shunt reactor and circuit breaker

$$I_{SR} = -x \cdot I_{UC} \tag{17}$$

$$I_{CB} = I_{SR} + I_{UC} = (1-x) \cdot I_{UC} \tag{18}$$

Where: I_{SR} is the AC current component in the shunt reactor, I_{CB} is the AC current component in the circuit breaker, I_{UC} is the AC current component in the cable and x is the reactive power compensation ratio

If the reactive power compensation ratio is higher than 50%, the AC current component in the shunt reactor is larger than the AC current component in the CB, and the DC component in the CB may be higher than the AC component. In this situation the current does not cross zero during several cycles, and zero-missing phenomenon occurs.

Figure 2.14 shows an example of zero-missing phenomenon for a 150 kV, 50 km cable, with 70% of the reactive power being compensated by a shunt reactor installed at the cable end. The system is energized when the voltage is zero, and therefore the value of the DC component is at maximum.

Figure 2.14.a shows the currents in the CB (blue), in the shunt reactor (green) and in the cable (red). It should be noted that the current in the CB does not cross zero. The second graph shows the current in the CB for a period of 5 s, please observe that it takes several seconds before the current crosses zero for the first time. The X/R ratio of a shunt reactor may vary quite a great deal from approximately 1350 [57], which means a decay time constant of 4.3 s, to 600 [58] meaning a decay time constant of 1.9 s. With a decay time constant of 4.3 s, the time needed for the current in the CB to cross zero is calculated by (19).

$$t = -\frac{L_s}{R_s} \ln\left(\left|\frac{x-1}{x}\right|\right) \Leftrightarrow t = -4.3 \cdot \ln\left(\left|\frac{x-1}{x}\right|\right) \tag{19}$$

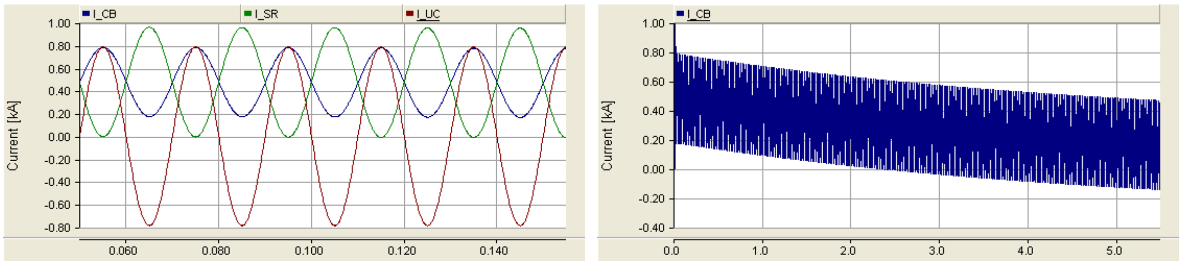

(a) (b)

Figure 2.14 - Zero-miss Currents for 70% Shunt Compensation

2.4.3 Cable Energisation - Short-circuit power level influence

The peak value of the switching overvoltage and its duration are functions of the grid short-circuit power [13]. The lower the short-circuit power level, the longer the transient duration and the lower the high-frequency component.

A problem that may arise when energising long HVAC cables in very weak networks is the appearance of a low-frequency component originating a temporary overvoltage. This low-frequency component may take several cycles to be damped, possibly resulting in damage to and a shorter life of the surge arresters and remaining equipment.

Figure 2.12 shows a typical cable energisation waveform for an infinite short-circuit power level. Figure 2.15 shows the energisation transient waveform for different types of short-circuit powers using the same cable. Note the decrease of the high-frequency component, when compared with Figure 2.12, and the longer duration of the transient. In Figure 2.15.b a low frequency component is shown, which, when added to the power frequency component, results in a voltage higher than 2 pu.

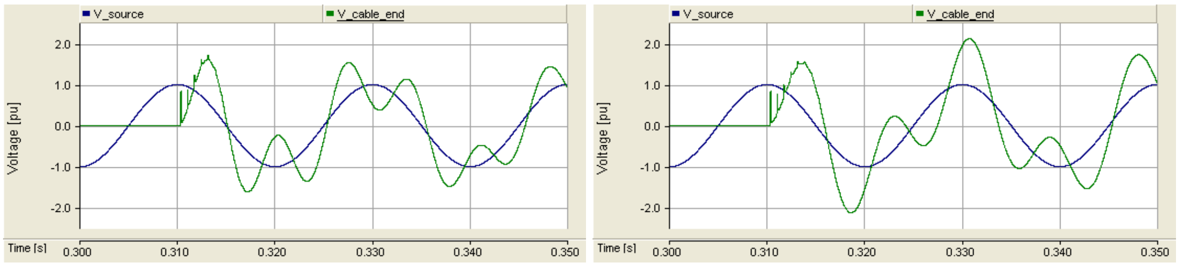

(a) (b)

Figure 2.15 - Voltages in the cable sending and receiving end during the energisation. a) S_{CC}= 5000MVA; b) S_{CC}=3400MVA

2.4.4 Cable Energisation - Energisation of cables in parallel

Electrically, cables are mainly capacitive elements. So, the energisation of cables in parallel can be regarded as similar to the energisation of capacitor banks in parallel [24].

When energising capacitor banks in parallel, the energisation of the second capacitor bank results in a higher resonance frequency and amplitude of the inrush current when compared with the energisation of the first capacitor bank. For instance, the current amplitude can go up to 100 pu [28] or even 200 pu [59].

A cable's capacitance is distributed along the cable, and thus the energisation of cables in parallel does not result in so large currents, but the phenomenon is still noticeable.

Figure 2.16 shows an example of the phenomenon. When the circuit breaker in the second cable is closed, the energy stored in the "capacitors" of the already energised cable is transferred to the "capacitors" of the cable being energised, as indicated by the arrows.

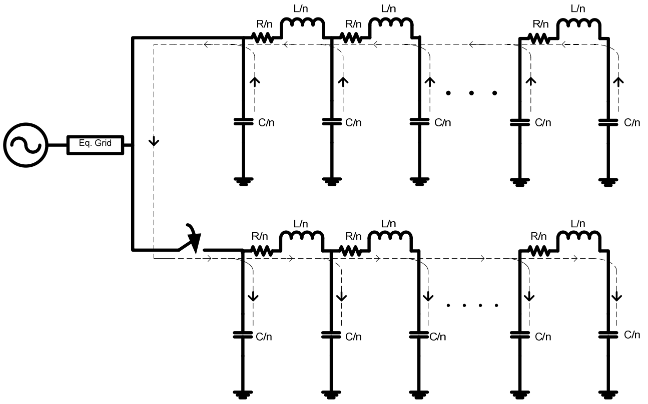

Figure 2.16 - Equivalent circuit for the energisation of cables in parallel

The amplitude and frequency of the inrush current are influenced by the cable lengths and the short-circuit power behind the busbar, both increasing when the short-circuit power decreases.

Figure 2.17 shows an example of the energisation of two cables of equal length in parallel. Figure 2.17.a shows the current in the first cable to be energised and Figure 2.17.b the currents in both cables during the energisation of the second cable. The magnitude and frequency of the current are both larger for the energisation of the second cable.

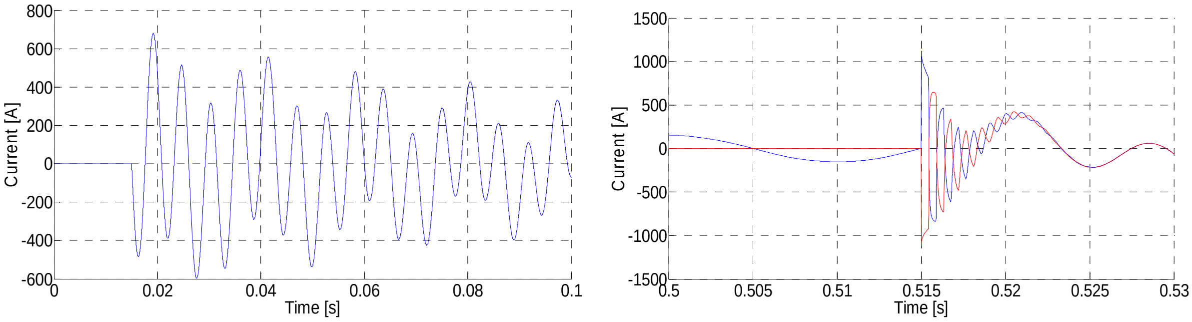

(a) (b)

Figure 2.17 - a) Current in Cable A during the energisation; b) Currents in the sending ends of Cable A and Cable B during the energisation of Cable B (Blue: Cable A; Red: Cable B)

This phenomenon is relevant as circuit breakers have a maximum tolerable amplitude and frequency for the inrush currents [29]. The exceeding of this limit results in a worn of the arcing contacts to a cone like shape, the consequent degradation of the circuit breaker efficiency and an increasing number of pre-strikes [30].

2.4.5 Cable Energisation - Resonance between the cable and transformer

Frequency scans are used to identify resonance points and resonant frequencies. A cable system tends to have lower resonant frequencies, because of higher capacitance or line charging. The first resonant frequency can be estimated by (20) [11].

$$f = \sqrt{MVA_s / MVA_c} \tag{20}$$

Where: f is the per-unit frequency of the resonance, MVA_s is the system short circuit strength at the cable, and MVA_c is the cable's reactive power at nominal voltage. Local shunt compensation can be added to MVA_s.

Resonances can be divided into two types [52]:
- Series resonance
- Parallel resonance

The series inductance of a transformer can create a series resonance circuit with the capacitance of a cable. This situation is characterised by a low-impedance path for the harmonic currents at the resonance frequency, which may result in high-voltage distortion and overvoltages.

Figure 2.19 shows, as an example, the frequency spectrums of the circuits shown in Figure 2.18.

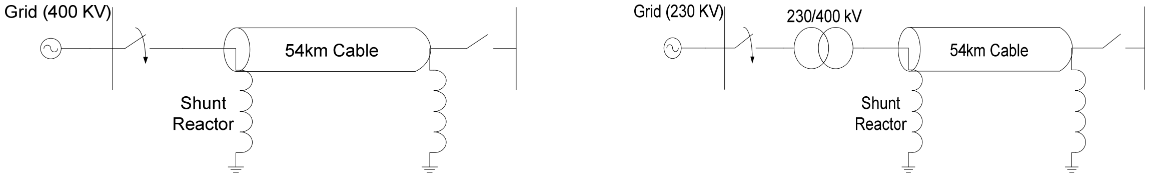

(a) (b)

Figure 2.18 - Single-line diagram of the energised system. a) Without transformer; b) With transformer

It can be seen that the first series resonance point is at approximately 535 Hz in pure cable systems, and that the series resonance point shifts to 100 Hz when a transformer is inserted in the sending end.

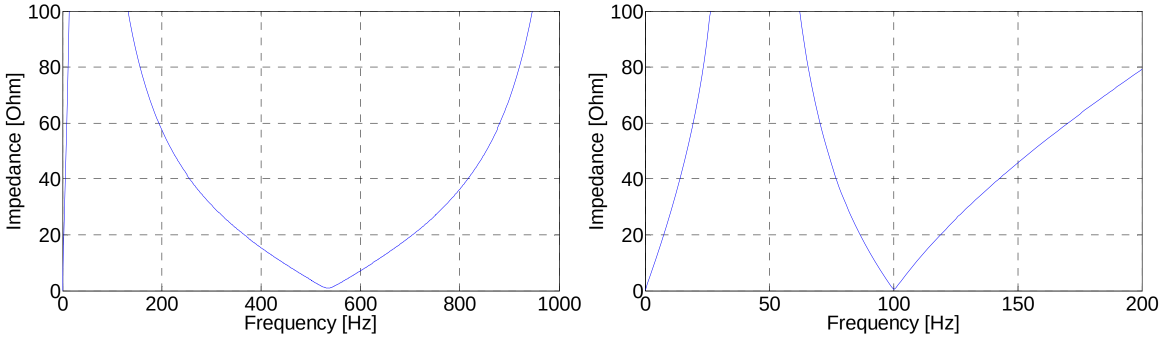

(a) (b)

Figure 2.19 - Frequency spectrum of the system. a) Without transformer; b) With transformer

The shifting of the resonance frequency will affect the energisation plots, as can be seen by comparing Figure 2.20 with Figure 2.21.

Figure 2.20 shows the cable energisation without a transformer, the noticeable element being a high frequency component during the first milliseconds. The resonance frequency is shown in Figure 2.19.a frequency spectrum.

The energisation simulation is redone, but with the cable being energised through a 230/400 kV transformer. The correspondent energisation plot is presented in Figure 2.21. The cable+transformer system had a series resonance frequency at 100 Hz (see Figure 2.19.b), which can be seen in the energisation transient waveform. Due to the transformer inductance, the 100 Hz frequency component decays slower than the high frequency component associated with the energisation of a cable without transformer, resulting in a longer transient and respective longer overvoltage.

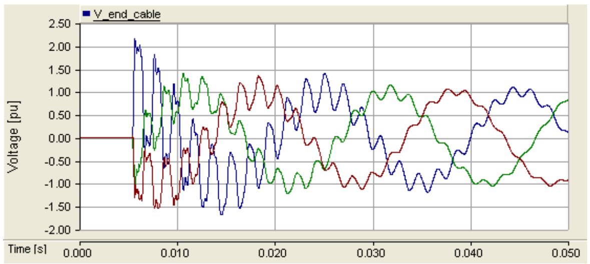

Figure 2.20 - Energisation transient without transformer

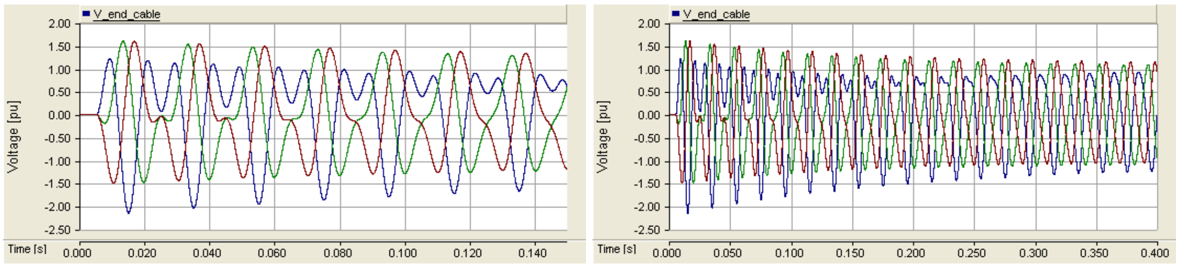

(a) (b)

Figure 2.21 - Energisation transient with transformer. a) First 0.15s; b) first 0.4s

2.4.6 Cable Energisation - Transformer inrush currents

A transformer's core may saturate during the energisation of the transformer, generating inrush currents that may go on for many seconds [52]. The harmonic content of the inrush currents is generally different for each cycle and due to the non-symmetrical waveform, the inrush current contains all the harmonic components: DC, fundamental, second, and so on [53].

If one these harmonics matches the system resonance frequency, an overvoltage is generated, the damping of which may take several seconds. Figure 2.22 shows an energisation transient equivalent to the one shown in Figure 2.21, but taking account of the transformer's saturation and resulting inrush currents. Note that in this situation the overvoltage is both higher and longer.

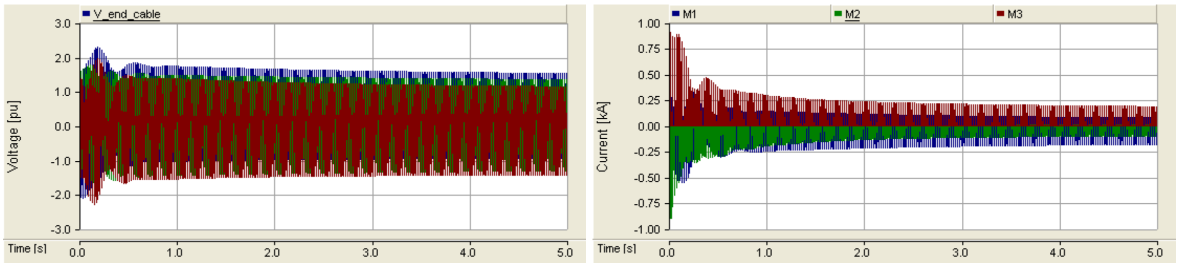

(a) (b)

Figure 2.22 - Energisation transient with saturated transformer. a) Voltage in the cable receiving end; b) Magnetisation currents

This overvoltage is present because the cable+transformer system has its series resonance at 100 Hz, which is excited by the second harmonic of the inrush current generating the overvoltage. As example, Figure 2.23 shows an energisation transient equivalent to the one shown in Figure 2.22 but for a shorter cable. The new cable has a lower total capacitance and therefore there is a shift in the resonance frequency, which is now 116 Hz and not excited by the inrush currents. Consequently, the transient is similar to the one that would be obtained by using an ideal transformer with no saturation (see Figure 2.21).

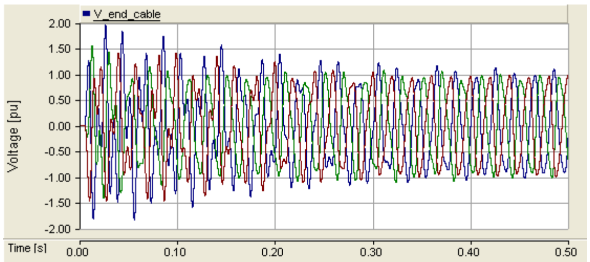

Figure 2.23 - Energisation transient with saturated transformer but no resonance frequency being excited

2.4.7 Cable Energisation - Parallel Resonance and Ferroresoance

The shunt reactor inductance and the cable capacitance can originate a parallel resonance circuit. A parallel resonance is characterized by a high impedance for the resonance frequency, and therefore the current does not flows into the resonance circuit unless it has nowhere to flow, i.e., the other possible paths have even larger impedances. [9].

Such situation may occur when a transformer is energised through a cable (see Figure 2.24). If the transformer is distant from a voltage source, or the cable is connected to a weak grid, there is a high impedance between the transformer and the source, which may resulting in the energisation currents flowing into the parallel resonance circuit instead of the voltage source.

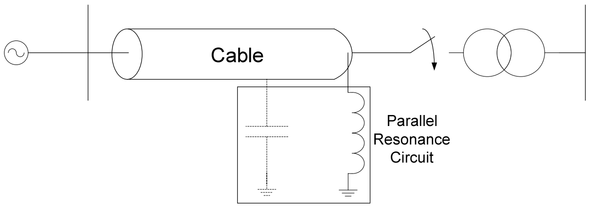

Figure 2.24 - Parallel resonance due to transformer energisation at the far end

Another resonance phenomenon associated with the use of a transformer in series with a cable is ferroresonance. Ferroresonance consists of interactions between capacitors and saturable iron-core conductors [49], [50]. It can occur when the transformer and cable become isolated, and the cable capacitance is in series with the transformer magnetising characteristic. This may lead to sustained temporary overvoltages that damage surge arresters and other equipment.

If one phase of a circuit breaker opens while the other two remain closed the open phase of the transformer is still energised through the mutual inductance to the other phases. Overvoltage occurs in all phases, with the highest magnitude occurring on the open phase. This type of ferroresonance is more common in low-voltage and medium-voltage systems [11].

2.4.8 Cable De-energisation - Cable+shunt reactor disconnection

When a cable is disconnected the energy stored in the cable has to be dissipated, which may take several seconds, because of the low cable resistance and high capacitance.

The disconnection of a cable is similar in many ways to the disconnection of a capacitor, and it is easier to understand if capacitance switching is explained first. Figure 2.25 shows the single-line diagram of the RLC circuit used to simulate a capacitor switch-off.

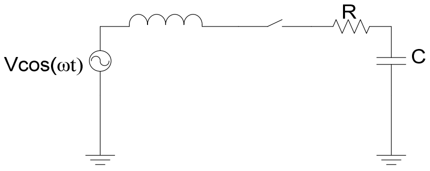

Figure 2.25 – Capacitance Switching-Single line diagram

A capacitor's current leads the voltage by approximately 90°. Thus, when a capacitor is disconnected, it is fully charged and has a voltage at its terminals of ±1 pu. The capacitor's energy is damped through the resistor, and as the resistor value is usually low when compared with the capacitance, the complete de-energisation of the capacitor can take a long time.

As an example, Figure 2.26 shows the typical de-energisation of a capacitive load. The de-energisation of a cable if it is not connected to a shunt reactor will be similar.

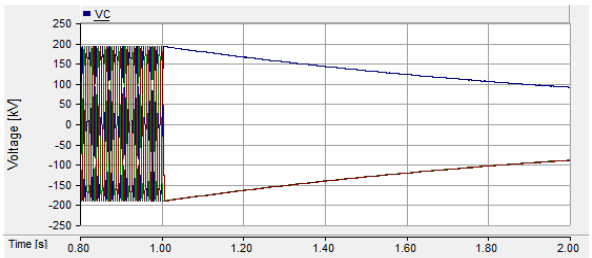

Figure 2.26 – Typical de-energisation of a capacitive charge

If the cable is connected to a shunt reactor and they are de-energised together, the voltage is no longer a decaying DC component, but a decaying AC component oscillating at resonance frequency, as shown in Figure 2.27.

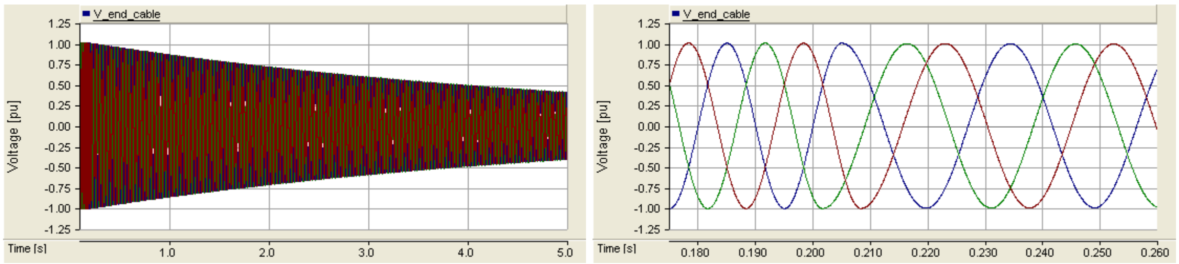

(a) (b)

Figure 2.27 - Cable+shunt reactor disconnection. a) First 5s of cable de-energisation; b) Zoom of the disconnection instant

In this situation, no overvoltage is expected, but this is because mutual inductances between the shunt reactor phases were not taken into consideration.

When the cable is disconnected the three phases are disconnected in different moments, and there is normally a time difference of approximately 3.333 ms between the disconnections of each phase. After the first phase is disconnected the voltage and current in that phase start to oscillate at resonance frequency while the voltage and current in the other two phases continue to oscillate at system frequency. Therefore, the system is not balanced after the disconnection of all the three phases, and the phase difference between phases is no longer 120º [33].

The mutual inductance in the shunt reactor make the voltage in each phase dependent on the current in the other two phases, possibly resulting in situations like the ones illustrated in Figure 2.28, where an overvoltage in phase C is presented. The plots corresponding to the vectorial representation made in Figure 2.28 are shown in Figure 2.29.

A similar situation can occur in hybrid cable-OHL lines due to capacitance between the phases of the OHL [16], [25].

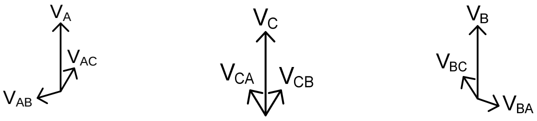

Figure 2.28 - Vectorial representation of the voltages after the disconnection all the three phases

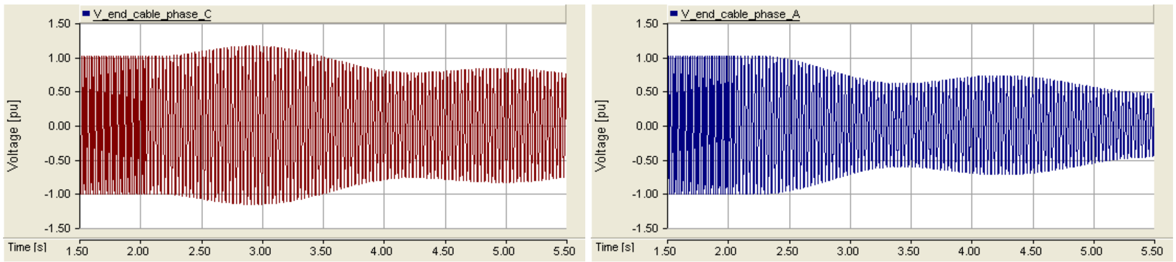

(a) (b)

Figure 2.29 - Voltage at the cable end. a) Phase C; b) Phase A

2.4.9 *Cable De-energisation - Restrike*

The disconnection of HV underground cables may, if unsuccessful, cause a restrike in the circuit breaker, resulting in the correspondently high overvoltages, potentially damaging the cable and nearby equipment. Due to the high cable capacitance, voltage damping is slow, resulting, in a voltage of approximately 2 pu at the circuit breaker terminals half a cycle after the disconnection. In case of restrike in that instant, it is theoretically possible to attain an overvoltage of 3 pu [28] (reference for a capacitor bank).

An example of a cable restrike is shown in Figure 2.30.

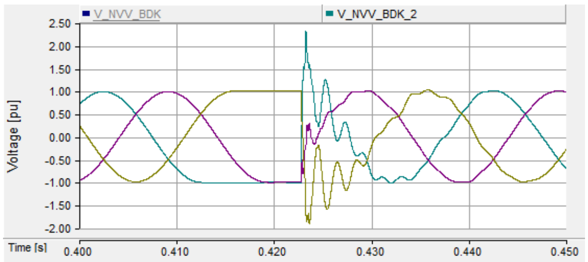

Figure 2.30 - Voltage in the cable receiving end during a restrike

Restrikes can also take place in hybrid cable-OHL lines. During re-energisation of a hybrid line there are reflections and refractions in the cable-OHL junction point, and if the restrike occurs in the cable end CB, the voltage is magnified in the junction point resulting in a larger overvoltage.

As an example, for a hybrid line equivalent to the cable (i.e. same length) used in Figure 2.30 the overvoltage would be 4.3 pu, 1.75 times higher than the overvoltage associated with the cable restrike, 2.45 pu. Such large overvoltage may damage the equipment, and it is therefore necessary to know the precise peak overvoltage when purchasing the surge arrester.

2.4.10 Ferranti Effect

Ferranti effect is a very well known phenomenon described in many books and papers, examples are [13], [18], [24] and [27], consisting in a power frequency voltage at the receiving end being higher than at the sending end.

For an unloaded cable the voltage in the receiving end is calculated for a lossless line by (21) [13], where V_1 and V_2 are the sending and receiving end voltages respectively, L the line inductance, C the line capacitance and l the line length.

$$V_2 = V_1 \frac{1}{1 - \frac{\omega^2 LCl^2}{2}} \tag{21}$$

Observing (21), it should be noted that the voltage increase is more accentuated in cables than OHLs, because of the larger capacitance of the cables. The voltage increase also depends on the square of the cable length; a situation that is especially relevant in Denmark where the installation of long cables is planned.

2.4.11 Phenomena categorization

The IEC standards [10] and [12] define the overvoltages into four different types:

- Temporary overvoltageOs (TOV). TOV are characterised by their amplitude, voltage shape and duration [10] and may have a long duration, up to one minute. These overvoltages can be caused by faults, switching conditions, resonance conditions and non-linearities.
- Slow-Front Overvoltages (SFO). SFO are characterised by their voltage shape and amplitude, they have a front duration of up to some milliseconds and are oscillatory by nature [10]. SFO can be caused by line energisations and de-energisations, faults, switching of capacitive/inductive elements (e.g. cables and shunt reactors) or lightning strokes.
- Fast-Front Overvoltages (FFO). FFO are mainly associated with lightning strokes and are characterized by the standard lightning impulse wave (1.2/50 μs) [10].
- Very-Fast-Front Overvoltages (VFFO). VFFO are associated with GIS switching operations and SF_6 circuit-breaker re-ignitions [12], topics that are not dealt with in this thesis.

The phenomena described in this chapter fall into the three first overvoltage types, especially TOV and SFO.

The guidelines for the proper simulation of these phenomena are available in [12], but as was pointed out earlier, the standard does not focus on cable-based systems and does not take account for the specific characteristics of a predominantly undergrounded cable electricity transmission system.

2.4.12 Summary

Table 2.1 presents the probability associated with each phenomenon and corresponding risk.

Table 2.1 - Phenomena probabilities and risks

Phenomenon	Peak overvoltage [pu]	Worst Case Probability	Risk of damages	Category
Normal Energisation	<2	Synchronize switching: Very Low Random switching: High	Low	TOV/SFO
Zero-Missing[1]	-	Synchronize switching: Very High Random Switching : Medium	Medium-Low	-
Weak Grid Energisation	>2[2]	Very High	High[3]	TOV
Energisation of cables in parallel	Inrush current problem	Synchronize switching: Very Low Random switching: Low-Medium	Low[4]	SFO
Energisation resonance	Variable	Medium-Low	Medium-High	TOV
Cable + shunt reactor de-energisation	<1.2pu	High	Very Low	TOV/SFO
Restrike	>2	Very Low[5]	Very High	SFO/FFO
Ferranti	<1.2pu[6]	Medium[6]	Low[7]	-

[1] Assuming >50% reactive power compensation

[2] Depends on the short-circuit power

[3] The overvoltage has a long duration

[4] Reduces the circuit breaker lifetime

[5] Assuming type C2 circuit breakers

[6] Assuming proper reactive power compensation

[7] It may increase other phenomena's voltage

This chapter described a typical HVAC cable and shunt reactor. The different models available for the simulation of cable systems were briefly described, and the advantages and disadvantages of each model were pointed out. It was concluded that frequency-dependent phase models should always be used for transient studies. Several cable transient phenomena were explained, and the risks posed by these phenomena to an electricity transmission system were summarised.

3. Implementation of the future HV grid in Jutland

3.1 Introduction

The Danish TSO (Energinet.dk) is presently planning the future HV grid in Denmark. Denmark's HV network is divided into two areas, Eastern and Western Denmark, which are connected by a 400kV, 58km DC link named Storebælt, as shown in Figure 3.1.
The two AC systems are decoupled as the East Danish grid is connected to the Nordic system (Eastern Denmark, Norway, Sweden and Finland) and the West Danish grid is connected to the European Continental system, which consists of a total of 25 countries [66].

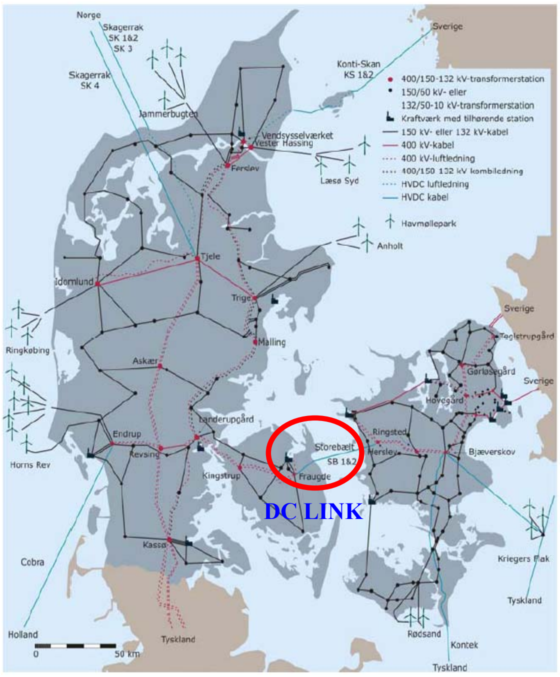

Figure 3.1 - East and West Danish electricity transmission grid in 2030 according to Energinet.dk's cable action plan [3]

The majority of the simulations and analyses made in this thesis are based on the 2030 West Danish grid, which is currently being re-designed by Energinet.dk planning department, as a base case. In 2030, the West Danish transmission network will be fully undergrounded at the 150 kV voltage level, but OHLs will still be used at the 400 kV voltage level. According to the existing grid plan, the network will comprise a total of 114 165 kV-cables covering a total of 2627.3 km, 27 400 kV-OHL covering a total of 1215.4 km and 36 165/400 kV-transformers. The network single-line diagram is available in Appendix A.

3.2 Data conversion to PSCAD/EMTDC

The network is implemented in PSCAD/EMTDC by converting the PSS/E file corresponding to the 2030 grid. The PSS/E file contains the entire West Danish network for the 10kV-400 kV voltage levels together with a part of the north German HV network. Carrying out such a conversion manually is a long, slow process and could easily result in modelling mistakes.

E-Tran is software designed to convert files from PSS/E to PSCAD/EMTDC [67]. In order to properly convert to PSCAD/EMTDC, the PSS/E files should contain load-flow information, as this information is used to initialise the PSCAD/EMTDC circuit, i.e. to design the N-port equivalent circuit [67]. The load flow information was obtained by solving a balanced power flow in Digsilent PowerFactory and exporting the resulting file to PSS/E.

In PSS/E, a line consists solely of resistance, reactance, susceptance, length and other minor information [68]. This information is sufficient to design lumped-parameters models of the lines, e.g. pi-models, but it is insufficient when it comes to designing the more complex frequency-dependent models, which require information about the line geometries and materials.

Therefore, it is not enough to simply convert the PSS/E data, as in PSCAD/EMTDC the lines would be represented by means of pi-models. The solution for this situation is to create an extra library containing information about all the lines in the system, where all the cables and OHLs are designed in detail by means of FD-models.

3.2.1 Cable modelling

For practical reasons, Energinet.dk' s planning department is considering to let the cables at the 150 kV voltage level have only one of three cross-sections (800 mm^2, 1200 mm^2 and 2000 mm^2). The cable data used in the PSS/E files is obtained from [69].

The resistivity of the cable conductor, together with the insulation thickness and permittivity, are corrected as explained in section 2.3.5 (for a practical example see chapter 4.5). The cables were assumed to be installed in trefoil formation.

Table 3.1 shows the cables parameters and layouts, while Figure 3.2 shows the layout of the 2000 mm^2 cable.

A library containing the 114 cables was made in PSCAD/EMTDC. The cables were modelled with one major cross-bonded section divided into three equal minor sections. The total length of the major section is the cable line total length. The bonding grounding resistance is set to 1 Ω and the cables used to cross-bonding the screens are assumed to be 1m long with an inductance of 1 μH/m. Figure 3.3 shows one of the 114 cable lines modelled.

The number of cross-bonded sections is relevant for the analysis of some phenomena. For those cases, the cable is divided into more sections. For more information consult section 6.3.3.

For the validation of the cable model see chapters 4.5 and 4.6.

Table 3.1 - Cables parameters and geometries

Cross-section area	800mm^2	1200mm^2	2000mm^2
Conductor outer radius	16.85	22	28
Conductor resistivity	3.122-8	3.547e-8	3.448e-8
Conductor relative permeability	1	1	1
Insulation outer radius	35.05	42	48
Insulation relative permittivity	2.796	3.018	3.001
Insulation relative permeability	1	1	1
Screen outer radius	35.479	42.358	48.314
Screen resistivity	1.72e-8	1.72e-8	1.72e-8
Screen relative permeability	1	1	1
Outer Insulation outer radius	41.5	47	54.5
Outer Insulation relative permittivity	2.3	2.3	2.3
Outer Insulation relative permeability	1	1	1

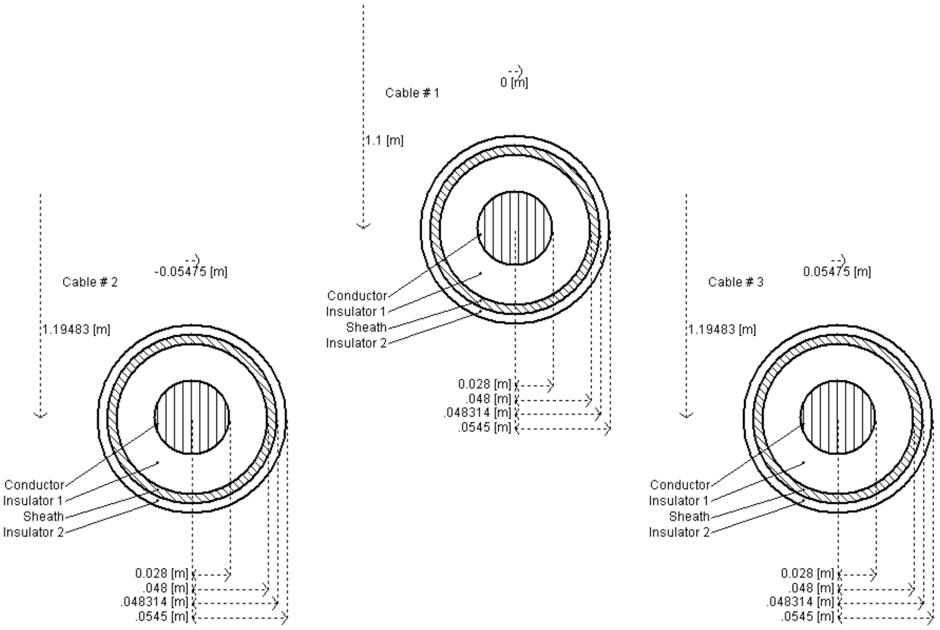

Figure 3.2 - 2000 mm^2 cable layout and configuration

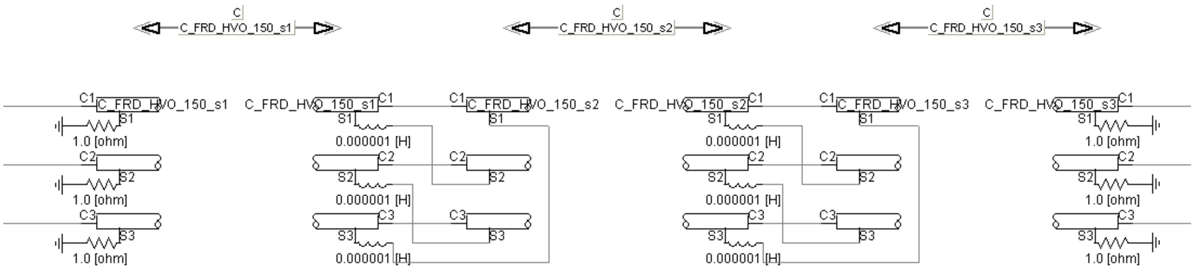

Figure 3.3 - Example of cable line layout

3.2.2 OHL Modelling

The 400 kV OHLs will not be replaced by cables before 2030, and therefore real data can be used in their modelling. The data used for the 400 kV OHLs can be seen in Figure 3.4. The modelling is performed by means of FD-models.

As is the case with the cables, a library comprising all 27 OHLs was created in PSCAD/EMTDC.

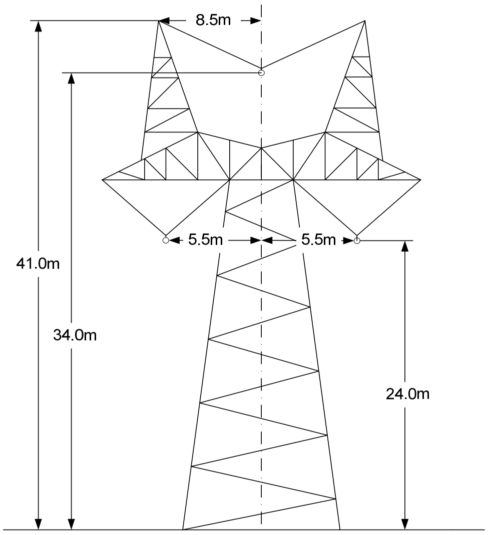

Nominal Voltage [kV]	400
Nominal Current [A]	2440
Conductor and earth sag [m]	8.5
Conductor Cross-section [mm^2]	636
Earth Wire Cross-section [mm^2]	153
DC Resistance [Ohm/km]	0.026
Reactance [Ohm/km]	0.316
Susceptance [µS/km]	3.578

Figure 3.4 - 400 kV tower mast and conductor data

3.2.3 Model validation

The cable model is validated through comparisons with the measurements done in chapter 4.6, and the conversion to PSCAD/EMTDC is validated through comparisons with the simulations done in PowerFactory for steady-state conditions. The PowerFactory file is a direct conversion of the PSS/E file comprising the entire network, and it can be used as reference when comparing steady-state results.

Three distinct points in the network were chosen for the comparison:

- Kassø-Landerupgård (KAS-LAG): Kassø is the strongest 400 kV node in Western Denmark;
- Idomlund-Tjele (IDU-THE): Idomlund is the weakest 400 kV node is Western Denmark;
- Lem-Stovstrup (LEM-STSV): Lem is connected to a phase-shift transformer;

Three different comparison cases are prepared; for all cases the voltage, current, active and reactive powers in the lines are compared:

- Case 1: The entire grid is modelled in PSCAD/EMTDC, by means of pi models. All the voltage levels and part of the north German network are considered.
- Case 2: The entire West Danish grid is modelled in PSCAD/EMTDC by means of pi models. Only voltage levels equal to or higher than 150 kV; the lower voltage levels and the north German network are modelled by an equivalent grid.

- Case 3: Two modelling approaches are used:
  - The first approach involves the modelling by means of FD models of nodes up to a distance of 3 busbars from the comparison points. The remaining network is modelled by an equivalent grid;
  - The second approach involves the modelling by means of FD models of nodes up to a distance of 3 busbars from the comparison points. The remaining lines having a voltage equal to or higher than 150 kV are modelled by means of pi-models. The lower voltage levels and the north German network are modelled by an equivalent grid;

The two modelling approaches used for Case 3 will be analysed in more detail in chapter 6.

Figure 3.5 and Figure 3.6 show the comparisons of the results for cases 1 and 2. The data in each of the four columns is for PSCAD-Case 1, PowerFactory-Case 1, PSCAD-Case 2 and PowerFactory-Case 2, respectively.

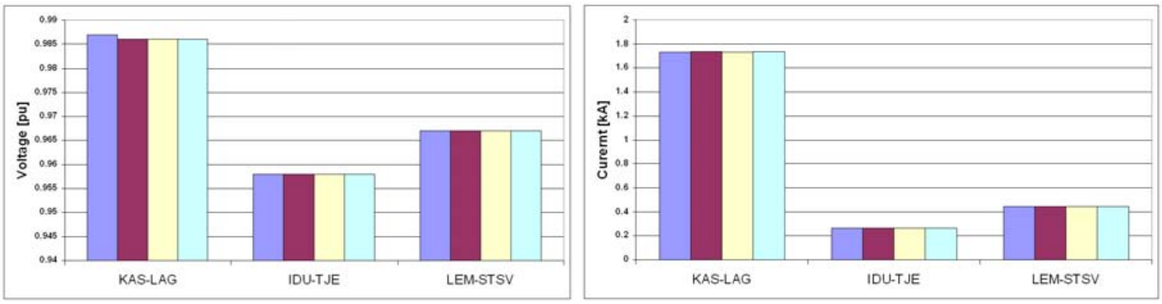

(a) (b)

Figure 3.5 - Comparison between PSCAD/EMTDC and PowerFactory for case 1 and case 2. a) Voltage; b) Current

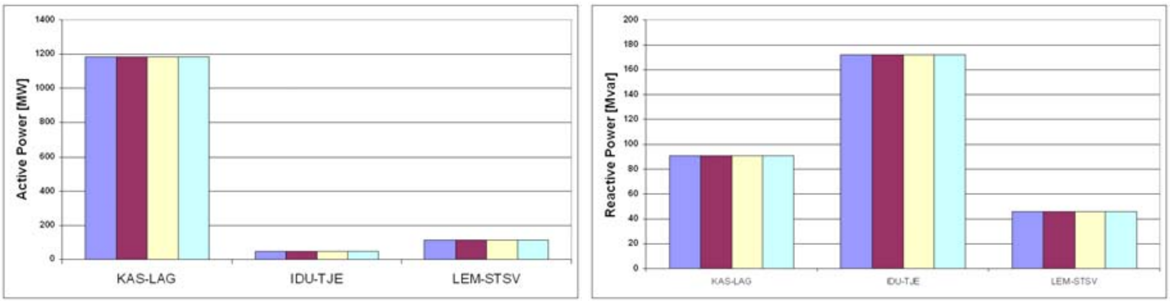

(a) (b)

Figure 3.6 - Comparison between PSCAD/EMTDC and PowerFactory for case 1 and case 2. a) Active Power; b) Reactive Power

Figure 3.7 and Figure 3.8 show the comparisons of the results for case 1. The data in each of the four columns are for PSCAD-Equivalent grid, PowerFactory-Equivalent grid, PSCAD-pi models and PowerFactory-pi models, respectively.

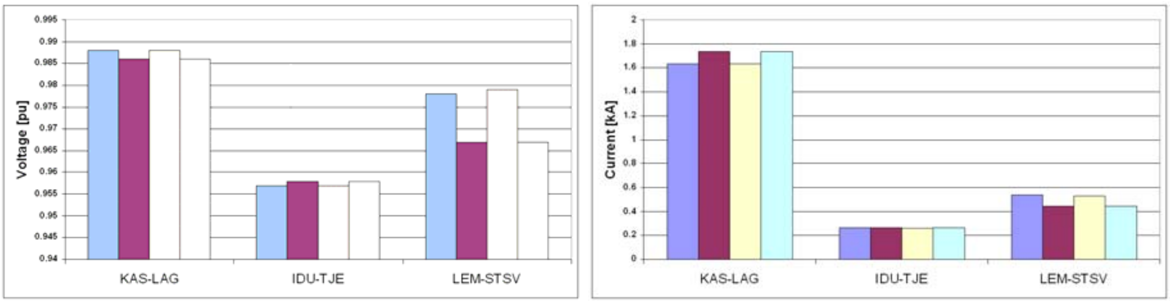

(a) (b)

Figure 3.7 - Comparison between PSCAD/EMTDC and PowerFactory for case 3. a) Voltage; b) Current

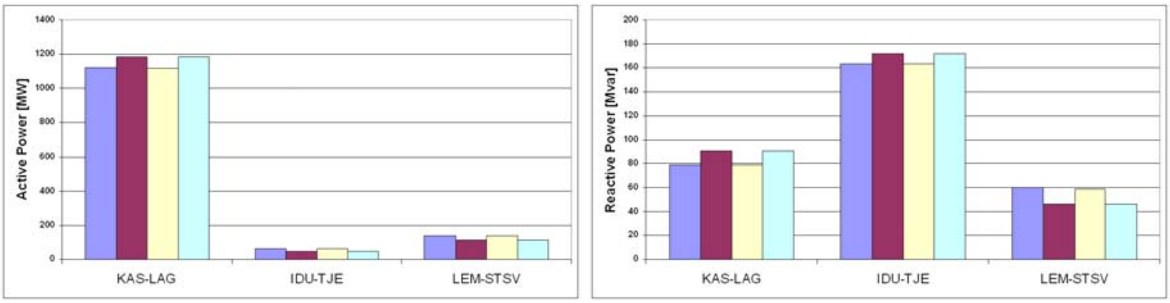

(a) (b)

Figure 3.8 - Comparison between PSCAD/EMTDC and PowerFactory for case 3. a) Active Power; b) Reactive Power

Besides calculating the voltage, current and powers shown in Figure 3.5 to Figure 3.8, are also drawn frequency spectrums for each of the nodes and cases. Figure 3.9 shows the frequency spectrums when using lumped parameters (Case 1). Appendix B shows the frequency spectrums for all three cases.

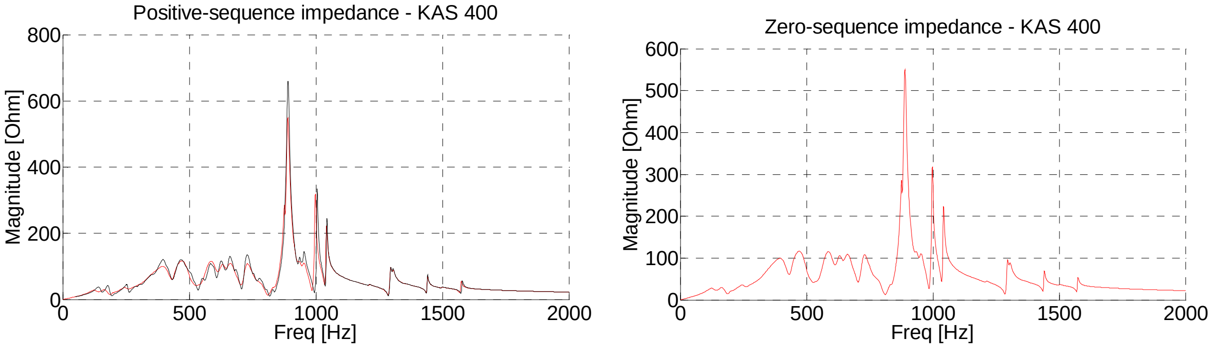

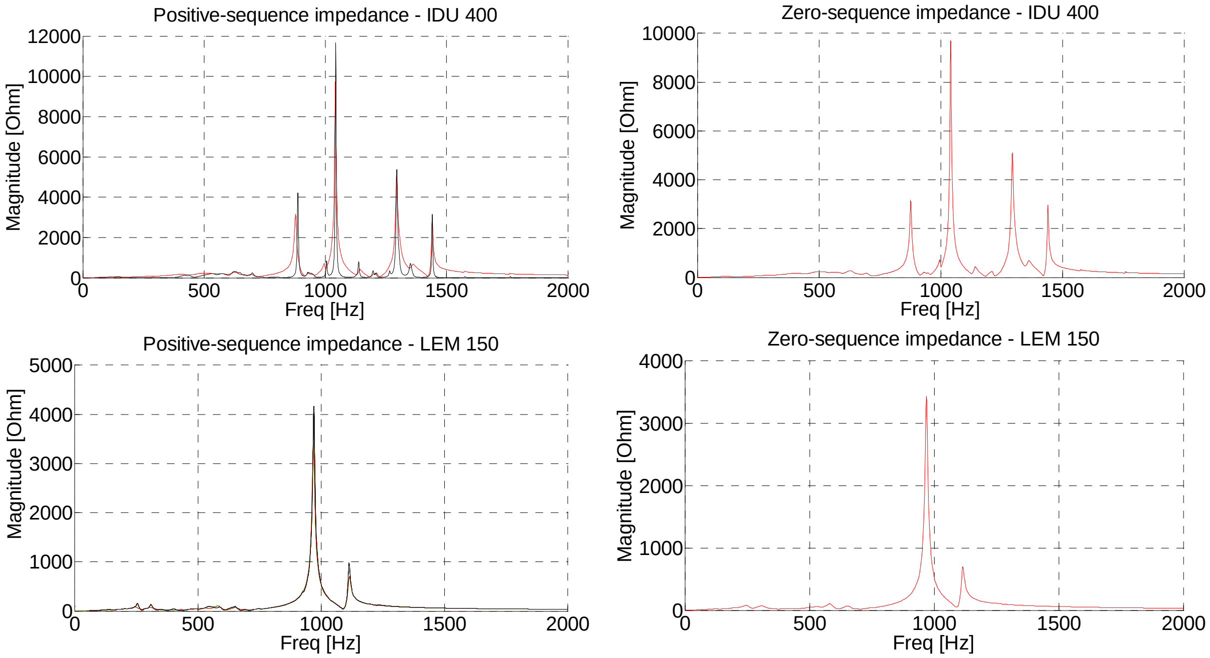

Figure 3.9 - Positive and zero sequence impedances when using lumped-parameters models (Red: PSCAD; Black: Power Factory)

When the PSCAD/EMTDC and PowerFactory results are compared, the following conclusions can be made:

Case 1

The results are virtually identical, and the differences found between the frequency spectrums are small. At higher frequencies small differences are found in the magnitudes of the resonance frequencies (see Appendix B), but they are too small to be considered relevant. Furthermore, the resonance frequencies are the same for both models.

Case 2

Again no relevant differences are found when comparing the two models for steady-state conditions. In the frequency scans, differences are found in the KAS-400 and IDU-400 nodes. This happens because these nodes are close to Germany, which for Case 2 is represented through an equivalent grid that is only correct at 50 Hz. The LEM-150 node presents a frequency scan similar to the ones of Case 1.

Case 3

In these cases small differences appeared at steady-state between PSCAD/EMTDC and PowerFactory, more noticeably in the LEM-STSV connection, due to the fact that all the cables are considered to be in trefoil formation, while in the PSS/E file and therefore also in the PowerFactory file some are considered to be in flat formation. Still, the differences are small and are present because the capacitance, resistance and inductance of the pi-models are not 100% similar to the ones of the FD-models.
More important than the differences at 50 Hz are the differences between the frequency spectrums.

Not only is the spectrum obtained in PSCAD/EMTDC different from the one shown by PowerFactory, but there are also differences between the system modelled by pi-models and the one using an extended equivalent grid, most notably a large reduction of the impedance magnitude at the resonance frequencies.

The comparison of the models shows good congruency between the results obtained when using PSCAD/EMTDC and those obtained in PowerFactory. Therefore, the conversion to PSCAD/EMTDC is considered as having been validated. The cable model itself is validated in chapter 4.6.

3.3 Equivalent pure-OHL system

It is desired to perform comparisons between the network previously described and an equivalent network comprising OHLs only.

The network planned for 2030 is not a direct conversion of the actual network, presenting substantial differences in its design and lines routes. Therefore, the pure OHL system is a direct conversion of the 2030 grid, with cables instead of OHLs.

At this moment Energinet.dk uses two different types of OHL configurations at the 150 kV voltage level, which are identified as Type 1 and Type2. The two configurations and the respective data are shown in Figure 3.10 and Figure 3.11.

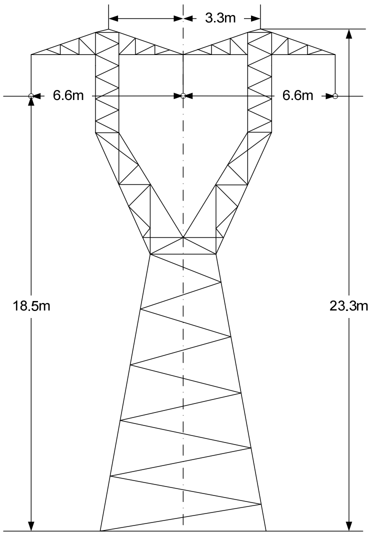

Nominal Voltage [kV]	170
Nominal Current [A]	725
Conductor and earth sag [m]	8.5
Conductor Cross-section [mm^2]	594
Earth Wire Cross-section [mm^2]	95
DC Resistance [Ohm/km]	0.056
Reactance [Ohm/km]	0.407
Susceptance [µS/km]	2.827

Figure 3.10 - Type 1 tower mast and conductor data

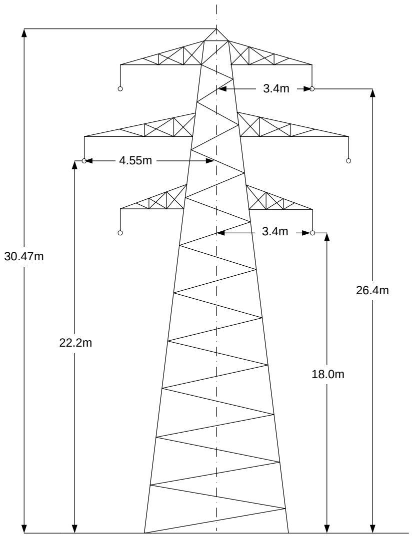

Nominal Voltage [kV]	170
Nominal Current [A]	990
Conductor and earth sag [m]	8.5
Conductor Cross-section [mm^2]	281
Earth Wire Cross-section [mm^2]	173
DC Resistance [Ohm/km]	0.119
Reactance [Ohm/km]	0.401
Susceptance [µS/km]	2.853

Figure 3.11 - Type 2 tower mast and conductor data

The Type 1 configuration was implemented directly in PSCAD/EMTDC without any changes.
The Type 2 configuration cannot be directly implemented as it contains six conductors. One option would be to eliminate three of the conductors, but that would unbalance the system due to the vertical disposition of the conductors. The solution applied was to use a mix of the two configurations; the flat formation of the Type 1 with Type 2 heights (22.2 m/30.47 m) and conductor's data.

The choice of the OHL configuration used was based on the nominal currents of the cables and OHL, as shown in Table 3.2.

Table 3.2 – Cable-OHL equivalence and respective nominal currents

Cable	Cable I_N [A]	OHL	OHL I_N [A]
800mm2	667	Type 2	725
1200mm2	797	Type 2	725
2000mm2	964	Type 1	990

3.3.1 Reactive Power Compensation

The substitution of the cables by OHLs corresponds to a substantial reduction of the generated reactive power. Therefore, the shunt reactors power level should also be reduced.
The method used for the reactive power correction was:

- The amount of reactive power per kilometre that is generated by the three types of cable at nominal voltage (165 kV) was calculated. In order to gain a better equivalence between the 2030 network and the purely OHL-based network, the cable's capacitance is considered as having been calculated by PSCAD/EMTDC;

- The nominal value of the shunt reactors installed in the cable ends is reduced, by a value equal to the reactive power that would have been generated by the attached cables at nominal voltage. If in the original model a shunt reactor was not compensating for all the reactive power generated by the attached cables, the shunt reactor becomes a capacitor bank;
- After the correction of all shunt reactors, all shunt reactors and capacitor banks with nominal power lower than 5 Mvar are eliminated. This action is performed to increase the system realism as shunt reactors/capacitor banks of such a small size are unlikely to be installed. This simplification introduces a negligible total error of 2.1 Mvar.

3.3.2 Model validation

The model validation is performed using the method described in chapter 3.2.3.

In the pure-OHL network the power flow is different from the one of the 2030 network. As a result, the voltages, currents, active and reactive powers are also different. Thus, the results are compared with PowerFactory simulations. The results match and the conversion is considered validated.

3.4 Equivalent pure-cable system

Another interesting comparison is the one between the 2030 network and a pure-cable network.

Using a method similar to the one described in chapter 3.3, the 400 kV OHLs are substituted by 400 kV, 2000 mm^2 copper cables, installed in trefoil formation, whose data can be obtained in [69].

It is not sufficient to substitute the OHL for cables of equivalent length as the nominal currents of the first ones are higher than the nominal current of the cables. Therefore, after the substitution, it is necessary to verify the steady-state currents in all the new 400 kV cables and check that no current is higher than the nominal.

The verification shows the current in five of the cables is too high. New cables are installed in parallel to those five cables.

The substitution of the OHLs for cables results in an increase in the system reactive power and thus an increase in the reactive power compensated by the shunt reactor. The method used to calculate the new compensation values is analogous to the method described in chapter 3.3.1.

4. Field measurements - Horns Rev 2 cable

4.1 Introduction

In 2009, Energinet.dk completed the installation of a 99.7 km, 150 kV AC cable connection between the offshore wind farm Horns Rev 2 and the West Danish 400 kV grid.

A set of measurements were prepared prior to cable commissioning. The objective of these measurements was to validate the simulation model, to demonstrate some of the expected phenomena and to increase the knowledge regarding measurement protocols.

Measurements performed in smaller sections of the cable were also performed by another PhD student and are available in [56].

4.2 System characterisation

The wind farm consists of 91 turbines, each with a power rating of 2.3 MW and a maximum power production of 209 MW. The connection between the wind farm and the HV network in Western Denmark is made through a cable line, which is divided into three main sections:

- 42 km of a three-core, both-ends bonded, submarine cable; connecting the offshore wind farm to the shore;
- 2.3 km of three single-core, cross-bonded, land cable; connecting the submarine cable to the shunt reactor;
- 55.4 km of three single-core, cross-bonded, land cable; connecting the shunt reactor to the 150/400 kV substation.

Figure 4.1 shows the equivalent single-line diagram. Table 4.1 presents the dimensions of the cross-section, insulation and sheath of the different cable sections.

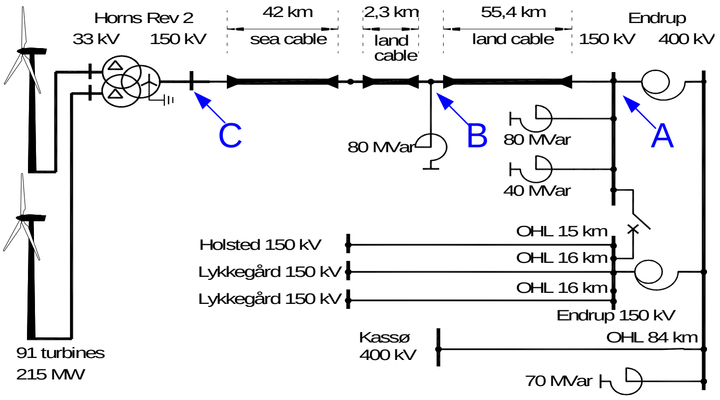

Figure 4.1 - Diagram of the connection between Horns Rev 2 and the onshore substation [18]

Table 4.1 - Data on the Horns Rev 2 cable line

	Length [km]	Conductor material	Cross-section [mm^2]	Insulation Thickness [mm]	Sheath thickness [mm]	Cable diameter [mm]
Sea cable	42	Copper	630	18	2.4	208*
Long land cable	55.4	Aluminium	1200	17	1.289	95
Short land cable	2.3	Aluminium	1200	17	1.289	95

*The diameter indicated is for the armour

To compensate for the reactive power generated by the cable-line three shunt reactors were installed. A 40 Mvar and an 80 Mvar shunt reactor were installed in the 150 kV side of the onshore substation (point A in Figure 4.1); a second 80 Mvar shunt reactor was installed in approximately the middle of the cable line (point B in Figure 4.1).

4.3 Measurement protocol

Measurements were carried out at three different points along the cable. The points and measured signals were located as follows:

- Onshore substation (Point A in Figure 4.1)
  - Three-phase voltages in the cable
  - Three-phase voltages in the busbar (before the circuit breaker)
  - Three-phase currents in the cable
  - Current in the surge arrester for one of the phases (not always measured)
- Shunt reactor (Point B in Figure 4.1)
  - Three-phase currents into the shunt reactor
- Wind farm (Point C in Figure 4.1)
  - Three-phase voltages in the cable

The CB was closed by means of synchronised switching at zero voltage. The voltage and current were reduced to values readable by the measurement equipment, by inductive voltage transformers and current transformers, respectively.

The shunt reactor installed in the middle of the cable (point B in Figure 4.1) is connected directly to the cable. The two shunt reactors installed in the substation onshore were always connected several minutes before the cable was energised and were both in steady-state at the time of energisation.

The cable was energised from the grid (Point A), while the receiving end (Point C) was kept open. The short-circuit power in the sending end remained virtually constant while the measurements were made, and was equal to $S_{SC} = 2372\angle 87.91^\circ$ MVA on the 150 kV side of the substation.

To ensure that the measurements were accurate the cable was energised and de-energised three times. Four steady-state measurements were also performed.

Steady-state measurements were performed at a sampling frequency of 28 kHz, the disconnections at 9 kHz and the connections at 28 kHz (the first one) and 9kHz (the last two).

4.4 Measurement instruments

The data was acquired using two Omicron CMC-256-6 installed at the measurements points A and C, and an Omicron CMC-356 installed in point B. An Omicron CMC is a testing equipment capable of doing digital signal acquisition.

The voltages in points A and C were reduced to measurable values by measuring transformers installed in the substation. The Omicrons were connected to secondary side of the measuring transformers.

The currents were acquired using LEM PR30 probes.

4.4.1 *Measuring voltage transformer*

A measuring transformer can distort the results as its transformation characteristic is not the same for all frequencies. To avoid such a problem, the measuring transformer installed in point A (onshore substation) was tested before to the full-scale measurements were carried out.

A 140 V peak voltage source was connected to the transformer's primary, while the voltage in the secondary measured for different frequencies. Figure 4.2 shows the transformer's transfer characteristic.

The transformer transfer characteristic is constant and equal to 1710 up to 1 kHz, and thus sufficiently accurate for measurements at full voltage.

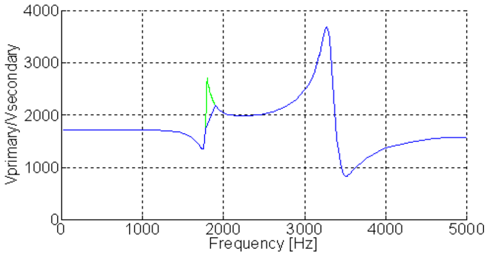

Figure 4.2 - Measuring voltage transformer transfer characteristic (at green fitting for the first resonance point)

4.5 PSCAD/EMTDC model

The validation of the cable models used in this thesis is of major importance in order to validate both the simulations of the different phenomena and the guidelines used for carrying out the insulation coordination studies.

The accuracy of the FD-models used by PSCAD/EMTDC was demonstrated in prior works, most notably [56]. Nevertheless, those works do not completely validate the models used in this study as design errors may be present. In addition, no validation has ever been made for a cable as long as the Horns Rev 2 cable.

This chapter validates not only the cable model, but the shunt reactor model as well. This validation is particularly important as the shunt reactor mutual inductance influences the waveform of some transients.

4.5.1 Land cable

The land cable is divided into two parts: a 54 km cable between the onshore substation and the shunt reactor and a 2.3km cable between the shunt reactor and the submarine cable.

The land cable is installed in trefoil formation at 1.3 m depth, measured for the top cable. The 55.4 km cable has 11 major cross-bonded sections, whose length of the minor sections varies between 587 m and 1846 m. The 2.3 km cable has one major cross-bonded section.

Figure 4.3 and Table 4.2 show the cable layout and nominal parameters.

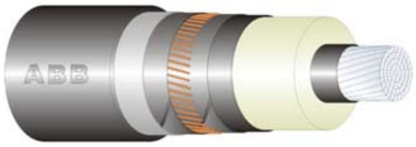

Figure 4.3 - 1200 mm^2 land cable [83]

Table 4.2 - Horns Rev 2 land cable design (nominal values)

Layer	Thickness (mm)	Material
Conductor	41.5*	Aluminium, round, compacted
Conductor screen	1.5	Semi-conductive PE
Insulation	17	Dry cured XLPE
Insulation screen	1	Semi-conductive PE
Longitudinal water barrier	0.6	Swelling tape
Copper wire screen	95**	Copper
Longitudinal water barrier	0.6	Swelling tape
Radial water barrier	0.2	Aluminium laminate
Outer cover	4	High-density PE
Complete cable	95*	-

* Diameter

** Cross-section

The cable is modelled in PSCAD/EMTDC as having four layers: Conductor, insulation, screen and outer insulation/outer cover.

Conductor

Segmental conductors cannot be modelled in PSCAD/EMTDC, and it is necessary to change the conductor resistivity, as explained in section 2.3.5.

For the Horns Rev 2 land cable, the conductor resistivity is 3.156x10^{-8} **Ω**.m (22).

$$\rho' = \rho\frac{\pi r^2}{A} \Leftrightarrow \rho' = 2.8\cdot 10^{-8}\frac{\pi\cdot 20.75^2}{1200} \Leftrightarrow \rho' = 3.156\cdot 10^{-8}\ \Omega.m \tag{22}$$

Insulation

Semiconductive layers cannot be modelled in PSCAD/EMTDC. Instead, they are considered as being part of the insulation and the permittivity is corrected [36].
The corrected relative permittivity is given in (23). The insulation thickness is increased from 17 mm to 20.1 mm.

$$\varepsilon' = \varepsilon \frac{\ln\left(\frac{r_2}{r_1}\right)}{\ln\left(\frac{b}{a}\right)} \Leftrightarrow \varepsilon' = 2.5 \frac{\ln\left(\frac{40.85}{20.75}\right)}{\ln\left(\frac{39.50}{22.25}\right)} \Leftrightarrow \varepsilon' = 2.95 \qquad (23)$$

Screen

The cable screen has a first layer of copper wires with a 95 mm^2 cross-section and a second 0.2 mm thick aluminium foil used as a water barrier.
The thickness of the copper wires is not given in the datasheet and the wires are too small to be measured with the desired accuracy. Instead, it the number of wires in one sample of the cable was counted, and the wires' radius was calculated (24), [62].

$$A = n\pi r^2 \Leftrightarrow r = \sqrt{\frac{A}{n\pi}} \Leftrightarrow r = \sqrt{\frac{95}{97\pi}} \Leftrightarrow r = 0.558mm \qquad (24)$$

The wires are spaced, see Figure 4.4. Consequently, the cable screen cannot be modelled as a solid layer. Applying the same method that was used to correct conductor resistivity, the copper wires' resistivity is corrected (25).

Figure 4.4 - Cross-section of the 150kV Horns Rev 2 land cable

$$\rho'_{S,Cu} = \rho_{S,Cu} \frac{\pi\left(r_w^2 - r_{ins}^2\right)}{A_{sh}} \Leftrightarrow \rho'_{S,Cu} = 1.724 \cdot 10^{-8} \frac{\pi\left(41.966^2 - 40.85^2\right)}{95} \Leftrightarrow \rho'_{S,Cu} = 5.269 \cdot 10^{-8}\ \Omega.m \qquad (25)$$

The aluminium foil can be modelled as a solid layer, but it is not possible to model two layers in PSCAD/EMTDC without having an insulation material in between. Instead, the thickness of the screen is increased to the sum of the copper wires and the aluminium foil, and the screen resistivity is corrected according to (26)-(28) [62].

$$A_{Cu} = \pi\left(41.966^2 - 40.85^2\right) \Leftrightarrow A_{Cu} = 290mm^2 \tag{26}$$

$$A_{Al} = \pi\left(42.166^2 - 41.966^2\right) \Leftrightarrow A_{Al} = 52.86mm^2 \tag{27}$$

$$\begin{gathered}\rho_S^{'} = \rho_{Cu}^{'}\frac{A_{Cu}}{A_{Cu}+A_{Al}} + \rho_{Al}\frac{A_{Al}}{A_{Cu}+A_{Al}} \Leftrightarrow \rho_S^{'} = 5.269\cdot 10^{-8}\frac{290}{290+52.86} + 2.83\cdot 10^{-8}\frac{52.86}{290+52.86} \Leftrightarrow \\ \Leftrightarrow \rho_S^{'} = 4.457\cdot 10^{-8}\ \Omega.m\end{gathered} \tag{28}$$

PSCAD/EMTDC Layout

Table 4.3 shows the parameters used for the simulation of the Horns Rev 2 land cable in PSCAD/EMTDC.

Table 4.3 - Land cable parameters for PSCAD/EMTDC

Conductor outer radius	20.75mm
Conductor resistivity	$3.156\text{x}10^{-8}$ Ω.m
Conductor relative permeability	1
Insulation outer radius	40.85
Insulation relative permittivity	2.95
Insulation relative permeability	1
Screen outer radius	42.166
Screen resistivity	$4.457\text{x}10^{-8}$ Ω.m
Screen relative permeability	1
Outer insulation outer radius	47.5
Outer insulation relative permittivity	2.3
Outer insulation relative permeability	1

Fitting parameters

The PSCAD/EMTDC standard fitting parameters are not adequate for the simulation of this cable as the number of poles is insufficient. Table 4.4 gives the parameters used to fitting of the cable in PSCAD/EMTDC.

Table 4.4 - Fitting parameters for the simulation of the Horns Rev 2 Land cable in PSCAD/EMTDC

Steady-State Frequency	50 [Hz]
Lower Frequency Limit	0.5 [Hz]
Upper Frequency Limit	1 [MHz]
Total Number of Frequency Increments	100
Max # of Poles per Column for Surge Admittance	40
Max # of Poles per Delay Group for Prop. Func.	40
Maximum Fitting Error for Surge Admittance	0.5 [%]
Maximum Fitting Error for Propagation Func.	0.5 [%]
0 to F0	1
F0	1
F0 to Fmax	1

Cross-bonding

Table 4.5 shows the length of each minor section of the 54 km cable. The minor section 1-2 is the first section seen from the sending end (Endrup) and the section 33-34 is the last one (shunt reactor).
The length of each of the three minor sections of the 2.3 km land cable is 0.7667 km.

Table 4.5 - Lengths of the minor sections of the 54 km land cable

Minor section #	Length [km]	Minor section #	Length [km]	Minor section #	Length [km]
Section 1-2	0.587	**Section 12-13**	1.830	**Section 23-24**	1.847
Section 2-3	0.930	**Section 13-14**	1.764	**Section 24-25**	1.832
Section 3-4	0.928	**Section 14-15**	1.744	**Section 25-26**	1.771
Section 4-5	1.743	**Section 15-16**	1.738	**Section 26-27**	1.770
Section 5-6	1.514	**Section 16-17**	1.769	**Section 27-28**	1.775
Section 6-7	1.780	**Section 17-18**	1.770	**Section 28-29**	1.861
Section 7-8	1.516	**Section 18-19**	1.770	**Section 29-30**	1.820
Section 8-9	1.512	**Section 19-20**	1.835	**Section 30-31**	1.816
Section 9-10	1.760	**Section 20-21**	1.761	**Section 31-32**	1.786
Section 10-11	1.827	**Section 21-22**	1.846	**Section 32-33**	1.783
Section 11-12	1.828	**Section 22-23**	1.824	**Section 33-34**	1.750

4.5.2 Submarine cable

The submarine cable is a three-core cable surrounded by an external armour, similar to a pipe-type cable. Figure 4.5 shows the 3x1x630 mm^2 copper submarine cable layout.

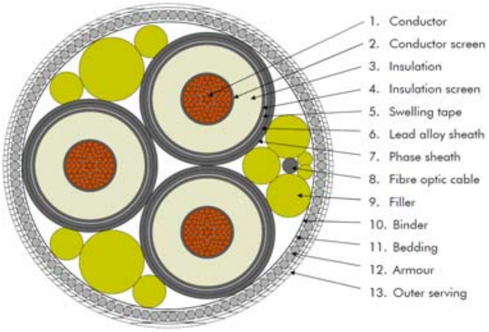

Figure 4.5 - Horns Rev 2 submarine cable layout [84]

At present, PSCAD/EMTDC does not allow to directly model pipe-type cables. As a result, it was decided to model the submarine cable as a single-core cable. An example using a new Beta version of PSCAD/EMTDC, which allows the modelling of pipe-type cables, is shown ahead. For stability reasons, that version is not use in this part of the thesis.

The correction of the submarine cable layers is made using the same approach used for the land cable. The corrected conductor resistivity is given by (29), and the corrected insulation permittivity by (30).

Table 4.6 gives the parameters used for the simulation of the submarine cable in PSCAD/EMTDC. The fitting parameters are identical to the ones shown in Table 4.4.

$$\rho' = \rho \frac{\pi r^2}{A} \Leftrightarrow \rho' = 1.724 \cdot 10^{-8} \frac{\pi \cdot 15.25^2}{630} \Leftrightarrow \rho' = 1.999 \cdot 10^{-8}\ \Omega.m \tag{29}$$

$$\varepsilon' = \varepsilon \frac{\ln\left(\frac{r_2}{r_1}\right)}{\ln\left(\frac{b}{a}\right)} \Leftrightarrow \varepsilon' = 2.5 \frac{\ln\left(\frac{37.75}{15.25}\right)}{\ln\left(\frac{34.75}{16.75}\right)} \Leftrightarrow \varepsilon' = 3.105 \tag{30}$$

Table 4.6 - Submarine cable parameters for PSCAD/EMTDC

Conductor outer radius	15.25 mm
Conductor resistivity	1.999x10^{-8} Ω.m
Conductor relative permeability	1
Insulation outer radius	37.75 mm
Insulation relative permittivity	3.105
Insulation relative permeability	1
Screen outer radius	40.15
Screen resistivity	2.2x10^{-8} Ω.m
Screen relative permeability	1
Outer insulation outer radius	42.45
Outer insulation relative permittivity	2.3
Outer insulation relative permeability	1

4.5.3 Shunt reactor

The shunt reactor installed in the middle of the cable line is energised together with the line. Thus, in order to study the transients, an accurate model of the shunt reactor is required.

The 80 Mvar shunt reactor has a nominal voltage of 170 kV and the three phases are mounted on a five-limp iron core, as shown in Figure 2.3. To avoid saturation and reduce the mutual coupling between phases air gaps are used in the three central limps.

The shunt reactor impedance is obtained directly from the test report [58] and given in Table 4.7. The resistance is given for a reference temperature of 75ºC and calculated by dividing the losses by the square of the nominal current.

Table 4.7 - Shunt reactor self-impedance

	Phase A	**Phase B**	**Phase C**
Resistance [Ω]	0.755	0.927	0.551
Inductance [H]	1.144	1.144	1.143

The resistance shown in Table 4.7 includes copper losses, magnetisation losses and additional losses (e.g. stray losses, skin effect …). The magnetisation and additional losses are frequency-dependent, meaning that the losses increase when the frequency increases.

The exact relation between the losses and the frequency is unknown. Therefore, the losses are considered to be independent of the frequency.

Mutual inductance

The coils are mounted in the same iron core. Therefore, when a current flows in one phase, a magnetic flux flows into all limbs, see Figure 4.6. The flux links with the two other coils inducing a voltage in the corresponding phases.

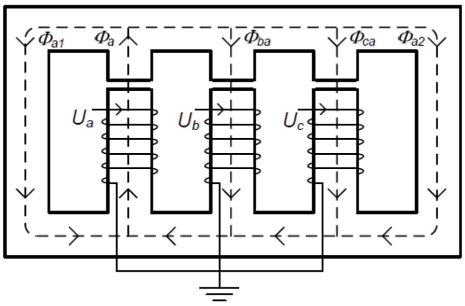

Figure 4.6 - Flux path for a voltage applied in Phase A [62]

The mutual coupling is measured by applying a voltage to one of the phases and measuring the induced voltage in the other two phases. Table 4.8 shows the test report results for an applied voltage of $98.15\text{kV}_{\text{RMS}}$.

Table 4.8 - Induced voltages due to mutual coupling

Phase	Applied voltage [kV]	Induced voltage [kV]		
		A	B	C
A	98.15	-	1.18 (0.51%)	0.39 (0.17%)
B	98.15	1.02 (0.44%)	-	1.09 (0.47%)
C	98.15	0.30 (0.13%)	1.09 (0.47%)	-

The mutual inductance in now calculated by applying (31), [85].

$$X_{MXY} = \frac{-U_X}{I_Y} \tag{31}$$

Where X_{MXY} is the mutual inductance between two phases, U_X the induced voltage in phase X by a current I_Y flowing in phase Y.

For a voltage of 98.15 kV the current in the phases are 273.3 A, 273.2A and 273.7 A in phases A, B and C, respectively. Table 4.9 shows the mutual inductance values calculated using (31) and the data of Table 4.8, resulting in the inductance matrix shown in (32).

Table 4.9 - Mutual inductance in Horns Rev 2 shunt reactor

	Phase A	Phase B	Phase C
Phase A	-	-0.0119	-0.0035
Phase B	-0.0137	-	-0.0127
Phase C	-0.0045	-0.0127	-

$$\begin{bmatrix} L_A & M_{AB} & M_{AC} \\ M_{BA} & L_B & M_{BC} \\ M_{CA} & M_{CB} & L_C \end{bmatrix} = \begin{bmatrix} 1.144 & -0.0119 & -0.0035 \\ -0.0137 & 1.144 & -0.0127 \\ -0.0045 & -0.0127 & 1.143 \end{bmatrix} \text{[H]} \tag{32}$$

The mutual inductances asymmetry is most likely a result of measurements inaccuracy and does not have a physical explanation. Thus, the shunt reactor is considered as having a symmetric mutual inductance.
The mutual inductance in the PSCAD/EMTDC file is given in (33).

$$\begin{bmatrix} L_A & M_{AB} & M_{AC} \\ M_{BA} & L_B & M_{BC} \\ M_{CA} & M_{CB} & L_C \end{bmatrix} = \begin{bmatrix} 1.144 & -0.0128 & -0.0040 \\ -0.0128 & 1.144 & -0.0127 \\ -0.0040 & -0.0127 & 1.143 \end{bmatrix} \text{[H]} \tag{33}$$

Saturation

Figure 4.7 shows the shunt reactor magnetic characteristic of Phase B as given in the test report. The shunt reactor does not saturate up to approximately 1.4 times the nominal current. One of the performed simulations is the energisation of the cable, which can originate a large transitory current. An accurate modelling of the shunt reactor saturation is therefore necessary.

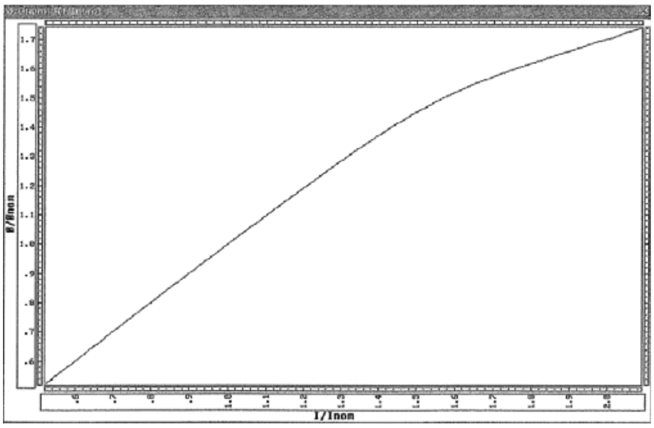

Figure 4.7 - Shunt reactor magnetic characteristic of Phase B [58]

Model implementation in PSCAD/EMTDC

PSCAD/EMTDC does not have a complete shunt reactor model, and other elements must be used to accurately model the shunt reactor.

The *couple wires element* allows the modelling of the resistance, self inductance and mutual inductances. The saturation is modelled using three single-phase transformers [62], which due to limitations in the software are also used to model the shunt reactor self-inductance.

Table 4.10 shows the values used to model the couple wires element in PSCAD/EMTDC, and Table 4.11 the values used to model the transformer. The "Inrush decay time constant" and the "Time to release flux clipping" values are unknown and it was decided to keep the default values.

Table 4.10 - Couple wires parameters in PSCAD/EMTDC

Resistance [Ohm]	Phase A	0.4293
	Phase B	0.4292
	Phase C	0.4314
Self inductance [H]	Phase A	0
	Phase B	0
	Phase C	0
Mutual inductance [H]	Phases A-B	-0.0128
	Phases A-C	-0.0040
	Phases B-C	-0.0127

Table 4.11 - Transformer parameters in PSCAD/EMTDC

Power [MVA]	26.667
Voltage [kV]	98.15/98.15
Leakage reactance [pu]	0.99487
Saturation winding	1
Air core reactance [pu]	0.42
Inrush decay time constant [s]	1
Knee voltage [pu]	1.47
Time to release flux clipping [s]	0.1
Magnetisation current [%]	0.4

Validation

The validation is made throughout:
- Steady-state test;
- Mutual coupling test;
- Saturation test.

Table 4.12 and Table 4.13 compare respectively the current and active power losses in each phase for steady-state conditions. The differences between the model and test report results are small and acceptable.

Table 4.12 - Steady-state currents [A] in each phase

	Phase A	**Phase B**	**Phase C**
Test report	273.3	273.2	273.7
PSCAD/EMTDC	272.0	271.0	272.0
Error [%]	0.5	0.8	0.6

Table 4.13 - Active power losses [kW] in each phase

	Phase A	**Phase B**	**Phase C**
Test report	56.40	69.19	41.24
PSCAD/EMTDC	55.86	68.08	40.77
Error [%]	0.9	1.6	1.1

Table 4.14 compares the voltage induced in the phases due to mutual coupling. The differences between the model and test report results are small and acceptable.

Table 4.14 - Voltage induced in each phase due to mutual coupling

Phase	Applied voltage [kV]	Induced voltage [kV] (simulated/test report)		
		A	B	C
A	98.15	-	1.09/1.18	0.34/0.39
B	98.15	1.09/1.02	-	1.09/1.09
C	98.15	0.34/0.30	1.09/1.09	-

Figure 4.8 shows the saturation curve of the shunt reactor model. A comparison with the test report is not possible, because of the method used to present the results in the test report. Nevertheless, it can be concluded that the saturation is present for voltages/currents higher than 1.4 pu. The same divergence point is found in the test report, see Figure 4.7

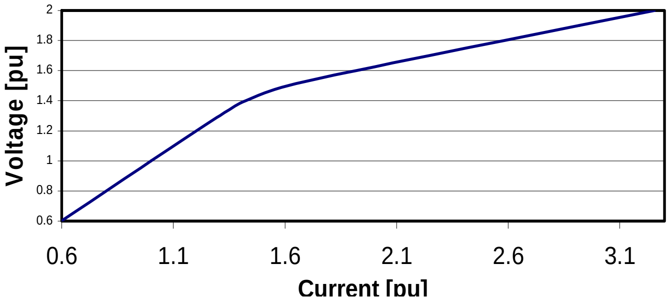

Figure 4.8 - Shunt reactor saturation curve

The validation tests result agree with the test report results. Therefore, the shunt reactor model is considered to be accurate and valid.

The model is valid only for frequencies up to 3 kHz. The test report shows several resonance points for frequencies higher than 3 kHz, which are not given by the model. In order to achieve an accurate modelling for such high frequencies it would be necessary to model the stray capacitance and the capacitances between phases, which are unknown.

The frequencies of the transients are lower than 3 kHz, and the model is therefore considered adequate.

4.5.4 Complete model

Figure 4.9 and Figure 4.10 show, respectively, a part of the land cable and the total the system as implemented in PSCAD/EMTDC.

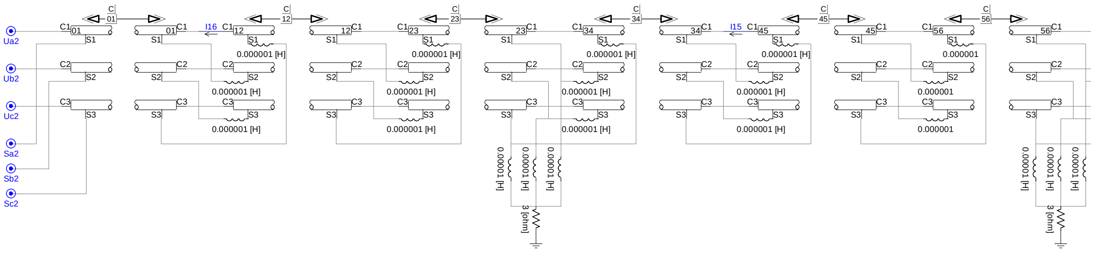

Figure 4.9 - Two major sections of the 54km land cable (from a total of 11 major sections)

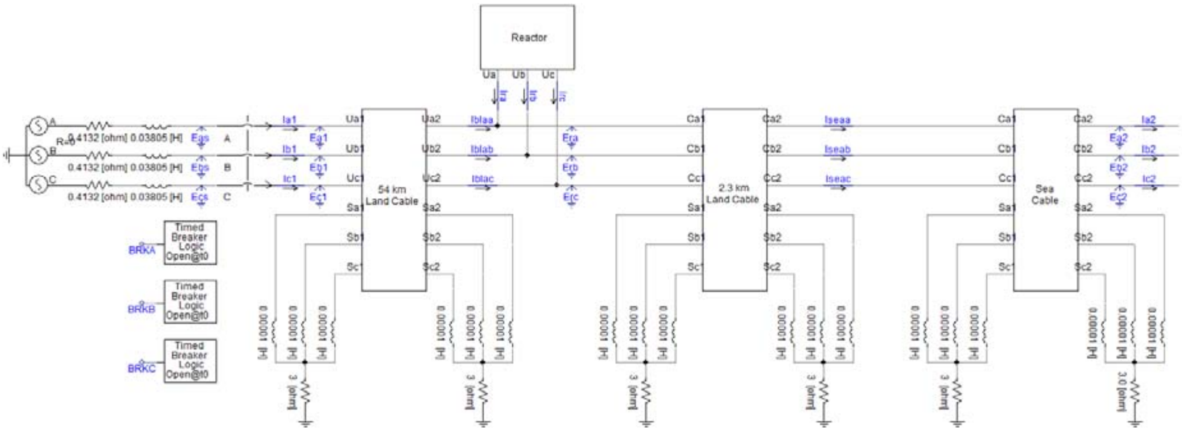

Figure 4.10 - Entire system in PSCAD/EMTDC

4.6 Comparison of the measurements with the PSCAD/EMTDC model

4.6.1 Steady-state

Figure 4.11 to Figure 4.14 compare the voltage and current in the sending end, receiving end and shunt reactor. The comparison is made between the measured results and PSCAD/EMTDC simulations. The colour code is: Phase A: Red; Phase B: Black; Phase C: Green.

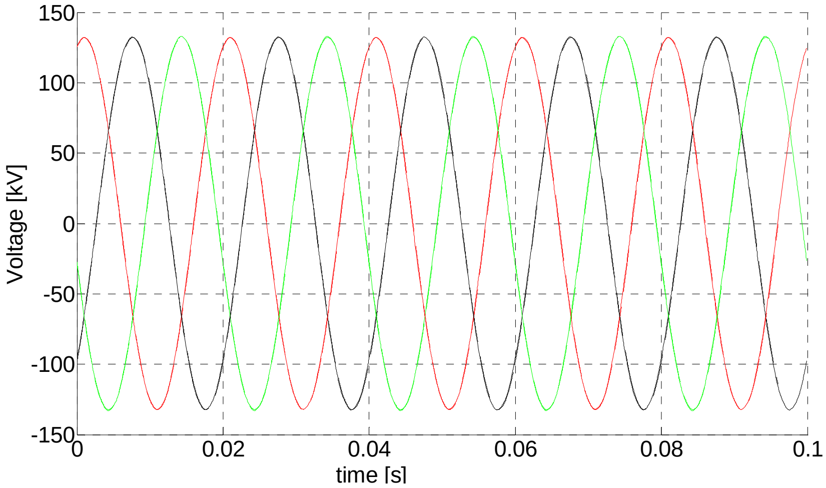

Figure 4.11 - Voltage in the cable sending end. Dashed: Simulation; Solid: Measurements

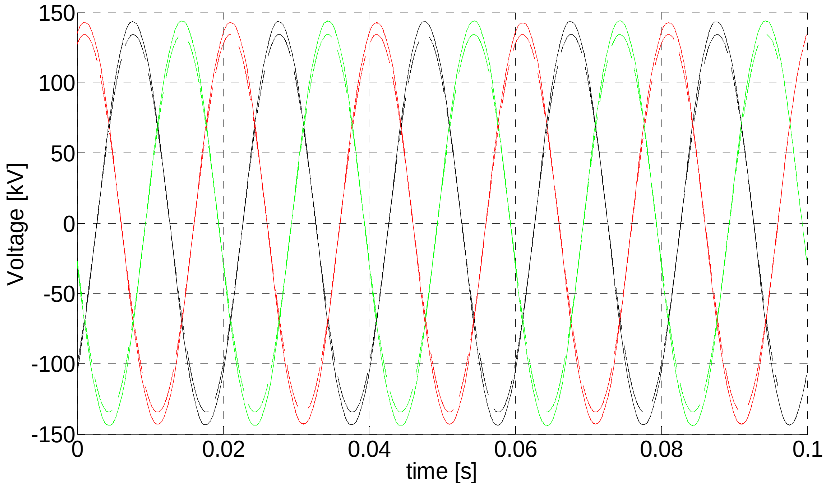

Figure 4.12 - Voltage in the cable receiving end. Dashed: Simulation; Solid: Measurements

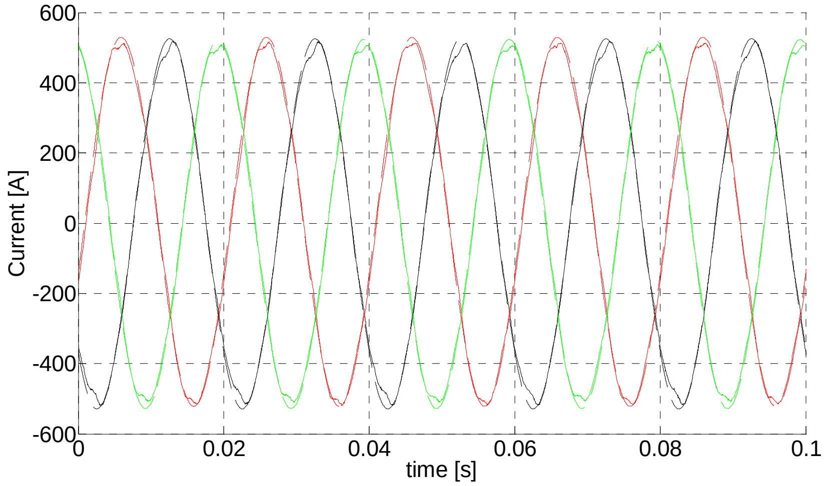

Figure 4.13 - Current in the cable sending end. Dashed: Simulation; Solid: Measurements

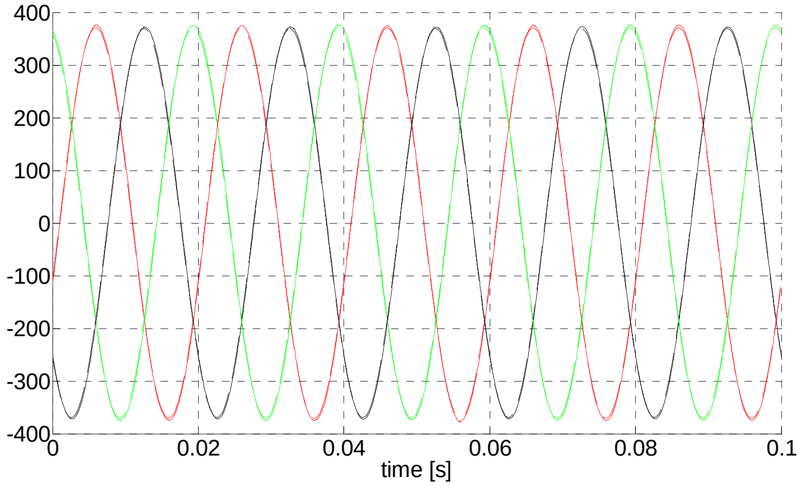

Figure 4.14 - Current into the shunt reactor. Dashed: Simulation; Solid: Measurements

- The voltage in the sending end is equal in simulations and measurements;
- The current in the sending end is lower and more distorted in the measurements. The difference between the peak values of the simulation and the measured results, filtered by a low-pas filter, is of approximately 16A or 3%;
- The voltage in the receiving end is lower in the simulation than in the measurements. The difference between the peak values of the simulation and the measured results is of approximately 8.3 kV or 6%;
- The current into the shunt reactor is practically equal in simulation and measurements;

The simulation results are accurate and alike the measurements with the exception of the voltage in the receiving end. The voltage is higher in the measurements, likely indicating a larger Ferranti Effect.

The current into the shunt reactor is practically equal in the simulations and measurements. The shunt reactor was modelled according to the information provided in the test report, and it was shown in section 4.5.3 that the shunt reactor model is accurate for steady-state condition. Therefore, as the current into the shunt reactor is the same in simulations and measurements, the voltage in that point, at a distance of 55.4km from the sending end, is also the same. Consequently, it is concluded that, for steady-state condition, the land cable model is accurate and the reason for the difference in the receiving end of the line is the submarine cable model.

4.6.2 Submarine cable model

A pipe-type cable is being prepared for a future version of PSCAD/EMTDC, which when on beta-testing at the beginning of 2011. At the time when this thesis was written, the model was still not completely stable, making it difficult to use it in more complex simulation, which is the reason for using three single-phase models in the previous section. However, the simulation results are similar for both models and the model is not the cause of discrepancy between the simulations and measurements.

There may be several reasons for the inaccuracy of the submarine cable model. Possible causes are given in the following pages.

Influence of the ground permeability

The submarine cable is installed 1m below the seabed, whose type of soil is unknown. The presence of iron or iron-bearing minerals in the seabed would increase the soil magnetic permeability [98].
A change in the soil magnetic permeability changes the earth return impedance (for the calculation formulas, refer to Appendix L) and waveform peak values.
It also influences the magnetic field and induced currents. Figure 4.15 shows the magnetic flux for two different seabed permeabilities. The cable configuration is the one shown in Figure 4.16 where the current flows in the conductor of one of the phases and return in the conductor of the other phase.
The magnetic flux is stronger for higher seabed permeability. Consequently, more current flows in the conductors and screens of the two cables connected to the voltage source when the seabed permeability is high.

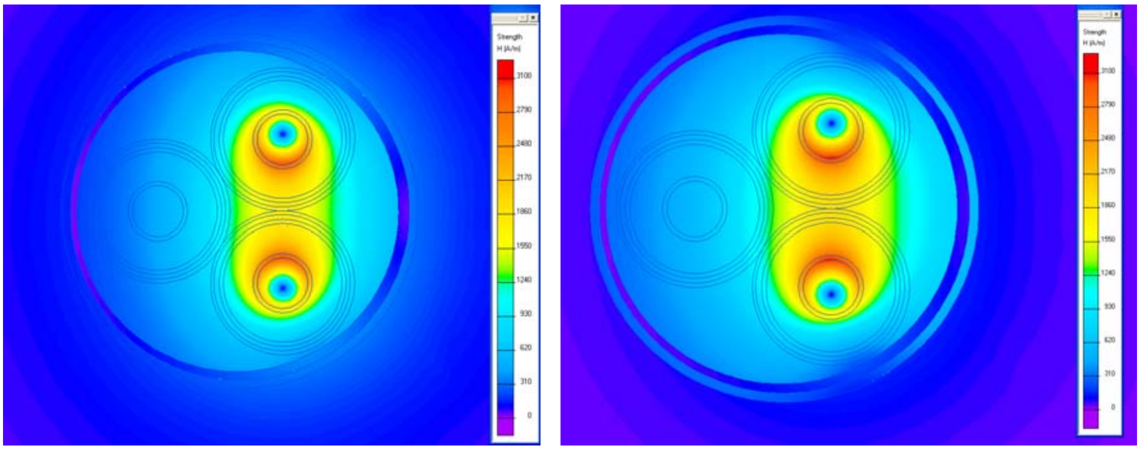

(a) (b)

Figure 4.15 - Magnetic flux for different seabed permeabilities. a) Relative permeability equal to one b) Relative permeability equal to four

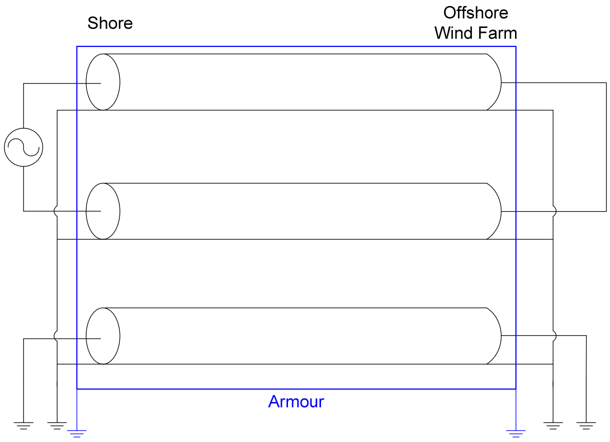

Figure 4.16 - Return current in the core

The armour permeability also has an influence on the flux distribution. In the simulation the armour is simulated as being a solid layer, while in reality it consists in 105 wires (Figure 4.17). Thus, the real penetration of the magnetic field into the seabed is higher than in the simulation and the influence of the seabed permeability may be even more noticeable.
Also, the saturation of the steel is not considered in the simulation. If saturated, the magnetic field propagating into the seabed would be larger, and, as was the case in the previous point, the influence of the seabed permeability would be more noticeable.

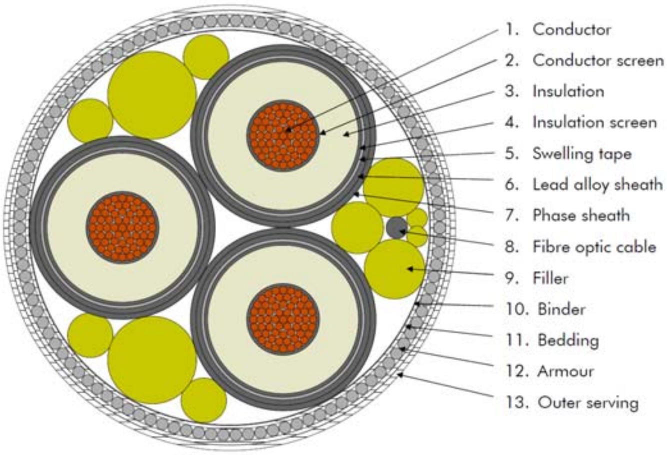

Figure 4.17 - Horns Rev 2 submarine cable layout [84]

Capacitance between phases

The pipe-type model is based on the model proposed in [99]. The model will typically result in an admittance matrix like the one shown in (34). The matrix indicates that a conductor has an electrical connection only with the screen of the same phase, whereas all the screens and armours have an electrical connection.

$$[Y]=\begin{bmatrix} A & -A & 0 & 0 & 0 & 0 & 0 \\ -A & B & 0 & -C & 0 & -C & -D \\ 0 & 0 & A & -A & 0 & 0 & 0 \\ 0 & -C & -A & B & 0 & -C & -D \\ 0 & 0 & 0 & 0 & A & -A & 0 \\ 0 & -C & 0 & -C & -A & B & -D \\ 0 & -D & 0 & -D & 0 & -D & E \end{bmatrix} \tag{34}$$

However, the cable is installed in the seabed, which presents a highly moisture content. The water barrier is installed between the insulation and the screen (layer 6 in Figure 4.17), meaning that the screens are in contact with the moisture, which has a high conductivity.

Consequently, the screens and filler can create an equalpotential surface, or have a close potential, which would result in a different admittance matrix, and consequently also in a different capacitance matrix.

Return Path

The cable in installed on the seabed, which have usually a lower resistivity. The return path is also different from the return path of a land cable, because of the sea water.
This last aspect, which cannot be included in the model, may lead to differences between the simulations and the measurements.

Conclusions

The proper simulation of an HVAC submarine cable poses several difficulties, which are briefly described in this section and can result in inaccurate simulations.The simulation results do not match the measurements, because of inaccuracies in the submarine cable model.
The measurements demonstrated that more work is necessary in order to have proper submarine cable models. However, the proper modelling of submarine cables is outside of the scope of this thesis and will not be addressed.
Nonetheless, this problem does not affect the remaining work made in this thesis. All simulations are made using single-core land cable-models, which have been demonstrated to be very accurate.

4.6.3 Energisation

Figure 4.18 to Figure 4.21 compare the voltage and current in the sending end, receiving end and shunt reactor for the energisation. The comparison is between the measured results and PSCAD/EMTDC simulations.
Table 4.15 and Table 4.16 compare the peak values during the energisation. This peak is normally the first one, and it is the more important as it defines the insulation co-ordination parameters. This means that very often it is sufficient to have an accurate simulation during the first milliseconds of the energisation.

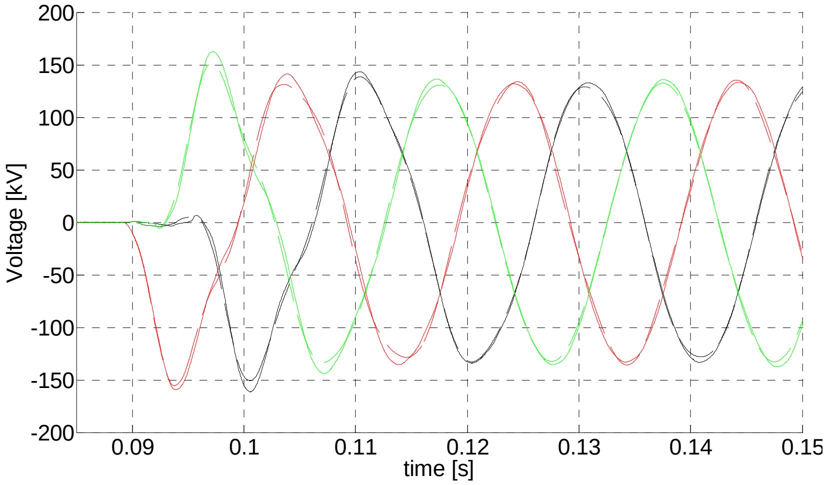

Figure 4.18 - Voltage in the cable sending end. Dashed: Simulation; Solid: Measurements

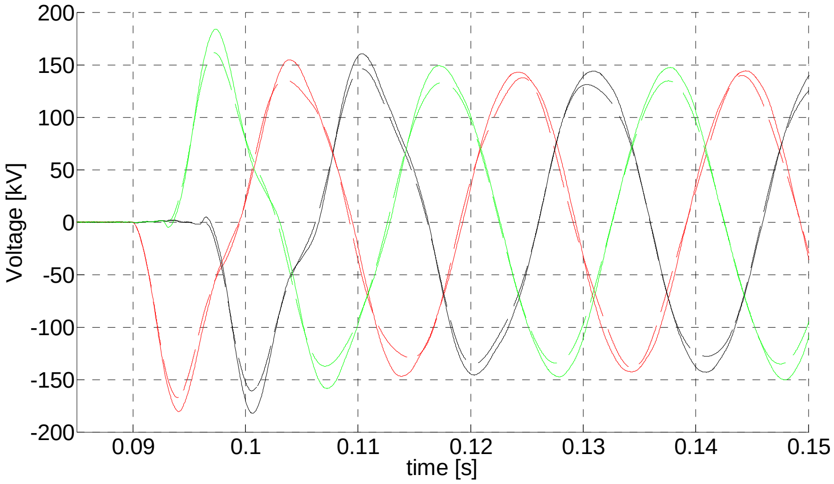

Figure 4.19 - Voltage in the cable receiving end. Dashed: Simulation; Solid: Measurements

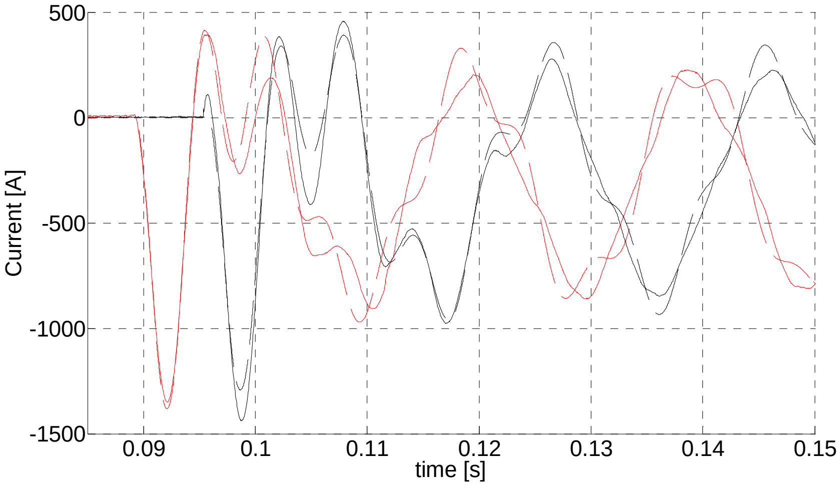

Figure 4.20 - Current in the cable sending end. Dashed: Simulation; Solid: Measurements

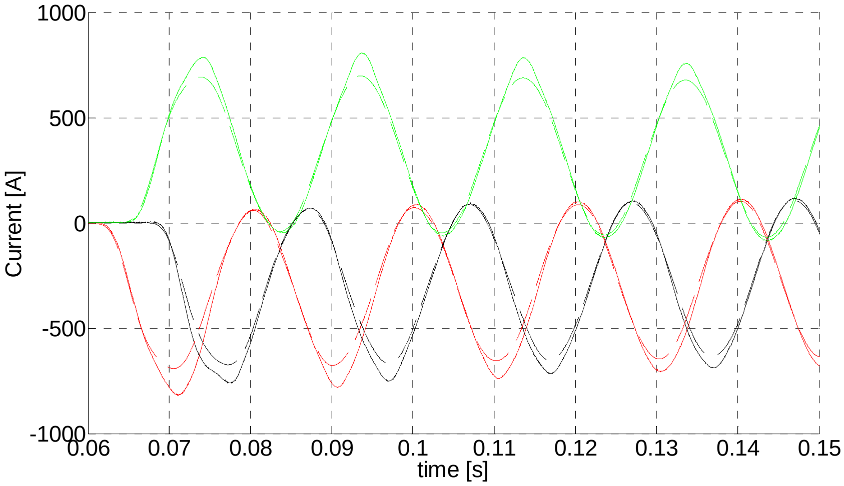

Figure 4.21 - Current into the shunt reactor. Dashed: Simulation; Solid: Measurements

Table 4.15 - Maximum peak voltage in the cable sending and receiving ends during energisation

	Sending end			Receiving end		
	Phase A	**Phase B**	**Phase C**	**Phase A**	**Phase B**	**Phase C**
Measurements	159.2	161.3	162.5	180.5	182.2	183.8
PSCAD/EMTDC	155.5	150.7	151.4	167.2	161.3	160.8
Error [%]	2.3	6.6	6.8	7.4	11.5	12.5

Table 4.16 - Maximum peak current in the cable sending end and shunt reactor during energisation

	Sending end			Shunt reactor		
	Phase A	**Phase B**	**Phase C**	**Phase A**	**Phase B**	**Phase C**
Measurements	1350	-	1437	817.1	786.9	758.0
PSCAD/EMTDC	1381	-	1293	691.5	694.1	673.3
Error [%]	2.3	-	10	15.4	11.8	11.2

There is good agreement between the simulated and measured voltage and current in the sending end during the first moments of the transient. Approximately 10 ms after the energisation, the simulation accuracy starts to reduce. This happens because the adjacent busbars, and consequently the reflections in those busbars, are not considered in the simulation. This topic is discussed further in chapter 6.

The voltage in the receiving end displays a similar behaviour for the simulations and measurements, but with a large voltage in the last ones. This discrepancy was explained in the previous section.

The current into the shunt reactor behaves differently when comparing the simulations with the measurements. The measured current has a larger peak value and is more distorted.

The peak current of the shunt reactor in steady-state is 386.5A. Theoretically, for an energisation at zero voltage, the peak current of the shunt reactor during the transient would be no more than two times the steady-state current, but in these measurements the peak current during the transient is 2.114 times larger than the steady-state current. This behaviour is similar to all three energisations, with small changes in the peak values.

The phases are not switched-off at the same time, meaning that there is zero-sequence flux between the disconnection of the first and third phases. Moreover, the system is unbalanced during the cable de-energisation.

As a result, flux will flow into the two outer limbs, and some flux may remain in the shunt reactor after the disconnection, leading to the higher current measured. This theory is reinforced by the current distortion, which indicates inrush currents. Remanence cannot be directly modelled in PSCAD/EMTDC, and the amount of flux that remains in the shunt reactor is also unknowing, making a more precise modelling of the shunt reactor very difficult.

A more attentive analysis of the results shows that the synchronised switching is not precise for all the phases. The energisation of phase A occurs at the same time for the measurements and simulations, but a small discrepancy seems to exist for phases B and C. Due to mutual coupling it is neither possible to be precise about the exact energisation instants for phases B and C, nor the correct CB closing times in the simulation. In [62] the same problem was faced, and it was concluded by means of multiple runs that the best correspondence between the results was obtained by having the switching of phases B and C taking place 0.5 ms later. Figure 4.22 to Figure 4.25 show the plots for a CB closing phases B and C 0.5ms later. The differences between the simulations and the measurements are reduced for the correct switching time.

Corrected switching instant

Figure 4.22 to Figure 4.25 compare the voltage and current in the sending end, receiving end and shunt reactor for the energisation, with the switching time corrected. The comparison is between the measured results and PSCAD/EMTDC simulations.

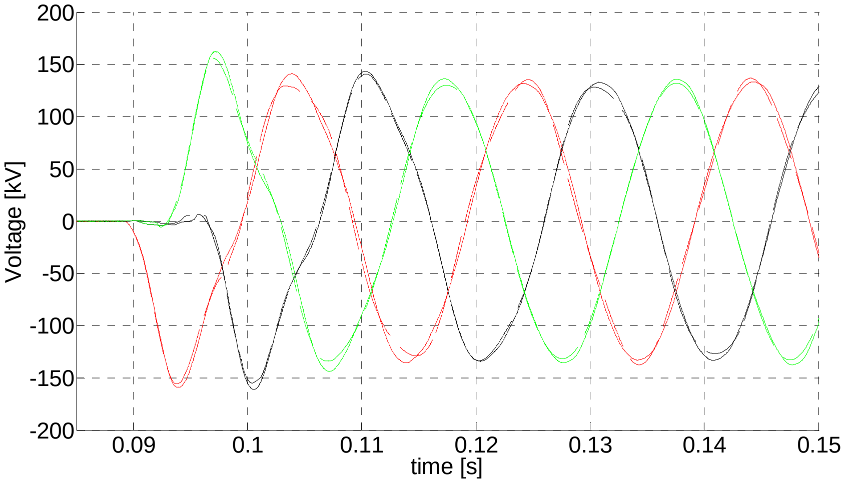

Figure 4.22 - Corrected voltage in the cable sending end. Dashed: Simulation; Solid: Measurements

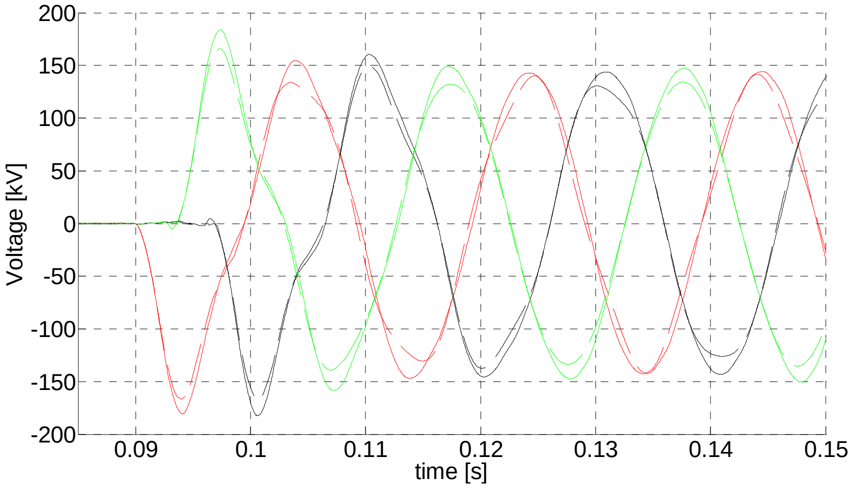

Figure 4.23 - Corrected voltage in the cable receiving end. Dashed: Simulation; Solid: Measurements

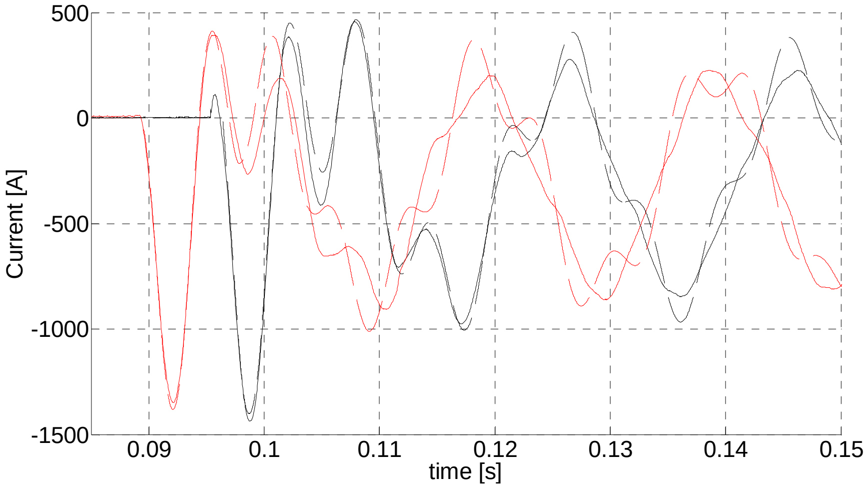

Figure 4.24 - Corrected current in the cable sending end. Dashed: Simulation; Solid: Measurements

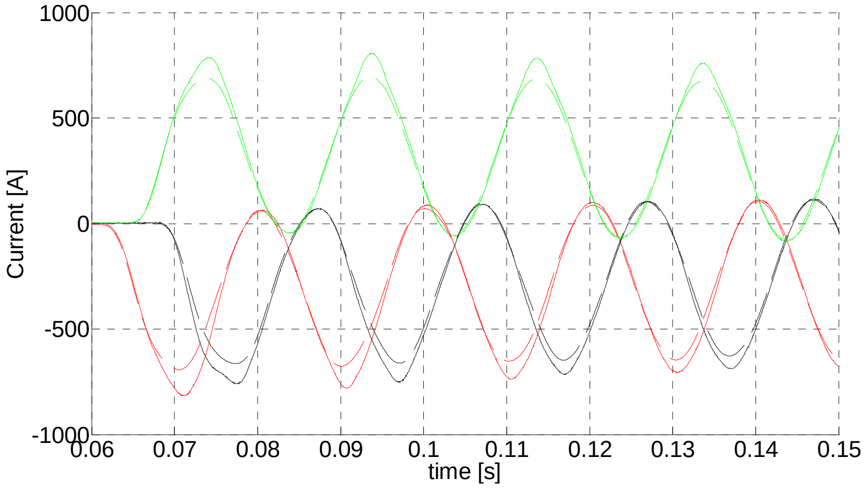

Figure 4.25 - Corrected current into the shunt reactor. Dashed: Simulation; Solid: Measurements

Table 4.17 - Maximum peak voltage in the cable sending and receiving ends during energisation

	Sending end			**Receiving end**		
	Phase A	**Phase B**	**Phase C**	**Phase A**	**Phase B**	**Phase C**
Measurements	159.2	161.3	162.5	180.5	182.2	183.8
PSCAD/EMTDC	155.8	155.9	154.9	166.3	167.6	165.9
Error [%]	2.1	3.3	4.7	7.9	8.0	9.7

Table 4.18 - Maximum peak current in the cable sending and shunt reactor during energisation

	Sending end			**Shunt reactor**		
	Phase A	**Phase B**	**Phase C**	**Phase A**	**Phase B**	**Phase C**
Measurements	1350	-	1437	817.1	786.9	758.0
PSCAD/EMTDC	1381	-	1402	692.7	664.3	688.0
Error [%]	2.3	-	2.4	15.2	15.6	9.2

The correction of the switching times shows an increase in the model accuracy for the voltage and current in the sending ends. For the reasons previously mentioned, both the voltage in the receiving end and the current into the shunt reactor continue to have a higher inaccuracy.

4.6.4 De-energisation

Figure 4.26 to Figure 4.28 compare the voltage in the sending and receiving ends and shunt reactor current during de-energisation. The comparison is between the measured results and PSCAD/EMTDC simulations and the disconnection sequence is Phase C-Phase B-Phase A (green-black-red).

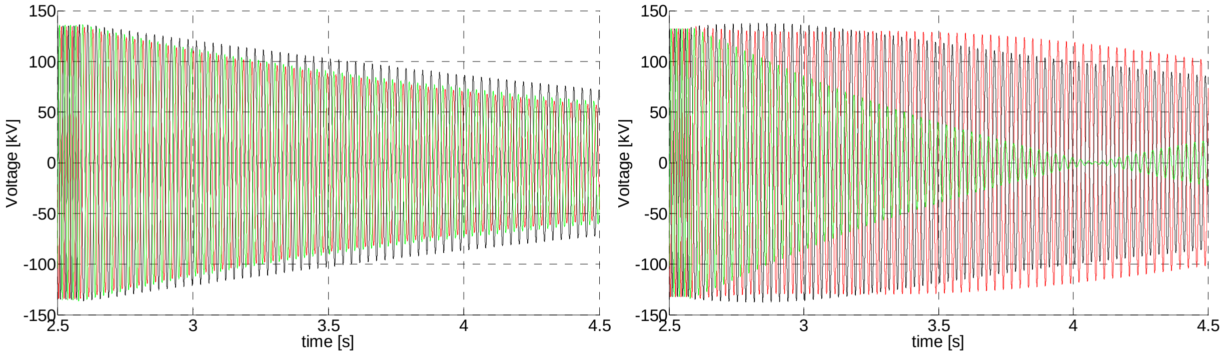

(a) (b)

Figure 4.26 - Voltage in the cable sending end during de-energisation. a) Measurements; b) Simulations

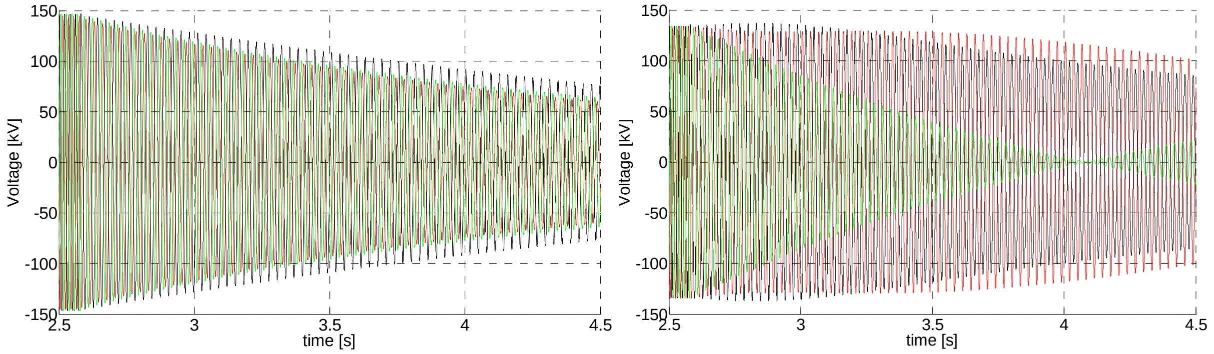

(a) (b)

Figure 4.27 - Voltage in the cable receiving end during de-energisation. a) Measurements; b) Simulations

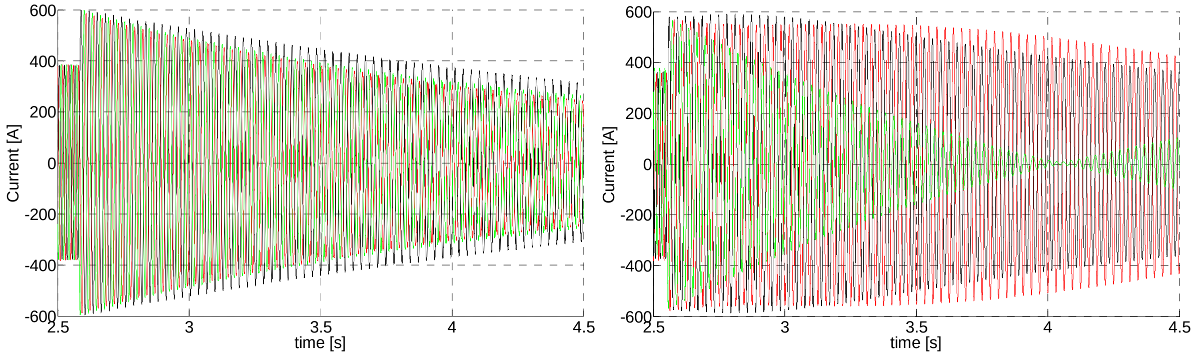

(a) (b)

Figure 4.28 - Current into the shunt reactor during de-energisation. a) Measurements; b) Simulations

Before the simulation results are commented upon, the measurements should be further analysed. The cable was energised and de-energised three times, and all transients were measured.

For the energisation transients all three waveforms were similar, with only minor differences in the peak values, but for the de-energisation the transients had some more noticeable differences.

The voltage in the cable sending end (Figure 4.26.a) is used as reference. After the switch off, the voltage in all three phases decreases and no overvoltage is present (Figure 4.29 shows a zoom of the first seconds of the disconnection). The disconnection sequence is Phase C-Phase B-Phase A.

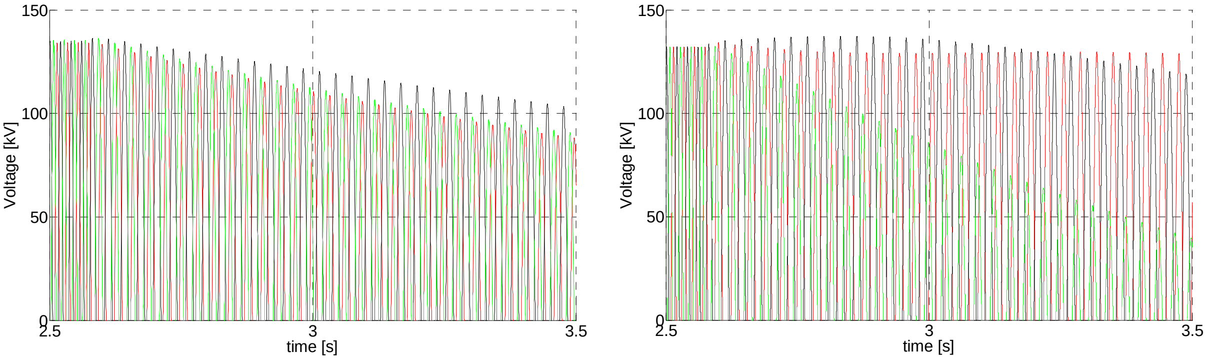

(a) (b)

Figure 4.29 - Zoom of the voltage in the cable sending end during de-energisation. a) Measurements; b) Simulations

Figure 4.30.a and Figure 4.31.a show the voltage in the cable sending end during the disconnection of respectively, the disconnection sequences Phase B-Phase A-Phase C and Phase A-Phase C-Phase B. For these disconnection sequences there is an overvoltage in the first phase to be disconnected.

The overvoltage is a result of mutual coupling between phases. The mutual coupling is not equal between all phases resulting in an overvoltage for only some disconnection sequences. The explanation of the phenomenon is done in chapter 5.7.

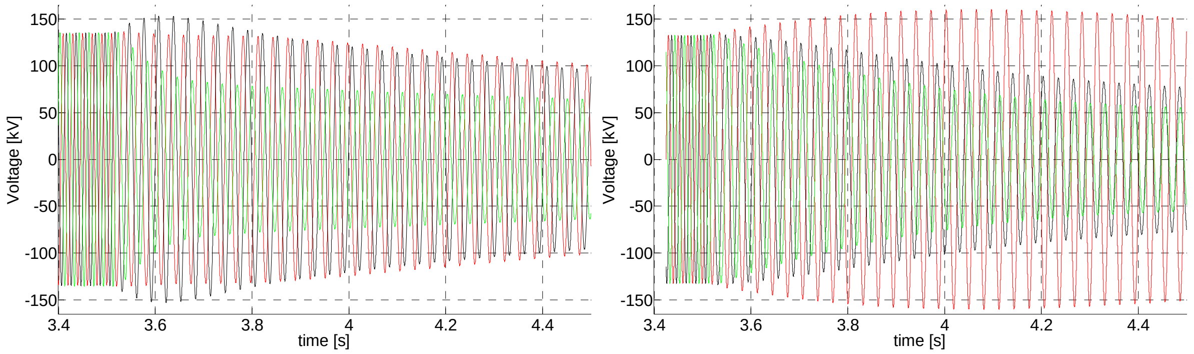

(a) (b)

Figure 4.30 - Voltage in the cable sending end during de-energisation for the disconnection sequence B-A-C; a) Measurements; b) Simulations

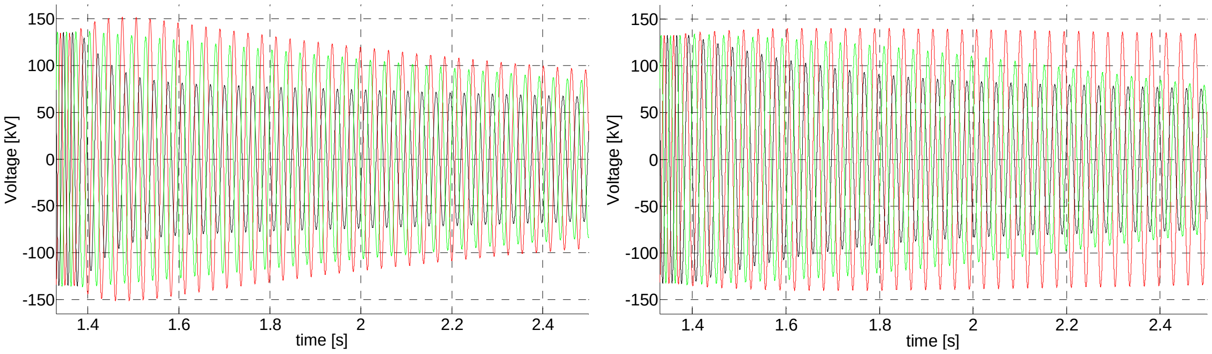

(a) (b)

Figure 4.31 - Voltage in the cable sending end during de-energisation for the disconnection sequence A-C-B; a) Measurements; b) Simulations

The measurements and simulations do not present similar results for the de-energisation of the line. The differences are related to modelling issues in the submarine cable, as previously explained.

The overvoltages registered in the measurements are the result of the mutual inductance between the phases of the shunt reactor and other unknown coupling effects in the submarine cable and cannot be obtained in the simulations.

4.6.5 Conclusions

The measurements validate the Horns Rev 2 single-core model, i.e. the land cable model, used in PSCAD/EMTDC both for transients and steady-state conditions. The Western Denmark 2030 network is composed of single-core cables only, similar to the land cable used in the connection to Horns Rev 2 offshore wind farm. The parameters of the models used in the 2030 network are corrected in the same way that the Horns Rev 2 land cable was corrected in chapter 4.5.1. Therefore, the models used to simulate the 2030 grid should provide accurate results, as happened in the simulation of the Horns Rev 2 connection, and the conclusions obtained in the following chapters are valid.

The shunt rector model was demonstrated to be accurate throughout a comparison with the manufacturer test report. The asymmetrical mutual coupling cannot be included in the model, but it was demonstrated that the error is negligible for typical values.

The submarine cable is the cause of the differences between measurements and simulations, and it should be studied in more detail. Such analysis falls outside of the thesis aim and it is therefore not done.

The chapter also demonstrated that the use of an inductive voltage transformer gives accurate results up to 1kHz frequencies and that it can be used to perform full-scale measurements.

5. Main transients and countermeasures affecting an HV cable system

5.1 Introduction

Chapter 2.4 briefly described several cable transient phenomena, which should normally be avoided as much as possible. This chapter provides a deeper explanation of those phenomena presenting simulations made in the 2030 grid described in chapter 3, and, when possible, results from measurements made in Horns Rev 2 cable.

The chapter also provides countermeasures that can be used to minimise the different transients.

5.2 Cable energisation when connected to a strong grid

The transient associated with cable energisation depends on the short-circuit power. Consequently, it is not the same to energise a cable in a strong or weak grid.

Energising a cable in a strong grid is the typical case in Denmark and most European countries, where there are unusually large areas with low population density. In the limit this energisation can be seen as the energisation of a cable connected to an ideal voltage source.

One of the strongest nodes in the Danish grid is the NVV node localized north of the city of Aalborg, which has a short-circuit power of approximately 10000MVA (refer to map in Appendix A). As an example, the energisation of a 47.49km cable from the NVV end will be shown.

The voltage in the receiving end of this cable during energisation is shown in Figure 5.1.a. In the simulation all phases are closed at the same time, the voltage in phase B (green curve) being at its peak in the energisation instant. The simulation was repeated with the cable connected to a voltage source, i.e. simulating an infinite short-circuit power, whose result is shown in Figure 5.1.b.

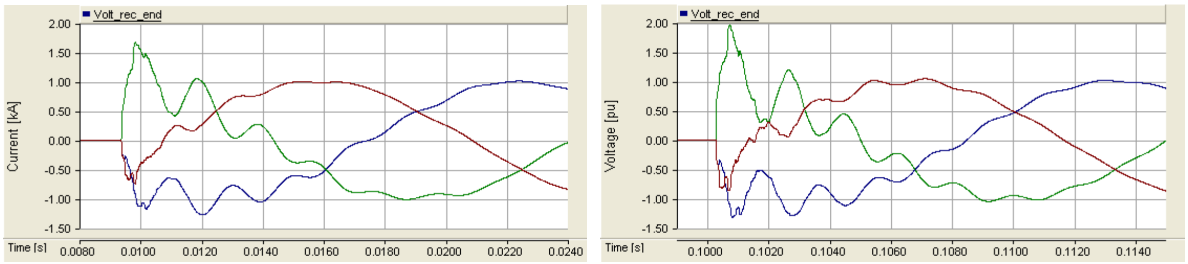

(a) (b)

Figure 5.1 - Voltage in the cable receiving end during energisation. a) Real system; b) Infinite short-circuit power

The two simulations are comparable, but with some relevant differences. The overvoltage is higher and the transient less damped when the cable is energised by an ideal voltage source. This happens because of reflections in the cable sending end. Situation that is further analysed in chapter 6.

A relevant parameter for the transient is the voltage value at the CB terminal at the energisation instant, which as explained in chapter 2.4.1, influences the transient and the respective peak voltage and peak current.

In a typical system, the voltage at the CB terminals is between 0 pu and 1 pu in the instant prior to energisation. The maximum overvoltage is associated with 1 pu voltage, which can go up to a theoretical maximum of 2 pu in a lossless line, while the minimum is associated with a 0 pu voltage difference.

It is typical of many transmission networks to have the CB operating in synchronised switching, i.e. the phases are not all closed at the same instant, as in the examples shown in Figure 5.1, but at different instants. The most common situation is to close all three phases at zero voltage, as shown in Figure 5.2.

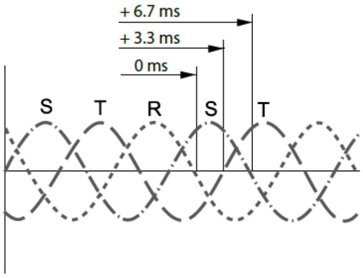

Figure 5.2 - Example of synchronised switching for zero voltage [72]

The influence of synchronised switching in a transient is shown in Figure 5.3, where the energisation shown in Figure 5.1.b is again simulated, but with synchronised switching for peak voltage (Figure 5.3.a) and zero voltage (Figure 5.3.b).

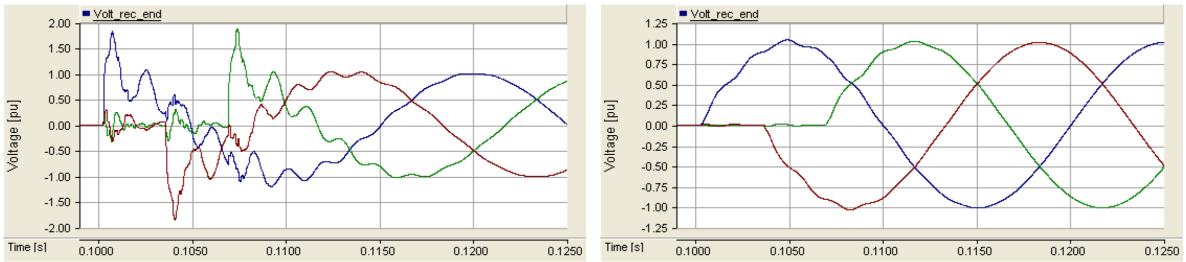

(a) (b)

Figure 5.3 - Voltage in the cable receiving end during energisation. a) Synchronised switching at peak voltage; b) Synchronised switching at zero voltage

One important feature of synchronised switching is that the transient is almost identical for all three phases; the existing differences are due to mutual coupling.

The mutual coupling is observed in both of the plots shown in Figure 5.3, but is more noticeable in Figure 5.3.a because of the higher currents associated with peak voltage energisation. This mutual coupling increases the overvoltage of the third phase to be connected when compared with the first. As an example, in Figure 5.3.a the peak overvoltages are 1.833 pu and 1.876 pu for the first and third phase to be connected, respectively. The voltage in the last phase to be connected is approximately -0.041 pu when the CB

switches on that phase, in contrast to the 0 pu of the first phase to be energised, which leads to the difference in the peak overvoltages.
Mutual coupling was also observed in the energisation of Horns Rev 2 cable. Figure 5.4 shows the voltage during cable energisation, with the vertical coloured lines indicating the switching instant. It should be noted that a shunt reactor is energised together with the cable, increasing the total system mutual coupling.

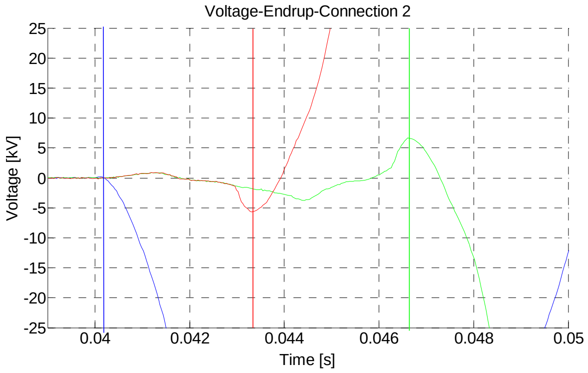

Figure 5.4 - Horns Rev 2 Measurements: Voltage in the sending end during energisation

When analysing the results presented in this section, it is concluded that it is advantageous to use synchronised switching and to energise each phase at zero voltage, avoiding the overvoltages associated with cable energisation. On the other hand, performing such energisation may result in the undesired zero-missing phenomenon.

5.3 Zero-missing phenomenon

In some situations, most notably for long cables, a cable and a shunt reactor are energised together, what may result into zero-missing phenomenon. When zero-missing occurs, it is not possible to open the circuit breaker without risk of damage, except if the circuit breaker is designed to interrupt DC currents or open at a non-zero current value [9], [74]. Zero-missing can last several seconds and represents a severe risk to the network equipment.

An easy way of understanding the zero-missing phenomenon is by analysing an inductor in parallel with a capacitor of equal impedance. In this situation the currents in the capacitor and inductor have equal amplitude and are in phase opposition. The current in the inductor can also have a DC component, whose value depends on the voltage at the moment of connection.
In an inductor there is a 90º phase difference between the current and the voltage at its terminals. Thus, if the voltage is zero, the current should be maximum and vice-versa. The current in an inductor is continuous with the value zero prior to energisation, and so it must also be zero after the connection regardless of the voltage at the moment of connection. Therefore, if the inductor is connected for zero voltage in order to maintain its continuity, the current will have a DC component with an amplitude equal to the amplitude of the AC component. If the inductor is connected for a peak voltage, no DC component is present [73].

Figure 5.5 shows an inductor in series with a resistor, both of them in parallel with a capacitor. The resistance is 100 times lower than the inductor reactance, which is equal to the capacitor reactance. Figure 5.6 shows a simulation of Figure 5.5. The circuit breaker closes when the voltage is crossing zero, and therefore the DC component in the inductor is maximum. The inductive and capacitive AC components cancel each outer out (*IL* and *IC* have equal amplitude and are in phase opposition), and the current *I1* contains only the decaying DC component

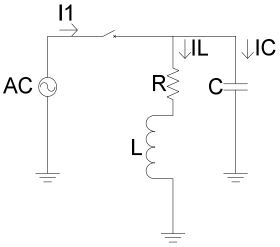

Figure 5.5 - Equivalent scheme of an inductor in series with a resistor, both in parallel with a capacitor

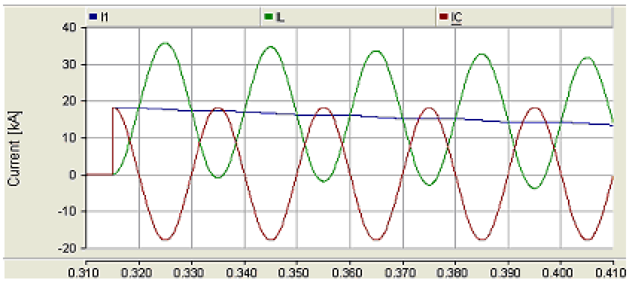

Figure 5.6 - Current in the inductor (IL), in the capacitor (IC) and the sum (I1=IL+IC)

The behaviour of a system consisting of a shunt reactor and a cable is not very different from the one depicted in Figure 5.5. The shunt reactor can be modelled as an inductor in series with a resistor, and the cable is mainly a capacitive shunt element [38]. There are, however differences between the behaviour of a simple RLC circuit and a physical cable/shunt reactor system.

The existence of zero-missing phenomenon depends on the compensation level. If the shunt reactor compensates for less than 50% of the reactive power generated by the cable, the AC component is larger than DC component. As a result, the current crosses zero value in all cycles, and there is no zero-missing.
Figure 5.7 shows for different compensation levels the minimum time required to open the cable CB, when energising the 47.49 km NVV-BDK cable. The cable is connected to an ideal voltage source and the shunt reactor is installed in the cable sending end. The simulations are made for a constant X/R relation and a constant shunt reactor resistance value.
As expected, the larger the compensation the longer is necessary to wait before opening the CB. In the unlikely event of the compensation exceeding 100%, the zero-missing duration decreases as the current through the CB becomes inductive and the AC component starts increasing.

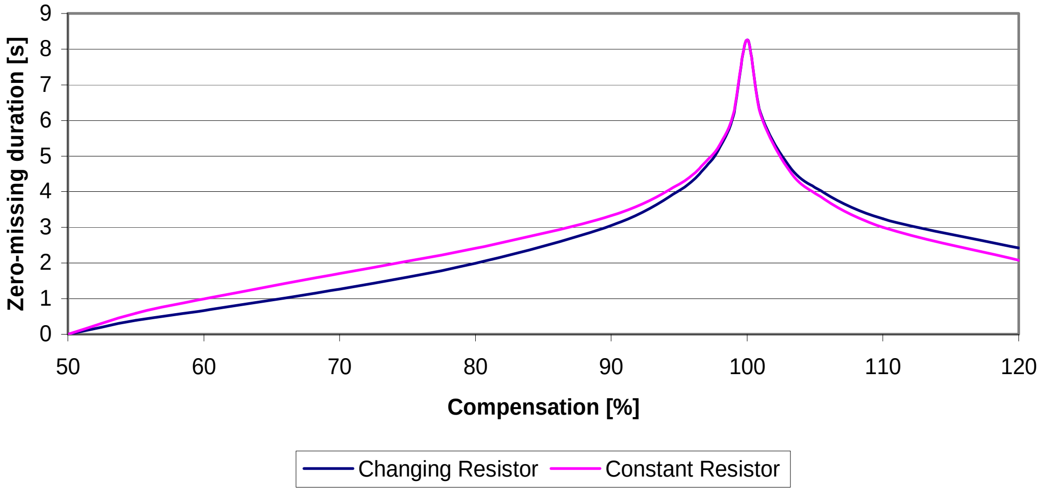

Figure 5.7 - Minimum time required for current zero-crossing for different compensation levels

Example using Denmark's 2030 network

This phenomenon can be observed in Denmark's 2030 transmission grid. As an example, the 47.49 km cable line between the NVV and BDK nodes will be used again, with one difference. In the original planning, the shunt reactors are installed in the substations located at the ends of the cable line. In this disposition, the shunt reactors are not energised together with the cable and zero-missing is not possible.

The shunt reactor installed in the cable receiving end compensates for 69% of the reactive power generated by the cable, and it will be considered to be directly connected to the cable instead of the busbar. By changing the location of the shunt reactor, the energisation transient changes and zero-missing phenomenon may occur.

The new simulation is presented in Figure 5.8; the CB closing sequence is identical to the one shown in Figure 5.3.b, i.e. synchronised switching at zero voltage.

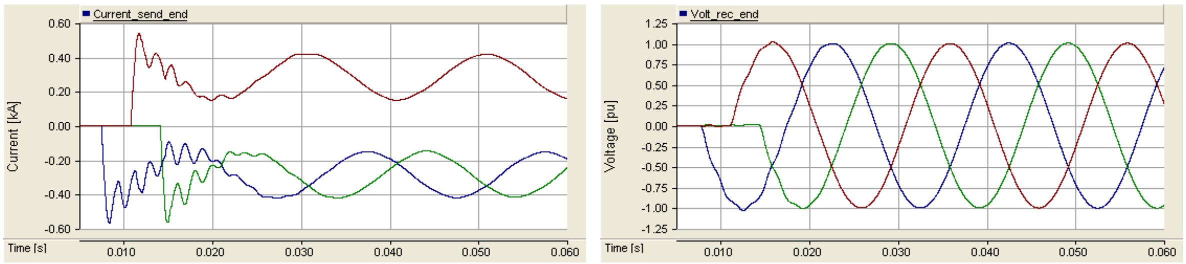

(a) (b)

Figure 5.8 - a) Current through the CB during energisation; b) Voltage in the cable receiving end during energisation

In the simulation all three phases are closed at zero voltage by means of synchronised switching, resulting in maximum DC current in the shunt reactor. As the shunt reactor compensates for 69% of the cable reactive power, the zero-missing phenomenon occurs.

For nominal voltage the cable charging current has a peak amplitude of 426 A, which for a 69% reactive power compensation corresponds to a DC current of 294 A and an AC current of 132 A flowing through the CB. These values are confirmed in Figure 5.8.a, where it can be seen that the minimum value for the fist cycles is approximately the expected 162 A, the minor differences are a result of the damping of the DC component and the fact that the voltage is not exactly equal to the nominal.

Thus, it seems that when compensating for more than 50% of the cable reactive power, the utility has to decide between having switching overvoltages or zero-missing phenomenon. Fortunately, there are countermeasures that can be applied.

5.3.1 *Countermeasures for zero-missing phenomenon*

The simplest countermeasures used to avoid zero-missing phenomenon are immediately deduced. If the shunt reactor is connected to the busbar or the cable through a CB, it is possible to control its closing time and energise the shunt reactor for peak voltages, avoiding DC currents. The drawback of this countermeasure is that it is necessary to buy an extra CB, which in order to be 100% efficient should have synchronised switching capability, thus increasing the financial costs.

Different reactive power compensation levels and locations

To have zero-missing phenomenon it is necessary that the shunt reactor compensates for more than 50% of the reactive power generated by the cable and is energised together with the cable.

The reactive power generated by a long cable is so high that very often the compensation can be made by more than one shunt reactor. When this happens, the shunt reactors can and should be installed at different locations, one possibility being to connect part of the reactive power compensation, less than 50%, directly to the cable and the remaining to the busbar, which can be also used to control the network voltage.

One example of this method is the already described Horns Rev 2 connection where 40% of the reactive power is compensated for by a shunt reactor connected directly to the cable, and the remaining 60% in the onshore substation.

This method is a possibility for meshed grids, where several cables are connected to the same busbar and it is necessary to use the shunt reactors to control the system voltage.

Use of a pre-insertion resistor

A pre-insertion resistor consists of resistor blocks connected in parallel with the circuit breaker's breaking chamber and closes the circuit 8-12 ms before the arcing contacts [72] (in this analysis the time considered is 10 ms).

The value of the pre-insertion resistor should be such that the DC component becomes very small (ideally null) after 10ms, in other words the DC component is damped in the first 10 ms.

To eliminate the DC component in the first 10 ms, the pre-insertion resistor value should be precise.

If the pre-insertion resistor is too small it will not be able to damp the entire DC component in just 10 ms. If the pre-insertion resistor is too large, it will be equivalent to an open circuit. Thus, when the pre-insertion resistor is bypassed the transient is similar to one obtained if no pre-insertion resistor was used. As the pre-insertion resistor is connected during 10 ms, when it gets disconnected the voltage value of the generator is symmetric to the value at the time of connection ($V_1(10ms)=-V_1(0ms)$), and so the DC component will persist, but with opposite polarity.

Figure 5.9 illustrates the consequences of using an incorrect pre-insertion resistor value to energise the 47.49km NVV-BDK cable.

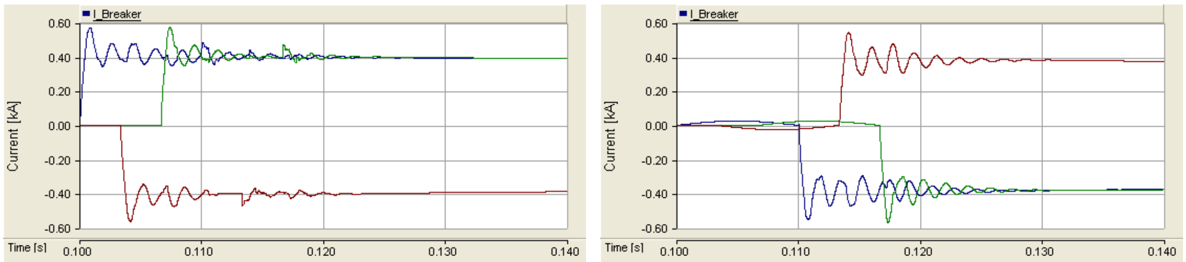

(a) (b)

Figure 5.9 - Current through the CB during energisation; a) Too small pre-insertion resistor (5Ω); b) Too large pre-insertion resistor (5kΩ)

Calculation of the pre-insertion resistor value

To calculate the pre-insertion resistor value a pi-model representation of the cable, as shown in Figure 5.10, will be used. Where V is the voltage source, R_S the shunt reactor resistance; L_S the shunt reactor inductance, R the cable's series resistance, L the cable's series inductance, C half of the cable's shunt capacitance and R_P the pre-insertion resistor.

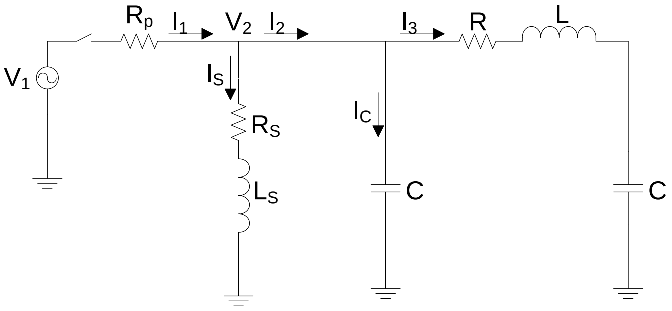

Figure 5.10 - Equivalent scheme of the shunt reactor and the cable when using a pre-insertion resistor

The system equations are shown in (35). As the system cannot be analytically solved [100], it is necessary to use of numerical methods.

$$\begin{cases} V_2 = L_s \dfrac{dI_s}{dt} + R_s I_s \\ V_2 = \dfrac{1}{C}\int I_c dt \\ V_2 = R \cdot I_3 + L\dfrac{dI_3}{dt} + \dfrac{1}{C}\int I_3 dt \\ I_1 = I_2 + I_3 + I_c \\ V_2 = V_1 \cos(\omega t) - R_p \cdot I_1 \end{cases} \tag{35}$$

However, it is possible to introduce some simplifications in order to obtain a first approximation of the pre-insertion resistor value. This is done by calculating the energy that the pre-insertion resistor should dissipate (36).

$$W = \frac{1}{2} L_s \left(I_s^{DC} \right)^2 \tag{36}$$

The energy dissipated in the pre-insertion resistor is calculated by the integral in (37), whose limits are the time during which the pre-insertion resistor is connected.

$$W = \int P dt \Leftrightarrow W = \int_0^{0.01} R_p I_1^2 dt \tag{37}$$

The objective is to calculate R_p, where both I_1 and I_S^{DC} depend on the connection instant and are unknown. For 100% reactive power compensation, the AC components of the shunt reactor and cable's currents cancel each other out, and at the moment of connection the current I_1 is equal to I_S^{DC}, whereas both should ideally be zero after 10 ms.

Considering that the current I_1 decreases linearly (this is an approximation, but as R_p is large the error is small), and neglecting R_S (which is much smaller than R_p), (37) can be simplified to (38), and the value of R_p is calculated by (40).

$$W = 0.01 R_p \left(\frac{I_1(0)}{2} \right)^2 \tag{38}$$

$$0.01 R_p \left(\frac{I_1(0)}{2} \right)^2 = \frac{1}{2} L_s \left(I_s^{DC} \right)^2 \Leftrightarrow 0.01 R_p \left(\frac{1}{2} \right)^2 = \frac{1}{2} L_s \tag{39}$$

$$R_p = \frac{2 L_s}{0.01} \tag{40}$$

Because of the simplifications this method is not always accurate. If the DC component is maximum, the error can be disregarded, but if the DC component is smaller, the error increases.

The use of differential equations allows a more accurate calculation of the pre-insertion resistor value, but an iterative process is required to calculate the value of R_p. The equation deduction is presented in Appendix C.

To perform the iterative process, a small program was written in Matlab, which can be consulted in Appendix D. The program increases R_p, until it reaches a value at which the DC component is damped in 10 ms.

To verify that the DC component is damped, the peak value of I_S is calculated 10 ms after connection. For that value to be equal to the amplitude of the AC component, the DC component must be equal to zero. So when the calculated value is equal to (41) plus a small tolerance the iterative process stops.

$$I_s^{peak} = \frac{V_2}{\sqrt{R_s^2 + (\omega L_s)^2}} \tag{41}$$

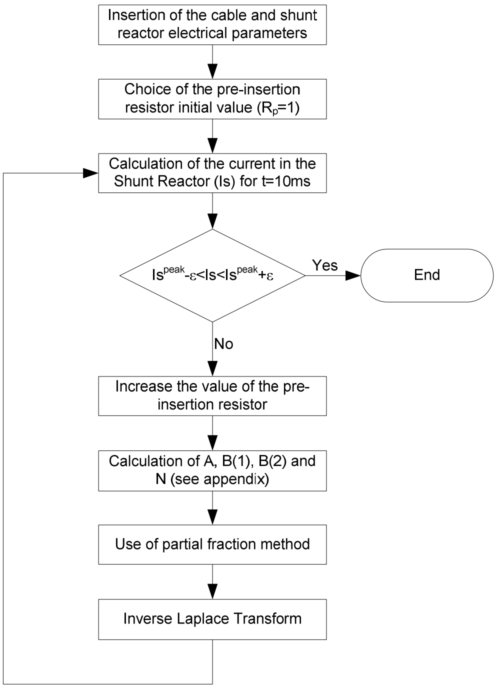

Figure 5.11 - Flowchart of the iterative process for the calculation of the pre-insertion resistor value

The value of the pre-insertion resistor depends on the initial value of the DC component. As this value depends on the connection moment, it was decided to solve the equations for the worst-case scenario, maximum DC component. For that case the calculated value of R_p is ideal, whereas for the other cases the error is small.

By solving the differential equations and using a cable equal to the NVV-BDK cable line connected to an ideal voltage source and compensated at 100%, 229 Ω is obtained as the ideal value for the pre-insertion resistor.

Figure 5.12 shows two simulations of a circuit breaker equipped with a pre-insertion resistor. In Figure 5.12.a the CB operates in synchronised switching and closes each phase for the maximum DC component in the phase. In Figure 5.12.b the CB closes the three phases at the same time for maximum DC component in just one of the phases.

In Figure 5.12.a all the three phases are zero during connection. In this situation the pre-insertion resistor completely damps the DC component in 10 ms and there is no zero-missing phenomenon. As the connection in all the phases is made for zero voltage, the switching overvoltage in the three phases is minimum.

For the situation depicted in Figure 5.12.b it is not possible to have zero voltage in the three phases when the CB closes, and therefore it is neither possible to eliminate the DC component nor completely minimise the switching overvoltages. However, in one of the phases there is neither a DC component nor switching overvoltage; this phase is the one where the voltage is zero at the connection moment.

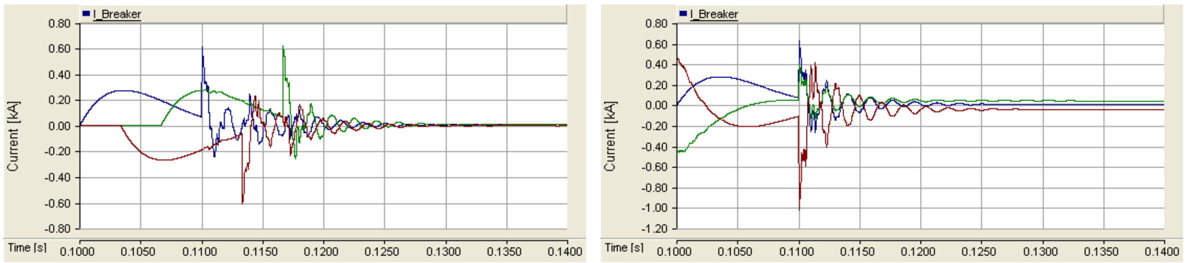

(a) (b)

Figure 5.12 - Simulation of cable energising for a circuit breaker using pre-insertion resistor. a) Synchronize switching at zero voltage; b) Ganged CB for peak voltage in phase A (blue curve)

Even if the value of the resistor is not ideal, the DC component of the shunt reactor current is always reduced, and it will be lower than a given maximum. Figure 5.13 shows the value of the DC component after 10 ms for different resistor values when the cable and the shunt reactor are connected for zero voltage.

The curve in Figure 5.13 is non-linear, and for pre-insertion resistor values close to the ideal; the DC component is very small, but for larger differences there is still zero-missing phenomenon during long periods of time.

If, for instance the value of the pre-insertion resistor value were calculated using the energy equations (40) instead of the differential equations, the initial DC current would be about 28.5 A, which is almost 20 times lower than the value of the initial DC component when no pre-insertion resistor is used (419 A). It can therefore be concluded that the method using the energy equations can be used to obtain a first approximation of the final resistor value.

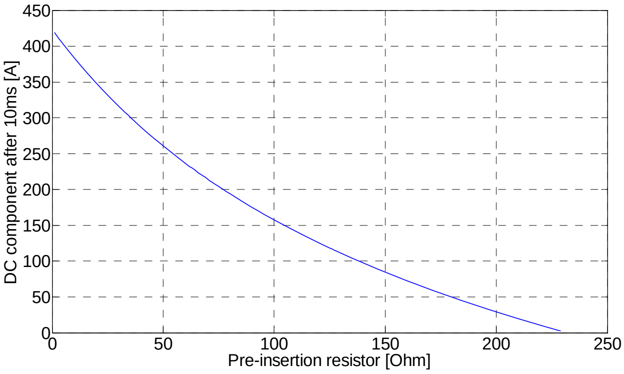

Figure 5.13 - Value of the DC component after bypassing the pre-insertion resistor, for phase closing when the voltage is zero and 100% of reactive power compensation

Example using Denmark's 2030 network

Figure 5.14 shows the current through a CB equipped with a pre-insertion resistor when energising the NVV-BDK cable line in 2030 Denmark network. The comparison of Figure 5.14 with Figure 5.8.a shows that the DC component is almost completely damped of when using the pre-insertion resistor and that zero-missing is no longer present. The pre-insertion resistor value was calculated using the developed Matlab code and it is equal to 322 Ω.

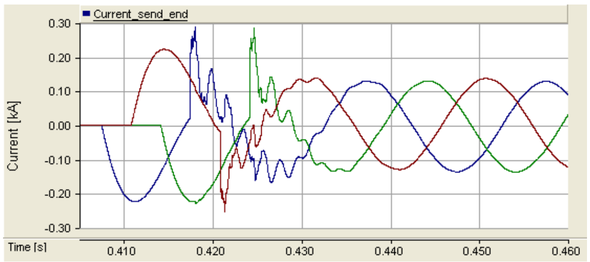

Figure 5.14 - Current through the CB during energisation when using a pre-insertion resistor (ideal value)

In this example the shunt reactor is not compensating for 100% of the cable reactive power. Thus, an AC component is present and the pre-insertion resistor can be smaller. Compensation is at 69%, which for this cable corresponds to a shunt reactor AC peak and DC currents of 293.5 A. The current through the CB will have a DC component equal to 293.5 A and an AC component equal to 161 A, calculated according to (42) and (43), where Q_S is the shunt reactor consumed reactive power, Q_{Cab} the reactive power generated by the cable, L_S the shunt reactor inductance, C the cable capacitance, I_S the current into the shunt reactor, I_{Cab} the current into the cable and I_{CB} the current through the CB.

$$Q_S = 0.69 Q_{Cab} \Leftrightarrow I_S^2 \cdot \omega L_S = 0.69 \cdot \frac{I_{Cab}^2}{\omega C} \Leftrightarrow I_{Cab} = I_S \omega \sqrt{\frac{L}{C}} \qquad (42)$$

$$I_{CB} = I_{Cab} - I_S \Leftrightarrow I_{CB} = I_S - I_S \omega \sqrt{\frac{L}{C}} \Leftrightarrow I_{CB} = I_S \left(1 - \omega \sqrt{\frac{L}{C}}\right) \tag{43}$$

Thus, the pre-insertion resistor should be such that the DC component value after 10 ms is equal to 132.5 A. From Figure 5.15 a value of 121 Ω is obtained as the minimum value for the pre-insertion resistor. Figure 5.16 confirms that for a 121 Ω pre-insertion resistor the DC component is not completely damped, but that zero-missing is no longer present.

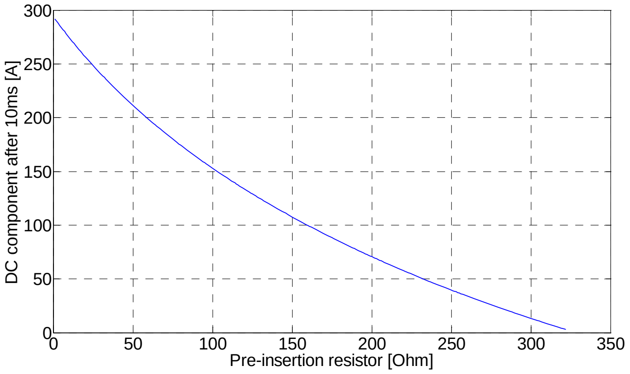

Figure 5.15 - Value of the DC component after bypassing the pre-insertion resistor, for a phase closing when the voltage is zero and 100% reactive power compensation (2030 network example)

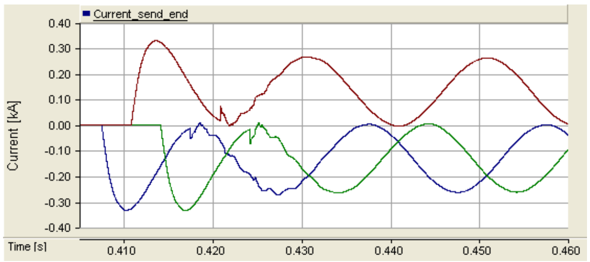

Figure 5.16 - Current through the CB during the energisation when using a pre-insertion resistor to energise the NVV-BDK cable compensated at 69% (minimum pre-insertion resistor value)

5.4 Cable energisation when connected to a weak grid

One of the factors influencing the transient is the short-circuit power level, which affects the transient's waveform, the overvoltage peak value and duration [75], [76].

In a strong grid the voltage in the sending end barely changes during the transient. The same does not happen when a cable in a weak grid is energised. Examples are the energisation of a cable in an isolated area, as is an island, or a black start.

5.4.1 Single-phase system example

The phenomenon is first explained for the energisation of an inductor in series with a capacitor. Figure 5.17 shows the simulation diagram where the inductor simulates an equivalent grid and the capacitor a cable.

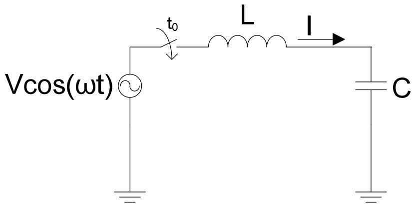

Figure 5.17 - LC System

The discharged LC system is described by (44).

$$V\frac{s}{s^2+\omega^2}=IsL+\frac{I}{sC} \tag{44}$$

Appling the partial fraction method to (44), (45) is obtained, whose time domain equivalent is (46).

$$I=\frac{-V\omega^2C}{\left(s^2+\omega^2\right)\left(1-\omega^2LC\right)}+\frac{VC}{\left(s^2LC+1\right)\left(1-\omega^2LC\right)} \tag{45}$$

$$I\left(t\right)=I_f+I_{res}=\frac{V}{\omega L-\frac{1}{\omega C}}\sin\left(\omega t\right)-\frac{V\sqrt{\frac{C}{L}}}{\left(\omega^2LC-1\right)}\sin\left(\frac{t}{\sqrt{LC}}\right) \tag{46}$$

Figure 5.18 and Figure 5.19 show a phasor representation of the phenomenon. The data used in the example is: L=0.6H, C=10.87µF and V=134kV, corresponding to a resonance frequency of 62.3 Hz.

In equation (46) the power frequency component and the resonance frequency component have opposite angle direction. Thus, at t_0 the phasors are in phase opposition. Since I_r rotates faster than I_f, the phasors will periodically be in phase and phase opposition, leading to higher and lower currents I, respectively, as observed in Figure 5.20.

For a t_1 equal to 35.9ms, the phasors are in the position shown in Figure 5.19, resulting in a current higher than the nominal (I(0.0359)=-2840A).

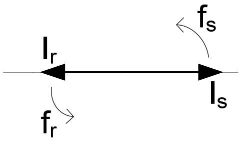

Figure 5.18 - Current phasors at t_0

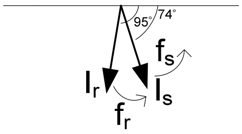

Figure 5.19 - Current phasors at t_1

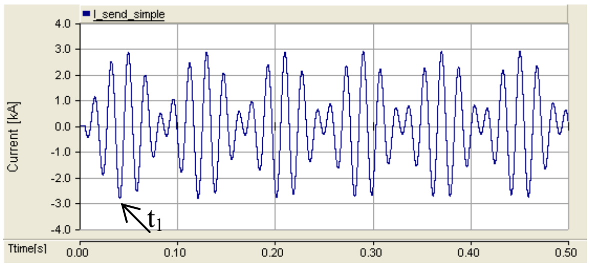

Figure 5.20 - Current in the sending end after energisation of the LC circuit

The previous example is very unrealistic, largely because the resonance component is not damped. The damping can be simulated by inserting a resistor in series with the capacitor and the inductor (see Figure 5.21); by doing this, (46) changes to (47).

Continuing to using the same parameters and inserting a 2.5Ω resistor, the plot shown in Figure 5.22 is obtained, whose behaviour is similar to the one shown in Figure 5.20, but with the important difference that the resonance component is now damped.

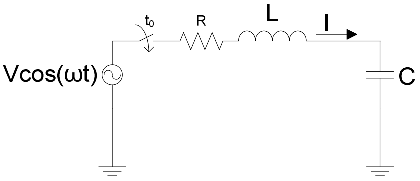

Figure 5.21 - RLC System

$$I(t)=\frac{V}{\sqrt{R^2+\left(\omega L-\frac{1}{\omega C}\right)^2}}\cdot\sin\left(\omega t+\alpha_1\right)+I_{aux}e^{-\beta t}\cdot\sin\left(\sqrt{\omega_0{}^2-\beta^2}\,t+\alpha_2\right) \qquad (47)$$

$$\beta=\frac{R}{2L} \quad \text{and} \quad \omega_0=\frac{1}{\sqrt{LC}} \qquad (48)$$

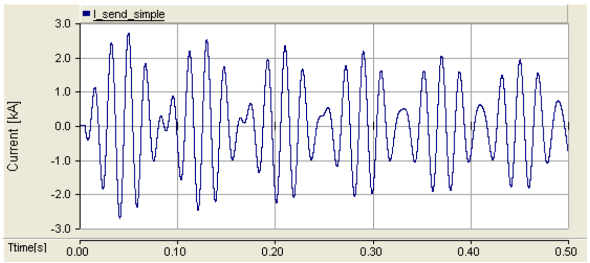

Figure 5.22 - Current in the sending end after energisation of the RLC circuit

Transposing the simple system to a real system, the C would represent the cable's capacitance and L and R the equivalent grid and the cable's impedances. The most important variable is L, whose value increases when the grid's short-circuit power level decreases.

5.4.2 Three-phase example

Figure 5.23 shows the energisation of a perfectly balanced cable, modelled by means of a FD-model equivalent to the RLC model used in the previous example. Because the system is balanced, and the circuit breakers operate in synchronised switching, the amplitudes are equal in all three phases, but with an opposite signal in the second phase to be connected (green curve in Figure 5.23). This means that when the peak amplitude of a cycle is equal to α in phase L1 and L3, the peak amplitude in phase L2 is -α.

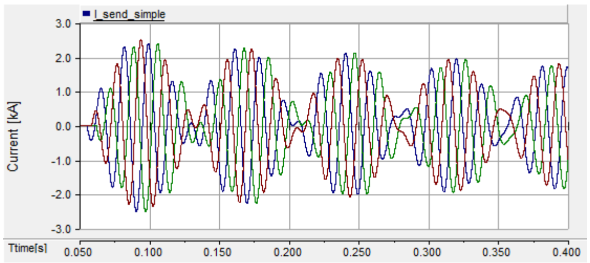

Figure 5.23 - Current in the sending end after energisation for a perfectly balanced cable connected to a weak grid

If the cable is not perfectly balanced (e.g. the cables are installed in flat formation or connected to an unbalanced shunt reactor), there are small changes in the resonance values, due to asymmetrical mutual coupling.

5.4.3 Grid influence

In the previous example the cable was directly connected to an equivalent grid, which may be an oversimplification of the system and result in a simulation inaccuracy. Therefore, the phenomenon is re-simulated using the circuit shown in Figure 5.24.

Figure 5.25 shows the voltage in the cable sending end during the energisation of the cable for a 172.8 MVA (L=0.5 H) equivalent grid. The peak voltage is 1.7 pu, and the temporary overvoltage have a duration of several power frequency cycles

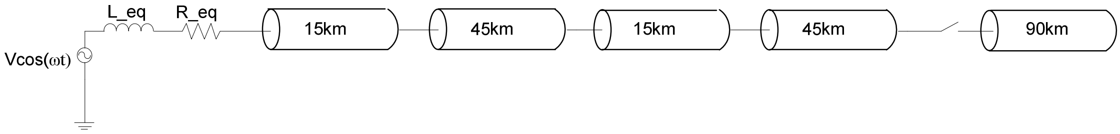

Figure 5.24 - Single-line diagram for the energisation of a 90km cable in a weak grid

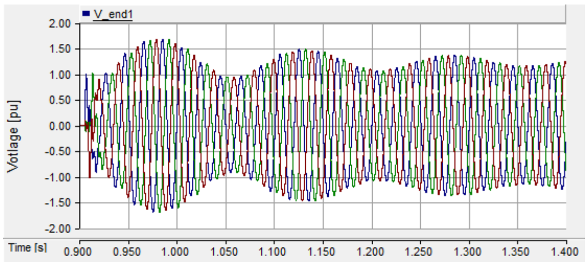

Figure 5.25 - Voltage in the cable receiving end during energisation (S_{SC}=172.8MVA)

The temporary overvoltage is strongly related to the short-circuit power. Figure 5.26 shows the peak voltage during the transient as a function of the equivalent grid short-circuit power.

The resonance overvoltage is also a function of the short-circuit power. Figure 5.27 shows the resonance frequency as a function of the equivalent grid short-circuit power. The lower the short-circuit power, the lower the resonance frequency.

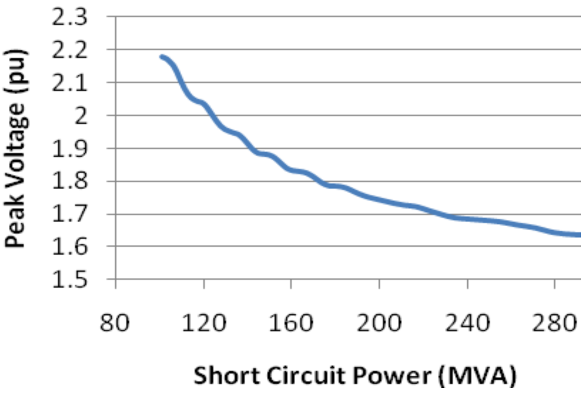

Figure 5.26 - Peak voltage during cable energisation for different short-circuit levels

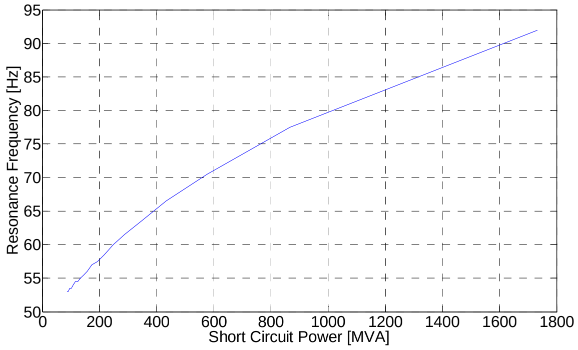

Figure 5.27 - Resonance frequency for different short-circuit power levels

5.4.4 Countermeasures

The location of the shunt reactor influences the overvoltage amplitude. Figure 5.28 shows two possible configurations for the installation of the shunt reactor.

Figure 5.29 shows the voltage in the cable receiving end during its energisation, assuming that a shunt reactor is either connected to the cable sending end or to the busbar. The shunt reactor is compensating for 95% of the reactive power generated by the cable.

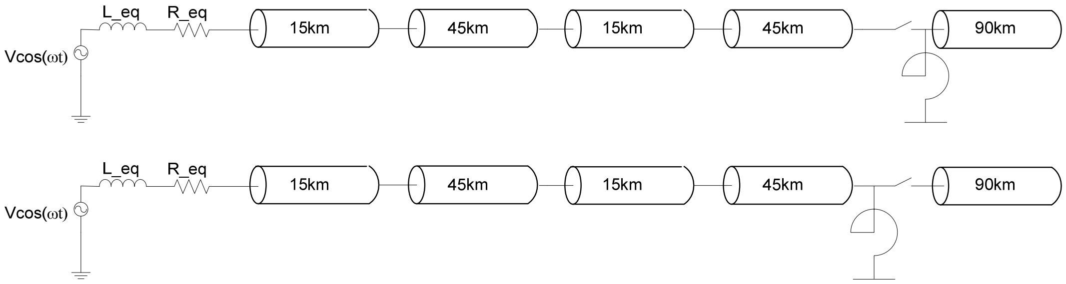

Figure 5.28 - Single-line diagram exemplifying the countermeasure. Up) Shunt reactor connected to the cable; Down) Shunt reactor connected to the busbar

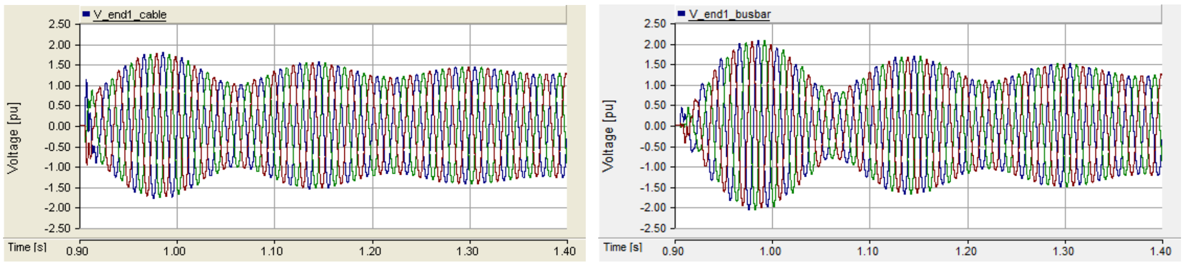

(a) (b)

Figure 5.29 - Voltage in the cable receiving end. a) Shunt reactor connected to the cable b) Shunt reactor connected to the busbar

The overvoltage is lower by approximately 0.26pu, when the reactive power compensation is done in the cable.

Another countermeasure would be to increase the resistance of the system, in order to obtain faster transient damping.

5.5 Energisation of cables in parallel

The energisation of a cable is not an isolated phenomenon as the lines and remaining equipment installed in the vicinity of the energised cable interact with the cable during the transient.
A cable can be modelled as an infinite series of RLC circuits as shown in Figure 5.30. The cable's inductance and resistance are very low when compared with the cable's capacitance. Thus, the "capacitors" of the two cables are almost in parallel. When in parallel, capacitors should have the same voltage, so that part of the charge on the "capacitors" of the previously energised cable(s) transfers almost immediately to the "capacitors" of the cable being energised, originating an inrush current, as indicated by the arrows in Figure 5.30.

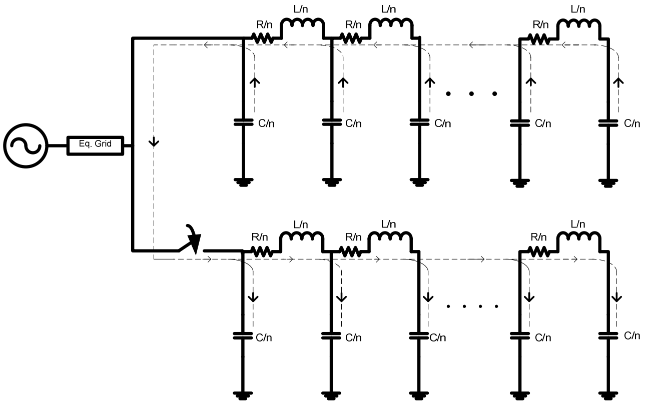

Figure 5.30 - Energisation of cables in parallel, lumped parameters equivalent model

5.5.1 Simple system

The energy transferred from the energised cable to the cable being energised depends on different parameters. The cables lengths, because of the capacitance, and the busbar short-circuit power.
Figure 5.31 shows two cables of equal length in parallel, connected to a voltage source though an equivalent grid, which will be used to explain the phenomenon. The cable used in the simulation is identical to the 47.49km NVV-BDK cable.

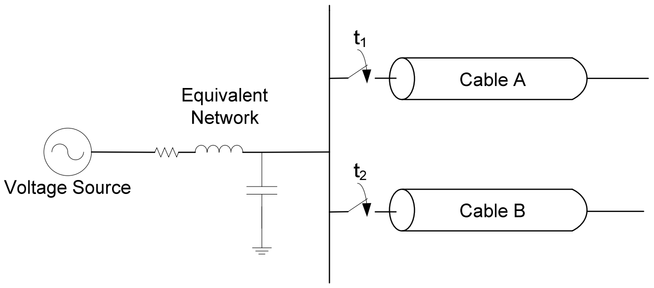

Figure 5.31 - Energisation of a cable in parallel with an already energised cable (t_2>>t_1)

The simulation consists in to energise first Cable A at t_1, while having Cable B disconnected from the system. At t_2, after Cable A reached steady-state conditions, Cable B is energised. The equivalent grid short-circuit power is 433 MVA (L=0.2 H).

Figure 5.32.a shows the current in Cable A during energisation at t_1, and Figure 5.32.b shows for one phase the current in both cables during the first milliseconds of the energisation of Cable B at t_2.

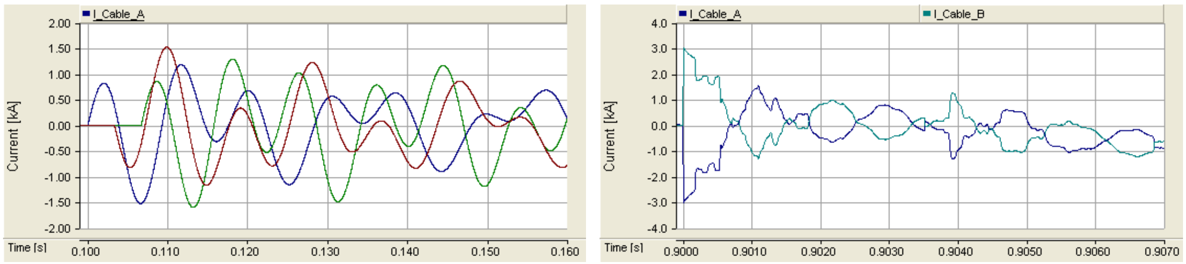

(a) (b)

Figure 5.32 - a) Current in Cable A during the energisation of Cable A; b) Current in Phase A of Cable A (blue curve) and Cable B (green curve) during the energisation of Cable B

Two important aspects should be noted when comparing the two simulations: The larger current's amplitude and frequency during the energisation of Cable B and the symmetry of the currents during the energisation of Cable B.

In this example, the node short-circuit power is low. As a result, the inrush current flows between Cable A and Cable B, resulting in the observed symmetry of the current.

Short-circuit power level

A factor influencing the inrush current amplitude and frequency is the short-circuit power. Figure 5.33 shows the maximum current associated with the energisation of Cable A and Cable B for different short-circuit powers. For the energisation of Cable A the maximum current decreases when the short-circuit power level increases.

For the energisation of Cable B, the peak current initially decreases, starting to increase only when the short-circuit power in lower than 578 MVA (L≥0.15 H). The reason for this behaviour is that for the stronger grids a substantial part of the current comes from the voltage source and not from Cable A.

Figure 5.34 shows the peak current value in both cables during the energisation of Cable B for different short-circuit power levels. For short-circuit powers lower than 578 MVA (L≥0.15 H), the currents are almost identical, meaning that the transients are almost symmetrical.

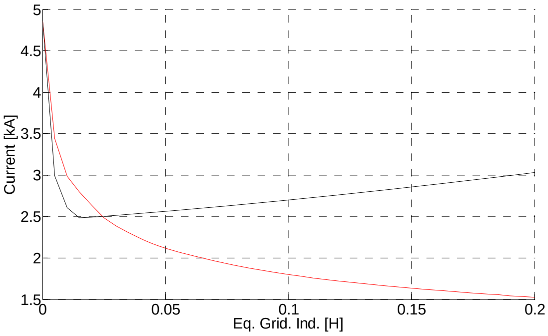

Figure 5.33 - Maximum current during the energisation of cables in parallel for different short-circuit power levels. Red: First cable to be energised; Black: Second cable to be energised

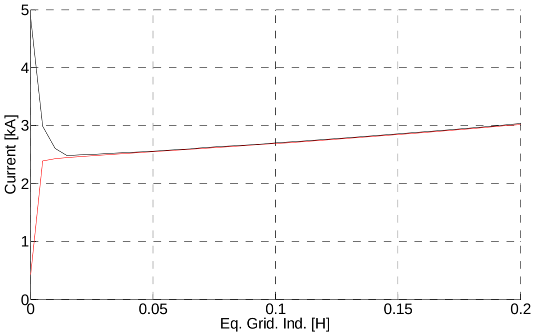

Figure 5.34 - Maximum current during the energisation of Cable A for different short-circuit power levels. Red: Cable previously energised; Black: Cable being energised

The current increase shown in Figure 5.33 and Figure 5.34 is not accurate. The inaccuracy is due to the use of an equivalent grid, which increases the voltage in the busbar, and consequently also the amplitude of the inrush current. For more information on this phenomenon see chapter 5.4.

However, the amplitude of the inrush current is proportional to the voltage drop in the cable sending end at the energisation instant. Therefore, one can extrapolate the behaviour of the current amplitude from the relative voltage drop. Figure 5.35 presents the relative voltage drop in Cable A sending end due to the energisation of Cable B. The voltage drop increases when the short-circuit power decreases, meaning that the inrush current amplitude is also higher when the short-circuit power decreases and that more energy is exchanged between the two cables during the energisation of cable B.

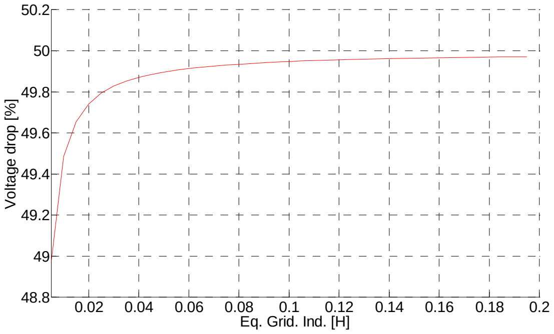

Figure 5.35 - Voltage drop in Cable A sending end due to the energisation of Cable B

Cable length

The length of the cables also influences the inrush current amplitude and frequency. Figure 5.36 assesses the impact of the cable length, by repeating Figure 5.33 energisations, for a Cable A and a Cable B of half the length. Shorter cables mean a lower total capacitance. Thus, it can be concluded that the inrush current peak amplitude is lower for smaller cables.

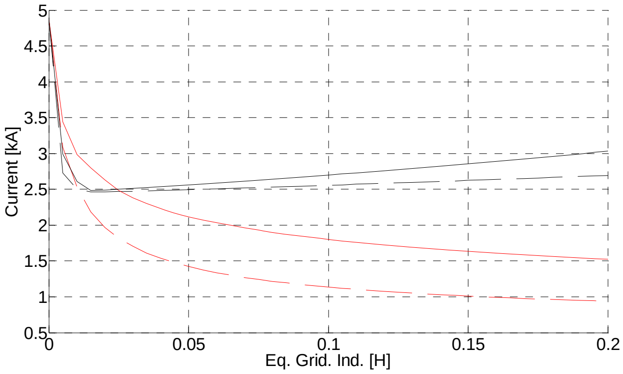

Figure 5.36 - Comparison of Figure 5.33 energisation (solid lines) with the energisation of cables of half the length (dashed lines)

Inrush Current Frequency

Circuit breakers have to fulfil requirements for the back-to-back capacitor making currents. According to the IEC standard 1st edition [29], the product of I_{bi} and f_{bi}, where I_{bi} designates maximum peak value and f_{bi} maximum frequency of the inrush current transient, for certain conditions is not to exceed the product of $I_{bi,N}$ and $f_{bi,N}$. This paragraph has been removed from the standard 2nd edition [77] and substituted by requirements for both a maximum I_{bi} and f_{bi}. Thus, when purchasing the CB it is necessary to know both the inrush current amplitude and frequency.

Reference [27] states that the inrush current *usually decays to zero in a fraction of a cycle of the system frequency.* Using this principle, it is calculated the frequency content of the current in the first 20ms after the energisation of Cable B. The frequency was calculated using a Short-time Fourier Analysis, meaning that it were also analysed the further cycles.

Figure 5.37 shows the frequency spectrum for the first 20 ms after energisation of Cable B for different short-circuit power levels.

From the graph it is concluded that the highest frequency is around 537 Hz. This frequency is constant for all short-circuit power levels, with the exception of the infinite short-circuit power case, meaning that it depends only on the cable parameters and possible inductances installed between the two cables. The magnitude of the impedance at the resonance point is not constant, increasing slowly when the short-circuit power decreases.

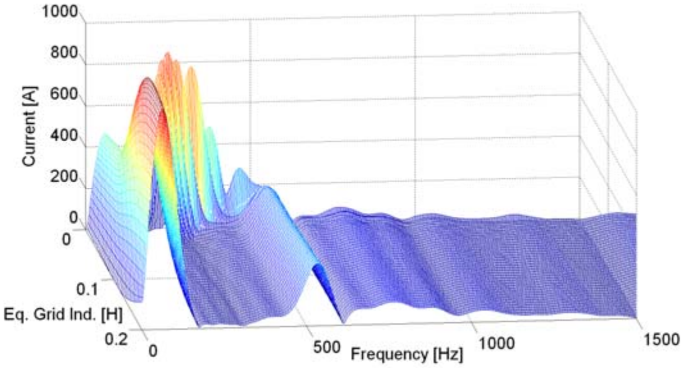

Figure 5.37 - Frequency spectrum for the first 20ms of the energisation for different short-circuit powers levels

The FFT was repeated for a system where the cables are half as long, analogous with the simulation of Figure 5.36. Figure 5.38 shows the frequency spectrum for the first 20 ms after energisation of Cable B for different short-circuit power levels.

From the graph it is concluded that the highest frequency is around the 1111 Hz, approximately the double of the previous example. The resonance frequency is again approximately constant for all short-circuit power levels, with the exception of the infinite short-circuit power case.

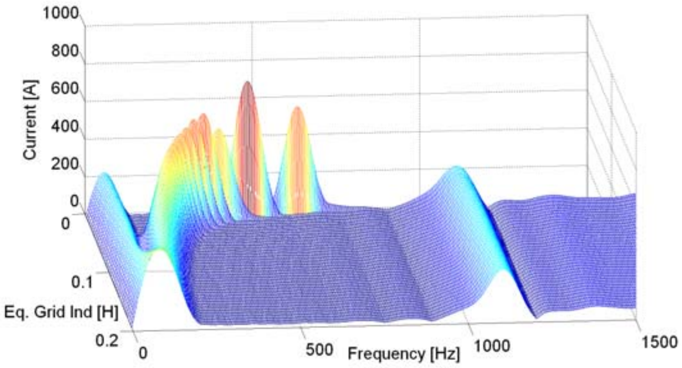

Figure 5.38 - SDFT for the first 20ms of the energisation for different short-circuit powers levels (cables of half the length)

Mathematical model

The standard [27] provides mathematical formulas that can be used to calculate the inrush current peak amplitude and frequency. The equations are shown in (49) and (50) respectively.

$$i_{1peak} = \frac{u_m - u_t}{Z_1 + Z_2} \tag{49}$$

$$f_{eq} = f_s \left[\frac{u_m - u_t}{\omega (L_1 + L_2) I_{ir}} \right] \tag{50}$$

Where: u_m is the crest of the applied voltage, u_t the voltage trapped in the cable, Z_1 and Z_2 the cables surge impedances, f_s the system power frequency, L_1 and L_2 the inductances between the cables and the terminal and I_{ir} the rated peak inrush current.
Table 5.1 indicates the values for the cable used in the simulations, its impedance and capacitance.

Table 5.1 - Cable lumped parameters

R	0.0518 Ω/km
L	0.3537 mH/km
C	0.2124 µF/km
Surge	42-9j Ω

Applying the standard formulas to the previous example, a peak current according to (49) of 2357 A it is obtained and the frequency cannot be calculated as no inductance was considered between the cables.
The equation provided for the calculation of the frequency (50) is particularly problematic. The simulations indicated that when the cables lengths were reduced to half, the resonance frequency approximately doubled. Such relation is not given in (50).

To solve this situation were solved the system equations. In the mathematical model the cables are modelled by means of pi-models, and it is not considered the source, i.e. during the first instants all the energy is exchanged between the two cables. The mathematical development is shown in Appendix H.

An approximate value of the peak current is given by (51). Where C is the capacitance of the cable being energised, ω_r the inrush current resonance frequency and ΔV the voltage rise in the sending end of the second cable at the energisation moment. For a weak grid, ΔV is equal to approximately half of the voltage value at the energisation moment.

$$I_{Peak} = \Delta V \cdot \omega_r C \tag{51}$$

The inrush current frequency depends on additional parameters and on the cables lengths.

Cables of equal lengths

The resonance frequency is calculated by (52), when are two cables of equal length and characteristics. Substituting (52) in (51), (53) is obtained.

$$\omega_r = \sqrt{\frac{2}{LC}} \tag{52}$$

$$I_{Peak} = \Delta V \sqrt{\frac{2C}{L}} \tag{53}$$

Applying (52) to the two examples previously used, resonances frequencies of 547 Hz and 1093 Hz are obtained, for the 47.49 km and 23.745 km cables, respectively. Both values are similar to the ones obtained in the simulations. By using these values in (51) peak currents of 2900 A and 2590 A, respectively, are obtained. The difference between the peak currents is because of ΔV. The use of an equivalent grid increases the value of the voltage in the entire system, resulting in a higher ΔV.

In a real system the voltage in the cable sending end would be approximately 1 pu prior to the energisation of the second cable, and the voltage drop equal for both cases. As a result, the amplitude of the peak current would also be the same.

Cables of different lengths

The energisation of cables of different lengths represents a substantial increase in the complexity of equations. To calculate the resonance frequency, the capacitance and inductance of the first energised cable are written as a function of the capacitance and inductance of the second cable to be energised (54)(55). If the cables are of the same type x is equal to y.

$$C_B = xC_A \tag{54}$$

$$L_B = yL_A \tag{55}$$

Using these relations, (56) is obtained for the calculation of the resonance frequency. If the two cables are of the same type $y=x$, then (56) can be simplified to (57). The equations are demonstrated in Appendix H.

$$\omega_{r1,2}^2 = \frac{\left(yx^2+2yx+2x+1\right) \pm \sqrt{y^2x^4+4y^2x^3-4yx^3+4y^2x^2-6yx^2+4x^2-4yx+4x+1}}{CL\left(yx^2+yx\right)} \tag{56}$$

$$\omega_{r1,2}^2 = \frac{\left(x^3+2x^2+2x+1\right) \pm \sqrt{x^6+4x^5-6x^3+4x+1}}{CL\left(x^3+x^2\right)} \tag{57}$$

The inrush current frequency is related to both the length of the cables and the relation between their lengths. Figure 5.39 shows the inrush current frequencies for a Cable A with 47.49 km in parallel with a similar type with varying length. The figure on left shows one of the resonance frequencies of (56) in function of Cable B length, whereas the figure on the right shows the other resonance frequency of (56). Figure 5.40 repeats Figure 5.39 simulations but varying the length of Cable A between 10km and 100km, in steps of 10km.

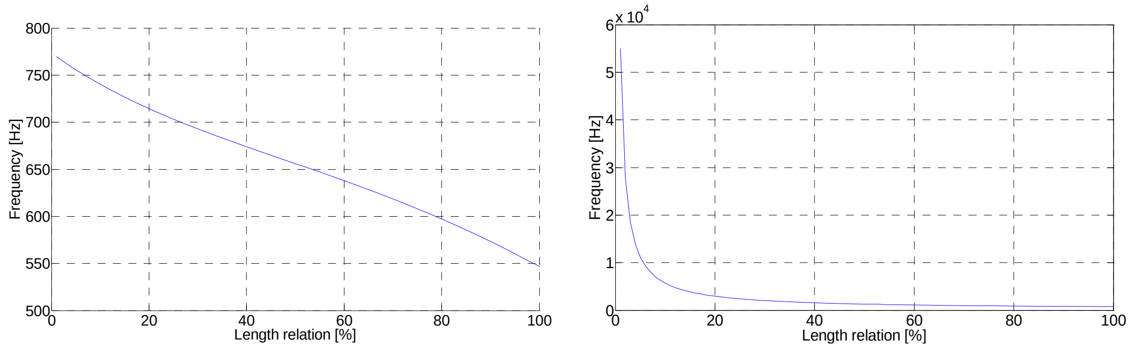

(a) (b)

Figure 5.39 - Frequencies as a function of cable length for C=10.087μF and L=16.8mH (length of reference equal to 47.49km). a) First resonance frequency; b) Second resonance frequency

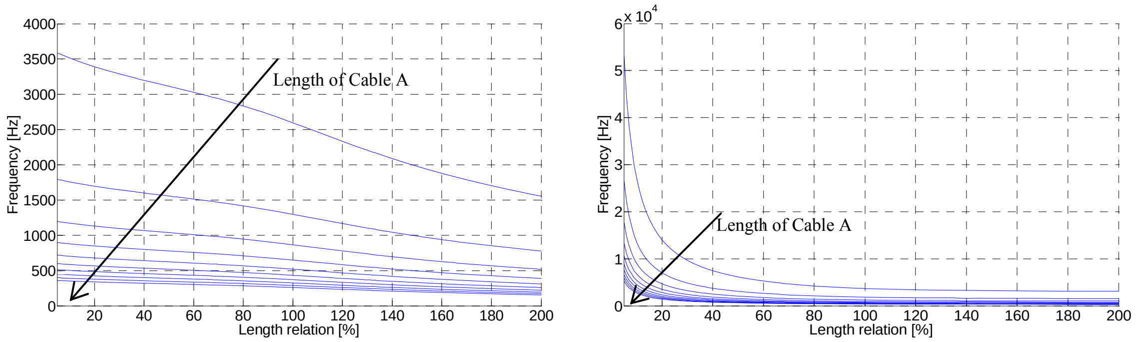

(a) (b)

Figure 5.40 - Frequencies as a function of cable length when changing the length of the already energised cable from 10km to 100km. a) First resonance frequency; b) Second resonance frequency

The increase in the cable length results in an increase in the capacitance and inductance. Thus, the frequency decreases when the length of the cables increases.

An important conclusion is that one of the frequency increases exponentially when Cable B is much smaller than Cable A, see Figure 5.40-B. The increase occurs because much more energy is stored in Cable A is than in Cable B, resulting in an inrush current with a higher frequency.

5.5.2 2030 network example

To demonstrate the phenomenon Denmark's 2030 network was changed slightly, and a new cable was installed in parallel to the previously used NVV-BDK cable. In order to validate the phenomenon, the new cable is identical to the NVV-BDK cable.

Figure 5.41 shows the current in the cable during the energisation from the NVV end with and without the new cable in parallel. The differences between the plots are very small, and it seems that the cable in parallel barely changes its waveform, thus contradicting the explanations given in the previous pages.

This occurs because the energised node is connected to two other cables, which also have a lower resistance per km. The cable was already being energised through the other two cables, and even with the installation of a cable in parallel, the cable continues to be almost completely energised through them.

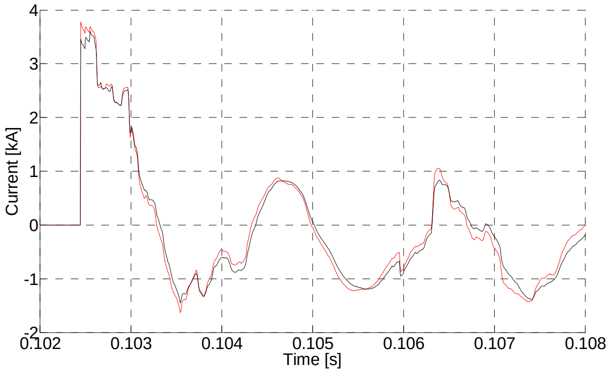

Figure 5.41 - Current in the cable during energisation. Black: 2030 System; Red: With an extra cable in parallel

The choice of another cable would yield different results, and this is done in Figure 5.42. The cable is connected to only one cable in the sending end, which is of the same type.

In this case the influence of the extra cable in the parallel is noticeable, especially in the peak current, which increases by approximately 900A.

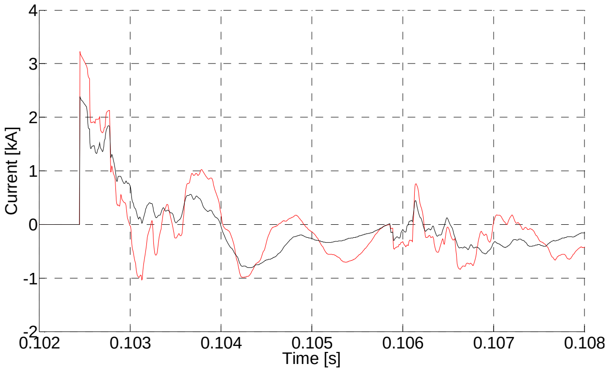

Figure 5.42 - Current in the cable during energisation. Black: 2030 System; Red: With an extra cable in parallel

5.5.3 Countermeasures

Several countermeasures can be used to minimise the inrush current. The countermeasures are demonstrated for the 2030 Western Denmark network and for the energisation of the NVV-BDK cable from the NVK end.

Synchronize switching

The inrush current occurs because the two (or more) cables do not have the same voltage at the energisation instant.

Assuming that the cable being energised does not have any remanent energy and its voltage is almost zero at the connection instant, it is not completely zero because of possible mutual couplings with adjacent cables or lines. For this reason, the use of synchronised switching would strongly reduce the inrush current amplitude and frequency as the voltage in the cable and busbar would both be zero.

Figure 5.43 demonstrates the countermeasure efficiency.

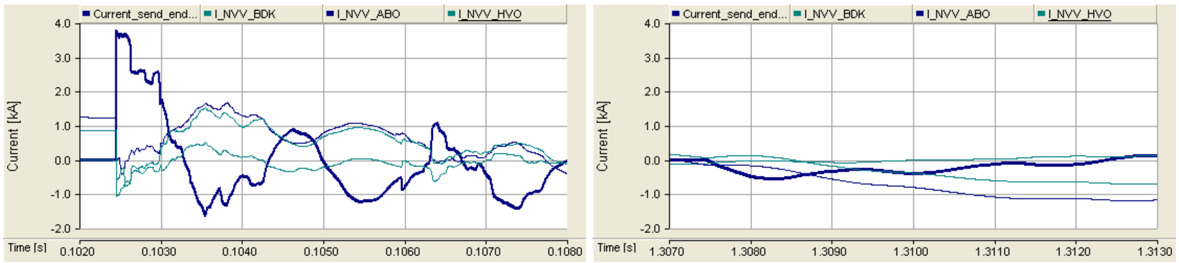

(a) (b)

Figure 5.43 - Current in the cable (bold) and adjacent cables during the energisation of Cable B. a) Energisation at peak voltage; b) Energisation at zero voltage (synchronised switching)

Energise first the smaller cable

The inrush current frequency is higher when the cable being energised is smaller than the cable(s) already energised and installed in parallel, as shown in Figure 5.40. Thus, the use of an appropriated connection sequence can reduce the frequency.

Figure 5.44 exemplifies the advantages of energising first the smaller cable for a 47.49 km cable in parallel with a 4.749 km cable. The amplitude of the inrush current is the same in both cases, but the frequency is lower when the small cable is energised first.

Figure 5.44.a shows a second inrush current just before the 1.306s. This current is a consequence of the energisation of one of the other phases (the CB operates with synchronised switching), which due to mutual coupling induces an inrush current in the phase(s) already energised. The same phenomenon occurs in Figure 5.44.b but is less noticeable because of the higher current during the transient.

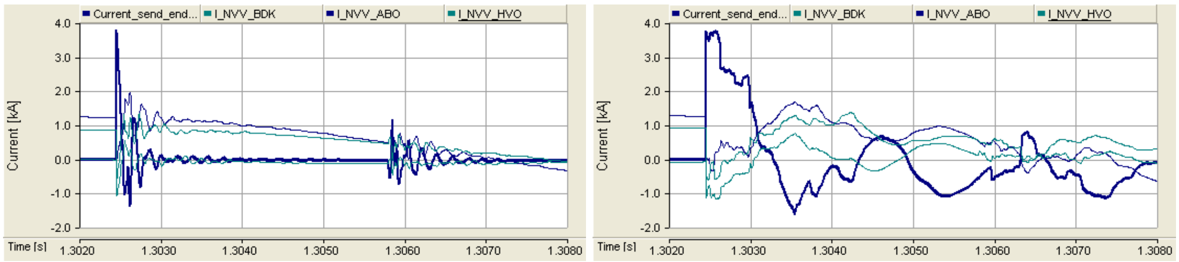

(a) (b)

Figure 5.44 - Current in the cable (bold) and adjacent cables during the energisation of Cable B. a) Long cable first; b) Small cable first

Pre-insertion resistor

Energising the cable through a CB with a pre-insertion resistor is equivalent to having a large resistance between the cable capacitances. Thus, the capacitances are no longer in parallel and the inrush current is reduced.

Figure 5.45 shows a strong reduction in both the amplitude and frequency of the inrush current when using a 50 Ω pre-insertion resistor for 10 ms.

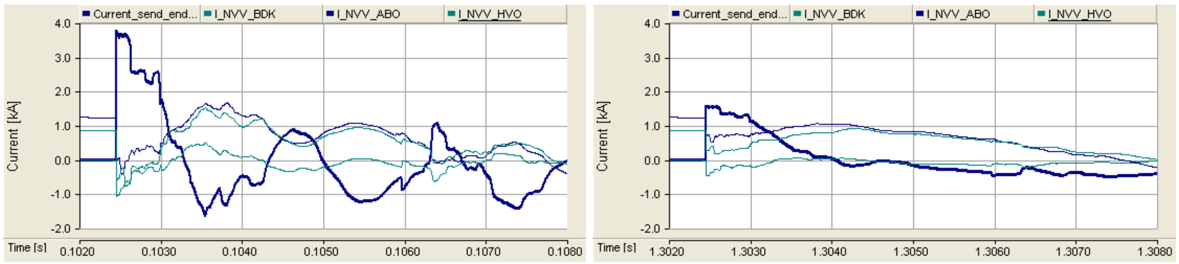

(a) (b)

Figure 5.45 - Current in the cable (bold) and adjacent cables during the energisation of Cable B. a) Without pre-insertion resistor; b) With pre-insertion resistor

5.6 Transformer-cable resonance

The cable and a transformer can originate a resonance circuit, as explained in sections 2.4.5 and 2.4.7. Having explained the resonances, this chapter will show examples for the 2030 Western Denmark network. Remanence is discarded from the simulations, because of the complications inherent to its modelling in PSCAD/EMTDC and lack of information. In the presence of remanence the overvoltage magnitudes could attain higher values.

5.6.1 2030 network example

To simulate the resonance the LEM-STSV cable-line is used instead of the NVV-BDK cable-line previously used. The LEM-STSV cable is connected to a phase-shift transformer in the LEM side, and it is one of the few points in the West Danish grid where a transformer is not interacting with several cables.

The transformer has not been installed yet and no information on its saturation characteristic is therefore available. Hence, typical values for the saturation [86] are used:

- Magnetization Current: 1%;
- Knee voltage: 1.1pu;
- Saturation slope: 0.145pu;

Series resonance

The cable energisation at peak voltage from the LEM and STSV sides is simulated. In both cases the transformer is energised prior to the cable.

Figure 5.46 shows the energisation form the STSV end (without transformer) while Figure 5.47 shows the energisation from the LEM end (with transformer). The resonance is easily observed when the cable is energised from the transformer side, see Figure 5.47.

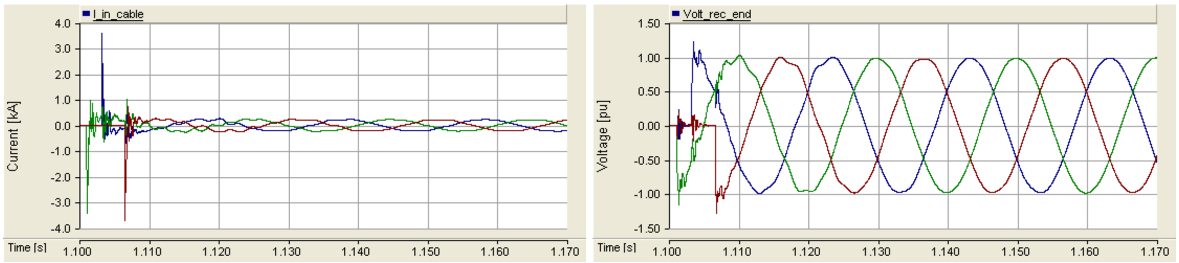

Figure 5.46 - Current into the cable and voltage in the cable receiving end when energising the cable from the STSV side (without transformer in series)

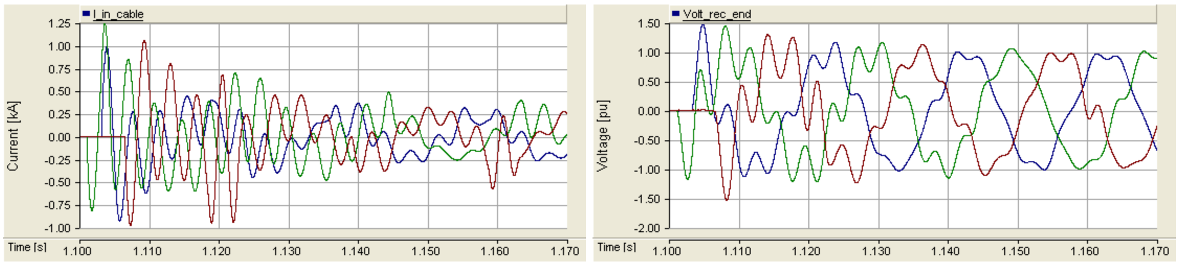

Figure 5.47 - Current into the cable and in the cable receiving end when energising the cable from the LEM side (with transformer). Note: The current scale is not the same of Figure 5.46

Parallel resonance

Chapter 2.4.7 explains a possible parallel resonance between the cable and the transformer. To verify the existence of this phenomenon in the 2030 network the LEM-STSV cable is energised from the STSV side. When the cable reaches steady-state conditions, the transformer is energised through the cable.

The parallel resonance is maximum if the transformer is energised at zero voltage and minimum if the transformer is energised at peak voltage. Therefore, for the simulation, the transformer is energised through synchronised switching at zero volts.

To have parallel resonance in this situation it is necessary to have saturation of the transformer as the resonance will occur due to interactions with the inrush currents.

Figure 5.48 shows the voltage in a non-saturated transformer secondary during its energisation. Figure 5.49 shows the same simulation, but with saturation of the transformer. As a result of the saturation, it can be seen a small overvoltage and voltage distortion during the first cycles.

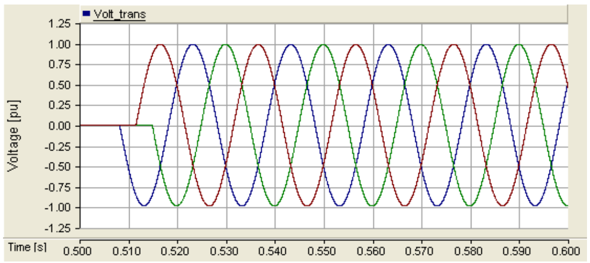

Figure 5.48 - Voltage in the transformer secondary during energisation (without saturation)

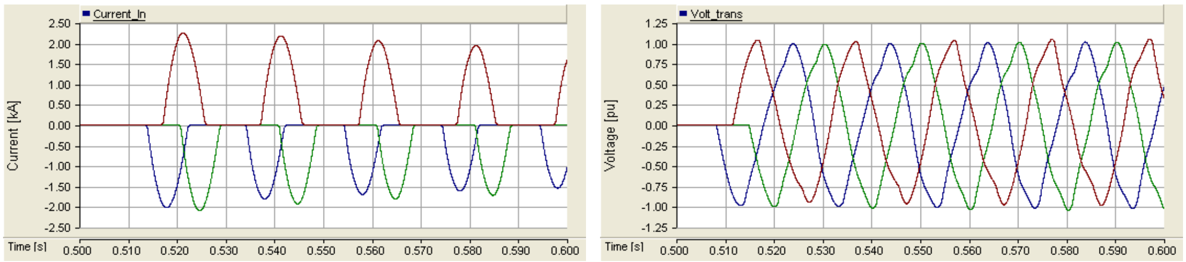

Figure 5.49 - Current in the transformer primary and voltage in the transformer secondary during energisation (with saturation)

Parallel resonance is more severe in weak grids where the effect of the inrush currents in the voltage profile is more pronounced. Therefore, the parallel resonance is not very noticeable in the 2030 network example, which have a short-circuit power of 5000 MVA at the cable sending end.

The simulation is repeated in a simplified system with the transformer, cable and an equivalent grid. Figure 5.50 shows the simulation plots for short-circuit power of 2000 MVA. Comparing with the 2030 network example, the inrush current has an approximate magnitude but the voltage is more distorted and higher in the weaker grid.

Because of the errors associated with the use of an equivalent grid, the simulation was repeated for short-circuit power of 5000 MVA, equal to the one of the 2030 network. Figure 5.51 shows the current in the transformer sending end and the voltage in the transformer receiving end.

The distortion and overvoltage are more pronounced when using the 5000 MVA equivalent grid than the 2030 system. However, they are also smaller for the 5000 MVA equivalent grid than for the 2000 MVA equivalent grid, demonstrating the influence of the short-circuit power.

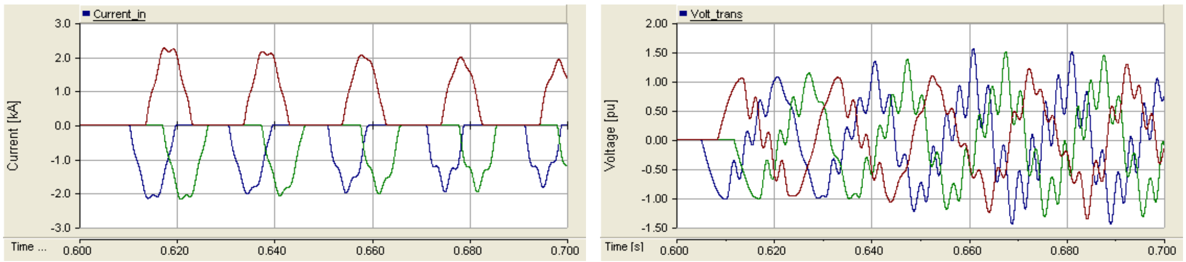

Figure 5.50 - Current in the transformer primary and voltage in the transformer secondary during energisation (short-circuit power: 2000MVA)

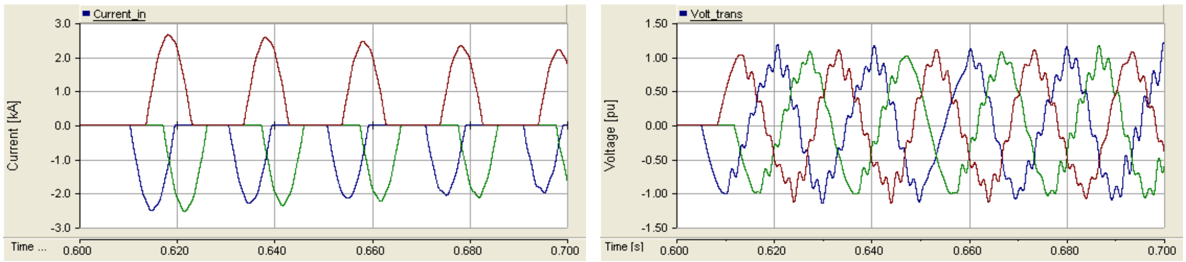

Figure 5.51 - Current in the transformer primary and voltage in the transformer secondary during energisation (short-circuit power: 5000MVA)

5.6.2 Countermeasures

The transformer/cable resonance is very dependent on the system characteristics, and it is possible to slightly change the system in order to avoid the resonance.

Another possibility is to use of synchronised switching or a pre-insertion resistor, countermeasures often used by the utilities when is necessary to minimize the phenomenon. Figure 5.52 and Figure 5.53 show the efficiency of these two countermeasures for the parallel resonance simulated in Figure 5.50.

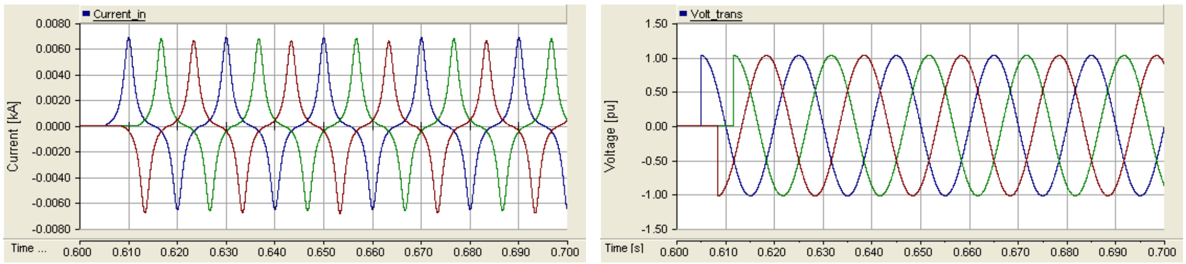

Figure 5.52 - Current in the transformer primary and voltage in the transformer secondary during energisation at peak voltage

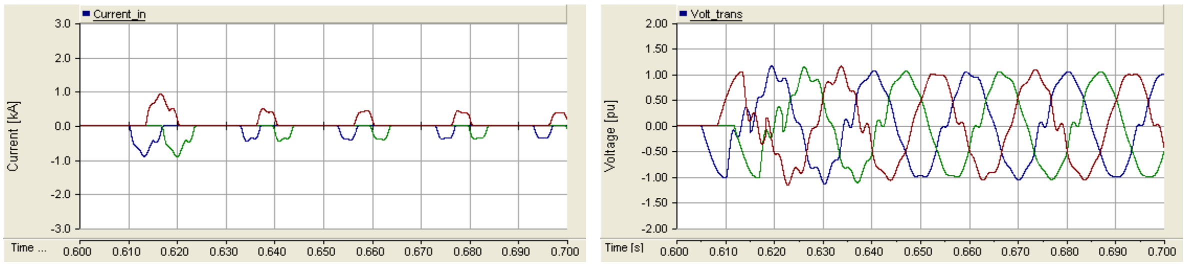

Figure 5.53 - Current in the transformer primary and voltage in the transformer secondary using a pre-insertion resistor (100Ω)

5.7 Cable de-energisation

The de-energisation of cable, either standing alone or connected to a shunt reactor, was briefly explained in section 2.4.8. Besides demonstrating the phenomenon through simulations and vector analysis, it is also interesting to do it mathematically for a cable being de-energised together with a shunt reactor, as done in Appendix E.

The calculations made in Appendix E show that during de-energisation the voltage can, with some simplifications, be described by (58).

$$V = \frac{V1(0)+V2(0)}{2} \cdot \frac{\cos\left(\frac{1}{\sqrt{LsC}}t\right)}{\exp\left(\frac{R}{8Ls}t\right)} kV \tag{58}$$

V1(0) – Voltage at the disconnection moment in the end without shunt reactor

V2(0) – Voltage at the disconnection moment in the end connected to a shunt reactor

C – The cable capacitance

R – Cable resistance

Ls – Shunt reactor inductance

Equation (58) demonstrates that the resonance frequency is a function of the cable capacitance and the shunt reactor inductance, equalling 50 Hz if the shunt reactor compensates for all the reactive power generated by the cable. Usually the shunt reactor will not compensate for such a large amount of reactive power, and the resonance frequency is lower than 50 Hz, typical between 30-45 Hz.

The voltage in (58) is a decaying sinusoidal, whose decaying ratio is inversely proportional to the reactive power provided to the shunt reactor.

From (58) it is concluded that no overvoltage is associated with the de-energisation of a cable. In the following section, it is shown that this conclusion is only true if mutual coupling is not present.

Figure 5.54 shows the voltage in the cable during de-energisation for a simulation in PSCAD/EMTDC (Figure 5.54.a) and using (58) (Figure 5.54.b). The cable used in the simulations is the 47.49 km NVV-BDK cable, and the shunt reactor compensates for 45% of the reactive power generated by the cable (L_S=1.46 H).

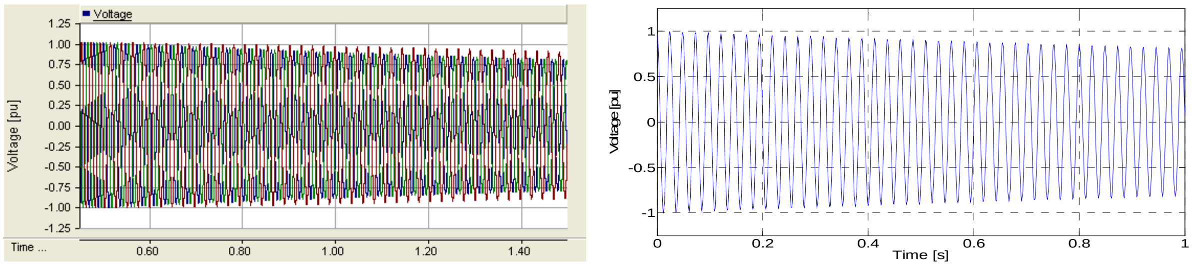

(a) (b)

Figure 5.54 - Voltage in the cable during de-energisation. a) PSCAD/EMTDC simulation; b) Matlab simulation

5.7.1 Shunt reactor mutual coupling

The mutual inductance between the shunt reactors phases was not considered in the previous section, a simplification normally used when performing transient studies [12]. The introduction of mutual inductance between the shunt reactor phases may lead to an increase in the voltage in one or more of the phases and result in an overvoltage.

The mutual inductance increases the complexity of the phenomenon's mathematical analysis. Equation (58) can no longer be used, making it necessary to do a new mathematical development, shown in Appendix F.

Contrary to (58), it is no longer possible to obtain a simple equation, as the voltage is obtained calculating the eigenvalues and eigenvectors of the impedance matrix.

Figure 5.55 and Figure 5.56 compare the voltage after the disconnection when using the equations presented in Appendix F (Figure 5.55) and PSCAD/EMTDC (Figure 5.56). The phases are disconnected in the following order: Phase A (blue curve), Phase C (red curve), Phase B (green curve).

To better analyse the phenomenon, mutual couplings values higher than the typical ones were used.

The mathematical model developed in Appendix E and Appendix F have some simplifications, the most notable one of which is to consider the cable as a single capacitor. Therefore, the plots obtained using the equations are not exactly equal to the ones obtained through PSCAD/EMTDC simulations.

By comparing Figure 5.55 with Figure 5.56, it is concluded that the voltage behaviour is similar for both, the major difference being the larger damping of the PSCAD/EMTDC simulations, which is a consequence of the lower resistance in the mathematical model.

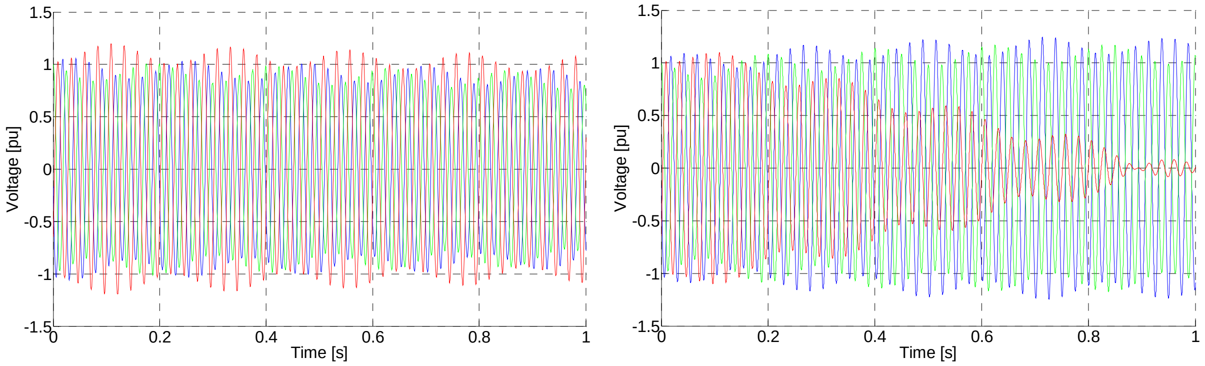

(a) (b)

Figure 5.55 - Voltage in the three phases during de-energisation of cable+shunt reactor using the Appendix equations; a) mutual inductance of 0.1H between all phases; b) M_{AB}*=0.1H,* M_{AC}*=0.09H ,* M_{BC}*=0.11H*

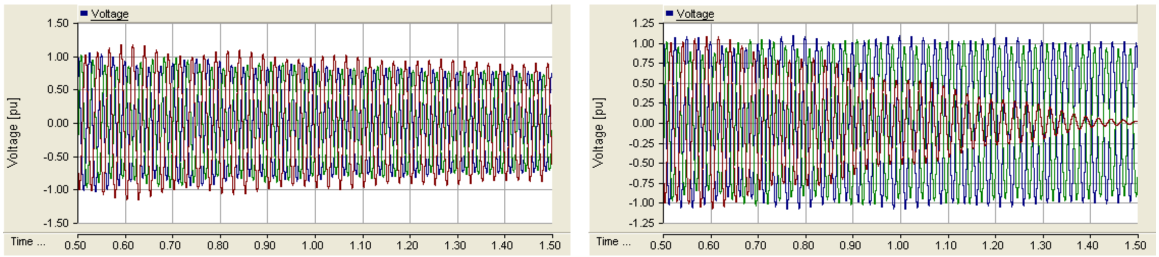

(a) (b)

Figure 5.56 - Voltage in the three phases during de-energisation of cable+shunt reactor using PSCAD; a) Mutual inductance of 0.1H between all phases; b) M_{AB}*=0.1H,* M_{AC}*=0.09H ,* M_{BC}*=0.11H*

Frequency

As previously explained, the frequency during de-energisation depends on the cable capacitance and shunt reactor inductance. Below are given the de-energisation frequency for different cable+shunt reactor configurations.

- Steady-state operation: 50 Hz
- Cable de-energisation : decaying DC;
- Cable+shunt reactor de-energisation (no mutual inductance): Resonance frequency (typically <50 Hz);
- Cable+shunt reactor de-energisation (equal mutual inductances): Resonance frequency + 2 mutual inductance frequencies (given by (59));
- Cable+shunt reactor de-energisation (different mutual inductances): Resonance frequency + 3 mutual inductance frequencies (given by (60)).

The deduction of (59) and (60) is available in Appendix F. Equation (59) was obtained through an analytical method, whereas (60) used a semi-analytical approach.

$$\begin{aligned} f_1 &\approx \sqrt{\frac{1}{C(L-M)}} \\ f_2 &\approx \sqrt{\frac{1}{C(L+2M)}} \end{aligned} \tag{59}$$

$$\begin{aligned} f_1 &\approx \sqrt{\frac{1}{C(L-M_{Max})}} \\ f_2 &\approx \sqrt{\frac{1}{C(L-M_{Min})}} \\ f_3 &\approx \sqrt{\frac{1}{C(L+2M_{avg})}} \end{aligned} \tag{60}$$

Overvoltage

Considering that the mutual inductance is the same between all phases (Figure 5.56.a), overvoltage is observed in only one of the phases, more specifically in the second phase to be disconnected.
In the example the shunt reactor compensates for 45% (59.35Mvar) of the reactive power. Thus, the resonance frequency is 33.5 Hz, as given by (61), where c is the compensation ratio.

$$f_r = 50\sqrt{c} \tag{61}$$

Figure 5.57 shows the voltage phasors after the disconnection of the last phase for a resonance frequency of 33.5Hz. The voltage in phase C, which was the second phase to be disconnect, increases because of mutual coupling from both Phase A and Phase B. Whereas, in the other two phases the mutual coupling from one of the other two phases decreases the total voltage, e.g., the mutual coupling from phase B decreases the voltage in Phase A. Together with damping, this makes that in Figure 5.56.a overvoltage is only present in the second phase to be disconnected (Phase C).

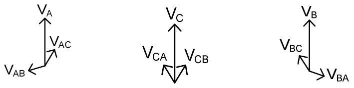

Figure 5.57 - Voltage phasors after the disconnection of the last phase

The resonance voltages are expected typically to be between 30-45 Hz. Figure 5.58 shows the voltage phasors after the disconnection of the last phase, for a resonance frequency varying between 30Hz and 45Hz. For a system with equal mutual inductances, the higher voltage will typically be in the second phase to be disconnected, along with similar voltages in the first and third phases to be disconnected.

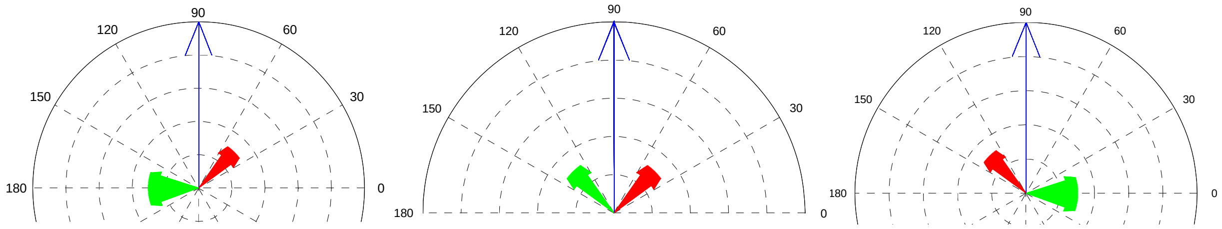

(a) (b) (c)

Figure 5.58 - Voltage phasors after the disconnection of the last phase for resonance frequencies between 30-45 Hz (Blue: Phase Voltage; Red and green: Voltages due to mutual inductance). a) 1st phase to be disconnected; b) 2nd phase to be disconnected; c) 3rd phase to be disconnected

The overvoltage is more difficult to predict when the mutual inductance is not the same between all phases. Figure 5.56 shows two plots, of which the second have a 10% imbalance in the mutual inductances, sufficient to drastically change the waveforms. Moreover, the overvoltage is no longer in the second phase to be disconnected, but in the other two phases.

The three frequencies superimpose each other, and the amplitude for each frequency depends on the mutual inductance values, as shown in Appendix F, resulting in the overvoltage observed in the simulations. No general rule can be given for this situation, and it is necessary to run a simulation or to solve the equation in order to know the overvoltage.

5.7.2 Hybrid cable-OHL lines

The disconnection of a hybrid cable OHL together with a shunt reactor introduces a new factor in the analysis, namely the capacitance between the OHL phases. This mutual capacitance may originate, for the de-energisation of a pure OHL, a small overvoltage in one or more phases, as explained more than half century ago in [25]. Thus, it is interesting to examine whether the same happens when a hybrid line is de-energised.

Figure 5.59, Figure 5.60 and Figure 5.61 show the voltage during the de-energisation for four different systems. The systems elements are the NVV-BDK cable, compensated at 45% at the cable sending end, and a 50km long OHL:

- System1: OHL-cable
- System2: Cable-OHL
- System3: Cable
- System4: OHL (no reactive power compensation)

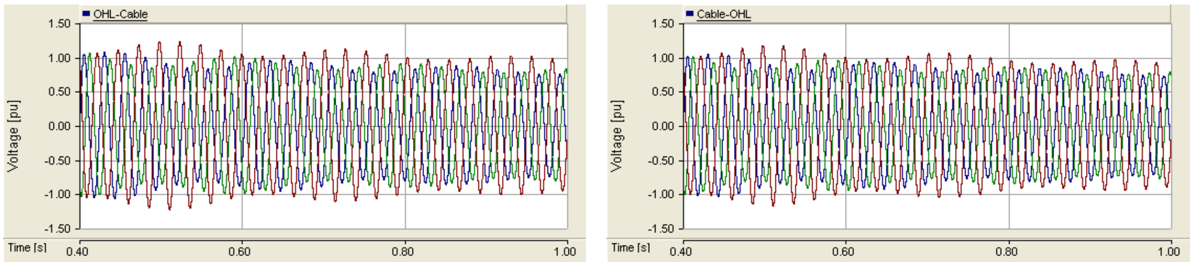

(a) (b)

Figure 5.59 - Voltage in the end of the line during system de-energisation. a) OHL-cable system; b) Cable-OHL system

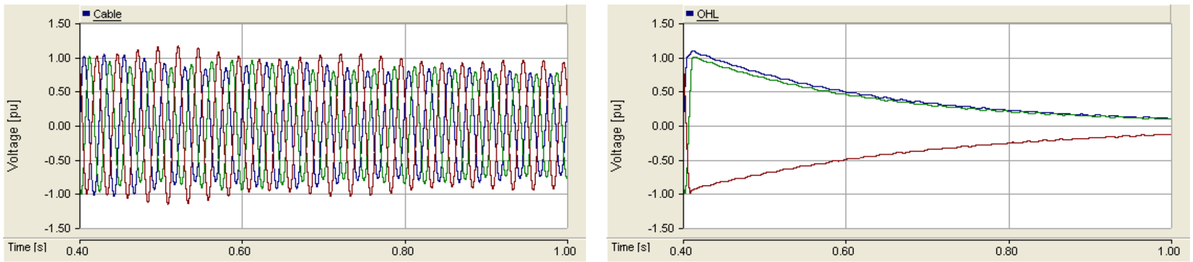

(a) (b)

Figure 5.60 - Voltage in the end of the line during system de-energisation. a) Cable system; b) OHL system (no reactive power compensation)

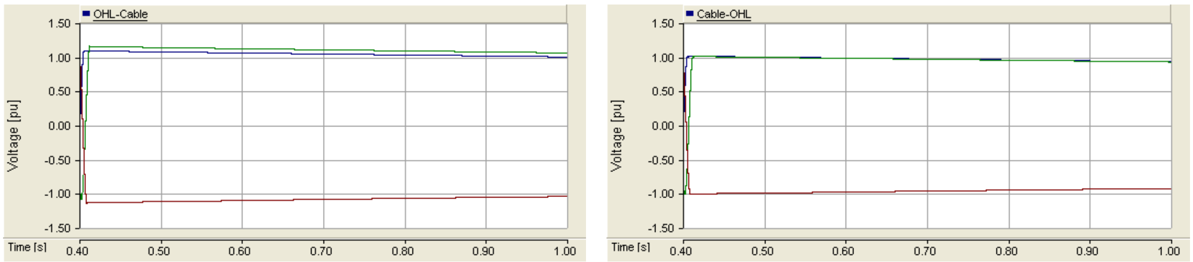

(a) (b)

Figure 5.61 - Voltage in the end of the line during system de-energisation (without reactive power compensation). a) OHL-cable system; b) Cable-OHL system

Table 5.2 shows the peak overvoltages for the simulations presented in Figure 5.59-Figure 5.61. Using the pure cable system as reference, it is seen that the overvoltage increases for the OHL-cable line, but not for the cable-OHL line. The same conclusion can be achieved by comparing the results for the two hybrid lines without reactive power compensation.

The current flowing into an OHL is higher in an OHL-cable line than in a cable-OHL line, because of the charging current of the cable, which has to flow through the OHL in an OHL-cable line. This higher current together with the coupling between phases in the OHL, results in a higher disconnection overvoltage in the hybrid OHL-cable line.

Table 5.2 - Phase peak overvoltage for the different systems during the de-energisation (means no reactive power compensation)*

	OHL-cable	Cable-OHL	Cable	OHL	OHL-cable*	Cable-OHL*
Phase A	1.069	1.041	1.038	1.092	1.093	1.015
Phase B	1.060	1.012	1.010	1.002	1.156	1.011
Phase C	1.234	1.169	1.158	1.002	1.144	1.015
Steady-state	1.037	1.011	1.009	1.001	1.088	1.011

The location of the reactive power compensation has a strong influence on the simulations. Figure 5.62 shows the voltage in the line receiving end for the de-energisation of an OHL-cable system, with the reactive power compensation being made in the sending end of the line.

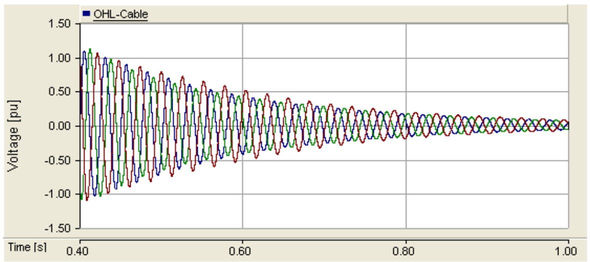

Figure 5.62 - Voltage in the end of the line during de-energisation of an OHL-cable line being compensated in the OHL sending end

During de-energisation, the OHL forms a series circuit with the shunt reactor, as shown in Figure 5.63. The resistance R_{eq} is much higher than R_S, leading to the faster damping observed in Figure 5.62. A similar behaviour would be observed in the cable-OHL if the shunt reactor were installed in the line receiving end.

Because of the fast damping, the influence of the mutual coupling between the shunt reactor phases is barely noticeable. As a result, the maximum overvoltage is lower, 1.184 pu instead of 1.234 pu.

This faster damping and the lower overvoltage can, if necessary, be taken into account when planning the line.

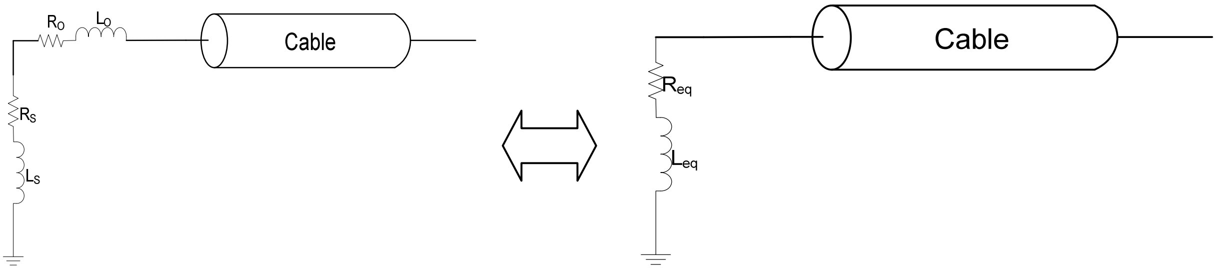

Figure 5.63 - OHL-cable line during de-energisation. R_0: OHL resistance; L_O: OHL inductance; R_S: Shunt reactor resistance; L_S: Shunt reactor inductance; R_{eq}: equivalent resistance; L_{eq}: equivalent inductance;

5.7.3 *Simulation errors*

The thesis author noticed that the simulating disconnection of a cable and shunt reactor can easily originate a numeric instability, characterised by a voltage increase. Usually the problem is easily detected as the voltage increases exponentially after the disconnection, see Figure 5.64.

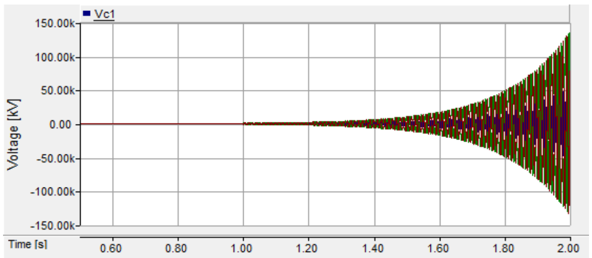

Figure 5.64 – Cable+Shunt Reactor disconnection – Unstable simulation

This instability is the result of fitting errors in the cable model. One way of verifying the accuracy of the model is to plot the eigenvalues of the model's Hermitian matrix for all frequencies and verifying that there are no negative eigenvalues [64], something that is far from being trivial.
Engineers from the Manitoba HVDC Research Centre suggest the use of a trial-error method, changing the fitting parameters in order not to have instability. As an example, in Figure 5.65.a the PSCAD/EMTDC initial fitting parameters are presented, which lead to the instability shown in Figure 5.64. If changing the fitting parameters to the ones shown in Figure 5.65.b, no instability is present, and the plot presented in Figure 5.66 is obtained.

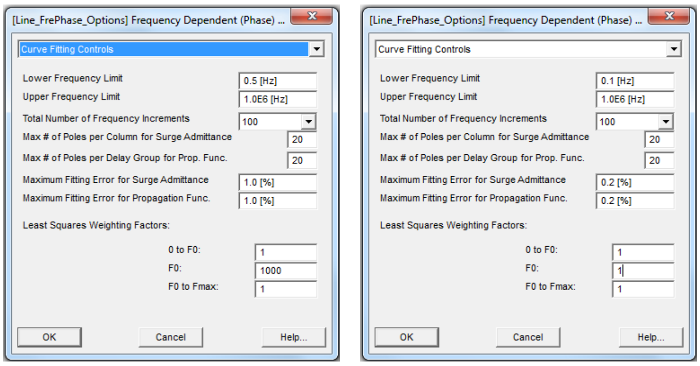

Lower Frequency Limit: 0.5 [Hz]
Upper Frequency Limit: 1.0E6 [Hz]
Total Number of Frequency Increments: 100
Max # of Poles per Column for Surge Admittance: 20
Max # of Poles per Delay Group for Prop. Func.: 20
Maximum Fitting Error for Surge Admittance: 1.0 [%]
Maximum Fitting Error for Propagation Func.: 1.0 [%]
Least Squares Weighting Factors:
0 to F0: 1
F0: 1000
F0 to Fmax: 1

Lower Frequency Limit: 0.1 [Hz]
Upper Frequency Limit: 1.0E6 [Hz]
Total Number of Frequency Increments: 100
Max # of Poles per Column for Surge Admittance: 20
Max # of Poles per Delay Group for Prop. Func.: 20
Maximum Fitting Error for Surge Admittance: 0.2 [%]
Maximum Fitting Error for Propagation Func.: 0.2 [%]
Least Squares Weighting Factors:
0 to F0: 1
F0: 1
F0 to Fmax: 1

(a) (b)

Figure 5.65 – Fitting parameters for a frequency-dependent cable model in PSCAD. a) Initial fitting parameters; b) Corrected fitting parameters

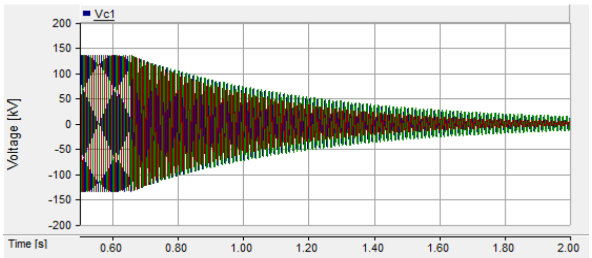

Figure 5.66 - Cable+Shunt Reactor disconnection – stable and accurate simulation

The risk of this method is that the user may be led to think that the simulation is accurate when it is not. Figure 5.67 shows another possible correction of the fitting parameters (the only change made to the stable and accurate simulation of Figure 5.66, was to increase the surge admittance and the propagation fitting errors), which, if used, generates the simulation results presented in Figure 5.68.

Looking at the plot, it seems that the simulation is stable and the results accurate, but as can easily be seen when comparing Figure 5.68 with Figure 5.66, this is not true. One may say that the accurate results are the ones shown in Figure 5.68 and not the ones shown in Figure 5.66, but that can be denied as it is known from (58) that no overvoltage should appear during de-energisation.

The problem is that (58) is not completely accurate because the mutual inductance between the shunt reactor phases and the cable phases is not considered in the equation. This mutual inductance, mainly the shunt reactor mutual inductance, is responsible for an overvoltage in the moments after the cable disconnection, which has a voltage shape similar to the one shown in Figure 5.68 [33]. In this particular case, it is known that there is a simulation error as the shunt reactor is ideal and there is no mutual inductance between its phases, but if the mutual inductance were considered, it would no longer be possible to make such a deduction.

This may be a very problematic situation when performing a simulation that considers the mutual inductance in the shunt reactor, as inaccurate results similar to the accurate results may be obtained, and there is no easy way of verifying the simulation exactness.

Discussion of this problem with Manitoba HVDC Centre engineers indicates that this error is associated with the numeric approximations used in the frequency-dependent model and that such problems are common to all EMTP software.

A suggestion to avoid this problem could be to de-energise the cable considering an ideal shunt reactor, and see if any overvoltage is present. If no overvoltage appears, the mutual inductance is then added.

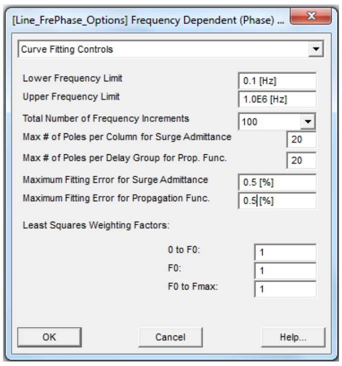

Curve Fitting Controls

Lower Frequency Limit: 0.1 [Hz]
Upper Frequency Limit: 1.0E6 [Hz]
Total Number of Frequency Increments: 100
Max # of Poles per Column for Surge Admittance: 20
Max # of Poles per Delay Group for Prop. Func.: 20
Maximum Fitting Error for Surge Admittance: 0.5 [%]
Maximum Fitting Error for Propagation Func.: 0.5 [%]

Least Squares Weighting Factors:
0 to F0: 1
F0: 1
F0 to Fmax: 1

Figure 5.67 - Fitting parameters for a frequency-dependent cable model in PSCAD

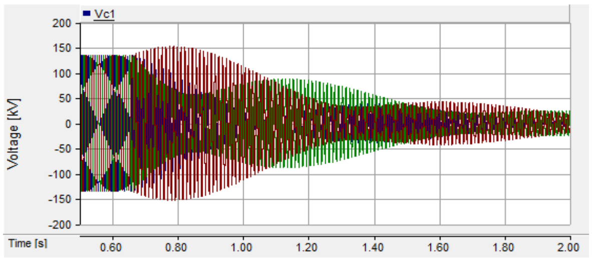

Figure 5.68 - Cable+Shunt reactor disconnection – stable and inaccurate simulation

5.7.4 Horns Rev 2 measurements

As explained in section 4.6.4 the measurements do not match the simulations due to inaccuracies in the submarine cable model.

However, it is possible to observe an overvoltage during system de-energisation, which is a consequence of the mutual coupling in the shunt reactor and other possible couplings in the submarine cable.

5.8 Restrike

Re-strikes rank among the worst transient phenomena that may occur in a cable and should therefore be given special attention. The phenomenon is rare, but when it occurs the overvoltage may reach very high values, resulting in severe damage to the network equipment.

5.8.1 Description of the phenomenon

The contacts of a CB do not separate immediately when they are switched off. During the time it takes for the contacts to separate, a restrike/reignition may occur. The occurrence of such phenomenon depends on the CB dielectric strength.

Figure 5.69 shows the CB's withstand voltage as a function of time, which increases with the time. It should be noted that this curve is linearised, and it is an approximation to a real curve.

If the voltage at the CB terminals does not exceed the withstand voltage, a restrike/reignition should not occur. In the example shown in Figure 5.70, the system voltage is at one point higher than the withstand voltage, and the system will be re-energised. As the CB reclosing occurs in the first quarter of the cycle, the phenomenon is called reignition instead of restrike.

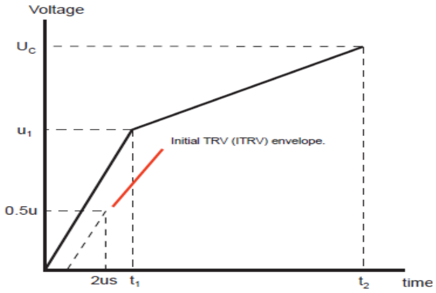

Figure 5.69 – Withstand voltage curve [78]

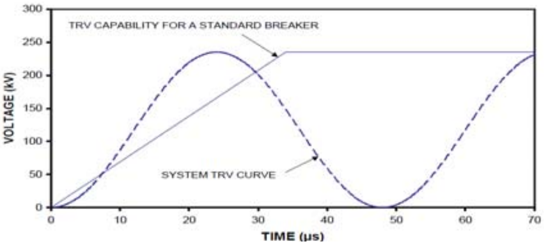

Figure 5.70 – Comparison of the CB TRV and the system curve [79]

When restrike/reignition occurs, there is a high frequency component that is superimposed to the system frequency. If the high frequency current is higher than the power current, the current through the CB may cross zero. If the CB has the ability to extinguish this high-frequency current, as most CB have, the CB may open immediately after the restrike [80]. If the CB is unable to open the high-frequency current, it will only be able to open in the zero crossing of the power frequency.

This interruption of the high frequency current can in some situations worsen the phenomenon and result in multiple restrikes, where the voltage increases until there is a cable failure or an external flashover [16]. This situation in shown in Figure 5.71, where the high-frequency current crosses zero when the capacitor voltages has a peak value of 3 pu after the first restrike, which results in even more energy being stored in the capacitor, and a large transient recovery voltage in the next restrike.

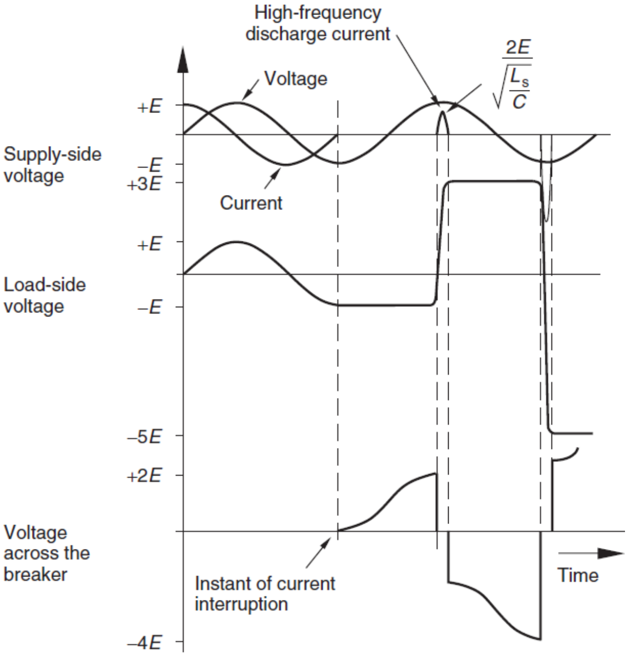

Figure 5.71 – Capacitance switching with multiple restrikes. E: Voltage magnitude; Ls: Inductance of the supply; C: Load capacitance [17]

When a restrike occurs, the voltage in the cable equalises the source voltage. If the voltage in the cable and the source were equal in the exact moment when the CB recloses, no transient would be present. As a result, there would not be an overvoltage either.

Therefore, the worst-case scenario is to have a voltage difference of 2 pu between the source's voltage and the cable's voltage, i.e. a restrike half a cycle after the CB opening. Figure 5.72 illustrates this situation for a cable bonded in both ends (in later sections the influence of the bonding type is demonstrated).

When the CB closes, it is initiated a transient, whose reference is the source voltage and whose resonance frequency is defined by the system parameters. If the cable had no resistance, the average value of each high-frequency cycle would be the value of the source voltage in the instant when the two voltage cross each other (e.g. the first cycle would have a peak voltage of 3 pu and an average voltage equal to 1 pu), but due to the cable resistance the high-frequency voltage is damped, decreasing through time, as previously explained to a normal energisation.

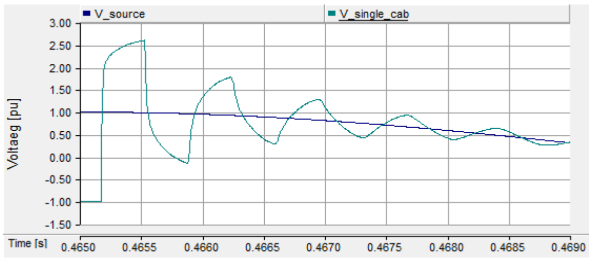

Figure 5.72 – Energisation of a cable line

5.8.2 Simulation

This phenomenon is simulated using the 47.49 km NVV-BDK cable. Two approaches are considered:

- The CB opens normally and is forced to re-close approximately half a cycle after the opening of the first phase (Phase A) so that the worst case can be simulated. The moment corresponding to the maximum overvoltage depends on several aspects, e.g., the cable parameters, short-circuit level, etc…, making it very difficult to calculate it a priori. Therefore, a statistical switching (50 simulations) is run, using a Gaussian distribution with a standard deviation of 1.8 ms. Table 5.3 shows the simulation results for this approach;
- The CB opens normally and is forced to close exactly half a cycle after the opening of the first phase (phase A). This is the expected worst case, but the obtained peak overvoltage was only 2.315 pu for phase A;

Table 5.3 - Maximum and average peak voltages during restrike using multiple runs

	Peak voltage [pu]
Max. BDK-Ph A	2.321
Max. BDK-Ph C	**2.435**
Avg. BDK-Ph A	1.822
Avg. BDK-Ph C	1.829

Analysing the results, it is seen that the restrike is dangerous for the cable and attached equipment (e.g. circuit breakers, shunt reactors, ...), as the voltage can go up to 2.45 pu.

Contrary to expectations, the worst-case scenario is not to reclose the CB exactly half cycle after opening of the first phase. Not only are higher voltage values obtained for the statistical switching than for the worst-case scenario, but these values are also obtained for Phase C and not for Phase A.

The worst case is if the CB recloses some instants before the half cycle point. The total voltage (V_T) is the sum of two components, the power frequency (V_P) and the high frequency component (V_{HF}), the peak overvoltage being equal to the peak high-frequency voltage plus the power frequency in that instant (62).

$$V_T = V_{PF} + V_{HF} \tag{62}$$

The peak voltage does not occur precisely after half cycle, but hundreds of microseconds later (it is similar to regular energisation, see [16] and [17]), when the power voltage in Phase A is no longer at its peak value, see Figure 5.73. The power voltage decreases in Phase A, while increasing in Phase C, between the CB reclosing and the peak overvoltage instants. Therefore, it is possible to have a higher peak overvoltage in phase C than in Phase A. It should be noted, however, that even not having the higher overvoltage in Phase A, this phase continues to have a larger high-frequency component (V_{HF}).

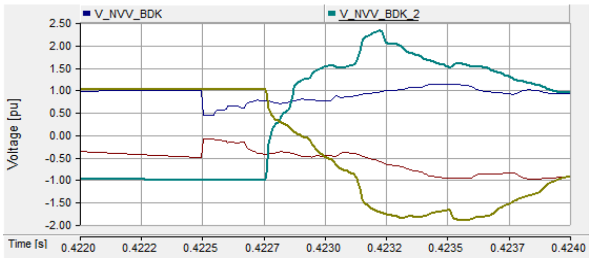

Figure 5.73 – Voltages (Phase A and Phase C) in both sides of the CB during re-energisation

5.8.3 Shunt reactor

Chapter 5.7 explains the de-energisation of a cable connected to a shunt reactor, demonstrating that the voltage is no longer a decaying DC, but a decaying AC oscillating at resonance frequency, resulting in a maximum voltage difference at the CB terminals later than half a cycle after the disconnection

From (58) it is easily seen that when de-energising a cable+shunt reactor system the symmetry, i.e. equal amplitude but opposite signs, between the source side and the load side voltages no longer occurs half a cycle after the disconnection. For a 50 Hz system the time necessary to obtain symmetry between the CB sides is given by (63), and for a typical resonance frequency of 30-45Hz it is equivalent to 2.5-10 cycles at power frequency.

$$t = \left| \frac{1800}{180 - 3.6 f_r} \right|, \qquad \text{t in miliseconds} \qquad (63)$$

As the voltage difference at the CB terminals is lower in the moments immediately after the disconnection, the likelihood of a restrike is lower and the overvoltage will in case of restrike be also lower.

As an example, the shunt reactor is connected to the NVV-BDK cable, and both are disconnected together. The voltage in one of the cable ends and the voltage at the CB terminals are shown in Figure 5.74. As can be seen, the voltage symmetry occurs one cycle and not half cycle after the opening of the CB, meaning that the resonance frequency is approximately 25 Hz.

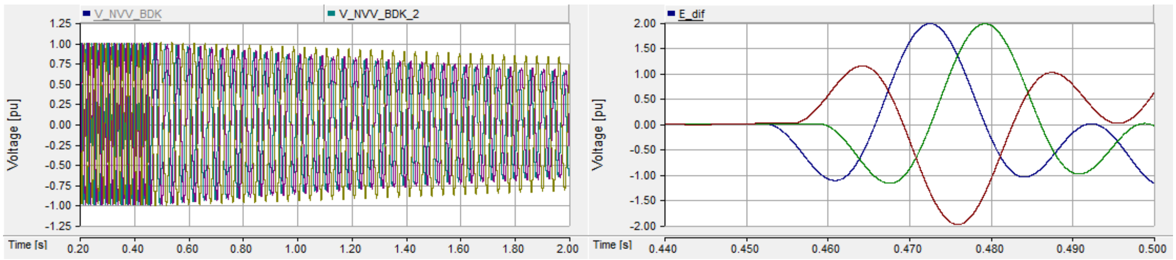

(a) (b)

Figure 5.74 – De-energisation of the system cable+shunt reactor – a) Voltage in cable end; b) Voltage difference at CB terminals

A restrike of the CB half a cycle after the opening, like the restrikes in the previous simulations, originates a 1.297 pu overvoltage; if the restrike happens one cycle after the overvoltage it is 2.285 pu.

So as expected, if the restrike occurs when the voltage at the CB terminals is maximum (i.e. 2 pu), the overvoltage has a magnitude similar to the one obtained when the shunt reactor is connected to the busbar. However, as the maximum voltage difference at the CB terminals occurs later in time the restrike is less likely, as the TRV is not so sharp.

5.8.4 *Clearing a fault in a cable connected to a shunt reactor*

The mutual inductance between shunt reactor phases may result in an overvoltage during cable de-energisation, and this must be taken into account when simulating the cable TRV. Another consequence is an increase in the overvoltage when clearing some types of faults.

Figure 5.75 and Figure 5.76 show the voltage during normal de-energisation and during the clearing of a single-line ground fault. Table 5.4 shows the simulation peak values.

Note: The simulations shown in Figure 5.75 and Figure 5.76 do not use neither the cable nor the system that is used in the rest of the report; this change is made in order to ensure better control of the system parameters.

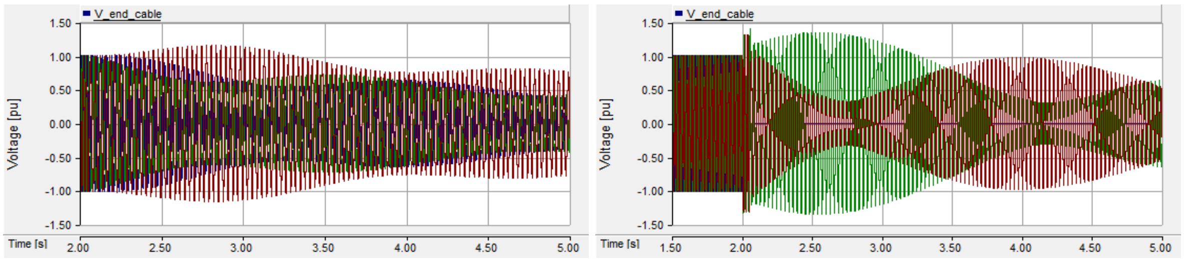

(a) (b)

Figure 5.75 – Voltage in the cable end during de-energisation. a) No-fault; b) Fault

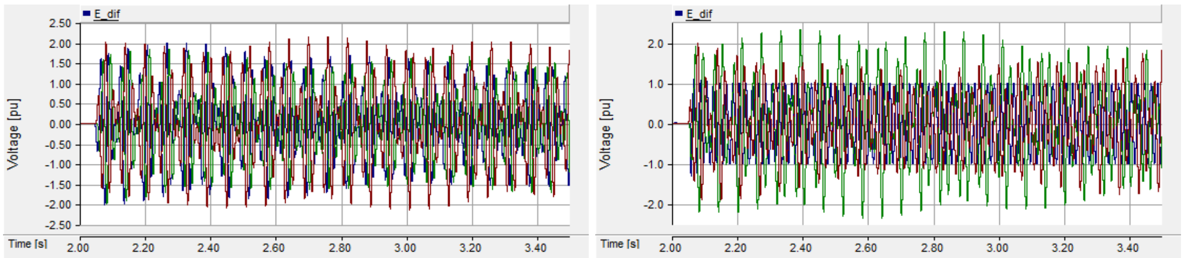

(a) (b)

Figure 5.76 – Voltage at the CB terminals during de-energisation. a) No-fault; b) Fault

Table 5.4 – Voltage in the cable end and voltage at the CB terminals

	No-Fault	**Fault**	**Fault& No mutual-coupling**
Max. Voltage	1.159	1.349	1.147
Max. Voltage difference CB	2.153	2.341	2.157

It can be seen that the overvoltage increases by around 0.2 pu due to a combination of the fault and mutual coupling. This should be taken into account when purchasing the CB as a higher TRV characteristic may be required.

Explanation of the overvoltage increase

To explain the voltage increases, a single phase-to-ground fault in phase A is considered. During the fault, the voltage in Phase A at the fault location is zero while the current in the phase increases to very high values. The shunt reactor is directly connected to the cable, and so the voltage in Phase A of the shunt reactor is either a slowing decaying DC component, if the shunt reactor is connected very close to the fault point, or a very small AC component, if the shunt reactor is installed some kilometres away from the fault location.

Assuming that the fault occurs very close to the shunt reactor, the current into the faulted phase of the shunt reactor is a DC current with derivate equal to zero. As a result, Phase A does not induce voltage in the other two phases, creating an asymmetry between the shunt reactor phases, which is responsible for the voltage increase. The mathematical demonstration of the phenomenon is shown in Appendix G.

This means that the higher overvoltage is not a direct consequence of the fault, but the result of not having phase A induce voltage in the other two phases. In other words, the higher overvoltage obtained with the single-phase fault is equal to the overvoltage obtained if there were only mutual inductance between phases B and C. A corollary of these results is that this phenomenon can only be present for a single-ground fault. If there is a fault to ground for more than one phase, there will be a DC current in more than one phase and no mutually induced voltage.

From the mathematical demonstration made in Appendix G it is seen that the voltage will not always increase when a single-line to ground fault is cleared. In the example presented in Appendix G the overvoltage only increases if the opening of the two sane phases is 6.66 ms apart.

The reasoning can be also applied if the fault is located some kilometres away from the shunt reactor, with the difference that some current is flowing in the faulted phase. Whereas, the current is very low, barely inducing any voltage in the other two phases.

5.9 Restrike of hybrid cable-OHL lines

In the previous section, only the restrike of a cable line was simulated. Hybrid cable-OHL lines are becoming more common, making it necessary to address this type of line.

To study this type of restrike, eight different hybrid line configurations, where part of the cable is substituted by an OHL, are studied.

- Case 1: ½ cable - ½ OHL
- Case 2: ⅓ cable - ⅔ OHL
- Case 3: ⅔ cable - ⅓ OHL
- Case 4: ½ OHL - ½ cable
- Case 5: ⅔ OHL - ⅓ cable
- Case 6: ⅓ OHL - ⅔ cable
- Case 7: ⅓ cable - ⅓ OHL - ⅓ cable
- Case 8: ⅓ OHL - ⅓ cable - ⅓ OHL
- Case 9: Pure OHL

The total line length remains the same in all the cases (47.49 km), the reactive power compensation provided by the shunt reactors installed in both ends of the cable is reduced as a function of the cable length and the restrike continues to be forced in the NVV side.
Statistical switching is again used to simulate the CB restrike. The maximum and average overvoltage values for the different cases are shown in Table 5.5.

Table 5.5 - Maximum and average voltage in the hybrid line receiving end for the statistical switching

	Pure Cable	**Case 1**	**Case 2**	**Case 3**	**Case 4**
Max. BDK-Ph A	2.328	**3.4175**	**4.4308**	3.8817	2.5682
Max. BDK-Ph C	**2.445**	2.7190	4.2434	**3.9079**	**2.7667**
Avg. BDK-Ph A	1.827	2.7919	3.5095	3.1174	2.0001
Avg. BDK-Ph C	1.832	2.0818	2.8968	2.7032	2.1171
	Case 5	**Case 6**	**Case 7**	**Case 8**	**Case 9**
Max. BDK-Ph A	2.4935	2.5381	2.6972	2.5112	**1.9911**
Max. BDK-Ph C	**2.6730**	**2.7633**	**2.8285**	**2.6415**	1.2658
Avg. BDK-Ph A	1.9506	1.9785	2.1144	1.9193	1.5208
Avg. BDK-Ph C	2.0654	2.0921	2.0964	1.9372	1.1216

Several differences are noted when comparing the results obtained for a pure cable line and the different hybrid line configurations:

- The overvoltage associated with the restrike of a hybrid line is higher than for a pure cable or a pure OHL;
- The overvoltage is higher if the restrike occurs in a CB attached to a cable;

When part of the cable is substituted by an OHL, there is a decrease in the total line capacitance, and less energy to be damped. Thus, the voltage difference at the CB terminals half a cycle after the disconnection is smaller, as can be observed in Figure 5.77, and one would therefore expect a lower overvoltage. Yet, the simulations show exactly the opposite, namely an increase in the overvoltage value by 81% more when comparing case 2 with a pure cable line (see Table 5.5).

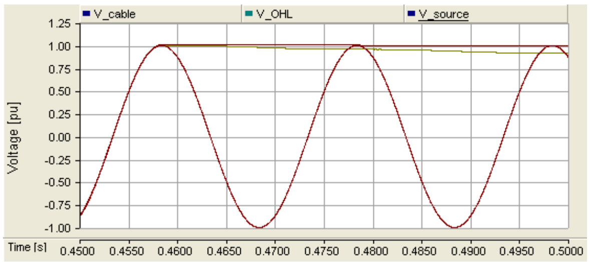

Figure 5.77 - Comparison between cable and OHL TRVs

The increase in the voltage is a result of reflections/refractions in the cable-OHL junction point(s).
The reflected and refracted voltages are calculated by (64)[16], where V_1 is the sending voltage, V_2 is the reflected voltage, V_3 the refracted voltage, and Z_A and Z_B the surge impedance of the lines.

$$V_3 = V_1 \frac{2Z_B}{Z_A + Z_B} \qquad V_2 = V_1 \frac{Z_B - Z_A}{Z_A + Z_B} \tag{64}$$

The surge impedance of an OHL is typically higher than the surge impedance of a cable, resulting in a voltage reduction when the wave flows from the OHL into the cable and a voltage magnification when the wave flows from the cable into the OHL [17].
By substituting in (64) the cable and OHL surge impedances, (65) and (66) are obtained for an incident wave flowing from the cable into the OHL and (67) and (68) for an incident wave flowing from OHL into the cable.

$$V_3 = V_1 \cdot 1.755 \tag{65}$$

$$V_2 = V_1 \cdot 0.755 \tag{66}$$

$$V_3 = V_1 \cdot 0.245 \tag{67}$$

$$V_2 = V_1 \cdot (-0.755) \tag{68}$$

As it can be seen in (65) the voltage should ideally increase 1.755 times when the restrike occurs in the cable end, explaining the voltage increase when comparing cases 1 to 3 with a pure cable line.
In the same way that a voltage increase is expected when a restrike occurs in the cable side of a hybrid line, a voltage decrease would be expected if the restrike occurs in the OHL end (see (67)). But, the simulations contradict the equation and show a voltage increase.
The voltage is reduced when flowing from the OHL into the cable, but it is later reflected back into the cable receiving end, being then reflected and refracted in the junction point. In this process the voltage builds up and would, in theory, for a lossless cable and OHL reach the peak value that would be obtained if no cable was present [16].
However, in the simulations the voltage surpasses this theoretical maximum value, meaning that not all aspects have been considered. Normally, the analysis of reflections and refractions in a cable-OHL line,

considers the cable to be very small when compared with the OHL. As example, a typical study-case is lightning hitting the OHL and propagate into the substation through a small cable, a situation that is shown in [16], [17] and [31]. In this situation the wave reflection in the OHL end is not considered as the OHL travelling time is too large when compared with the cable travelling time. For the cases shown in Table 5.5 the cable and OHL travelling times have the same order of magnitude, making it necessary to consider the wave reflections in the OHL end and the following refractions in the junction point.

Figure 5.78 shows the voltage in the junction point and cable receiving end for the re-energisation of a hybrid OHL-cable line. In this particular example, the cable is bonded in both ends, and the OHL is connected to an ideal voltage source, resulting in a reflection coefficient of -1 at the OHL sending end; the voltage difference at the CB terminals at the restrike instant is 1.936 pu.

The restrike occurs at 0.4650s and the wave travelling times are 55.5 µs and 176 µs, respectively, for the OHL and cable. As a result, at approximately 0.4654 s the voltage that was reflected in the cable receiving end reaches the junction point and is part refracted to the OHL and part reflected back to the cable, reaching the cable receiving end at approximately 0.46556s; before the peak voltage instant, thus, increasing the voltage when compared with the equivalent pure-cable example. At this point, the voltage analysis becomes more complicated as all the refractions and reflections start to superimpose each other.

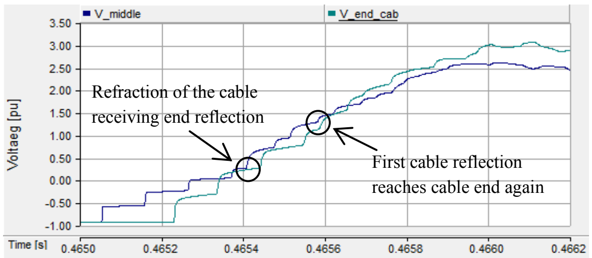

Figure 5.78 - Voltage in the junction point and cable receiving end during re-energisation of OHL-cable line

Due to the wave reflection in the OHL sending end, the peak overvoltage will depend on the cable and OHL travelling times. In this example the lines are modelled by means of Bergeron models, which allow defining the cable and OHL surge impedances, travel times and resistances. Therefore, the resistances can be reduced to zero and the worst-case scenario can be obtained.

Figure 5.79 shows the comparison between the restrike using Bergeron models and FD-models. The restrike occurs at the same time for both models, but, as expected, the voltage is higher in the Bergeron model. The peak values obtained using the Bergeron model are identical to those obtained by using lattice diagrams and the reflection/refraction constants of (65)-(68).

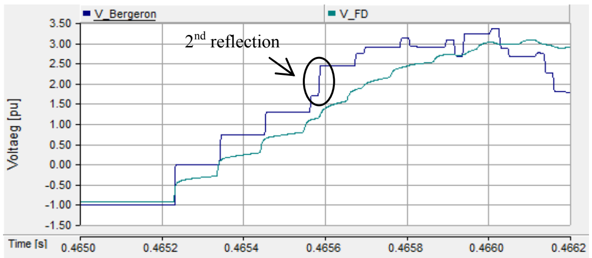

Figure 5.79 – Voltage in the cable receiving end using the Bergeron model and the FD model

5.9.1 Worst-case scenarios

In a normal system the peak overvoltage associated to the restrike depends of the following factors:

- Wave travelling time in the OHL and in the cable;
- Reflection and refraction coefficients;
- Initial voltage difference between the CB terminals;
- Location of the cross-bonding points (explain in the next section).

The reflection and refraction coefficients are a function of the cable and OHL surge impedances, which are independent of the lengths. The relation between a cable and OHL surge impedances depends on the electrical characteristics of both lines, but a typical case is the surge impedance of an OHL to be about eight times higher than a cable's surge impedance. For this relation are obtained reflection and refraction coefficients of 0.777 and 0.222, respectively, for a wave flowing from an OHL to a Cable, and of 0.777 and 1.777 for a wave flowing from a cable to an OHL.

The worst-case scenario is to have maximum voltage difference between the CB terminals at the time of restrike, i.e. 2 pu. Please note that in a real hybrid line the voltage will be lower than 2 pu as part of the energy is damped between disconnection and re-energisation.

The wave travelling time depends on the cable and OHL lengths and the wave speeds. For obvious reasons there are no typical values for the cable and OHL lengths

It is not easy to predict the maximum overvoltage for an OHL-cable line. Therefore, a Matlab code was written to calculate the maximum overvoltage of a lossless OHL and cable as a function of the reflection coefficient, initial voltage difference and waves travelling times. The algorithm and tables containing the voltage value as a function of the reflection coefficient and the waves travelling times are available in Appendix I.

Figure 5.80 shows for different cable lengths the peak overvoltage associated with a restrike, keeping the OHL length constant and using a reflection coefficient of -0.777. Figure 5.81 shows the peak voltage as a function of the cable length and the reflection coefficient.

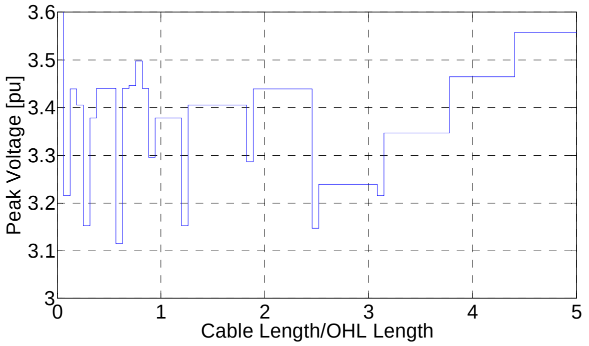

Figure 5.80 - Maximum overvoltage as a function of the cable length due to restrike

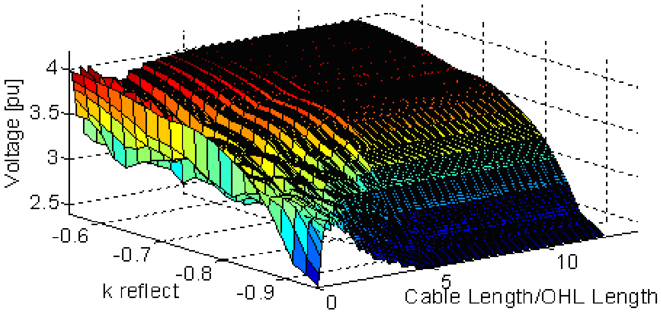

Figure 5.81 - Maximum overvoltage as a function of cable length and reflection coefficient due to restrike

While the cable is no more than 2.5 times longer than the OHL, the voltage presents an erratic behaviour, increasingly constantly after that point.

Figure 5.82 compares the voltage in the cable end as a function of the number of reflections in the cable receiving end for a cable travelling wave that is 8.4 times larger than the OHL travelling wave and a cable travelling wave that is 7.4 times larger than the OHL travelling wave.

Until the ninth reflection the voltage is equal for both systems. The divergence is when the first cable reflection, which is later reflected back into the joint, reaches the cable receiving end again. This reflection is preceded by several waves that were reflected back to the OHL in the joint before being refracted to the cable, as the cable travelling time is 8.4 times higher than to the OHL travelling time in one of the systems and 7.4 times in the other, there will for the first system an extra OHL reflection reaching the cable receiving end before the "big jump". This extra reflection will result in the higher voltage registered when the cable is longer.

This is exactly what happens in Figure 5.80 when the cable is at least three times longer than the OHL. The changing in the overvoltage value occurs when the cable travelling time increases by an amount equal to the OHL travelling time. So in the example it would be for tb=7ta, tb=8ta, tb=9ta….

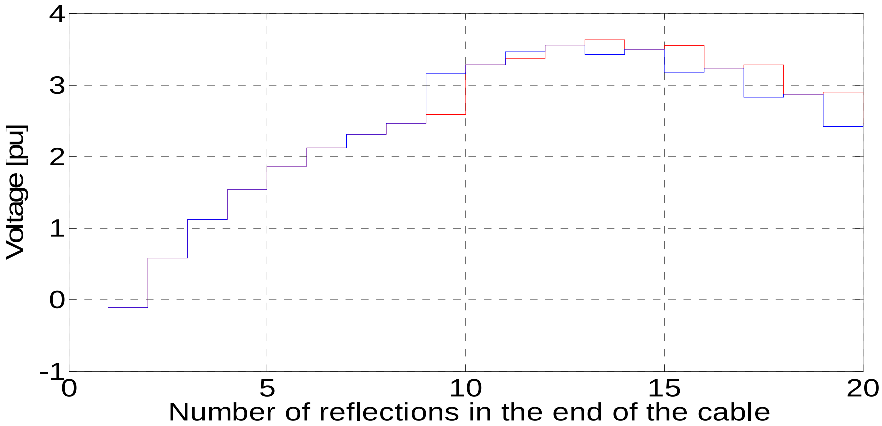

Figure 5.82 – Voltage in the cable receiving end for a tb=7.4ta (blue line) and tb=8.4ta (red line)

5.9.2 Influence of the cross-bonding points

In the previous simulations the cables were bonded at both ends, but as will be shown, the cross-bonding of the cable screen, which is normally done for long HV cables, can dramatically change the waveforms and peak voltages [101], [102] .

The restrike/re-energisation of a cable is a high-frequency phenomenon, which results in high currents flowing into the cable's screen and the induction of voltages in the conductors. Thus, the type of bonding used has a strong influence on the waveforms.

Figure 5.83 shows the voltage at the end of a cable line during a restrike, for different bonding types. It can be observed that the voltage for a both-end bonded cable is reflected only in the cable ends, while the voltage in the cross-bonded cable presents several small reflections in each of the cross-bonding points.

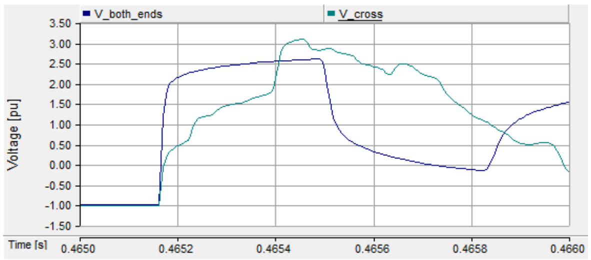

Figure 5.83 - Voltage in cable receiving end for a pure cable line. Blue: Both-ends bonding; Green: Cross-bonding

Figure 5.84 shows the voltage in the cable and OHL receiving ends, for a hybrid line consisting of a cable and OHL of equal lengths.

In Figure 5.83 it is seen that the maximum voltage is higher in the cross-bonded cable than in the both-ends bonded cable. Thus, one would expect that in a hybrid line the maximum voltage would also be higher when using a cross-bonded cable, but as can be seen in Figure 5.84.b, this is not the case.

The maximum overvoltage at the end of the cross-bonded cable, i.e. the junction point, does not occur when the first wave impulse reaches that point, but hundreds of microseconds after (for more details see chapter 6).

In this example the cable and the OHL have equal lengths, meaning that the OHL travelling time is lower than the cable charging time. Thus, when the cable maximum voltages reaches the OHL receiving end, the voltage in that point has already decreased due to several reflections in the OHL receiving end and joint point.

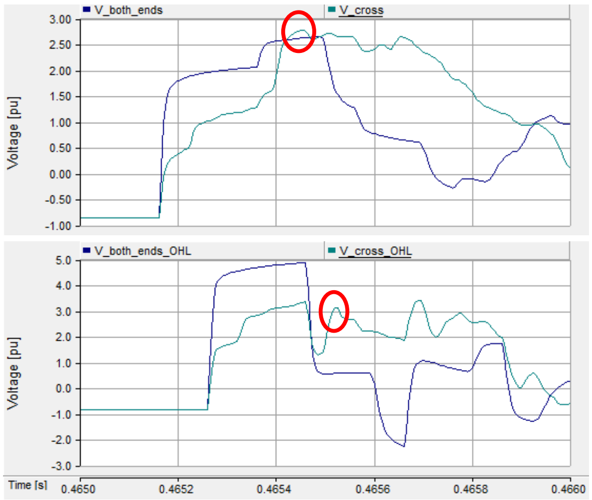

Figure 5.84 - Voltage in the cable (upper graph) and OHL (lower graph) receiving ends for a hybrid cable-OHL line. Blue: Both-ends bonding; Green: Cross-bonding

Having a cross-bonding installation does not by itself neither decrease nor increase the overvoltage value. In the example shown in Figure 5.84, the cable and the OHL have the same length, but if the OHL length increases enough the voltage would be higher in the hybrid line with the cross-bonded cable.
The amount of cross-bonded section also has an influence on the overvoltage magnitude. The importance of accurately modelling all the cross-bonded sections is analysed in chapter 6.2.

It can be concluded after this exposition that when performing re-strike simulations, no simplifications can be performed in the cable model, it being necessary when simulating a cross-bonded cable to precisely design all minor sections. The ground resistance should also be modelled as precisely as possible as it can originate small differences in the peak values (see [82] for lighting impulse examples).

5.9.3 Countermeasures

Hybrid line opening sequence

By comparing the different cases it can be seen that for two hybrid lined having the same cable and OHL lengths the overvoltage will be substantially lower if the restrike occurs in the CB attached to the OHL (compare Case 1 with Case 4, Case 2 with Case 5 and Case 3 with Case 6 in Table 5.5 and Table 6.1).
Thus, when opening a hybrid line, the CB attached to the cable should be opened first. As a result, even if the CB fails to open, the restrike will be small and not constitute a risk to the system.
One or two cycles after the opening of the cable's CB, the CB of the OHL end can be opened.

Insertion of a cable between the OHL and the substation

It is common to have the connection between the OHL and the substation made through a small cable. This cable may reduce the overvoltage amplitude as explained in section 5.9
Using Case 2 as an example, the insertion of a 500 m cable after the OHL would reduce the overvoltage by 0.251 pu, from 4.5722 pu to 4.3212 pu.

Shunt reactor connected to the cable

As shown in section 5.8.3, when de-energising a cable together with a shunt reactor, the maximum voltage at the CB terminals occurs later and the TRV is less sharp, reducing the likelihood of a restrike.

Circuit-Breaker Class

The likelihood of a restrike also depends on the CB class. The standard [77] divides the CB into the following classes, according to their restrike performance:

- C1: CB with a low probability of restrike during capacitive current breaking;
- C2: CB with a very low probability of restrike during capacitive current breaking.

The difference between low and very low probability lies in the way that the CB is tested. For a class C1 CB, the tests are performed under new conditions, while the C2 class requires a test-duty T60 as a preconditioning test; a test that is related to the breaking capability of the CB [77].
A CB being tested under class C2 conditions can be reclassified as class C1 if it does not present more than a defined number of restrikes during the test, one or two depending on the test. In order to be classified as class C2, no restrikes are allowed to occur during the test. If a restrike occurs, the test should be repeated without doing any maintenance work on the CB, and no restrikes are allowed to take place.
The choice of CB class depends on financial analyses, which is outside of the scope of this thesis.

5.10 Summary

This chapter described the main transient phenomena associated with the use of HVAC cables and the respective countermeasures.

For some of the phenomena new formulas/methods were presented which can be used to save time and/or confirm the results. Examples are:

- Zero-missing phenomenon: A method to calculate the ideal pre-insertion resistor value and a method that can be used to calculate an approximate value of the pre-insertion resistor.
- Cables in parallel: Equations for the calculation of the peak current and frequency during the transients;
- De-energisation of cable and shunt reactor: A method to simulate the overvoltage in Matlab; Equations for the calculation of the resonance frequencies;

Some of the countermeasures are contradictory, most notably the synchronised switching, which depending on the phenomena, it may be desirable to use for zero or peak voltage. Table 5.6 summarises the type of switching desirable for the different phenomena.

Normally, it is choose to switch on at zero-voltage, in order to avoid the overvoltage and the high-frequency currents, but where the energisation of a transformer through a cable is concerned, it is suggested to energise the transformer at peak voltage in order to avoid the resonance.

The use of a pre-insertion resistor is effective when it comes to avoiding the overvoltages of all the energisation transients analysed.

Table 5.6 - Types of switching that should be used for the different phenomena

Phenomenon	**Zero Voltage**	**Peak Voltage**
Normal energisation	**X**	
Zero-missing		**X**
Cables in parallel	**X**	
Transformer-cable resonance		**X**

For de-energisation it was shown that de-energising the shunt reactor and cable together reduces the risk of restrike, but at the expense of a small overvoltage resulting from the mutual coupling between the shunt reactor phases. In the case of a hybrid line, one should open first the CB in the cable end.

6. Insulation Co-ordination Studies

6.1 Introduction

The transmission modes of an overhead line, except a vertical twin-circuit untransposed line, are typically not very frequency dependent, i.e., the voltage and current transformation matrix eigenvalues are almost constant with respect to the frequency, when compared with a cable, of which transformation matrix eigenvalues are very dependant on the frequency [87]. As a result, the simulation of underground cables typically requires higher-order functions, hence increasing the computational effort. Consequently, the simulation of a transient in a cable-based system is usually several times slower than the same simulation in an equivalent OHL-based system.

The number of cables included in the model and the number of cross-bonded sections are two of the parameters that have more influence on the total simulation time. Minimising these two parameters would mean a substantial increase in the efficiency of the simulation.

The insulation co-ordination computational guide [12] recommends to have one or two-substation depth, and to model all cross-bonding points. The next sections present a new method that can be used to estimate the required modelling depth and guidelines for the choice of the number of cross-bonding points to be included in the model.

6.2 Modelling of the cross-bonded points

For several reasons, the modelling of all cross-bonded sections represents a substantial increase in both the simulation running time and the time necessary to design the system:

- To design *n* minor cross-bonded sections instead of three;
- The software needs more time to complete each time step;
- The time step has to be reduced in order to accommodate the shorter cable sections;
- Increases the probability of fitting and memory problems;

The standard [12] suggests the modelling of all cross-bonded sections. Some phenomena require this level of detail, while for other phenomena the model can be simplified. This chapter shows examples of both situations and provides guidelines to help in deciding whether to use, or not use, the simplified model.

If a precise modelling is required, it is necessary to know the required modelling depth. Section 6.3.3 provides a method that can be used for it.

6.2.1 Example for a restrike

Chapters 5.8 and 5.9, respectively explained the restrike of a cable and a hybrid cable-OHL line. It was shown how the cross-bonding of the cable affected the transient waveform and the magnitude of the overvoltage.

In the previous examples, the cross-bonded cable was modelled by only one major section, divided into three equal minor sections. A comparison of this model with an equivalent model with more cross-bonded sections would be a good way of verifying the influence of the cross-bonded points on the results.

A more detailed model, where the cable was divided into three major sections, each of them subdivided into three minor sections, was designed. Figure 6.1 compares the voltage in the cable receiving end for a cable bonded at both ends with a cable with one cross-bond section and a cable with three cross-bond sections.

The overvoltage magnitude is approximately 1.7 times larger for the cable with three major cross-bonded sections, equivalent to nine minor-sections, than for the cable with a single major cross-bonded section.

To have more cross-bonded sections does not mean to have a larger or lower overvoltage values. In this particular case, the total overvoltage is increased because of the length of the minor sections. However, there are also cable lengths for which the overvoltage would decrease, as explained in section 5.9.2.

Table 6.1 presents the maximum and average overvoltage values for the different cases (refer to chapter 5.9) for the cable with three major cross-bonded sections. Figure 6.2 shows that for these particular examples the overvoltage is higher for cables with three major cross-bonded sections.

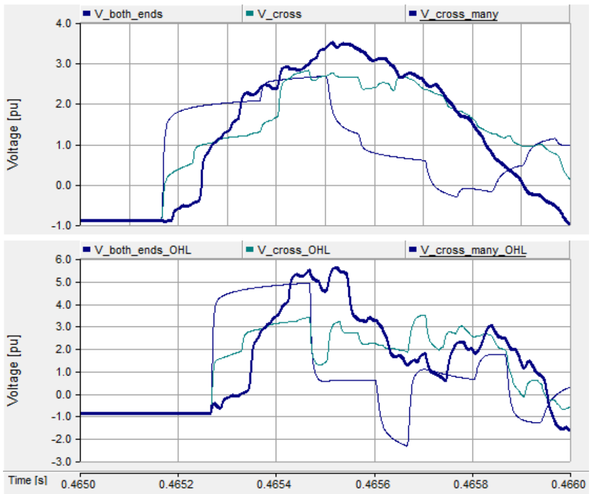

Figure 6.1 - Voltage in the cable (upper graph) and OHL (lower graph) receiving ends for a hybrid cable-OHL line. Blue: Both-ends bonding; Green: Cross-bonding (one major section); Blood Purple: Cross-bonding (three major sections)

Table 6.1 - Maximum and average peak voltages in the hybrid line receiving end for statistical switching, when modelling the cable with three major cross-bonding sections

	Pure cable	**Case 1**	**Case 2**	**Case 3**	**Case 4**
Max. BDK-Ph A	2.4678	3.8031	4.4912	3.8074	2.5879
Max. BDK-Ph C	2.6890	4.2958	4.5722	4.3005	2.8152
Avg. BDK-Ph A	1.9215	2.9764	3.5082	2.9798	2.0244
Avg. BDK-Ph C	2.0138	3.2172	3.2254	3.2207	2.1616
	Case 5	**Case 6**	**Case 7**	**Case 8**	
Max. BDK-Ph A	2.5604	2.5923	2.7915	2.5866	
Max. BDK-Ph C	2.7987	2.8868	2.9968	2.7459	
Avg. BDK-Ph A	1.9961	2.0199	2.1612	1.9758	
Avg. BDK-Ph C	2.1527	2.1691	2.2090	2.0245	

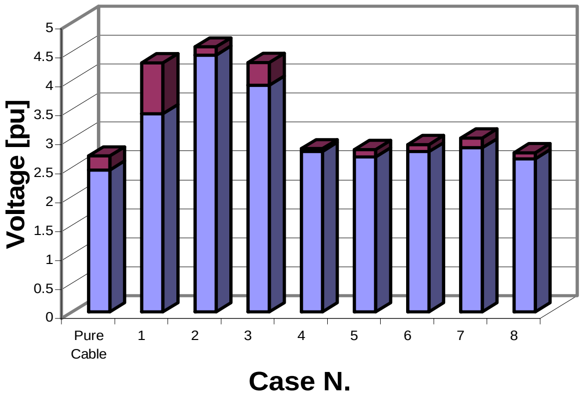

Figure 6.2 - Peak overvoltage for the pure cable and the eight hybrid cases. Blue: One Cross-section; Magenta: Three cross-sections

6.2.2 *Energisation at zero voltage - Example for Horns Rev 2 measurements*

The simulation of the restrike in the previous section demonstrated that it is necessary to have a precise modelling of all cross-bonded points in order to obtain an accurate simulation of the phenomenon.

This section demonstrates the exact opposite, namely a phenomenon that does not require the modelling of all cross-bonded sections.

The Horns Rev 2 cable has a total of thirty three minor cross-bonded sections. Section 4.6.3 demonstrated that the PSCAD/EMTDC model can simulate the energisation transient with a high accuracy. The simulation is repeated using a simplified cable model with one major cross-bonded section instead of eleven.

Figure 6.3 and Figure 6.4 show the voltage and current in different points of the system during energisation for both modelling approaches. The comparison of the waveforms shows that a precise modelling of the cross-bonded points is not necessary for a proper modelling of the energisation transient.

The cable was energised at zero-voltage and the current flowing in the screen during the transient is rather low with a small influence in the waveform. Consequently, few differences are found when compared the model containing all cross-bonded sections with the simplified model.

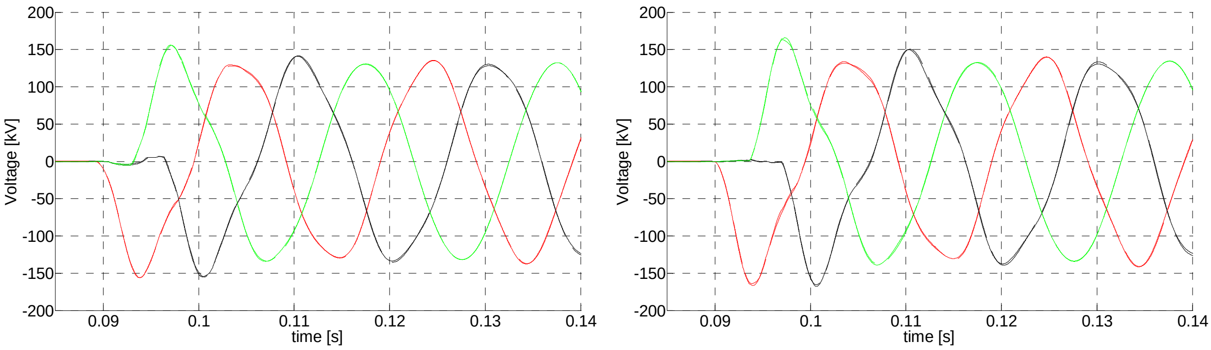

(a) (b)

Figure 6.3 - Voltage during energisation. Solid lines: All cross-bonded sections; Dashed Lines: One major cross-bonded section. a) Sending end; b) Receiving end

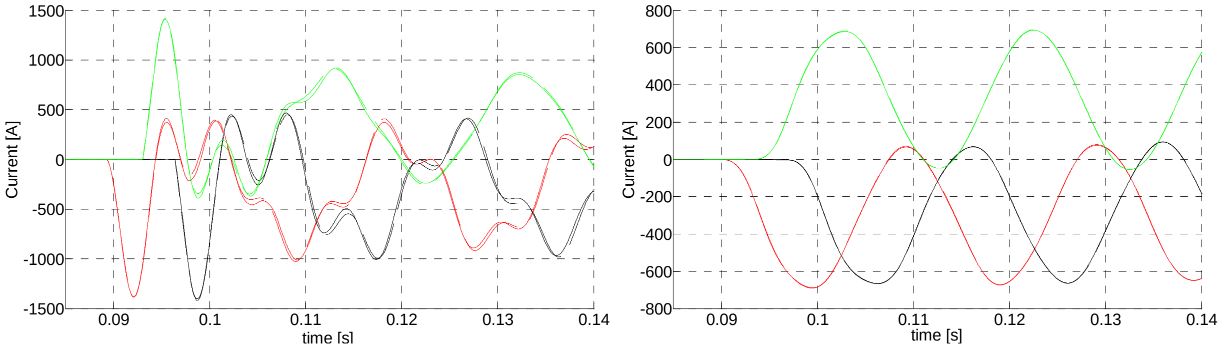

(a) (b)

Figure 6.4 - Current during energisation. Solid lines: All cross-bonded sections; Dashed Lines: One major cross-bonded section. a) Sending end; b) Shunt Reactor

6.2.3 Guidelines

The previous two sections presented very distinct situations concerning the modelling of the cross-bonded sections. It was demonstrated through practical examples that in some situations it is important to model all cross-bonded sections, while in other situations simplifications can be made.

The current flowing in the screen induces a voltage in the conductor and vice-versa. Thus, the need for a precise modelling of the cross-bonded sections is correlated with the current flowing in the cable screen. If the current flowing in the screen is small, e.g. a balanced system in steady-state, the model can be simplified. If the current flowing in the screen is high, e.g. a short-circuit, the model must contain all the cross-bonded sections.

The previous section demonstrated that the transient's waveform, the current magnitude and voltage magnitude are strongly related to the voltage value at the moment of energisation. An insulation co-ordination study consists of simulations of the worst-case scenarios, which depending on the phenomenon may correspond to energisation at peak voltage, e.g. switching overvoltage, or energisation at zero voltage, e.g. zero-missing phenomenon.

Thus, all the cross-bonded sections should be included in the model when simulating energisation at peak voltage. The current flowing in the cable screen during this type of transients is high, with a magnitude comparable to the magnitude of the current in the conductor, and the voltage induced in the conductor is significant.

When simulating energisation at zero voltage, the transient current in the conductor and screen is small, and the cable model can be simplified to only one major cross-bonded section, with a length equal to the cable total length and divided into three minor-sections of equal length. The exceptions are phenomena presenting high zero-sequence currents, e.g., cable-transformer resonance.

When necessary, the modelling of all the cross-bonded sections should include both the cable being energised and adjacent cables. The modelling of the adjacent cables is addressed in section 6.3.3.

6.3 Modelling depth

The modelling depth has a strong influence on the simulation results. The modelling depth of the models used in chapter 5 was larger than necessary. This approach was used in order to ensure maximum accuracy, but at the expense of long simulation times. The minimisation of the number of lines and busbars in the model would represent enormous time savings.

The peak voltage associated with cable energisation/re-energisation is not attained in the energisation/re-energisation instant, but some hundreds of micro-seconds later. The exception is the energisation of a cable in a weak grid, which is a special case as explained in section 5.4.

For an isolated cable, i.e. connected to an ideal voltage source, switched on at peak voltage, the instant of maximum voltage magnitude is a function of the cable geometry and length. For a cable incorporated into a network, the peak voltage will normally occur at the same instant.

Figure 6.5 shows the voltage in one phase during a restrike for different modelling depths. The phase is restriked half a cycle after the CB switch-off; the cable being restriked is the NVV-BDK cable on the NVV side, and the colour code is: Blue: 2 busbars depth, Black: 3 busbars depth, Green: 4 busbars depth, Red: 5 busbars depth.

Figure 6.6 shows the voltage in one of the phases during normal energisation and re-energisation, for the NVV-BDK cable connected to an ideal source. The transient waveform is similar for both phenomena, but with larger oscillations in the restrike due to the larger initial voltage difference at the CB terminals. As an example, the voltage drop around the 0.423s is more pronounced for the restrike than for normal energisation. The peak voltage occurs at the same instant for both phenomena and modelling depths.

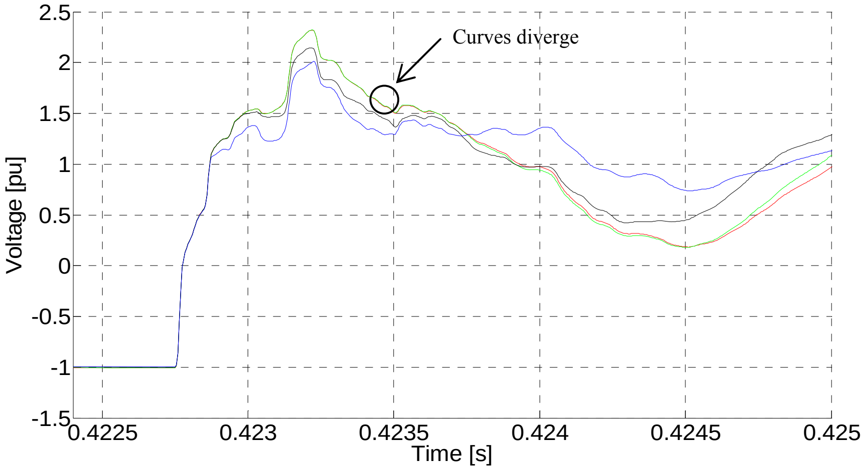

Figure 6.5 - Voltage transient in one of the phases after re-strike for different modelling depths. Blue: 2 busbars depth, Black: 3 busbars depth, Green: 4 busbars depth, Red: 5 busbars depth

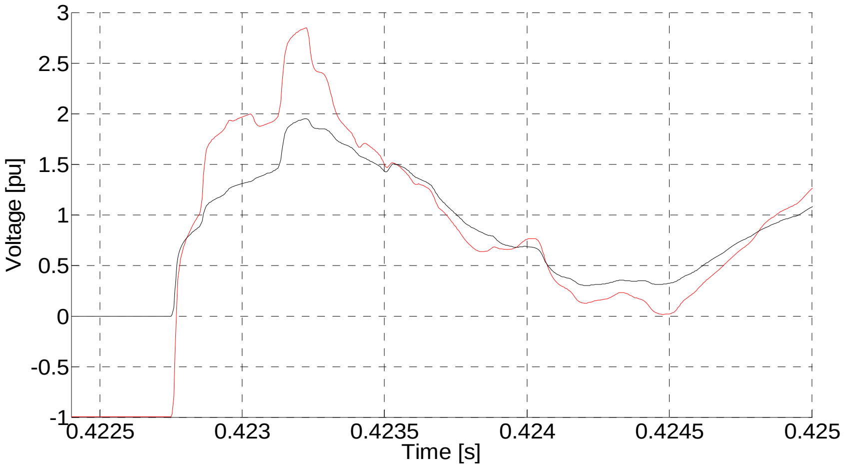

Figure 6.6 - Voltage transient in one of the phases after re-strike (red curve) and normal energisation (black curve)

In these two examples, the peak voltage instant is independent of both the modelling depth and the energisation phenomena, i.e. normal energisation or restrike. On other hand, the magnitude of the peak voltage is very dependent on both the type of phenomenon (because of the initial voltage difference at the CB terminals in the initial instant) and the modelling depth (because of the reflections and refractions in the neighbour lines and equipments).

The reflections in the neighbouring cables affect the peak voltage and can therefore also affect the moment at which it occurs even if such situations normally do not happen in a grid operating in normal conditions. The same cannot be said for weak grids or black-start operations.

Yet, there are two other cases when this may not be true:

- The reflected wave reaches the cable precisely after the expected peak;
- An OHL is installed in the vicinity of the cable.

Both situations are also analysed in this chapter.

6.3.1 Modelling depth calculation

The previous section explained how the peak voltage depends on the modelling depth, and how important is to know which lines/busbars to model. This section presents a method that can be used to obtain that information. The method is first explained through a practical demonstration for the energisation/re-energisation of the NVV-BDK cable.

For the energisation/re-energisation of this specific cable, the peak voltage is attained 470 µs after the wave has reached the cable receiving end (see Figure 6.5 or Figure 6.6).

Table 6.2 shows, for different typical wave speeds, the distances travelled by a wave during 470 µs. In order for the reflections of the neighbouring busbars to reach the receiving end of the NVV-BDK cable before the peak overvoltage, the busbars have to be at a distance lower than half of the distance travelled by the wave in that period of time as the wave has to reach the reflection point and be reflected back to the cable receiving end.

Table 6.2 - Distance travelled by the wave during 470µs for different wave speeds

Wave speed [m/µs]	Distance [km]	Busbar distance km]
300 (light speed)	141	70.5
179* (coaxial mode)	84	42
80 (inter-sheath mode)	38	19

* *Value obtained for the simulated cable by means of simulations in PSCAD/EMTDC*

Different approaches can be applied. The worst-case scenario is to consider that the wave speed is equal to the speed of light and model all the lines up to a distance of 70.5 km from the NVV busbar. This is an incorrect approach as in a cable the wave speed is approximately half the speed of light. Therefore, in a pure cable network, such approach would result in excessive modelling and longer simulation times.

The situation changes when OHLs are in the vicinity of the cable being restriked. In that case, the wave in the OHL travels at a speed close to the speed of light. In this example, the 165 kV network is a pure cable network, and the wave speed is the cable's coaxial mode speed.

So, by knowing the grid configuration, the wave speed in the different cables and the time required to have the first peak, the required modelling depth can be estimated.

Grid configuration

Typically, most of the utility companies have a PSS/E file (.raw), or equivalent, containing the entire grid. This file contains information on all grid equipment (lines, shunt reactors, transformers, generators, loads, etc…), respective characteristics and connections between busbars.

This file can be used to obtain the grid layout and to design two matrices equivalent to the grid, one containing the distance between the busbars and the other the wave speed in each line.

Figure 6.7 shows part of the network in the vicinity of the NVV busbar, whose equivalent distance matrix is shown in Figure 6.8. The wave speed matrix is equivalent to the matrix shown in Figure 6.8, but containing the wave speed in the line instead of the length. The distance between the busbars can be obtained directly from the PSS/E files, but the same is not possible for the wave speeds, since the PSS/E files lack information about the lines geometry [87]. One solution could be to use values than are slightly larger than the average wave speed values, e.g. 181m/µs and 280m/µs for a cable [87] and an OHL, respectively, or to create an extra file containing that precise wave speed in each line.

In general, it is only necessary to model the elements whose voltage level is the same as that of the cable being switched [12]. Thus, the matrices contain busbars with the same nominal voltage only.

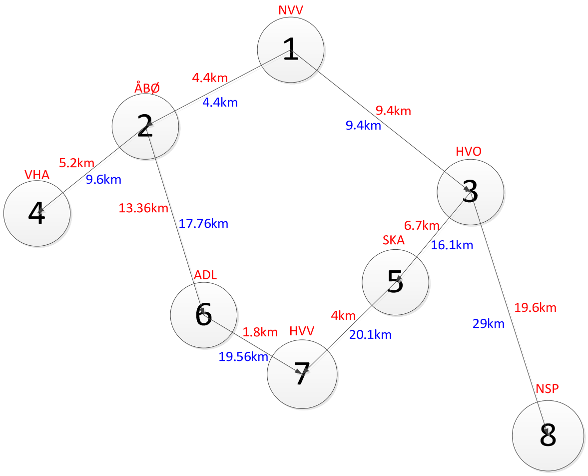

Figure 6.7 - Busbars in the vicinity of the restriked node. Red: Distance between nodes; Blue: Distance between the nodes and the NVV node

$$\begin{bmatrix} 0 & 4.4 & 9.4 & 0 & 0 & 0 & 0 & 0 \\ 4.4 & 0 & 0 & 5.2 & 0 & 13.36 & 0 & 0 \\ 9.4 & 0 & 0 & 0 & 6.7 & 0 & 0 & 19.6 \\ 0 & 5.2 & 0 & 0 & 0 & 0 & 0 & 0 \\ 0 & 0 & 6.7 & 0 & 0 & 0 & 4 & 0 \\ 0 & 13.36 & 0 & 0 & 0 & 0 & 1.8 & 0 \\ 0 & 0 & 0 & 0 & 4 & 1.8 & 0 & 0 \\ 0 & 0 & 19.6 & 0 & 0 & 0 & 0 & 0 \end{bmatrix}$$

Figure 6.8 - Distance matrix for Figure 6.7 system

Time for the first peak

The first peak instant can be obtained by simulating the energisation of the cable connected to an ideal voltage source. This peak corresponds to the wave travelling into the cable receiving end, being reflected back to the sending and finally being reflected back once again to the cable receiving end.

The time can be obtained by measuring the time between the moment when the wave reaches the cable receiving end (t_1 in Figure 6.9) and the peak voltage instant (t_2 in Figure 6.9). This time is also equal to two times the wave travelling time in the cable.

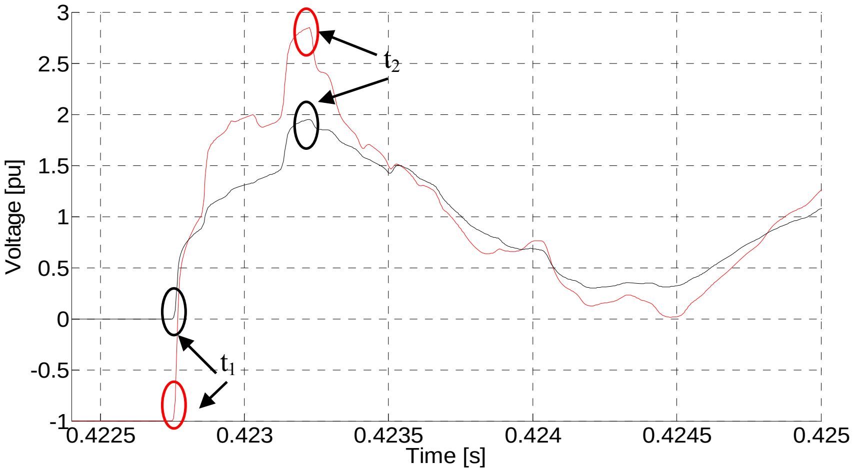

Figure 6.9 - Voltage transient in one of the phases after restrike (red curve) and normal energisation (black curve)

Matlab code

A Matlab code was written to calculate the required modelling depth. Figure 6.10 shows the code equivalent flowchart, and the code is available in Appendix I.

The required modelling is obtained through the following steps:

1. Insert the time for the first peak and the wave speeds (if not available)
2. The code reads the grid information directly from the PSS/E files, designing two matrices equivalent to the network
3. The first matrix contains the distance between the busbars, in which the line and column identify the busbars. The matrix is symmetrical
4. The second matrix is equivalent to the first, but the distance is substituted by the wave speed in the cable (coaxial mode) or OHL
5. The distance and the travelling time between the energised/re-energised node and all busbars up to a distance of 8 busbars are calculated. At the same time, all possible paths up to a distance of 8 busbars are calculated
6. Calculates which busbars are located up to a distance of less than 0.525 times the charging time of the cable being energised/re-energised. Ideally it would be 0.5, but it is given a security margin for the case of a reflection reaching the cable immediately after the expected peak time;
7. Indicates which busbars need to be modelled, i.e., the modelling depth.

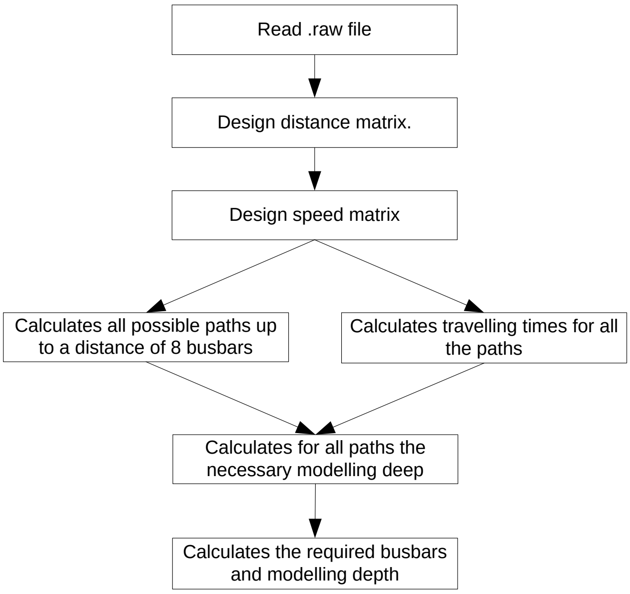

Figure 6.10 - Matlab code flowchart

The Matlab code indicates that for the NVV-BDK cable the network should be modelled up to a distance of 4 busbars. Figure 6.5 showed that the same conclusion was achieved through simulations in PSCAD/EMTDC.

The method described provides not only the required modelling depth, but also the busbars that have to be included in the model. Using this information the model can be optimised, and instead of having a 4 busbars modelling depth it can have only the necessary busbars.
The energisation/re-energisation of the NVV-BDK cable from the NVV side needs 14 busbars, but the use of a 4 busbar modelling depth corresponds to 29 busbars. Thus, optimising the model to only 14 busbars would represent a substantial reduction in the simulation time.
Figure 6.11 compares the voltage in the cable receiving end using these two approaches. It can be observed that the voltage maximum value is the same for both models.

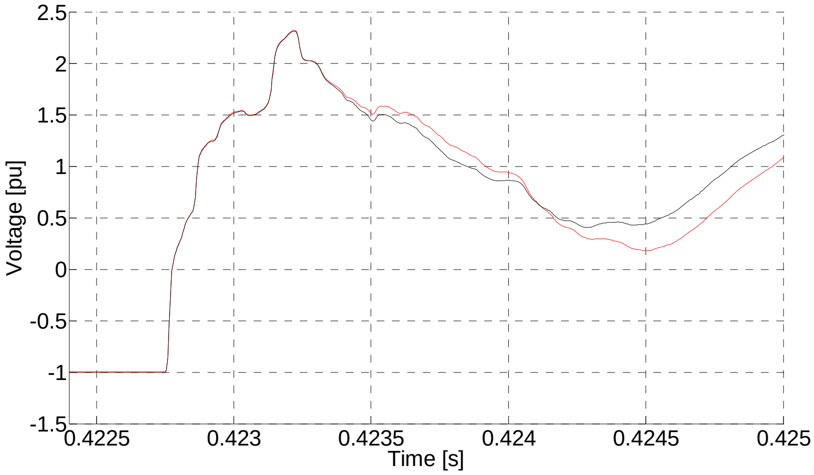

Figure 6.11 - Voltage transient in one of the phases after the restrike for a 4 busbar modelling depth (red curve) and a model containing only the required busbars (black curve)

6.3.2 Possible inaccuracy

The method presented in the previous section assumes that the first voltage peak is the maximum one, which may not always be the case.

An example is a system consisting of two both-end bonded cables, as shown in Figure 6.12. Assuming an ideal CB and equal surge impedance in the two cables, two symmetrical waves are generated at t_0 when the CB switches on. One of the waves propagates into *Cable B* (blue wave in Figure 6.12), while the other propagates into *Cable A* (red wave in Figure 6.12).

If *Cable B* were energised connected to an ideal voltage source, the maximum peak of the voltage transient would occur when the generated wave had reached the cable receiving end after being respectively reflected once in the receiving and sending ends of the cable (draw V in Figure 6.12).

The reflection coefficient is almost zero at the joint point because of the cables' equal surge impedances. Thus, in III there is almost no reflection, the existent reflection is due to the screen bonding, and the wave propagates almost entirely into *Cable A* instead of being reflected back into *Cable B*. Such a situation does not normally occur in a normal system where part of the wave is reflected back into the cable. As the reflection is minimum, there is no overvoltage when the wave reaches the cable receiving end (draw V in Figure 6.12 and point V in Figure 6.13).

Not only is there almost no reflection in the joint point as the entire wave that was initially reflected into *Cable A* is reflected back at 100% in the source (draw II in Figure 6.12). But this wave is then almost totally refracted in the joint point (draw IV in Figure 6.12), eventually reaching the receiving end of *Cable B* (draw VI in Figure 6.12 and point VI in Figure 6.13). The maximum transient overvoltage occurs at this instant.

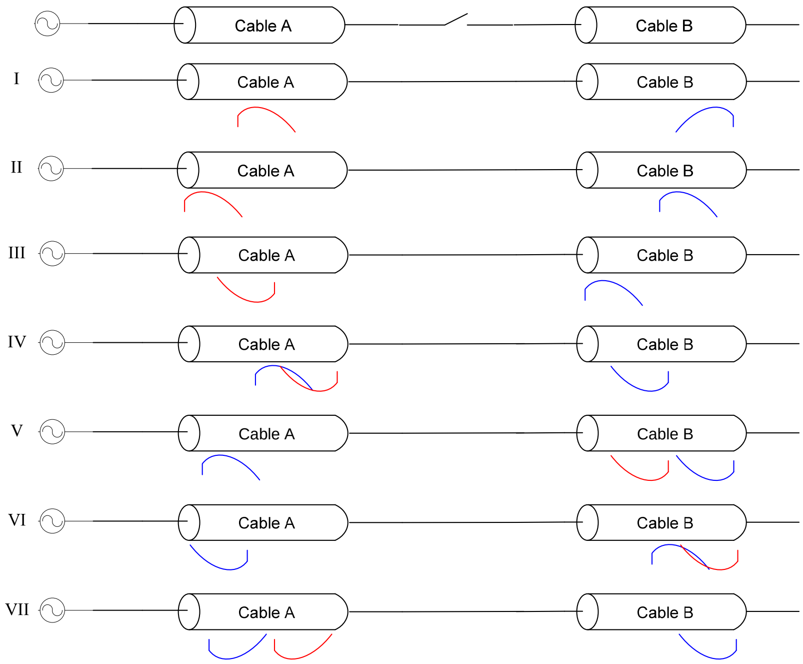

Figure 6.12 - Waves during the energisation of Cable B, for a Cable B longer than Cable A

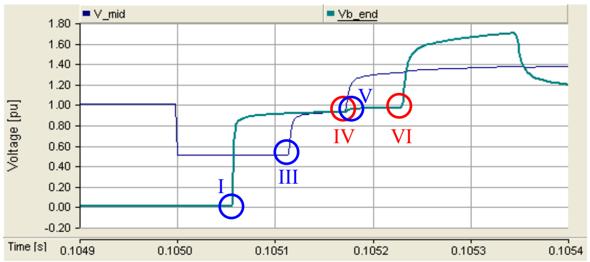

Figure 6.13 - Example of the voltage in the end of Cable B (green curve) and the joint point (blue curve) during the energisation of Cable B. Cable A: 10km; Cable B:15km; Short-circuit Power: Infinite

The previous example is very unrealistic as it assumes an infinite short-circuit power at the *Cable A* sending end. Figure 6.14 repeats the simulation considering a more realistic 4333 MVA short-circuit power at the *Cable A* sending end, resulting in a drastic change to the waveform.

The first major change occurs when the wave injected into *Cable A* reaches the cable sending end (draw II). In the previous example the voltage in that point would be imposed by the voltage source and the entire wave would be reflected back. But in this example, the voltage in the sending end reduces to a value close to zero, and the wave is then reflected back with a negative polarity, similar to a reflection in a capacitive termination [16], as observed in Figure 6.15 at 0.1051 s. Thus, instead of being increased, the voltage is reduced when the wave reaches the joint point and the *Cable B* receiving end. Figure 6.14 shows the voltage reduction in points *IV* and *VI*, respectively.

The second changes occur when the wave initially injected into *Cable B* and reflected back in the receiving end of that cable reaches the *Cable A* sending end. The polarity of this wave is symmetric to the polarity of the wave initially injected into *Cable A*. Thus, the voltage at the *Cable A* sending end increases substantially when the wave reaches the node, see Figure 6.15 at 0.1052 s. The wave is then reflected back to the joint point, reaching the *Cable B* receiving end, point VII in Figure 6.14, increasing the voltage in that node.

This behaviour continues for some hundreds of microseconds while the transient is damped, Figure 6.14.b. This is the situation that could occur in a real, small system, where the peak voltage is only attained after several reflections.

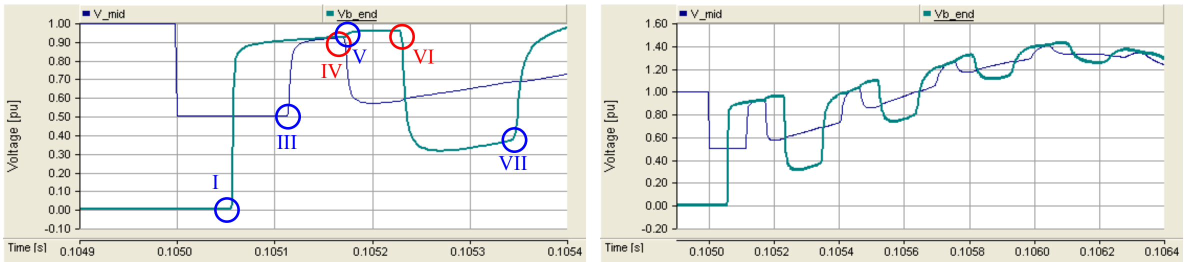

(a) (b)

Figure 6.14 - Example of the voltage in the end of Cable B (green curve) and the joint point (blue curve) during the energisation of Cable B. Cable A:10 km; Cable B:15 km; Short-circuit Power: 4333 MVA. a) First 0.4 ms; b) First 1.4 ms

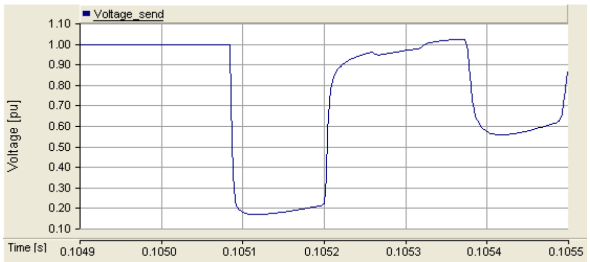

Figure 6.15 - Voltage in Cable A sending end for a short-circuit power of 4333 MVA

The method explained in the previous section works on the premise that the transient overvoltage peak would occur in the drawn V of Figure 6.12. In the previous example, due to a conjugation of an almost inexistent reflection coefficient in the joint point together with a large reflection at the *Cable A* sending end, the maximum peak occurs later, and the method may no longer be accurate.

This situation occurs due to a conjugation of several factors, which are not expected in a normal meshed system:

- Very few lines;
- Low reflection coefficients in the joint points, meaning that the cables are connected in series and there is almost no load/generation in those points;

This problem is expected in weak systems with few nodes, and in that situation one could simply model the entire system [12].

However, the smaller the modelling area, the larger the reflection coefficient in the last modelled node.

Figure 6.16 shows a network reduction. To maintain the simplicity, the network is reduced from one busbar depth to one cable.

The *Eq. B* represents the lower/higher voltage levels connected to the node. If the node's only connection is to lines at the same voltage level, *Eq. B* does not exist. The *Eq. A* represents the entire equivalent network seen from the *Cable A* sending end.

The *Eq. C* is the parallel of *Eq. B* with the series of *Eq. A* with *Cable A*. Thus, the impedance of *Eq. C* is always lower than the impedance of *Eq. A*. The exception is for an *Eq. B* non-existent; in that situation the impedance of *Eq. C* is equal to the sum of impedance of *Eq. A* with the impedance of *Cable A*.

The smaller the equivalent impedance, the larger the wave reflection. Thus, the model with fewer nodes will have a larger reflection coefficient. In addition, the more complex the model, the later this reflection occurs and the more the wave is damped before the reflection reaches the receiving end of the cable being energised/re-energised.

Referring back to the example of Figure 6.14, this means that the voltage at point VII is higher in the model with fewer nodes. Thus, in principle, if an overvoltage does not occur after the expected point in the model calculated according to the method previously explained, it should also not be present in the more complex model, i.e. with more busbars.

There may, however, be some special configurations, more specifically areas with many short cables that may lead to a voltage build-up, where the previous explanation cannot be applied. Yet, such configurations should be unusual in a transmission network.

This reasoning is valid assuming there are no OHLs installed in the vicinity of the cable, which may lead to voltage magnification. This topic is analysed in section 6.3.5.

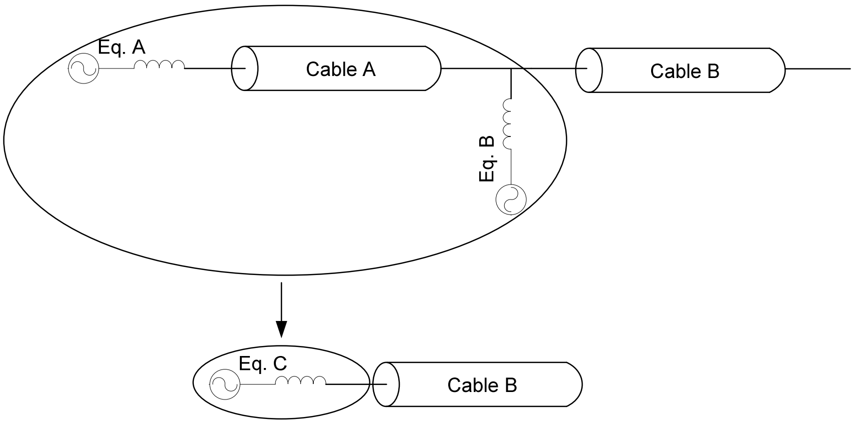

Figure 6.16 - Network reduction example

In summary, the inaccuracy should not be a problem as it is possible, in principle, to detect it if an overvoltage is observed after the expected point.

When an inaccuracy is detected, the calculation method should be run again, but with a different peak time. The new time should be the one corresponding to the maximum peak voltage in the possibly inaccurate model. It should be noted that this overvoltage may disappear when the simulation is run in the more complex model.

Section 6.3.4 will also present an adaptation of the method described in section 6.3.1, which can be used to minimise the likelihood of the inaccuracy occurring.

6.3.3 Cross-bonding modelling depth

Section 6.2 demonstrated the importance of having an accurate modelling of the cross-bonded sections for some of the simulations. Besides it being necessary to model all the cross-bonded sections of the switched cable, it may be also necessary to model all cross-bonded sections of the neighbouring cables.

In a normal meshed system, the modelling of the cross-bonded section of the cable(s) adjacent to the cable being energised should not have a major influence on the results as the current flowing in the screens of those cables should not be very high. Nevertheless, inaccurate modelling of the cross-bonded sections could result in small inaccuracies in the simulation plots.

Figure 6.17 shows the voltage in the receiving end of the NVV-BDK cable for a re-energisation similar to the re-energisation shown in Figure 6.5. All three plot lines are for a model with a 2-busbar modelling depth, the difference lying in the modelling of one of the cable lines adjacent to the NVV-BDK cable.

The cable in question is installed between the NVV and HVO nodes over a total length of 8.6 km (refer to Figure 6.7 for a description of the system in the vicinity of the NVV node), and it is modelled in three different ways:

- Both-end bonding, i.e., one section of a total of 8.6 km (black line in Figure 6.17);
- One major cross-bonded section, i.e. three sections of 2,866 km each (red line in Figure 6.17);
- Two major cross-bonded sections, i.e. six sections of 1,433 km each (blue line in Figure 6.17);

The simulations in Figure 6.17 are not expected to have maximum accuracy (the previous section demonstrated that a four-busbar depth would be necessary to ensure accurate modelling), but to show that the modelling of the cross-bonded sections of the neighbouring cables can affect the simulation results, which it does. Thus, the cross-bonded sections of the neighbouring cables should be modelled, but again the question is whether all the cross-bonded sections should be modelled, as recommended in [12], or whether it is possible to simplify the model.

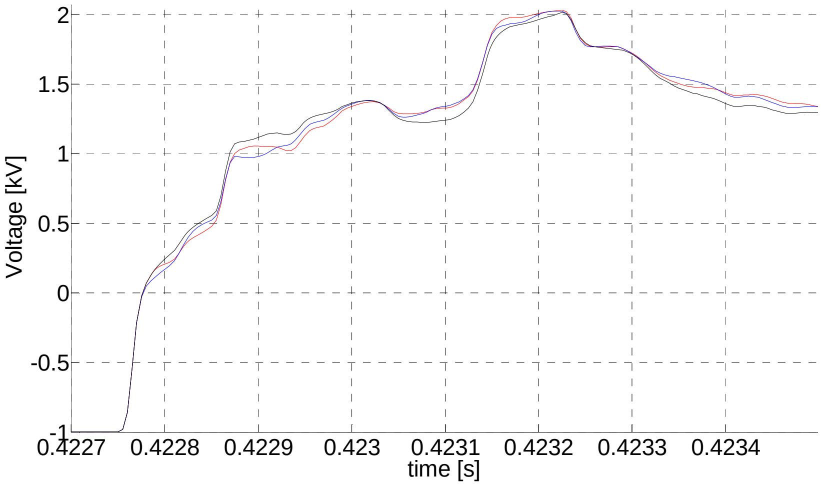

Figure 6.17 - Voltage in the cable receiving end during the restrike for different levels of detail. Black: Both-ends bondings; Red: One major cross-bonded section; Blue: Two major cross-bonded sections

The modelling of all the cross-bonded sections always results in maximum accuracy, but it may not be necessary. The wave speed in inter-sheath mode is lower than the wave speed in coaxial mode. Therefore, simpler modelling may be possible.

A method similar to the one proposed in the previous section can be used to determine which cross-bonding sections to model. For the particular example of a restrike in the NVV-BDK cable it would be necessary to model all the cross-bonded sections of the system. Thus, another part of the network will be chosen to demonstrate the theory; in this way it is also possible to demonstrate once again the method used to calculate the minimum required modelling and to show an example of the inaccuracy problem referred to in section 6.3.2.

To exemplify the theory, a restrike is simulated in the STSV end of the STSV-LEM cable. To better observe the differences between the different models, the cable length is increased to 40.5 km.

The application of the modelling depth calculation method indicates that six busbars have to be modelled. As one of the busbar is connected to two transformers, a seventh busbar is added so that the transformers are included in the model. Figure 6.18 shows the single-line diagram of the model, while Figure 6.19 shows an equivalent diagram with the distance between the STSV node and the neighbouring nodes.

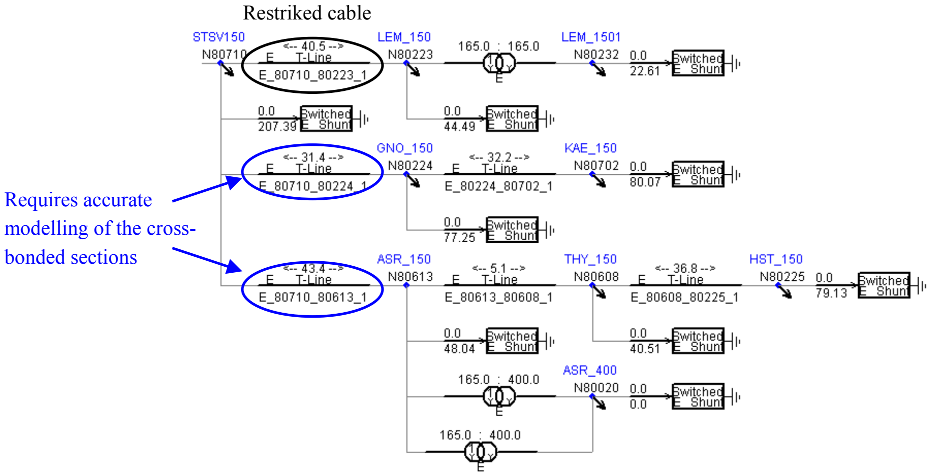

Figure 6.18 - Diagram of the simulated system

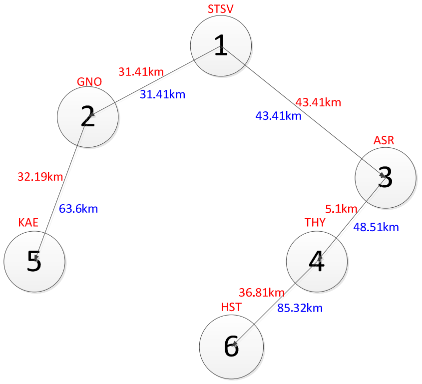

Figure 6.19 - Equivalent diagram of the system during the restrike with the distance between the restrike cable and the neighbouring nodes

To calculate the modelling required for the cross-bonded sections, the same method that was used to calculate the modelling depth is used, but substituting the coaxial mode speed for the inter-sheath mode speed, which is approximately 80 m/μs. According to the method, it is necessary to accurately model the cross-bonded sections in only two of the cables, more specifically the two cables adjacent to the restriked cable, the STSV-GNO and STSV-ASR lines.

To simplify the analysis and the comparison, the model is kept as simple as possible. Moreover, the real length of the cross-bonded sections is unknown. As a result, three different models are prepared:

- Model 1: All the cables in the model are modelled with one major cross-bonded section;
- Model 2: Equal to model 1, but the two cables adjacent to the STSV node (STSV-GNO and STSV-ASR) are modelled with two major cross-bonded sections;
- Model 3: Equal to model 2, but with two more cables (GNO-KAE and ASR-THY) modelled with two major cross-bonded sections.

According to the theory, model 1 has an insufficient level of detail, model 2 has the minimum level of detail required to have an accurate simulation of the maximum voltage peak, and model 3 has an excessive level of detail.

Figure 6.20 shows the voltage in the receiving end for the re-energisation of the STSV-LEM cable using models 1 and 2. Figure 6.21 shows the same phenomenon for models 2 and 3.

The results confirm the accuracy of the method. The differences between models 1 and 2 are visible before the peak, while the differences between models 2 and 3 are only visible after the peak.

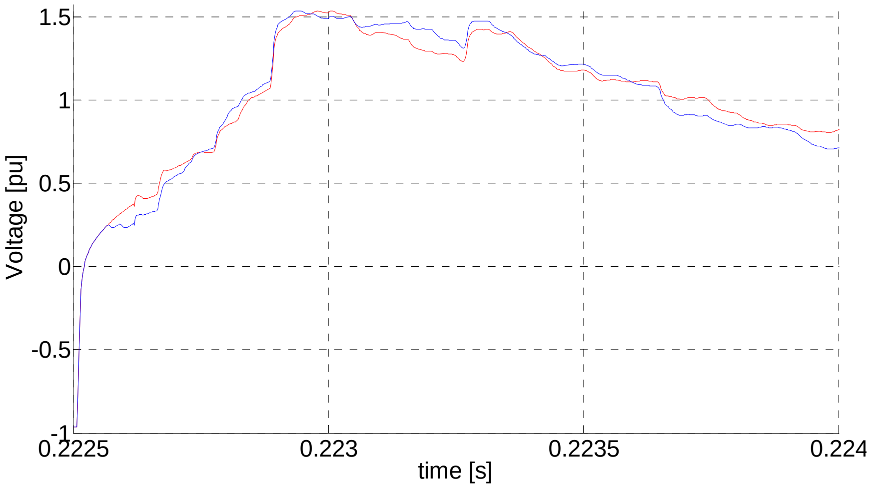

Figure 6.20 - Voltage in the cable receiving end during re-energisation. Red: Model 1; Blue: Model 2

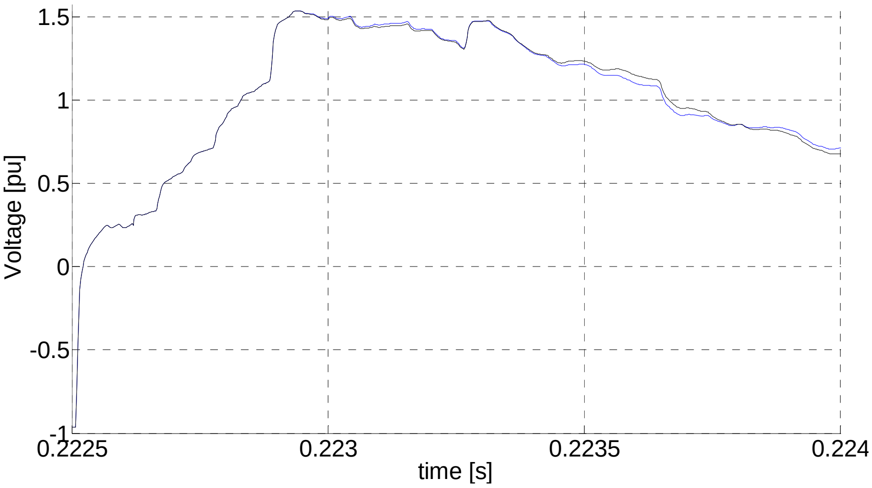

Figure 6.21 - Voltage in the cable receiving end during re-energisation. Blue: Model 2; Black: Model 3

6.3.4 Mix of FD-models with pi-models

Figure 6.20 and Figure 6.21 showed the voltage in the cable receiving end during the first 1.5 ms, but if the time span were extended, a higher overvoltage would be observed at a later instant. This overvoltage is a simulation inaccuracy, appearing due to a reflection in the KAE node (see Figure 6.18), for the reasons explained in section 6.3.2.

The overvoltage would disappear if the system were expanded to include more busbars as the reflection in the node would be lower. To demonstrate this situation, a model 4 is prepared, which contains all nodes up to a distance of three busbars from the STSV node. Figure 6.22 shows the equivalent diagram for model 4.

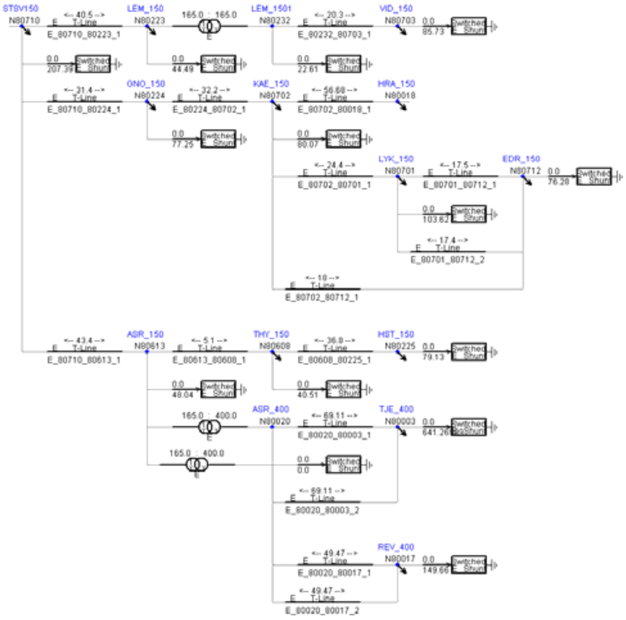

Figure 6.22 - Equivalent diagram for model 4

To better compare the results, two cables are modelled with two major cross-bonded sections, the same cables of model 2, and the remaining cables are modelled with one major cross-bonded section.

Figure 6.23 shows the voltage in the cable receiving end during re-energisation for models 2, 3 and 4. The model 2 and 3 simulations show an overvoltage between 0.2245 s and 0.225 s, which is a simulation error. The same overvoltage does not appear in model 4, which has more busbars.

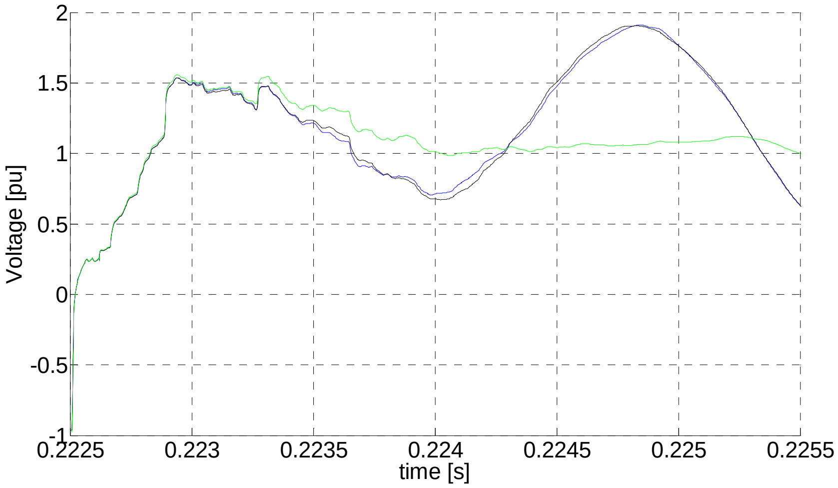

Figure 6.23 - Voltage in the cable receiving end during re-energisation. Blue: Model 2; Black: Model 3; Green: Model 4

Up to this point, a method has been presented and developed that can both be used to estimate the modelling depth and determine which cables need an accurate representation of the cross-bonded sections. Simultaneously, it was shown that the method may not be completely accurate due to large, inaccurate reflections in the model boundaries. Moreover, the simplest models can show overvoltages that are not really present; an example is shown in Figure 6.23.

The inaccuracy problem is solved in this section by developing the previous method into a more complex modelling technique.

The inaccuracy is a result of the reflections in the outermost nodes of the model. One could solve this problem by a combination of FD-models and lumped-parameter models. The addition of the lumped-parameter models increases both system complexity and simulation running time, but less so than if FD-models were used. A comparison between the running times when using FD-models or lumped-parameter models is made in section 6.3.6.

Like before, the cables adjacent to the energised/re-energised cable are modelled with maximum detail, i.e. FD-models and all the cross-bonded minor section with the exact lengths; as the distance increases, the cables are still modelled by means of FD-models but with only one equivalent major cross-bonded section or ideal cross-bonding. According to the method previously explained, the model would now be complete.

To avoid the high reflections that would lead to inaccurate results, a third level is added where the cables/lines are modelled by means of lumped-parameter models. This third level increases the simulation running time, but considerably less than if FD-models were used, and has a small influence on the total running time.

Figure 6.24 shows a diagram with the three levels, with the lines representing cables or overhead lines.

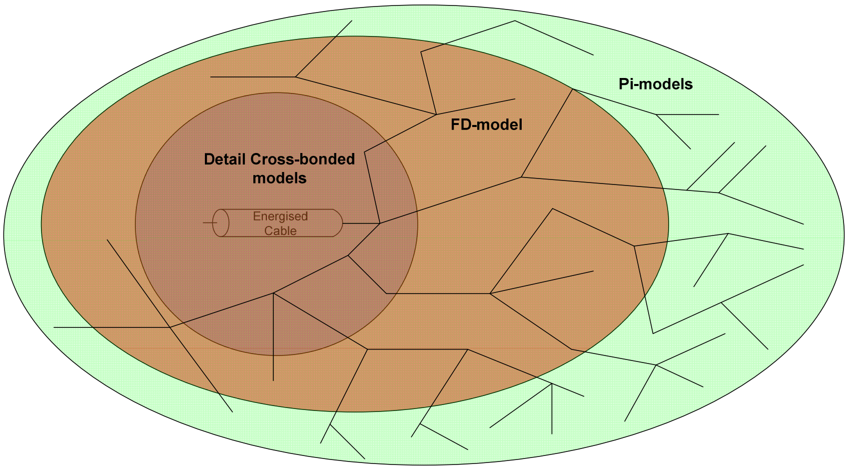

Figure 6.24 - Diagram for the different levels of detail

Example

A new model, designed according to the philosophy described, is used. The model uses FD-models for exactly the same cables as model 2 and represents the rest of the network through pi-models. This model is called model 5.

Figure 6.25 and Figure 6.26 show the voltage in the cable receiving end using models 2 and 5. The simulations confirm that the hybrid modelling used in model 5 yields better results:

- The waveforms are identical for both models during the first hundreds of microseconds;
- Because of the lower reflection coefficients, the voltage oscillations have lower amplitude in model 5. As a result, there is no overvoltage at 0.2248 s;

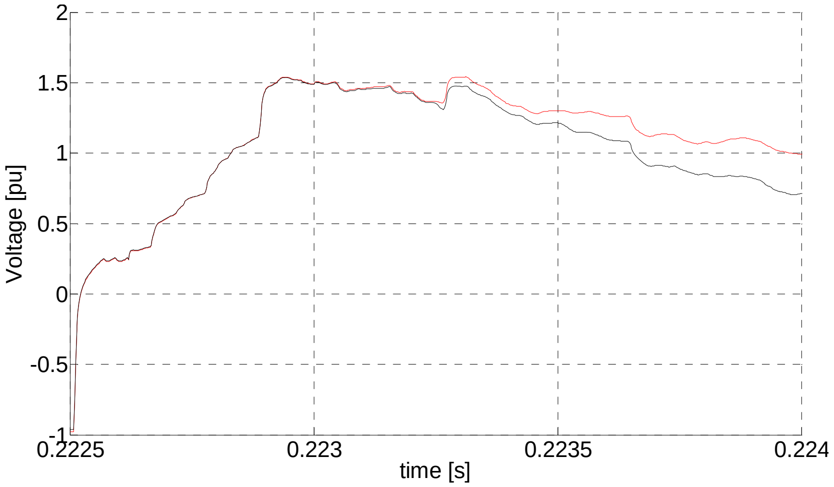

Figure 6.25 - Voltage in the cable receiving end during re-energisation. Black: Model 2; Red: Model 5

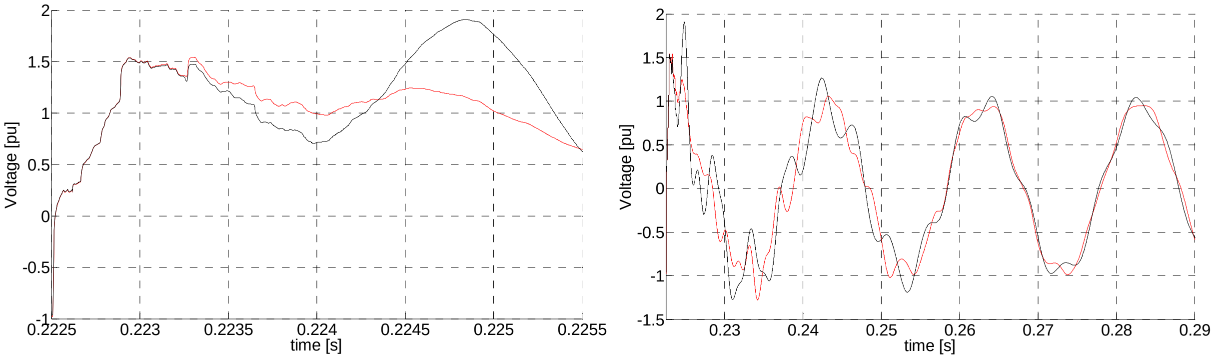

Figure 6.26 - Voltage in the cable receiving end during re-energisation. Black: Model 2; Red: Model 5

Depth of the lumped-parameter modelling

It is not possible to decide in advance the depth of this extra modelling. A good rule would be to repeat the process of section 6.3.2.

The simulation is run a first time with only the required busbars, and it is verified whether the peak overvoltage occurs after the expected instant. If it does, another level is added to the model, but using lumped parameters to model the lines. And the process is repeated.

A more efficient approach would be to model from the beginning an extra level by means of lumped parameters. This approach increases the user's trust in the results at the expense of only a small increase in the simulation running time. The process explained in the previous paragraph is then performed.

If one wants to be completely safe, the entire network can be modelled by means of lumped parameters as done in Figure 6.25, but this high detail is normally unnecessary.

6.3.5 Hybrid Cable-OHL systems

The presence of an OHL represents an added difficulty when estimating the modelling depth because of the reflections and refractions in the cable-OHL junctions.

Three different scenarios are possible:

- Scenario 1: The OHL(s) is/are inside the area to be modelled;
- Scenario 2: The OHL(s) is/are adjacent to the modelling area, i.e. the OHL is the first line not to be included in the model;
- Scenario 3: The OHL(s) is/are distant from the modelling area;

Scenario 1

There is no problem. The OHL(s) would always be included in the model.

Scenario 2

The OHL(s) and the cable(s) immediately adjacent to the OHL should be included in the model.

The voltage is magnified in this point. Thus, the OHL(s) and the cable(s) connected to it should be included in the model.

Scenario 3

The possible influence of the OHL on the waveform can be assessed by using a mix of FD models and pi models.

Three different versions of a same system and phenomenon are prepared. The cable is re-energised and according to the calculation method outlined in section 6.3.1 an FD model with up to only one-busbar depth is required. An OHL is installed at a distance of three busbars from the re-energised cable, and it is therefore neither part of the model nor adjacent to the last line of the model.

The cable installed between the OHL and the modelled area is a short cable of 5.1 km. Thus, the waveform is likely to be influenced by the OHL.

- Case A: 2030 without changes, i.e., only cables, and use of FD-models up to a distance of four busbars;
- Case B: Identical to Case A, but with the OHL;
- Case C: FD-models up to 1 busbar depth and the remaining network represented through lumped parameters models. System equivalent to Case A;
- Case D: FD-models up to 1 busbar depth and the remaining network represented through lumped parameters models. System equivalent to Case B;

Figure 6.27 shows the voltage during the re-energisation of the cable for the three cases.

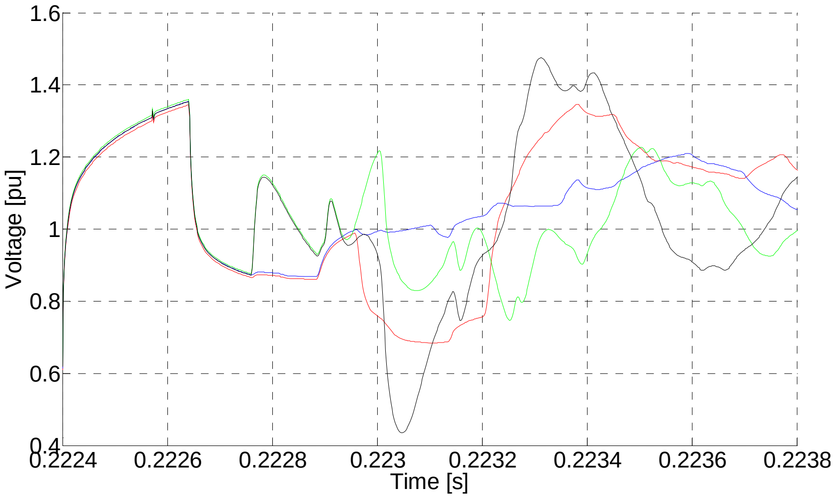

Figure 6.27 - Voltage in the cable receiving end during re-energisation. Blue: Case A; Red: Case B; green: Case C; Black; Case D

The comparison of Case A with Case B shows that the OHL has a noticeable influence on the voltage waveform and that it should be included in the model.

The influence of the OHL is even more exacerbated in the Case D waveform, which shows a higher voltage variation. The larger voltage variation is normally expected when using lumped-parameters models. Not only is there more damping in a FD-model than in an equivalent lumped-parameters model, because of skin and proximity effects, the voltage oscillation is also larger in the last, because of the capacitors and inductor.

According to the method suggested in the previous section, the original model would be the one of Case D. This model would indicate that a deeper modelling was required for this particular case because of the OHL. Thus, this modelling approach will normally indicate when it is necessary to expand the model to include the OHL and line(s) adjacent to it.

6.3.6 *Comparison of the simulation times for the different modelling approaches*

Several possible modelling techniques were presented in the previous sections. It was concluded that the one presenting the best results used a mix of FD-models and pi-models. This section compares both the making and running times. Five models are used in the comparison:

- Model A: The modelled busbars and cross-bonded sections are obtained through the method explained in the previous sections. This model is equal to model 2 mentioned in section 6.3.3;
- Model A.2: Equal to model A, but with pi models (used only to compare the running times, the simulation results are not accurate);
- Model B: FD models are used to model the same cables of model A. The rest of the transmission network (U≥150 kV) is modelled by means of pi models;
- Model C: FD models are used to model the same cables of model A .The rest of the transmission network (U≥150 kV) up to a distance of five busbars (i.e., five-busbar depth) is modelled by means of pi models;
- Model D: FD-models are used to model all the cables for a five busbars depth. I.e., this model contains the same busbars as Model C;

Figure 6.28 demonstrates the accuracy of models C and D. Both models contain more busbars than required, and a high accuracy is expected.

The differences between models C and D in Figure 6.28.b are the result of two different factors. The voltage before of the restrike is different in both models, resulting in a slightly higher peak overvoltage in model D. This voltage difference is a result of the larger capacitance of the FD models. For more details see section 3.2.

The travelling times in the FD models and lumped-parameter models are different, resulting in an increase in the difference between the models after the 0.2235 s.

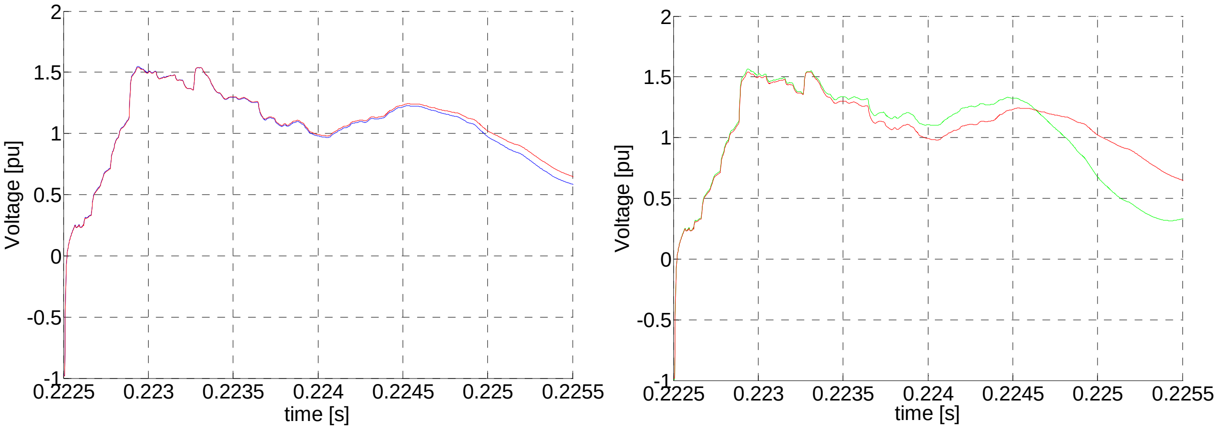

(a) (b)

Figure 6.28 - Voltage in the cable receiving end. a) Model B (red) and model C (blue); b) Model B (red) and model D (green)

Table 6.3 and Figure 6.29 show the making and running times of the models in PSCAD/EMTDC. By making time is understood the time required to write the system FORTRAN code and files, to write the input files for all the FD-model lines and do their fitting before running the simulation for the first time. The running time is the time required to run the simulation. In this example, the simulation is of 0.4 s and the time step 2 µs.

Table 6.3 - Making and running times for the different models (in seconds)

	Number of lines (FD-models)	Number of lines (pi-models)	Number of busbars	Make [s]	Run [s]
Model A	24	0	9	50	168
Model A.2	0	6	9	7	34
Model B	24	106	132	70	409
Model C	24	62	62	56	285
Model D	139*	0	62	303	1066

*25 are OHL

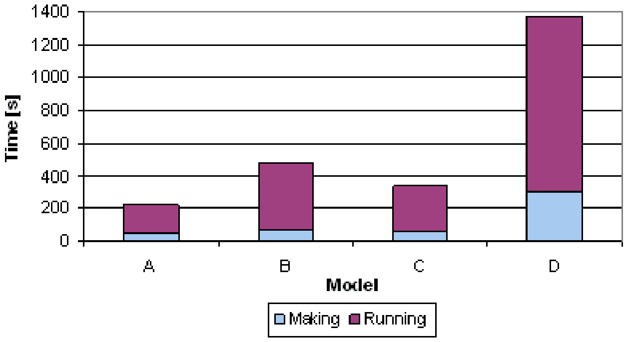

Figure 6.29 - Time required by the different models to make and to run the simulation

The comparison of the running times is not an easy task as they are influenced by more factors than just the number of lines in the system, e.g., the number of transformers, the extension of the equivalent network, the exchange of information between the modelling pages, etc….

Model A can be directly compared with model A.2 and model C with model D. These models have the same busbars and equivalent network, the only difference between them is that one of the models uses FD-models while the other uses pi-models.

Models A/A2 are simple models with few lines. Thus, the total running time is mostly a function of other elements, like transformers or generators, and not the lines. As a result, the running time as a function of the number of lines is almost identical for both the models.

The opposite situation occurs in the models C and D, which contain several dozens of lines. This situation is noticed in Table 6.4, which compares the running times when using FD-models and pi-models.

Table 6.4 - Running time as a function of the number of line section (in seconds)

	FD-models	**Pi-models**	**Relation**
Model A/A2	7	5.667	1.235
Model C/D	7.667	1.629	4.706

Therefore, better control of the parameters is required in order to compare the running times when using FD-models or pi-models. To do it, four models containing 10, 20, 30 and 40 lines, respectively, have been prepared specifically for this. The models have only an ideal voltage source, the lines are connected in series, and a voltmeter has been installed at the end. Table 6.5 shows the times required to both make and run the simulation

Table 6.5 - Making and running times for different number of lines (in seconds)

	Making		**Running**		
	FD-models	**Pi-models**	**FD-models**	**Pi-models**	**Relation**
10 Lines	20	1*	54	12	4.5
20 Lines	39	1*	101	16	6.3
30 Lines	59	1*	149	21	7.1
40 Lines	80	1*	194	25	7.76

*The values increases somewhat when the number of lines increases, but it was too fast to be measured

Making time

A line modelled by means of a lumped-parameter models neither needs an external file containing the line input parameters nor to do the fitting of the model. As a result, the making of the file when running the simulation for the first time is very fast and negligible.

The same is not the case when FD models are used. According to the results, it is necessary in average 2s, to create the files and do the fitting for each of the lines. Moreover, the fitting of the lines used in the simulation was relatively easy, requiring only six poles and six attempts. Different lengths or cable parameters may require a longer time.

Running time

For every 10 extra lines the running times increases by an average of 46.67 s and 4.33 s, for the FD models and pi models systems, respectively, which is equivalent to an increase in the simulation running time of 4.667 s for every extra section modelled by means of an FD model or 0.433 s if modelled by means of a lumped-parameter model. In other words, a simulation of this specific cable through an FD model is approximately ten times slower than if made by means of a lumped-parameter model.

A change in cable geometry or length would result in a change in the order of the fitting function, which would change the running time. Table 6.6 shows the running times for different cable lengths, to which a different number of poles of the propagation function correspond. The simulations are made for the system with 10 and 40 lines.

Table 6.6 - Running time for different number of lines and poles

Cable length	**Poles of the propagation function**	**10 Lines**	**40 Lines**
1km	**13**	47	167
5km	**17**	54	194
15km	**28**	73	270
30km	**44**	99	374

The increase in the simulation running time is on average 0.17s for each extra pole.

Conclusions

Cable simulation by means of an FD model requires a larger computational effort than if the same simulation was made using a lumped-parameter model, leading to a larger simulation time when using FD models.

The time required to simulate a cable depends on the number of poles in the FD model, but it can be several dozen times higher when using an FD model instead of the equivalent lumped-parameter model. This disparity represents a difference of many minutes when simulating a system with dozens or hundreds of cable sections.

The total simulation time depends not only on the number of lines, but also on the number of generators, transformers, shunt reactors and remaining equipment.

6.3.7 Method summary

This chapter explained how to estimate the required modelling depth. It was concluded that the best modelling approach for a simulation of energisation/re-energisation consists in using a model with three different levels of detail.

A first level with maximum detail, where the model includes all the minor cable sections and uses FD models.

A second level with high detail, where it is not necessary to model all the minor cable sections, instead an equivalent major-section is modelled or an ideal cross-bonding is used, but it is still necessary to use FD models.

A third level with a lower detail, where lumped-parameter models are used.

The modelling depth of the first and second levels is estimated by knowing the line lengths and the wave speeds. The estimation of the second level modelling depth will always contain all the busbars present at the first level, and, depending on the network configuration, some more. In the event of an equal modelling depth for the first and second levels, the second level is not used.

The third level is not always necessary, but it should be used to increase the trust in the results as it does not represent a substantial increase in the simulation running time. One suggestion is to have one busbar modelling depth for this level.

The guidelines for the modelling of the resonance phenomena are given in chapter 7.

6.4 Shunt reactor modelling

The standard [12] recommends including in the model only the shunt reactor inductance and saturation if the transient overvoltage amplitude is large enough.

The importance of having a precise modelling of the shunt reactor resistance and mutual coupling was previously demonstrated for some other phenomena, see sections 2.4.8, 4.5.3, 5.3 and 5.7.1.

6.4.1 Resistance

The resistance should always be included in the model. It does not represent a perceptible increase in the simulation running time, but it is necessary to the proper simulation of some phenomena.

The decaying ratio of the DC component depends of the different resistances present in the system, including the shunt reactor resistance. The decaying ratio of the voltage during the de-energisation of a cable and shunt reactor together is function of the cable and shunt reactor(s) resistances.

Consequently, it is concluded that the resistance of the shunt reactor should be included in the model.

6.4.2 Mutual coupling

Section 5.7 demonstrated the influence of the shunt reactor mutual coupling on the waveform during cable de-energisation. Thus, the shunt reactor mutual coupling should be included in the model when this phenomenon is simulated.

Section 5.2 showed that the mutual coupling is also noticed when a cable is energising. However, the influence on the waveform is minimum and need not be taken into account, because the use of synchronise switching.

Thus, one has to decide depending on the phenomenon being simulated. For a specific example see chapter 8.

7. Harmonic studies on cable-based grids

7.1 Introduction

A frequency spectrum calculated for a given point of a cable-based network is substantially different from a frequency spectrum calculated for the same point of an equivalent OHL-based network.

First, the cable network has its resonance points at lower frequencies. As a result, undesirable resonance phenomena are more likely to occur in a cable-based network.

Second, the magnitude of the higher frequencies is lower in the cable. Consequently, the higher frequencies are damped less in a cable-based network.

A frequency spectrum can also provide information about what transients to expect and is a valuable tool that can be used for insulation co-ordination studies.

7.2 Similarities between the frequency spectrums and the energisation transients

Section 6.3 provided guidelines that can be used to estimate which busbars to include in the simulation model, i.e., the modelling depth. The method was explained for normal energisations and re-energisations, but not for resonances.

In general, the energisation transient waveform can be predicted by plotting the frequency spectrum in the node to be energised.

To demonstrate this relation, the LEM-STSV cable line, which has already been used in previous chapters, is used again. The cable is connected to a phase-shift transformer in the LEM terminal and to a typical busbar in the STSV terminal. As a result, the energisation of the cable from the LEM end is expected be very different from the energisation of the cable from the STSV end.

Figure 7.1 shows the frequency spectrum as seen from both ends of the cable. The spectrum is obtained with the other end of the cable open.

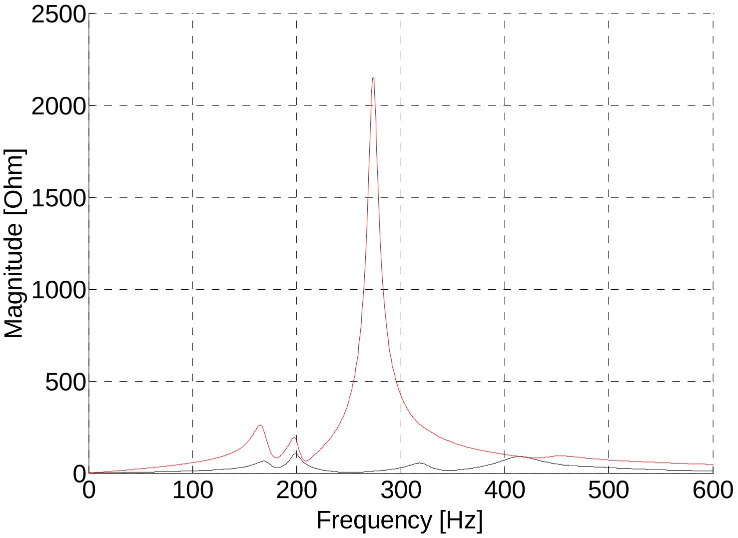

Figure 7.1 - Frequency spectrum. Red: Seen from the LEM node; Black: Seen from the STSV node

The two frequency spectrums are very distinct, with much larger resonance impedance at the LEM side. As a result, resonance is expected during the energisation of the cable by the LEM end.

To confirm this idea, the energisation of the cable at the LEM and STSV nodes is simulated. Figure 7.2 shows, for both types of energisation, the voltage in the cable receiving end for a phase connected at peak voltage. Different modelling depths are used for the energisation at LEM node:

- Model D1-L: 1 busbar modelling-depth, using FD-models and the rest of the network modelled by means of lumped-parameters models;
- Model D2-L: 2 busbar modelling-depth, using FD-models and the rest of the network modelled by means of lumped-parameters models;
- …..
- Model D5-L: 5 busbar modelling-depth, using FD-models and the rest of the network modelled by means of lumped-parameters models;

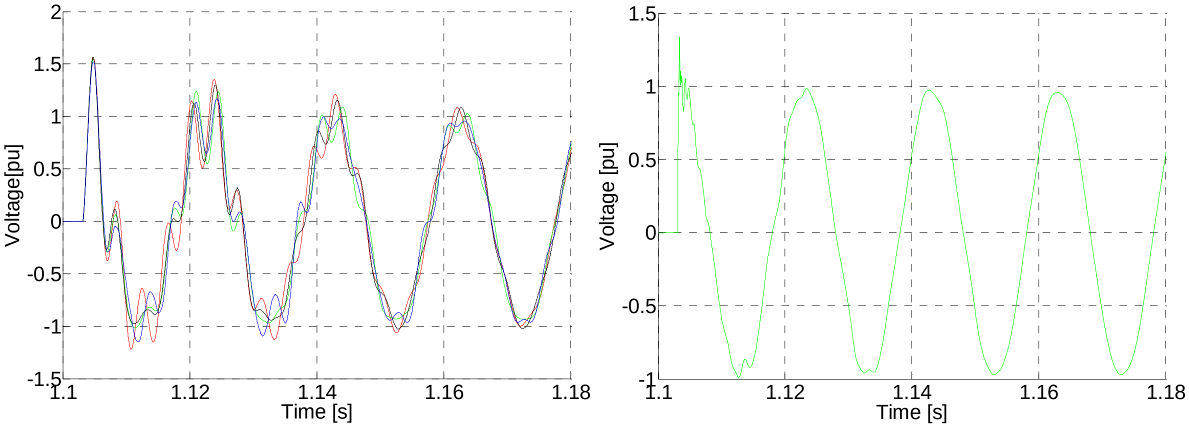

(a) (b)

Figure 7.2 - Energisation Transient plot. Red: Model D5-L; Orange: Model D4-l; Green: Model D3-L; Black: Model D2-L; Blue: Model D1-L. a) Energisation from the LEM node; b) Energisation from the STSV end

Observing Figure 7.2.a, the presence of one or more high frequency components during the first instants of the energisation, can be seen. It takes several cycles to damp these components, which indicates a resonance when energising the cable from the LEM end. Such behaviour is not seen in the energisation at the STSV end, which presents the typical waveform for cable energisation.

Figure 7.3.a shows for the different modelling depths the frequency spectrum calculated for the LEM node, with the cable open in the STSV end. Figure 7.3.b shows the FFT for the first 0.13 s of the energisation transient shown in Figure 7.2.a. The main interest of this analysis is the higher frequency components, and therefore the dominant 50 Hz component is not shown.

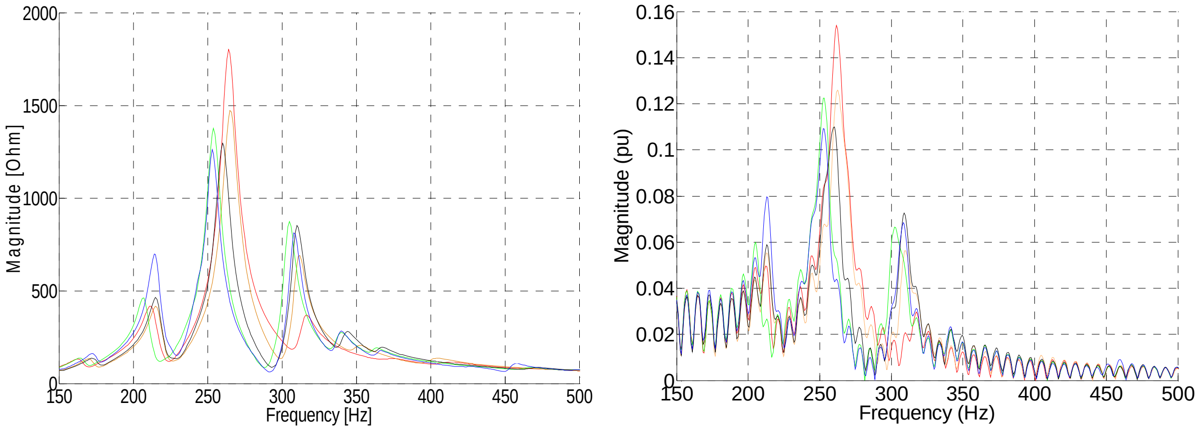

(a) (b)

Figure 7.3 - a) Frequency spectrum on the LEM end; b) Harmonic content of the voltage curve in the first 0.13 s after energisation. Red: Model D5-L; Orange: Model D4-L; Green: Model D3-L; Black: Model D2-L; Blue: Model D1-L

The comparison of Figure 7.3.a with Figure 7.3.b shows a strong correlation between the resonance frequencies of the frequency spectrum and the high frequency components present in the first moments of the cable energisation, inclusive in the magnitudes.

Because of the chosen modelling approach, use of a mix of FD-models and lumped-parameters, the frequency spectrums and waveforms are similar for all the models. In the next section it is shown that the use of simple models results in accuracy loss.

The first peak overvoltage, which is also the largest, has approximately the same magnitude for all five models. The differences between the models only start after the first peak, and one could say that the resonance should not influence the choice of model.

However, Figure 7.3.a shows that model D3-L and model D1-L have a resonance component close to the 5th harmonic. The 5th harmonic is not excited during cable energisation, and all models present similar results for the energisation transient. However, in the event of a 5th harmonic excitation the results could be substantial differences between models.

A current source generating a 50 A/250 Hz current is connected to the primary side of a phase transformer, which has the secondary connected to the LEM node.

Figure 7.4 and Figure 7.5 show for the new configuration with the current source and, for the different models, the voltage in the cable receiving end during the energisation transient. In the simulation the CB at the cable sending end is switched on at 1.1 s and the CB at the cable receiving end at 1.3 s.

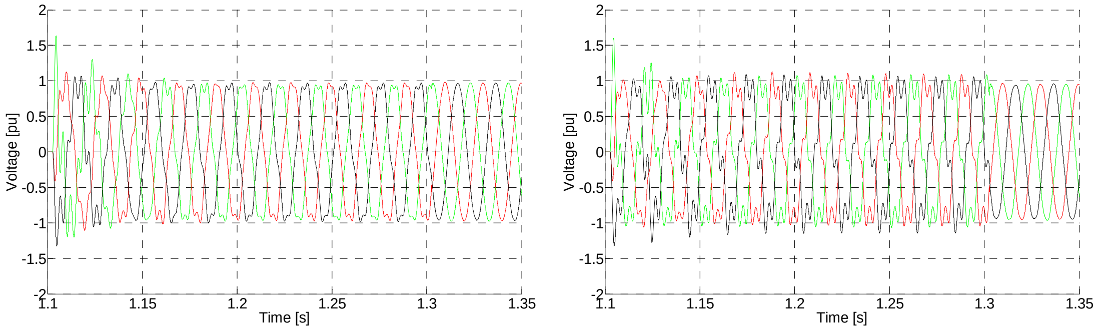

(a)

(b)

Figure 7.4 - Cable energisation with 5th harmonic excitation. a) Model D5-L; b) Model D3-L

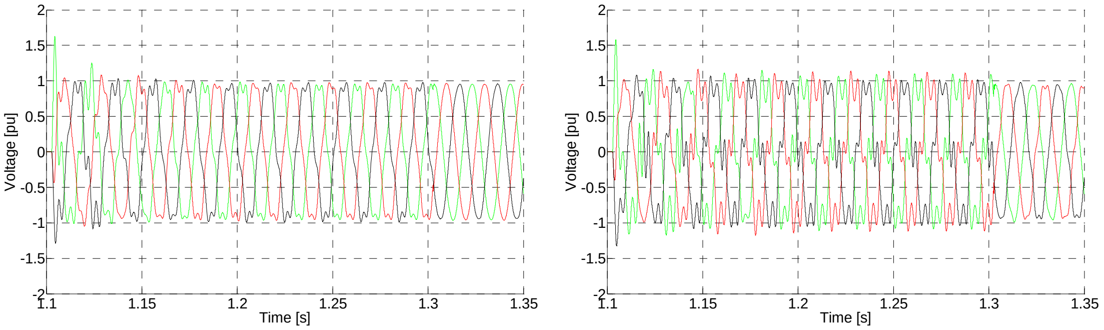

(a)

(b)

Figure 7.5 - Cable energisation with 5th harmonic excitation. a) Model D2-L; b) Model D1-L

Model D3-L and model D1-L have a resonance point very close to 250 Hz, and a larger distortion of the waveforms of these two models is therefore expected. The simulations confirm the expected results and show a larger voltage distortion for these two models.

It is important to note that in this case an increase in the modelling detail is not followed by an increase in the results accuracy. Using model D5-L as reference, it is seen that in the case of a 5th harmonic excitation the results provided by model D2-L are more accurate than the results obtained using model D3-L.

The choice of model is also important in case of a very large overvoltage, which can take several cycles to damp. In such situation it is necessary to have a good model in order to calculate the energy dissipated by the surge arresters.

7.3 Modelling approaches

Unless frequency scan field measurements are available, it is not feasible to do an accurate FD-network without designing the entire system by means of FD-models. Thus, simplifications are necessary.

The normal approach is to divide the system into two areas, a detailed study area and an external network area [90]. As an example, the method presented in section 6.3 of this thesis is a variation of this classic principle.

The conventional approach used for the modelling of the external network is to match the frequency response of the original network with a lumped-parameter network, as originally proposed in [90]. Besides not being completely exact, this approach has the problem that it is necessary to know the frequency response of the system, seen from the analysed area. This is easily done for a small system, but not for a large system, like is the West Danish network.

This thesis does not deal with the technical details of designing the external network. When necessary to do it, it is used the E-Tran software, which uses an N-Port equivalent. The method is described in [67].

As demonstrated in several parts of this thesis, the size of the detailed area, or in other words the modelling depth, influences the simulation results. Section 6.3 provided guidelines for the design of the detailed network when simulating energisation, re-energisation or faults, but not for resonance phenomena. The previous section demonstrated that for a resonance, the harmonic content of the voltage during energisation is correlated with the frequency spectrum.

The common approach in this case is outlined in [92]:

1. Design a detailed system up to at distance of two or three busbars from the point of interest and use an equivalent network for the rest of the grid;
2. Repeat the previous point, but increase the modelling depth of the detailed area in one busbar;
3. Compare the frequency spectrums for both systems;
4. Repeat the process until the difference between the spectrums is minimum around the frequencies of interest.

Similar to section 6.3 different modelling approaches can be used:

- The detailed area is modelled by means of FD-models. The external network is modelled by means of an equivalent network, using a N-ports or 2-ports equivalent;
- The entire system is modelled. The detailed area using FD-models and the external network by means of lumped-parameter models;

Besides comparing these two modelling approaches the influence of the cross-bonding sections in the frequency spectrum should also be taken into account, whose simplification may represent an important reduction in both simulation time and model complexity.

7.3.1 N-Ports equivalent network (Eq-Net) vs extended lumped-parameters network (L-Net)

Figure 7.6 to Figure 7.8 compare the frequency spectrums at the LEM node for the two modelling approaches previously described. The cables modelled by means of FD-models are the same in both models, the difference lies in the modelling of the remaining network.

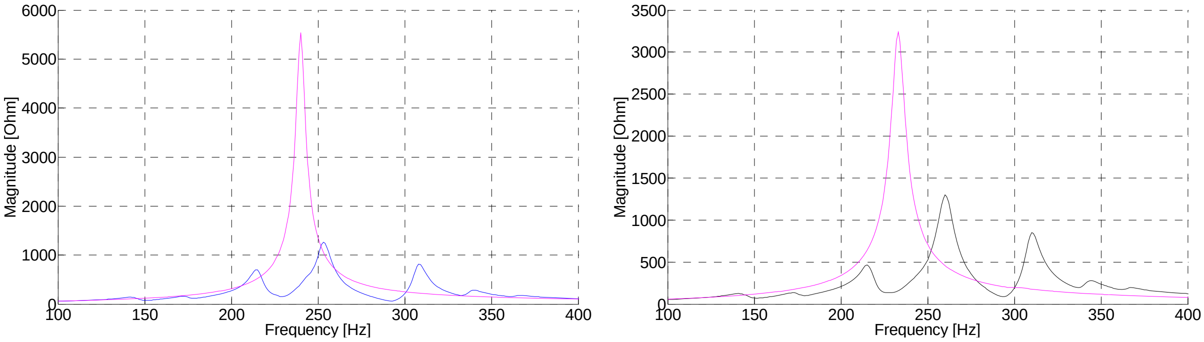

(a) (b)

Figure 7.6 - Frequency spectrums seen from the LEM node with the cable open in the STSV end. a) Blue: Model D1-L; Magenta: Model D1-Eq b) Black: Model D2-L; Magenta: Model D2-Eq

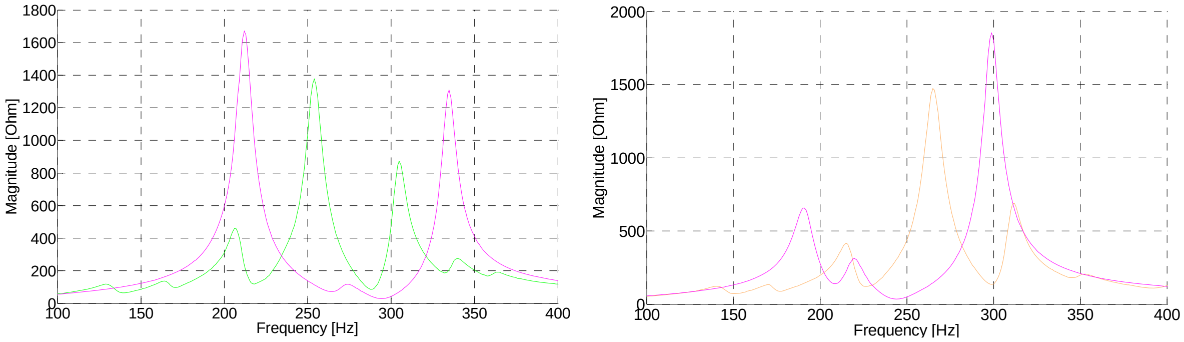

(a) (b)

Figure 7.7 - Frequency spectrums seen from the LEM node with the cable open in the STSV end. a) Green: Model D3-L; Magenta: Model D3-Eq b) Orange: Model D4-L; Magenta: Model D4-Eq

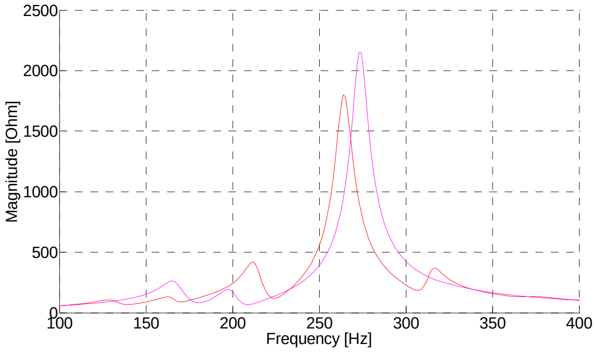

Figure 7.8 - Frequency spectrums seen from the LEM node with the cable open in the STSV end. Red: Model D5-L; Magenta: Model D1-Eq

The observation of the frequency spectrums leads to the following conclusions:

1. The number of resonance frequencies of the L-Net is equal or superior to the number of resonance frequencies of the equivalent Eq-Net;
2. The magnitude of the impedance at the main resonance frequency (~250 Hz) is larger in the Eq-Net than in the equivalent L-Net;
3. The modelling depth has more influence on the Eq-Net frequency spectrum than on the L-Net frequency spectrum;
4. Only the model D5 presents similar results for both modelling approaches.

The Eq-Net is always less complex than the corresponding L-Net, with the notable exception of the limit case when the entire network is modelled. As an example, the detail area of the D1-Eq network consists only of a cable and a phase-shift transformer, as shown in Figure 7.9. This simple configuration results in fewer resonance frequencies as there are only two elements interacting with each other and a larger magnitude at the resonance frequency.

As the modelling depth increases, the number of lines and other elements in the model also increases, followed by an increase in the size of the N-port external equivalent network. As a result, an increasing number of resonance points is expected.

This behaviour is not a rule as the spectrum depends on the network configuration and in some situations this may not happen; an example is model D3-eq in Figure 7.7. These situations are expected to be more common in cable-based networks, which due to high cable capacitances have lower resonance frequencies and dampings

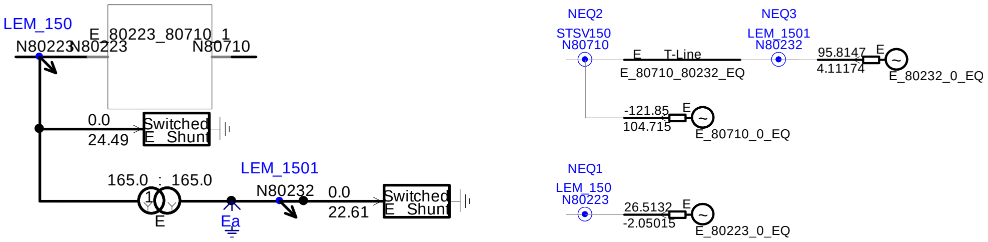

(a) (b)

Figure 7.9 - D1-Eq system. a) Detailed network (FD-model); b) External network (lumped parameters)

The L-Net contains all network generators, transformers and loads, and the only difference when the modelling depth increases lies in the modelling of some of the cables, which changes from lumped-parameters models to FD-models. Thus, an increase in the modelling depth does not affect the frequency spectrum of the L-Net as much as in the Eq-Net.

A corollary of the previous paragraph is that the Eq-Net model may require the modelling of a large area of the network in order to present accurate results.

7.3.2 Conclusion

The L-Net has a much larger accuracy than the Eq-Net, having also the advantage of being less sensitive to changes in the modelling depth. These conclusions were expected and are not surprising.

The difference is that in this case the frequency studies are being made for cable-based networks, instead of the usual OHL-based networks. The simulation of a cable by means of a FD-model is more time consuming than the simulation of an OHL. As a result, the relative increase in the simulation time when using a L-Net instead of an Eq-Net is small for a detail area with several dozens of cables, as demonstrated in section 6.3.6. As an example, the D2-L presented more accurate results than the D5-Eq model and it had a lower simulation time.

Consequently, it is advised to use the L-Net instead of an Eq-Net as it will yield more accurate results at the expense of a relative small increase in the simulation time.

The required modelling depth can be obtained using the classic method of increasing the number of cables modelled by means of FD models until the frequency spectrum stops changing. As a starting point, the procedure described in section 6.3 can be used.

7.4 Comparison of frequency spectrum for a cable-based and an OHL-based system

The 2030 West Danish network is a hybrid system that uses cables at 150 kV and OHL at 400 kV.

In many countries such system would be composed of OHLs only. Therefore, it is interesting to compare the frequency spectrum for the two systems.

The Danish TSO also plans to substitute in a distant future most of the 400kV OHL for cables. Thus, the frequency spectrum is also compared with an example where all network is undergrounded. The networks are described in chapters 3.3 and 3.4.

Figure 7.10 shows the three frequency spectrums.

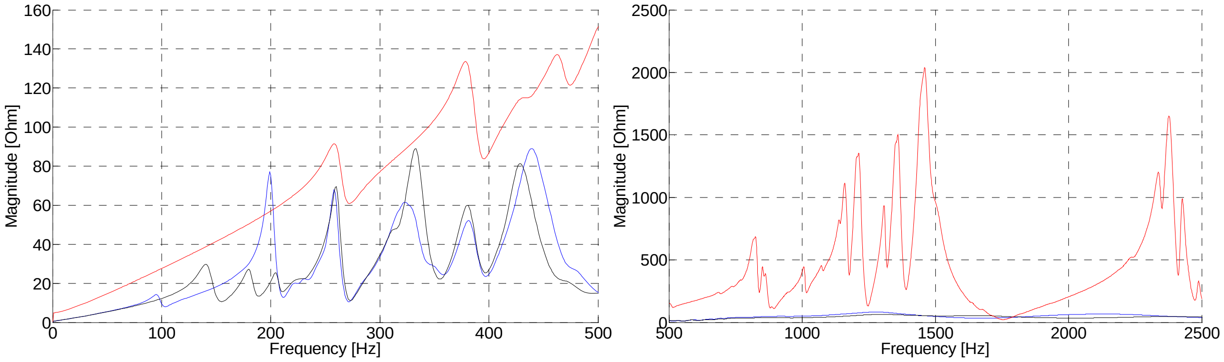

Figure 7.10 - Frequency spectrums seen from the LEM node using the model D5-L. Red: Pure-OHL network; Blue: Pure-cable network; Black: 2030 network

The frequency spectrum is obtained for a point in the 150kV network. Thus, the 2030 network and pure-cable network frequency spectrums are similar, while the pure-OHL network is completely different. These results are expected as the area around the simulated node consists of cables.
It can also be seen that the magnitude of the impedance is lower in the pure-cable and 2030 networks than in the pure-OHL network. Thus, a harmonic propagates deeper in a cable-based network than in an equivalent OHL-based network, because of the lower damping of the former.

The previous frequency spectrums are for different reactive power compensation schemes, as explained in chapters 3.3 and 3.4. Thus, the differences between the frequency spectrums are both the result of changes in the lines and in the shunt reactors/capacitor bank.
Figure 7.11 repeats the simulations, but using the same reactive power compensation scheme to all, more precisely the one of the 2030 network. The conclusions given to Figure 7.10 continue to be valid.

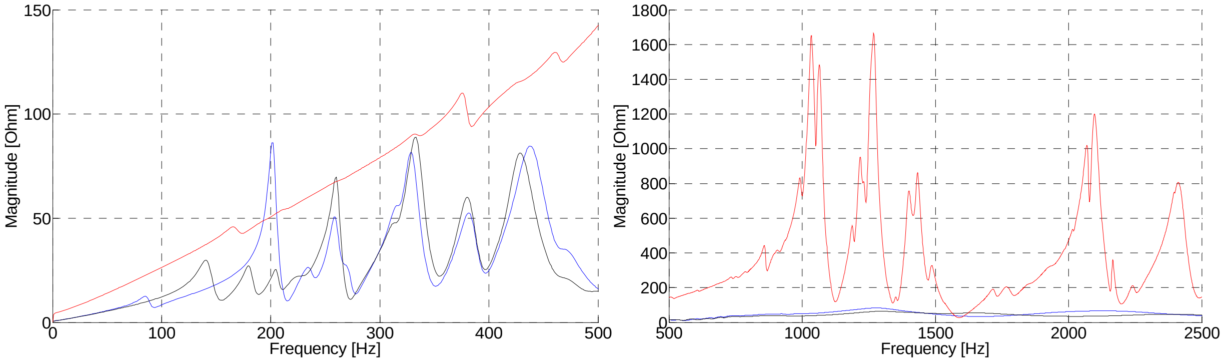

Figure 7.11 - Frequency spectrums seen from the LEM node using the model D5-L and the same reactive power compensation scheme. Red: Pure-OHL network; Blue: Pure-cable network; Black: 2030 network

Figure 7.12 shows the frequency spectrum seen from a 400 kV level node. In this case, the 2030 network frequency spectrum is similar to the frequency spectrum of the pure-OHL network instead of the one of the pure-cable network, especially when the correct reactive power compensation scheme has been chosen.

The 400 kV lines of the 2030 network are OHLs. Thus, a similarity between the 2030 network and the pure-OHL network frequency spectrums is expected.

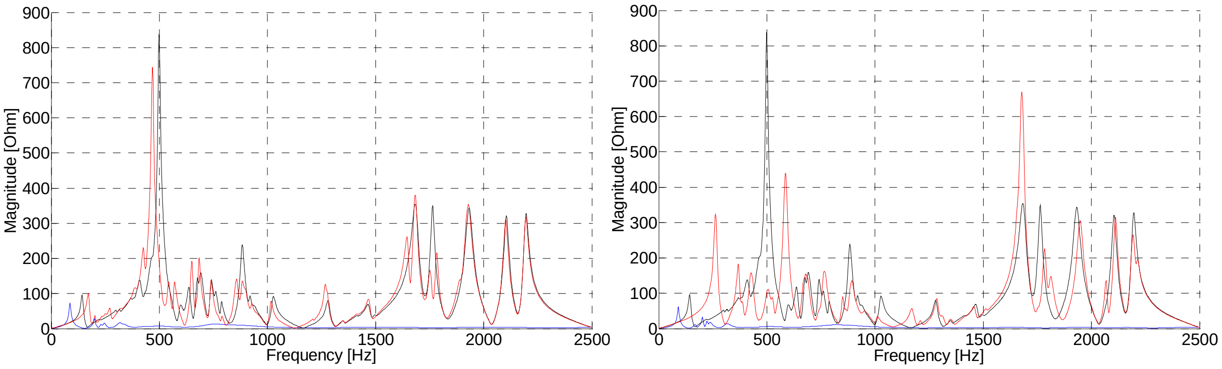

(a) (b)

Figure 7.12 - Frequency spectrums seen from the TJE node using the model D3-L. Red: Pure-OHL network; Blue: Pure-cable network; Black: 2030 network. a) Correct compensation schemes; b) Same compensation scheme

7.5 Influence of the cross-bonded sections on the spectrum

The influence of the cross-bonded sections on the frequency spectrum should also be ascertained as the bonding can shift the resonance frequencies.

For the first examples, the 2030 West Denmark network is used. The results are later validated through theoretical equations.

For different cable bonding configurations the frequency spectrum seen for the LEM node is calculated using the D2-Eq system.

It is known that this model does not yield accurate results, but the objective of the study is to determine the differences between having and not having a cross-bonded cable. Thus, it is better to use a simple model.

Four different bonding configurations of the LEM-STSV cable have been prepared:

- Both-Ends Bonding
- Cross-bonding
  - 1 Major-section
  - 6 Major-sections
  - 12 Major-sections

The frequency spectrums obtained by means of simulations in PSCAD/EMTDC are compared with simulations made in Matlab, which calculates the frequency-dependent series impedance and shunt admittance matrices of the cable. The Matlab code assumes very few simplifications and can also be used to validate the PSCAD/EMTDC models. The description of the two matrices and the Matlab code are available in Appendix L.

7.5.1 Comparison of both-ends bonding with cross-bonded cable with 12 major-sections

Figure 7.13 shows the impedance spectrum considering the LEM-STSV cable as being bonded in both-ends or cross-bonded with twelve major sections.

The resonance frequency seen around 250 Hz is the cable-transformer resonance. The resonance points seen in the second figure for frequencies higher than 600 Hz are the cable resonance frequencies.

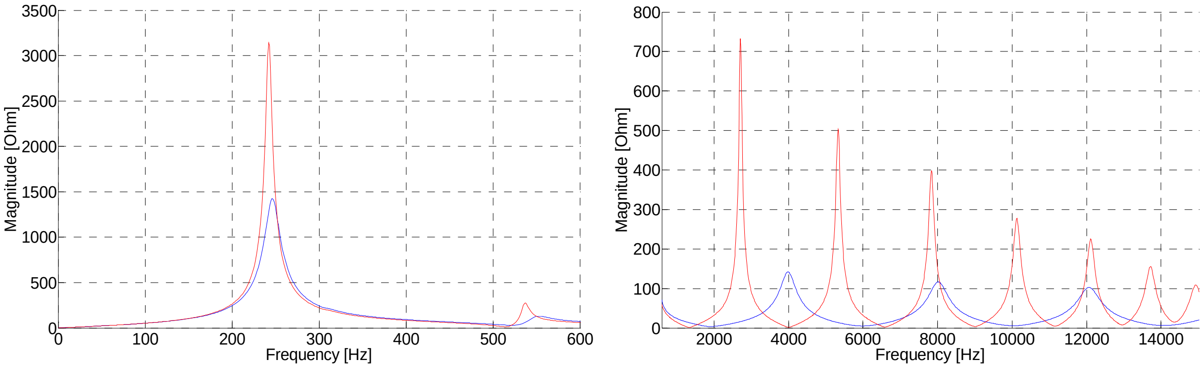

Figure 7.13 - Frequency spectrums seen from the LEM node with the cable open in the STSV end. Red: Cross-bonded with 12 major-sections; Blue: Both-ends bonding

The first resonance point is at approximately 250 Hz or the 5th harmonic. At this frequency, there is a minimum difference between the impedances of the two bonding configurations, and the resonance frequency is almost the same for both configurations.

As the frequency increases, the differences between the two bondings start to become evident:

- The cross-bonded cable has more resonance points than the cable bonded in both-ends;
- The magnitude of the cross-bonded cable impedance is larger at the parallel resonance points and lower at the series resonance points, when compared with the cable bonded in both-ends;

To explain these results, the Matlab code developed in Appendix L is used. Figure 7.14 compares the results obtained using the Matlab code with the PSCAD/EMTDC simulations.

The results for the both-ends bonded cable are identical, but differences are found in the cross-bonded cable as the frequency increases. These differences are the result of a limited number of major sections in the PSCAD/EMTDC model and are addressed in the following section.

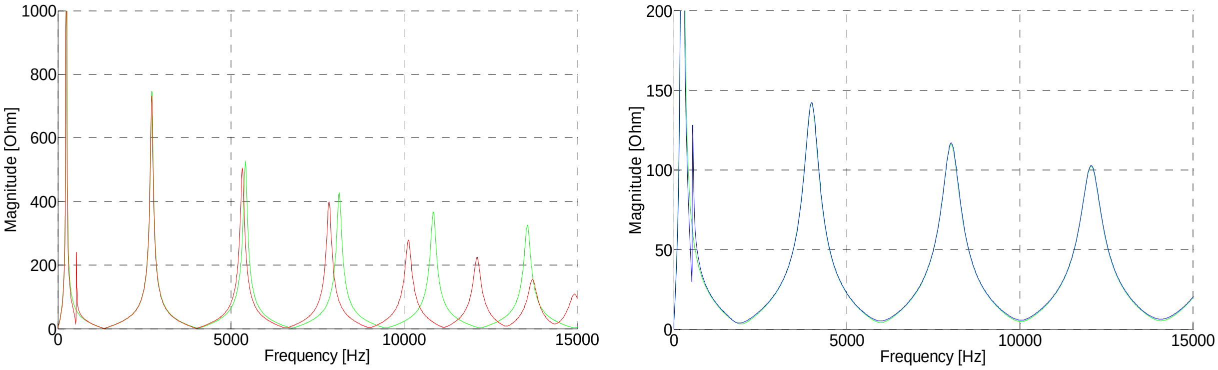

(a) (b)

Figure 7.14 - Comparison of the frequency spectrum in PSCAD/EMTDC and Matlab simulation (green curve). a) Cross-bonded cable with 12 major-sections; b) Both-ends bonding

The conductor positive series inductance is larger in a cross-bonded cable than in an equivalent both-end bonded cable, while the series resistance is larger for a both-end bonded cable. The conductor positive shunt admittance is equal for both bonding configurations.

These differences in the series impedance result in lower resonance frequencies for a cross-bonded cable. They are also responsible for the larger impedance magnitude at the parallel resonance points and lower impedance magnitude at the series resonance points of the cross-bonded cable, when compared with the cable bonded in both-ends.

From a physical point of view the larger inductance in the cross-bonded cable is result of having a lower current circulating in the screen when compared with the both-end bonded cable. As the current is lower, the magnetic field induced by screen current is also lower, resulting in a lower inductance value.

The mathematical demonstration of the conclusions presented is done in Appendix M.

7.5.2 Comparison of cross-bonded cables with different number of sections

The comparison done in Figure 7.14.a shows that for the cross-bonded cable, the PSCAD/EMTDC simulations results only match the equations results for the first resonance points. The discrepancy is the result of the limited number of cross-sections in the PSCAD/EMTDC, as opposed to the ideal cross-bonding in the equations.

Figure 7.15 compares the frequency spectrum for the D2-eq system for a LEM-STSV cable with a different number of major cross-bonded sections.

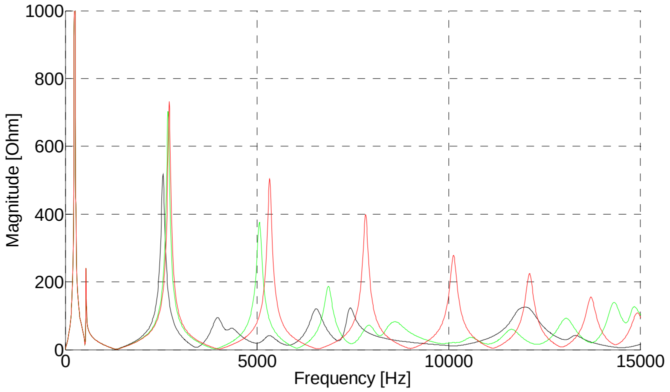

Figure 7.15 - Comparison of the frequency spectrum in PSCAD/EMTDC. Black: One major cross-bonded sections; Green: Six major cross-bonded sections; Red: 12 major cross-bonded sections;

The higher the number of cross-bonded sections, the closer the results are to the ideal cross-bonding. Using the 12 major cross-bonded sections scenario as reference, it is seen that the cable with only one major section starts to diverge after the first parallel resonance point (~2.5 kHz) and the one with 6 major sections after the third parallel resonance point (~7k Hz).
After these frequencies, the respective spectrums present an unexpected behaviour. They have more resonance points, whose magnitude does not always decrease with the increase in frequency.

This behaviour is the result of the larger imbalance present when less cable sections are used. Figure 7.16 shows the voltage in the cable receiving end when injecting a 134.5kV peak voltage in the sending end at different frequencies. The figure shows the results for a cable bonded in both-ends and an equivalent cable with a major cross-bonded section.

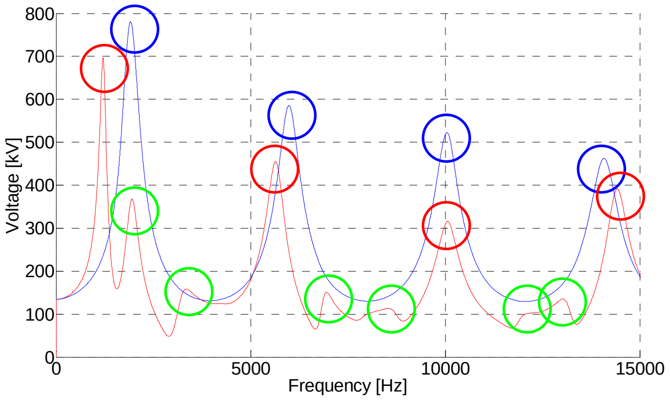

Figure 7.16 - Voltage in the cable receiving end for a 134.5 kV peak voltage in the cable sending end. Blue: Bonded in both-ends; Red: One major cross-bonded section

When observing the cross-bonded cable spectrum it can be seen that between two larger peak voltages (red circles) two smaller overvoltages (green circles) are present, being the result of the two crossing of the screens.

The higher the number of major cable cross-bonded sections, the more balanced the cable and the coupling are. As a result, the entire cable behaves like a uniform single section; if only one major cross-bonded section is present, the cable behaves almost like three different cables.

7.5.3 Zero-Sequence

Most of the zero-sequence components of a buried cable return through the screen of the cable [93]. As a result, the current in the screen is roughly equal to the current in the conductor for any random given point of the cable.

Consequently, there should not be almost no current flowing into the ground at the grounding points, and the frequency spectrums should be the same for all types of bonding.

Figure 7.17 shows the frequency spectrums for several bonding configurations.

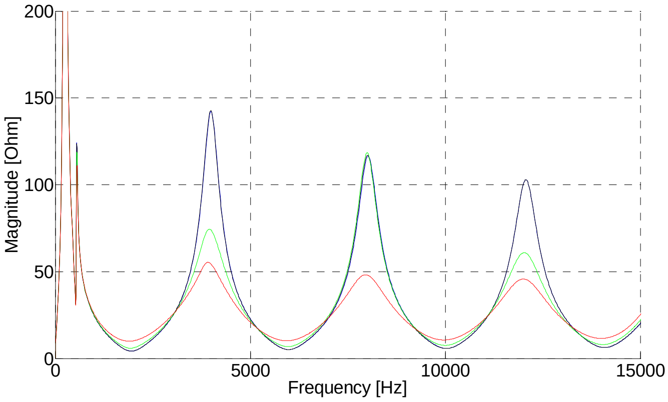

Figure 7.17 - Frequency spectrum for the D2-eq system. Blue: Both-ends bondings; Black: One major cross-bonded section; Green: Six major cross-bonded sections; Red: 12 major cross-bonded sections

The resonance frequencies are the same for all the examples because of the reasons explained in the previous two paragraphs. The both-end bonded cable and the cable with only one major cross-bonded section have the same magnitude at all times, but the same it not the case for a cable with more cross-bonded sections that have a different magnitude for some of the resonance frequencies.

Figure 7.18 shows the line reactance as a function of the length, using the line wavelength as reference. The reactance of an open line is not the same at all points of the line

A cable with multiple cross-bonded sections also has multiple grounding points. If one of those grounding points corresponds to a point of the line where the reactance has a very high value, the current in the screen flows to the ground at that point, changing the magnitude of the impedance.

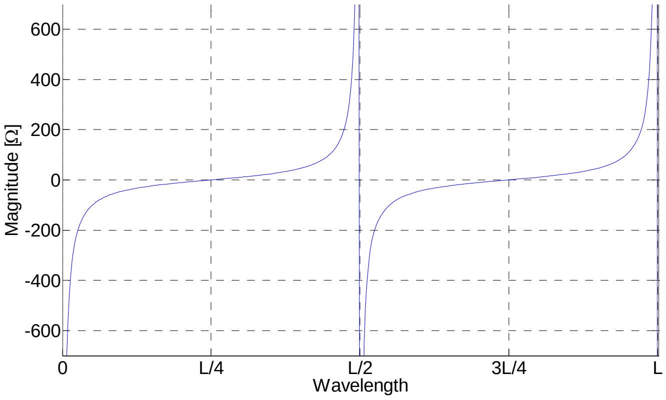

Figure 7.18 - Reactance of an open line as a function of the wavelength

Example

The example is given for the cable with six major cross-bonded sections. For a parallel resonance situation the maximum current in the cable occurs for the point(s) that are equal to or a multiple of the cable wavelength, i.e., λ/2; 3λ/2; 5λ/2 ….

Figure 7.19 shows the relative current along the cable for the first two parallel resonance frequencies. For the first resonance frequency the maximum current is in the middle of the cable line. For the second resonance frequency the peak currents are in the first and last quarter of the cable line.

In the first case the screen is grounded in a point corresponding to maximum current, which means a very high reactance in that point. Thus the current flows to the ground in that point, but this does not happen in the second case, which have the peak currents in the middle point between two grounds.

As a consequence of this, and using the both-end bonded cable as reference, the magnitude of the impedance is smaller for the first resonance point (~4 kHz) and equal for the second resonance point (~8 kHz).

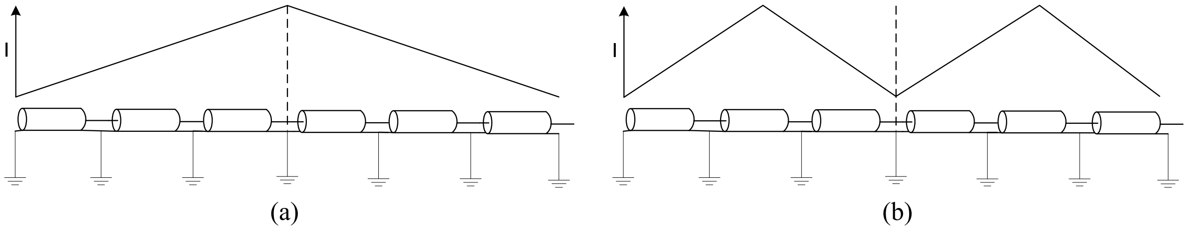

(a) (b)

Figure 7.19 - Relative current along a cable with six major cross-bonded sections. a) 1st parallel resonance point (~4 kHz); 2nd parallel resonance point (~8 kHz)

It should be noted that the presence of other conductors near the cable can change the results presented in this section as these conductors present a possible path for the zero-sequence components.

7.6 Sensitivity analysis

The frequency spectrum is very sensitive to the cable parameters. The existing standards [94] and [95] allow a deviation in the thickness of some of the cable layers of up to 10%. It is therefore important to assess how the spectrum is affected by the use of inaccurate values.

The thickness of the cable layers is changed and the frequency spectrum calculated:

- Conductor thickness -> Changes the conductor resistivity as well;
- Insulation thickness -> Changes the insulation permittivity as well;
- Screen thickness;
- Outer insulation thickness;

The layers are analysed separately, meaning that for a deviation in the conductor thickness, only the conductor thickness is changed. However, an increase in the conductor thickness also represents a change in conductor resistivity (see section 2.3.5) and in the cable *xy* position.

A deviation in the resistivities of the conductor/screen and in the permittivity of the insulations has also been simulated, keeping all thicknesses unchanged.

The standard limits the thickness deviation to a maximum of 10%, but in this analysis a maximum of 20% is considered, allowing the gathering of more data. The simulated deviations are of ±1%, ±5%, ±10%, ±15% and ±20%. The frequency spectrums range between 1 Hz and 1 kHz (20th harmonic), with a step of 1 Hz.

The thicknesses of the several layers and the different resistivity and permittivity values are available in Appendix K.

7.6.1 Extended lumped-parameter network

The system was previously analysed in section 7.2 and is expected to have a main resonance frequency around the 5th harmonic (250 Hz).

Figure 7.20 shows the frequency spectrum for different insulation thicknesses when using model D1-L. The increase in the insulation thickness results in a decrease in the capacitance. Thus, the resonance frequency increases when the insulation thickness increases and decreases when the thickness decreases.

A change in the thickness of the cable insulation will result in larger changes at the ~250 Hz resonance frequency than at the other resonance frequencies. The ~250 Hz resonance frequency is the direct result of the cable-transformer interaction. Consequently, a change in the cable is more noticeable at the ~250 Hz resonance frequency.

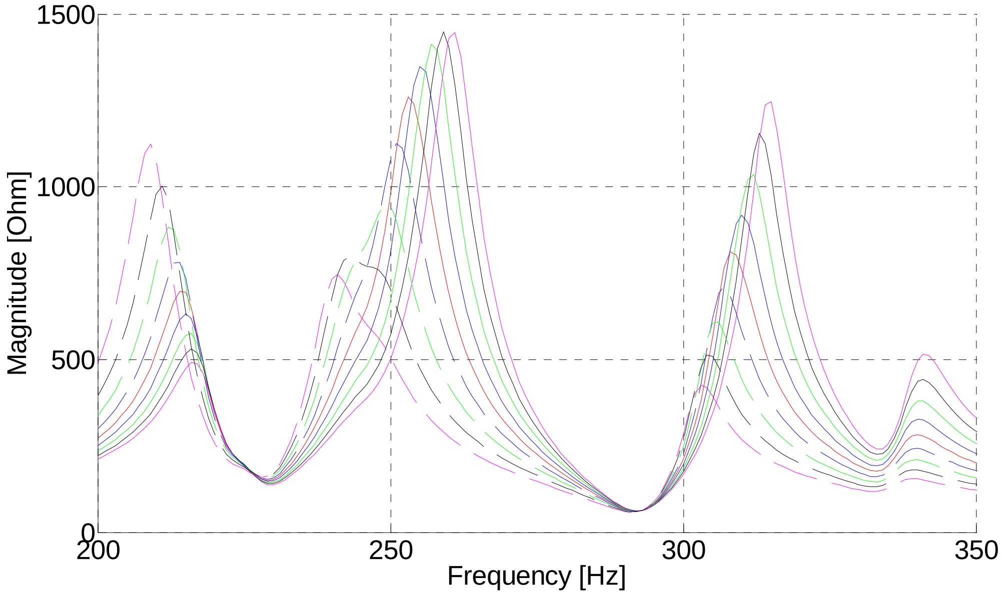

Figure 7.20 - Frequency spectrum for different insulation thicknesses for the model D1-L. Red: Reference; Blue: 5%; Green: 10%; Black: 15%; Magenta: 20%. Solid lines: Thickness increases; Dashed Lines: Thickness decreases

The behaviour of the impedance magnitude is not so linear. It increases, for example, when the thickness decreases for the first resonance point (~210 Hz), but it has the opposite behaviour for the main resonance point (~250 Hz).

The increase of the capacitance is normally followed by a decrease in the impedance at resonance frequency, e.g., a parallel *LC* circuit. The opposite behaviour at ~210 Hz is explained by a high capacitance and inductance of the network behind the transformer, including the transformer at that specific frequency.

Resonance frequency variations

Figure 7.21 shows the frequency variation of the three resonance points as a function of a deviation in the thickness of the conductor or insulation.

The screen and outer insulation of the cable have a negligible impact on the capacitance of a bonded cable, ideally none [88]. As a result, the resonance frequency is barely affected by changes in the thickness of these two layers of the cable.

As expected, the resonance frequency with larger variation is f~250Hz and the variation is larger for a deviation in the insulation thickness than in the conductor thickness, because of the larger change in the capacitance values when changing the thickness of the insulation.

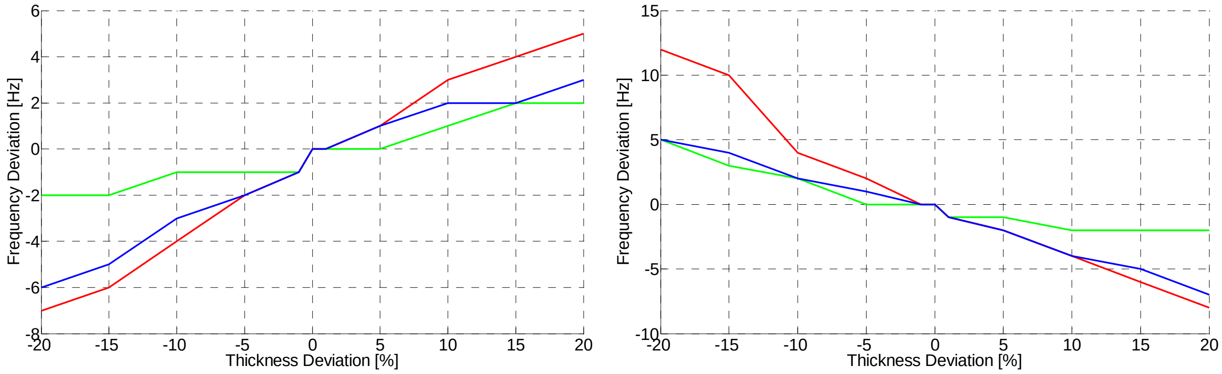

Figure 7.21 - Difference between the resonance frequencies for deviations in conductor thickness (figure on the left) and insulation thickness (figure to the right) when using model D1-L. Green: f~210Hz; Red: f~250Hz; Blue: f~310Hz;

For the simplified circuit of Figure 7.22, where C_2 is the cable and C_1, R and L the remaining network, the frequency variation as a function of C_2 is given by (69). The equation is demonstrated in Appendix N.

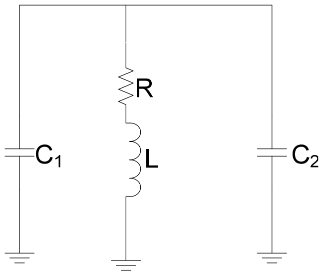

Figure 7.22 - Simplified circuit for the calculation of the frequency variation as a function of C_2

$$\frac{d\omega}{dC_2} = -\frac{L}{2\left(L\left(C_1 + C_2\right)\right)\sqrt{L\left(C_1 + C_2\right)}} \tag{69}$$

The application of (69) for model D1-L is not possible as the values of L and C_1 are unknown. Moreover, Figure 7.13 circuit only has one resonance frequency while a real system has several.

However, the equation can be confirmed when using the simplified D1-eq model. In that case C_2 can be neglected and L is calculated using the resonance frequency of the base-case. By applying (69), a shift is obtained in the resonance frequency of -18 Hz and 22 Hz for the respective deviation of +20% and -20% in the thickness of the insulation. These values are very similar to those obtained by means of simulations, as can be verified in Figure 7.23.

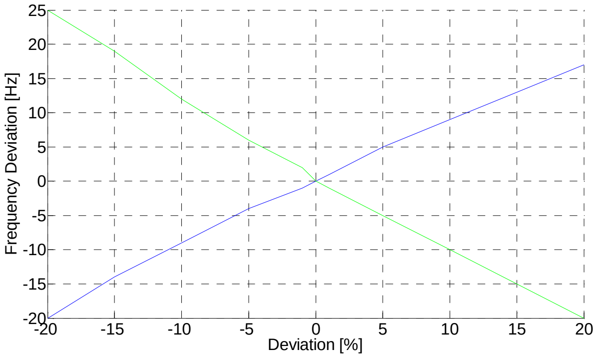

Figure 7.23 - Difference between the resonance frequencies for deviations in the conductor thickness (blue curve) and insulation thickness (green curve) when using model D1-eq

Equation (69) also provides also of the frequency variation as a function of the model used. As an example, the D1-L (Figure 7.20), the D3-L and the D5-L models (Figure 7.24) are used. The variations in the resonance frequencies values as a function of the thickness deviation are similar for models D1-L and D3-L but different for model D5-L.

Figure 7.3.a shows that the ~250 Hz resonance frequency of model D5-L is larger than the one for models D1-L and D3-L. This means that the value of C_1 is smaller for model D5-L than for models D1-L and D3-L. As the value of C_2 is equal in all the models, the frequency variation as a function of the thickness deviation (69) is larger for model D5-L than for models D1-L and D3-L.

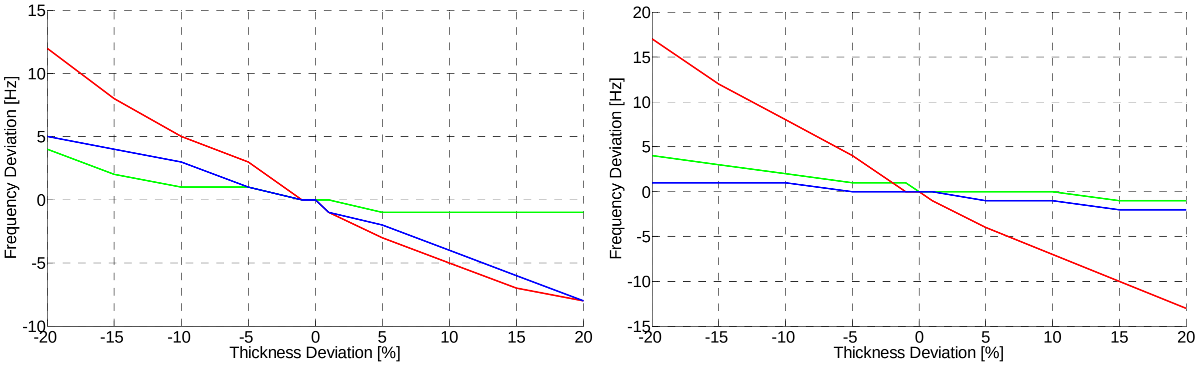

Figure 7.24 - Difference between the resonance frequencies for deviations in the insulation thickness when using model D3-L (figure on the left) and model D5-L (figure on the right). Green: f~210Hz; Red: f~250Hz; Blue: f~310Hz;

7.7 Conclusions

The method proposed in chapter 6.3.1 cannot be used when simulating a resonance. The method is based on the reflections in the neighbouring nodes, whereas in the case of resonance the main factor influencing the overvoltage is the interaction between the cable and the transformer.

It was shown in chapter 7.2 that the frequency spectrum and the transient harmonic content are correlated. Therefore, the adequate modelling depth for the simulation of a resonance can be based on the frequency spectrum as seen from the node to be simulated.

The classic method, which is used for most types of simulation, is to compare the frequency spectrum for increasing modelling depths and to stop when the frequency spectrum stops changing. However, the total simulation time of a cable-based network is mostly a function of the amount of cable modelled by means of FD-models. Consequently, the modelling of the network outside of the area of interest by means of lumped-parameters models does not represent a substantial increase in the total simulation time, whereas the accuracy of the frequency spectrum increases substantially.

The type of bonding used affects the positive-sequence resonance frequencies, whereas the influence in the zero-sequence spectrums is only on the magnitude of the resonance points. A cross-bonded cable has more resonance frequencies than a similar both-end bonded cable.

However, the type of bonding has little influence in the event of a cable-transformer resonance, which occurs for frequencies lower than the cable's first resonance frequency.

For other phenomena, like propagation of harmonics generated by different harmonic sources, the type of bonding used is relevant, especially for long cables with low resonance frequencies.

The cable capacitance changes when the thickness of the conductor or insulation changes, by scarcely affected by changes in the other parameters. Consequently, the frequency spectrum is affected if the datasheet values are incorrect or the permittivity and resistivity constants are not properly corrected.

The total frequency deviation depends on the model used, but the use of a more complex model does not result in a lower frequency deviation.

8. Systematic Method for the Simulation of Switching Transients

Throughout this thesis, several phenomena have been demonstrated. At the same time, methods have been presented that can be used when to perform an insulation co-ordination study.
This chapter shows the example of such a study for one cable in the 2030 West Danish transmission network. The study is divided into four phases, going from cable design and validation to the simulation of specific phenomena.
It is also indicated where in the thesis a more detailed explanation of each step can be found.

Phase 1 - Design cable

The first phase consists of the design and validation of the cable.

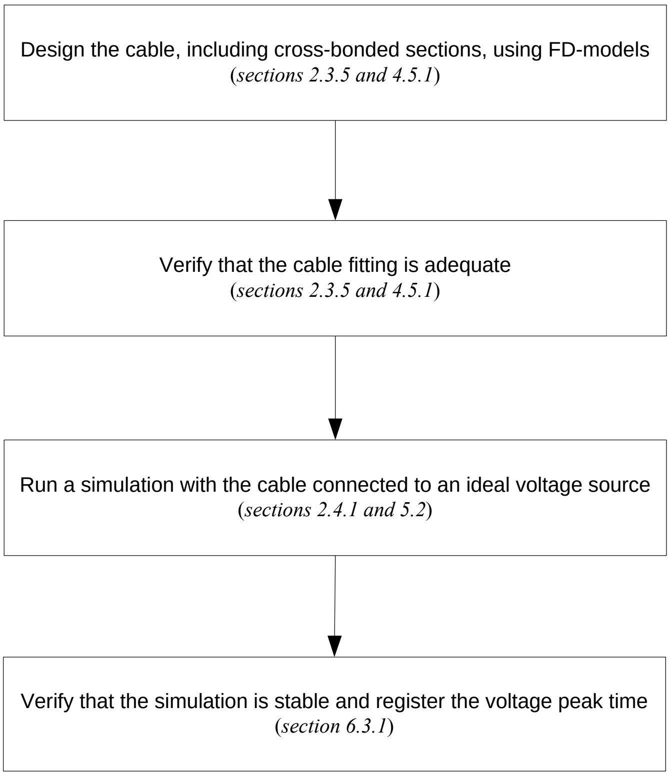

The Matlab code available in Appendix L can also be used to verify that the model is properly designed and the fitting is correct. This is done by comparing the frequency spectrums.

Phase 2 - Design network

The second phase is to design the network.

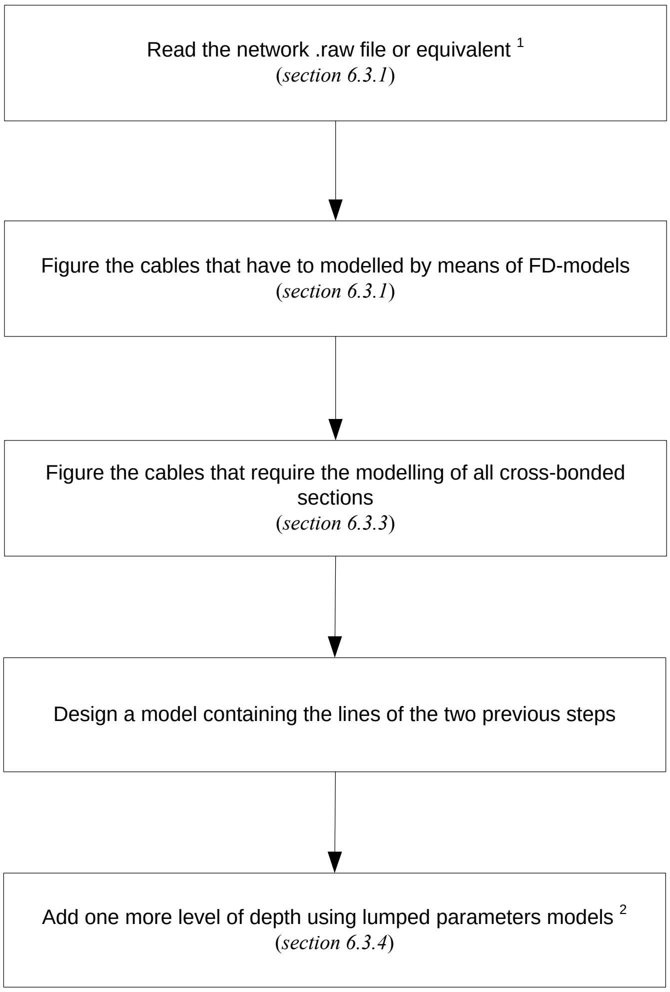

[1] When Matlab is used the file must to be modified or divided into several parts in order to be read

[2] It is advised to increase the modelling depth of the lumped-parameter area, if the detailed area of the network is small or an OHL is in the direct vicinity of the detailed area

[2*] If the model boundary finishes in a transformer, the transformer should be included in the model, because of the reflections

Phase 3 - Simulations (resonance)

The third phase is to verify the type of phenomenon and do the respective analyses.

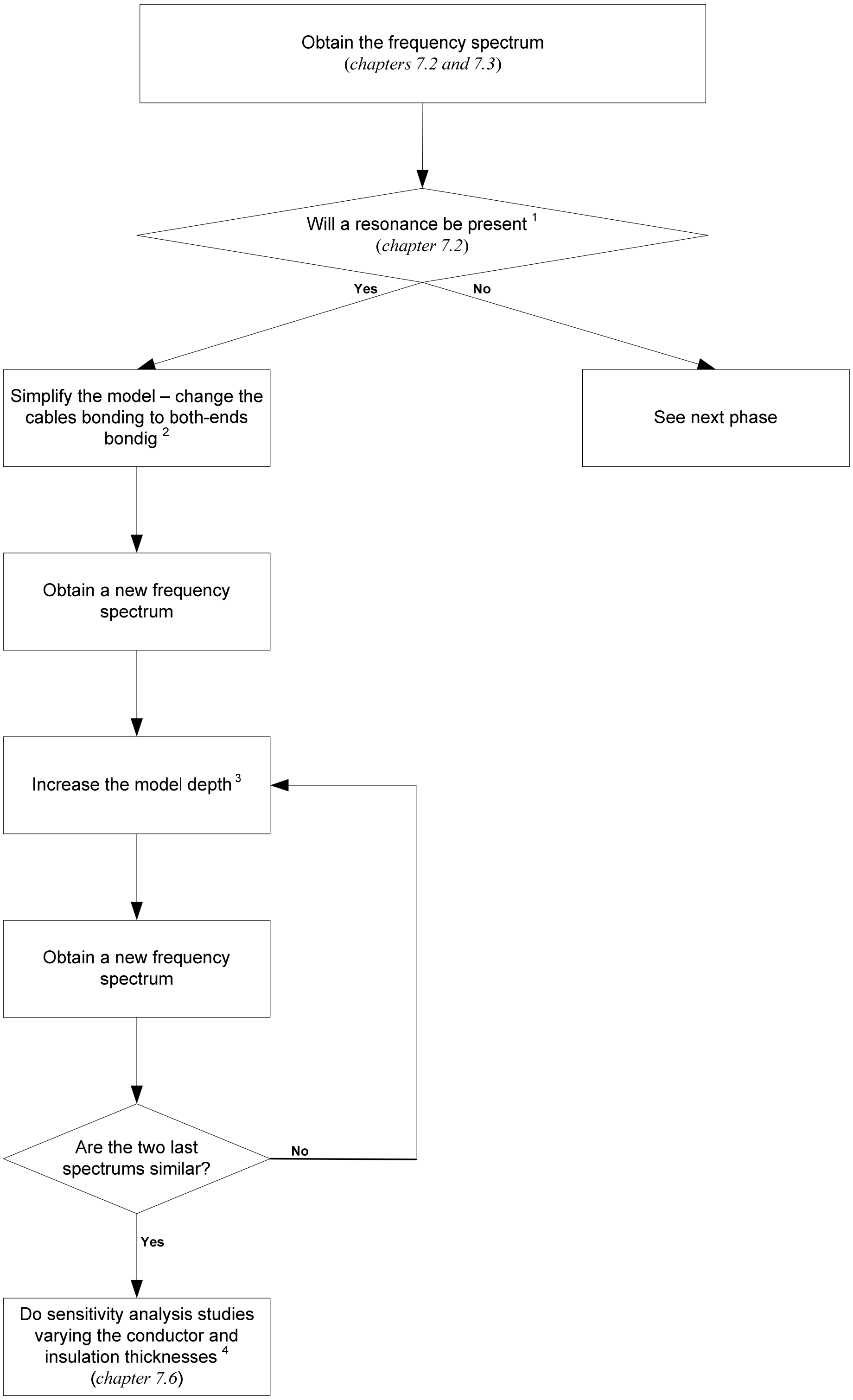

[1] By resonance is understood either the excitation of a harmonic in steady-state or a cable-transformer resonance.

[2] The change depends on the frequencies of interest and the length of the cables. A good first test is to use the code available in Appendix L to simulate the spectrum of the longest cable in the system and verify wheter the lower resonance point is inside the area of interest. If it is, the cable should not be simplified. This change is made with the sole purpose of enhancing the total simulation time.

[3] The area modelled by means of lumped parameters should be increased for resonance studies.

[4] The simpler of the two models is used

Phase 4 - Energisation and de-energisation simulations

The fourth phase consists of simulating the transient(s) and registering the results.

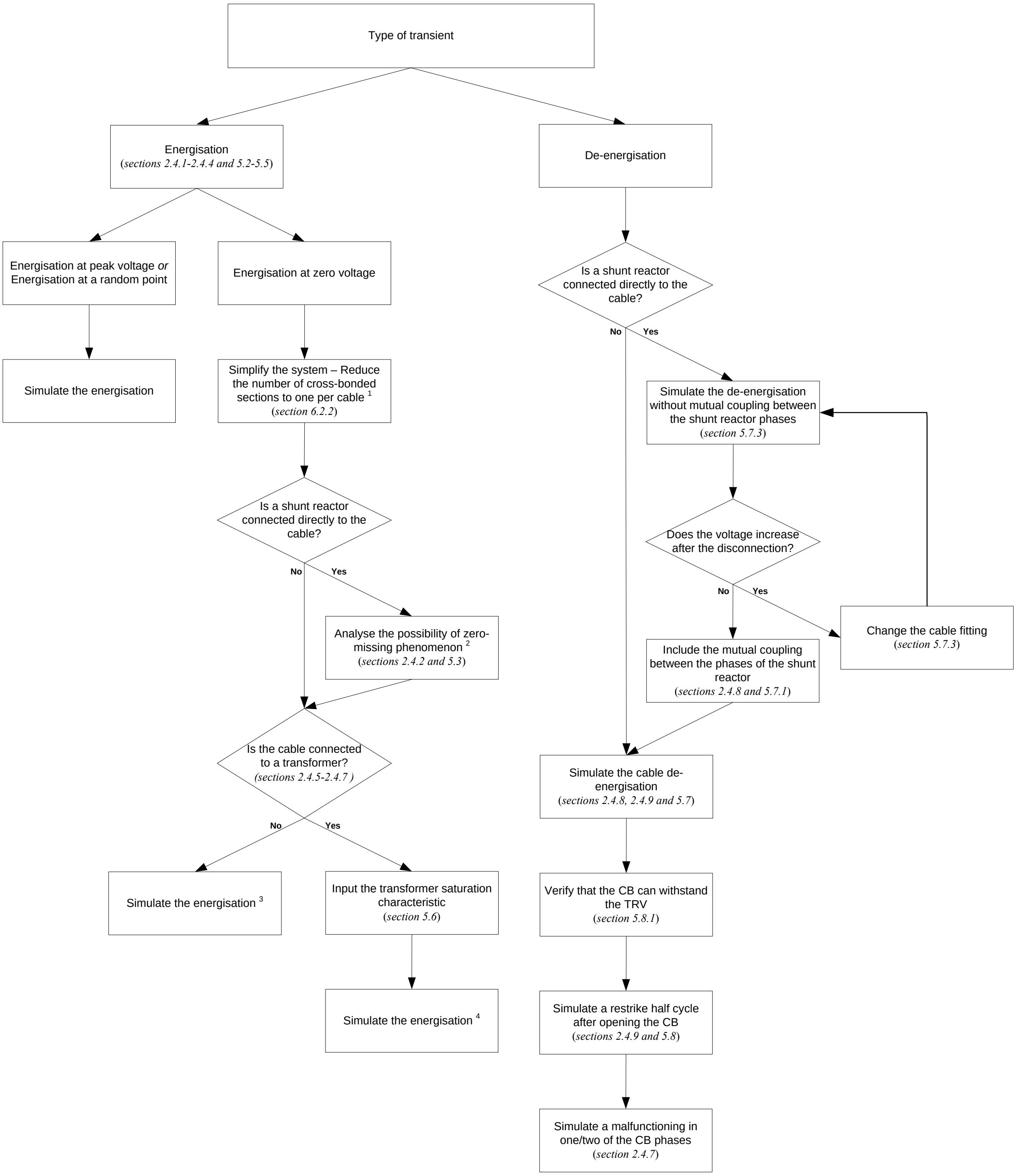

[1] This step is not necessary, but it will decrease the total simulation time without loss of accuracy. To be done if it is necessary to repeat the simulations several times.

[2] A simple first verification consists of seeing whether the shunt reactor(s) compensate for more than 50% of the reactive power generated by the cable.

[3] In these circumstances the presence of any undesired phenomena is not expected.

[4] Series-resonance, parallel-resonance and ferroresonance

8.1 Example

The method will be demonstrated for a node that has not yet been used in the thesis. The chosen node is TRI, whose single-line diagram for a distance of up to two nodes is shown in Figure 8.1. The node being energised is the TRI-ÅSP node.

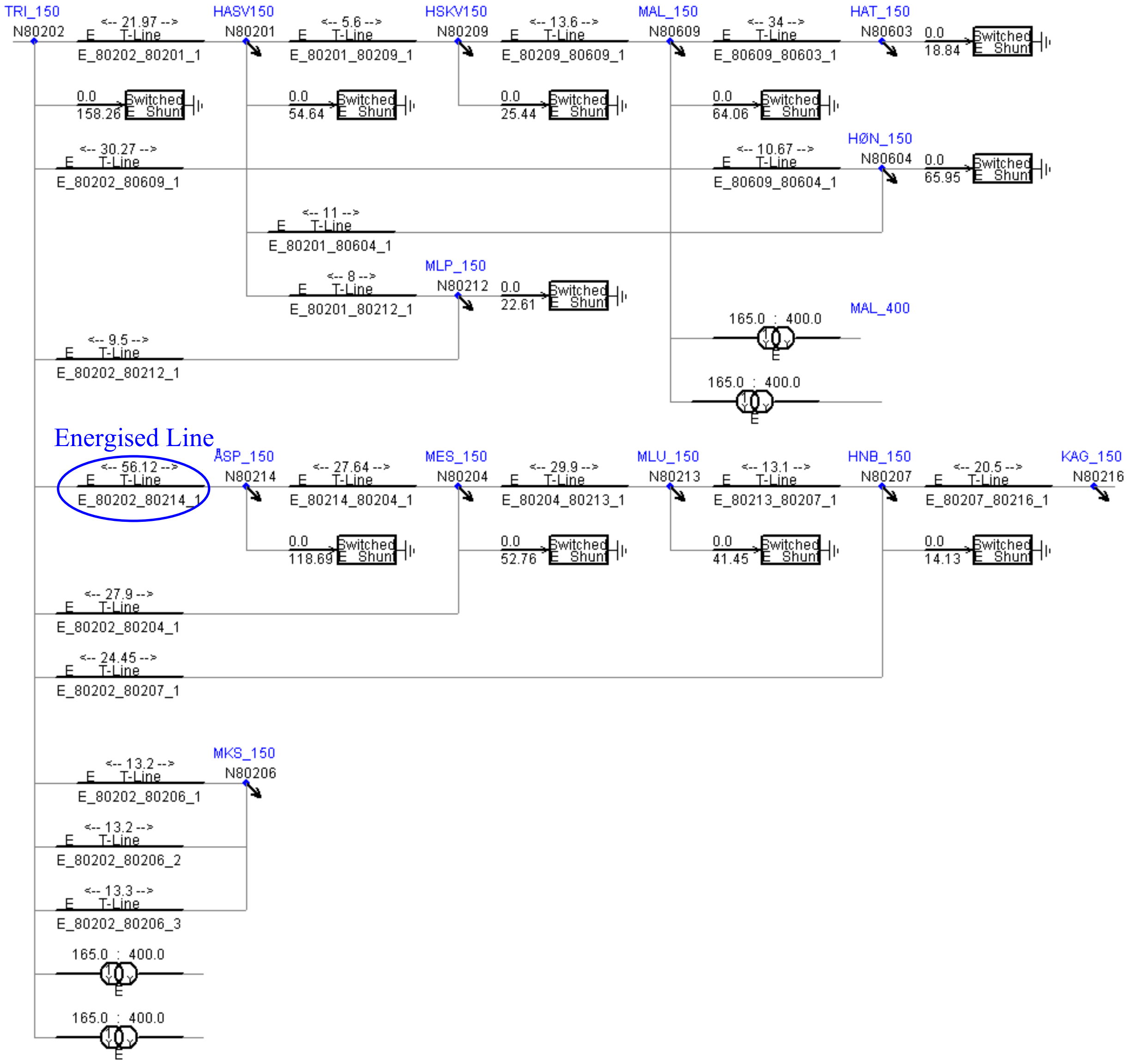

Figure 8.1 - Single-line diagram for a distance up to two nodes from the TRI node

Phase 1

1. The cable is designed using the datasheet and the required corrections are done.

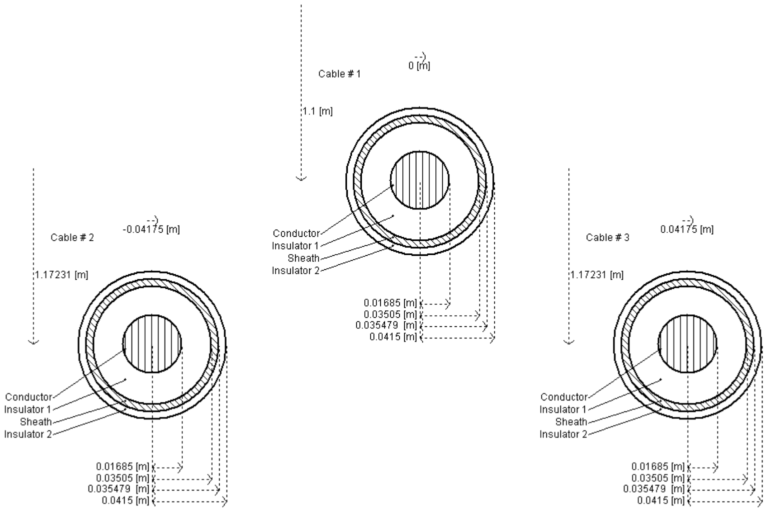

Figure 8.2 - TRI-ÅSP cable layout

2. The fitting of the cable is verified. The number of poles is sufficient;
3. The simulation is stable and the charging time is 559 μs;

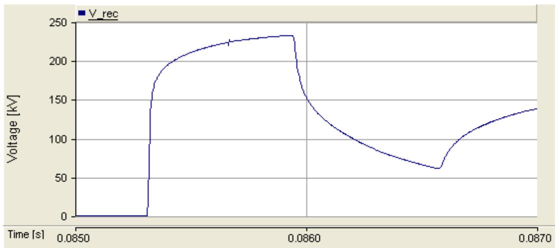

Figure 8.3 - Voltage during the energisation transient when connected to an ideal voltage source;

4. The PSCAD/EMTDC frequency spectrum aggregates with the Matlab simulation (Appendix L). The simulation is made considering the cable bonded in both-ends for the reasons explained in section 7.5;

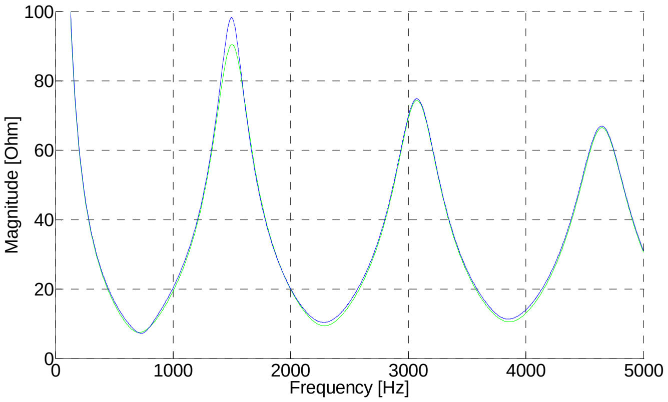

Figure 8.4 - Comparison of the frequency spectrum in PSCAD/EMTDC and Matlab simulation

The cable modelling is adequate and can be used in more complex simulations.

Phase 2

1. The PSS/E file is read and the charging time inserted;
2. It is necessary to include 16 nodes in the model:
   2.1 As two of those nodes are connected to a transformer, the model has a total of 18 nodes;
   2.2 The most distant of the boundary nodes is at a four-busbar distance, while the closest is at a two-busbar distance;
3. It is necessary to have a precise modelling of the cross-bonded sections in 13 of the nodes;
4. The model is designed;

Figure 5.80 shows the voltage waveform during the transient for three different approaches:
1. The system is over-modelled through a D5-eq model (red curve);
2. Only the required nodes are included in the model, but all cables have a precise modelling of the cross-bonded sections (blue curve)
3. Optimised model, minimum required number of nodes and cross-bonded sections (black curve);

The following conclusions can be drawn from the simulations:
- The same maximum peak value is obtained for all three models;
- The differences between the second (blue curve) and third (black curve) models are very few. This result is expected as only three of the cables do not have a precise modelling of the cross-bonded sections;
- The optimised model provides accurate results;

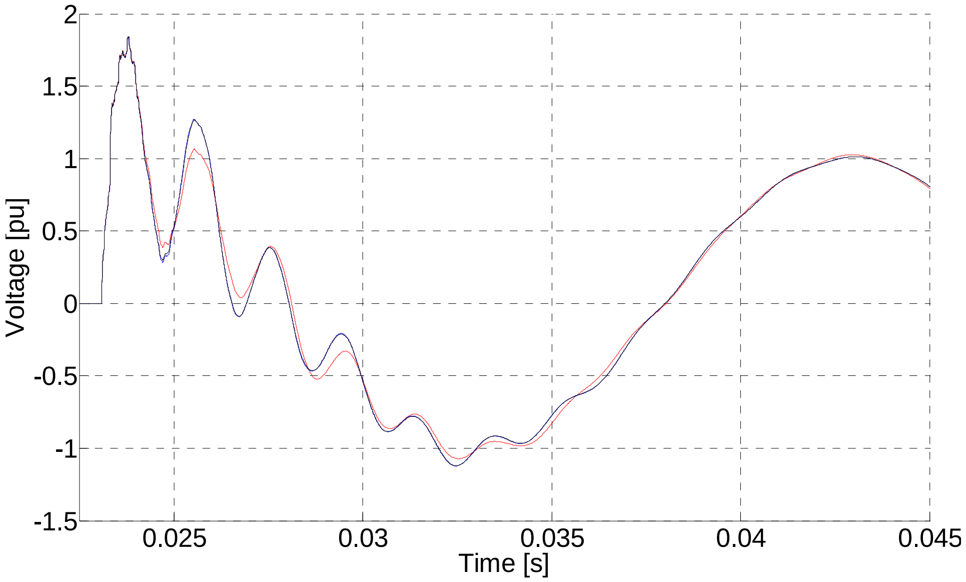

Figure 8.5 - Energisation of the cable using three different models. Red: D5-eq Model with detailed modelling of cross-bonded sections for all the cables; Blue: Minimum number of nodes, but detailed modelling of the cross-bonded section for all cables; Black: Minimum number of nodes and cross-bonded sections;

Phase 3

Figure 8.6 shows the frequency spectrum for the TRI node with the TRI-ÅSP cable open in the ÅSP end. The observation of the spectrum shows that no resonance is associated with the cable energisation.

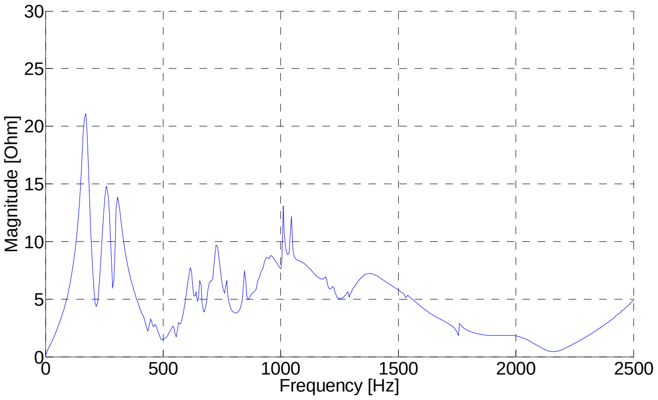

Figure 8.6 - Frequency spectrum seen from the TRI node with the cable open in the ÅSP end

Phase 4

In order to increase the number of possible phenomena, the 118.69 Mvar shunt reactor installed in the Åsp node is directly connected to the receiving end of the cable.

Energisation at peak voltage

Figure 8.7 shows the voltage and current during the first milliseconds of energisation.

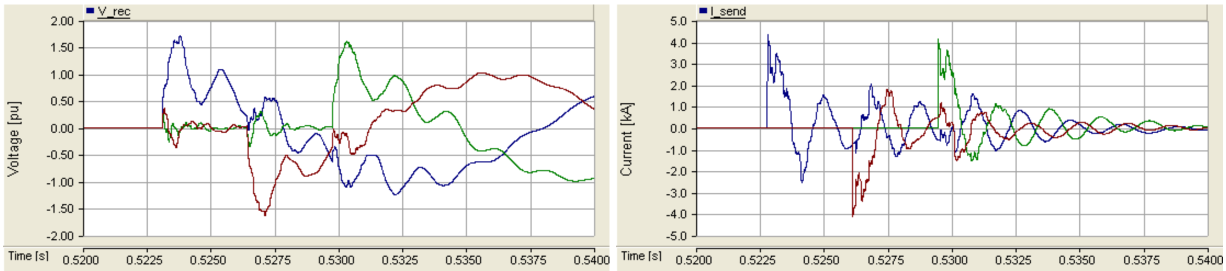

Figure 8.7 - Voltage and current during cable energisation

The energisation of the cable at peak voltage should not arise any problems. Both the peak overvoltage and the peak current amplitude/frequency are below the maximum acceptable values, which are respectively 2 pu [10], 20kA and 4.25kHz [29].

Energisation at zero-voltage

Figure 8.8 shows that zero-missing phenomenon is present when the cable is energised at zero voltage. The cable is neither near a transformer nor connected in a weak point of the grid. Thus, no other problems are present.

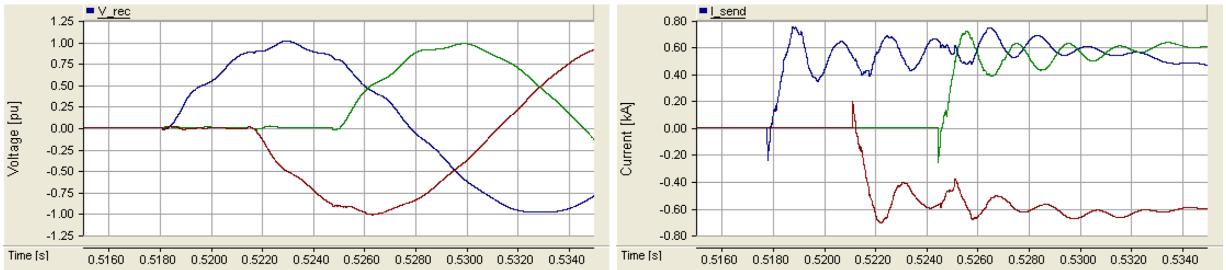

Figure 8.8 - Voltage and current during cable energisation

Figure 8.9 shows that the use of a 160Ω pre-insertion resistor eliminates the problem.

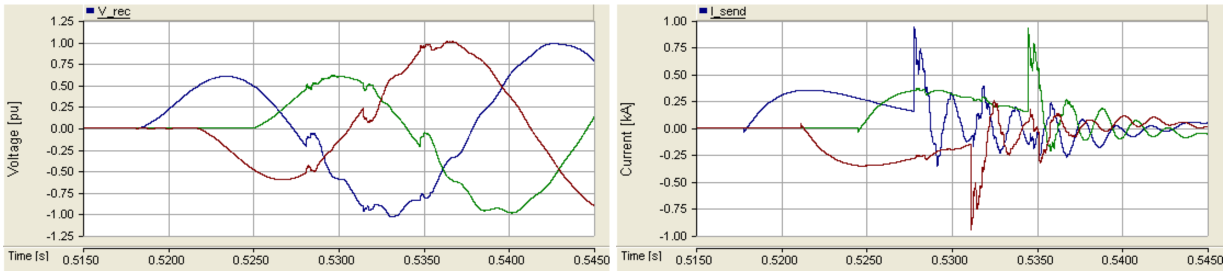

Figure 8.9 - Voltage and current during the cable energisation when using a 160Ω pre-insertion resistor

De-energisation

The cable is first de-energised without considering the mutual coupling between the shun reactor phases. Figure 8.10 shows the voltage in the cable receiving end, which increases after the disconnection. This behaviour indicates a problem in the model, as referred to in section 5.7.3.

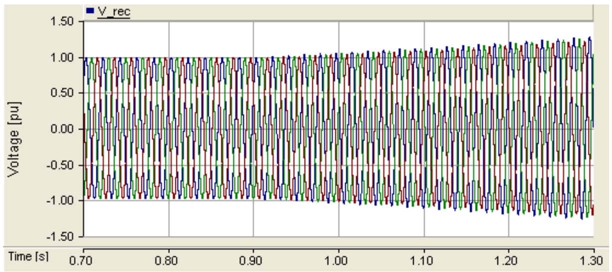

Figure 8.10 - Voltage in the cable receiving end during the de-energisation of the cable+shunt reactor (without mutual coupling) system

Figure 8.11 shows the voltage in the cable receiving end after the correction of the fitting parameters, more specifically a decrease in the maximum fitting error. The overvoltage is no longer present and the model is adequate for the simulation of the de-energisation.

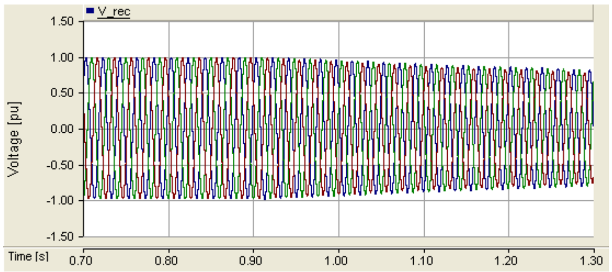

Figure 8.11 - Voltage in the cable receiving end during the de-energisation of the cable+shunt reactor (without mutual coupling) system

Figure 8.12 shows the voltage in the cable receiving end during the de-energisation, where is possible to observe a small overvoltage due to the mutual coupling between the shunt reactor phases (0.1 H).

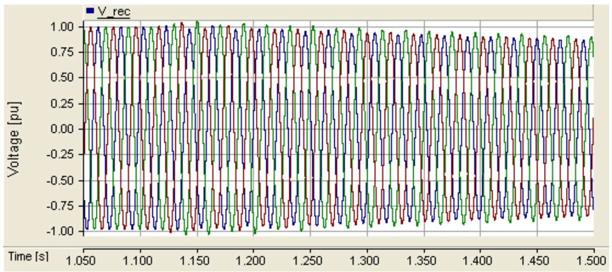

Figure 8.12 - Voltage in the cable receiving end during the de-energisation of the cable+shunt reactor (with mutual coupling) system

For the simulation of the disconnection the shunt reactor is again assumed to be connected to the busbar, so that the worst-case scenario is simulated.

Figure 8.13 shows the voltage in the cable due to a restrike half a cycle after the CB switch-off. The overvoltage has a peak value of 2.67 pu

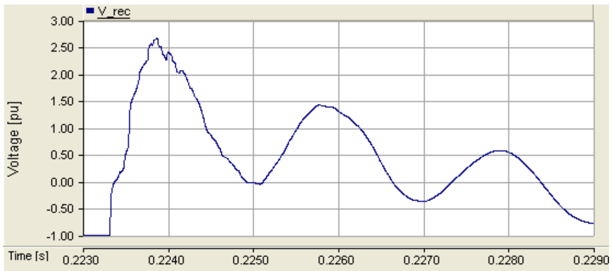

Figure 8.13- Voltage in the cable during restrike

9. Conclusions

9.1 Summary

Energinet.dk started this project with two main objectives in mind: to describe the main electromagnetic phenomena on cable-based networks and to provide guidelines for the proper simulation of those phenomena. The guidelines would be used in future insulation co-ordination studies that the TSO will have to perform in the next years when replacing the existing 150 kV OHLs by cables and installing new 400 kV cables (chapter 1).
The state-of-the-art made a brief description of the several phenomena demonstrating the need for insulation co-ordination studies prior to the installation of a new cable. It was also demonstrated in the state-of-the-art that the present IEC insulation co-ordination standard does not reflect the special needs for studies in cable-based networks (chapter 2).

To study electromagnetic transient phenomena it is necessary both to trust the software models and to have complex/extended networks.
The accuracy of single-phase land-cable models was previous validated in studies made by different authors and also in this thesis by means of measurements (chapter 4).
On the other hand, it was demonstrated that the submarine cable model needs improving. Submarine cable models were not used in the remaining chapter of the thesis and the topic was not further addressed, seeing as that the necessary improvements are considered to be future work.

Several transient phenomena were described theoretically and demonstrated by means of simulations performed both in simple systems and the complex 2030 West Danish transmission grid (chapter 5).
The risks that the phenomena pose to an electric system were demonstrated, and countermeasures that could be used to minimise them were studied.
Some of the phenomena are very unlikely to occur and have an uncertainty associated with them (e.g. restrikes), while others can be predicted with a high degree of certainty (e.g. zero-missing). Some depend only on the cable and equipment directly attached to it (e.g. de-energisation), while others depend on the cable and surrounding area (e.g. energisation). For all these reasons, one cannot immediately say which phenomena should be prioritised when performing an insulation co-ordination study.
The application of the countermeasures depends on the phenomenon that must be minimised. However, some of the countermeasures (e.g. synchronised switching) intensify some phenomena while at the same time minimising others.
Shunt reactors are normally installed, either in the busbar or directly in the cable, when operating long HVAC cables, and play a central role in several of the transient phenomena. As in the case with synchronised switching, the location of the shunt reactor can mitigate some of the phenomena and at the same time exacerbate others.

The proper simulation of a phenomenon, more specifically the modelling depth and level of detail, are of the utmost relevance.

A too simple/short model will yield inaccurate results, which can lead to wrong conclusions and result in damage to the grid.

A too complex/long model will provide correct results, but at the expense of long simulation running times, besides the extra time required to design the model. These models also have the drawback of more easily becoming unstable, and it is easier to make mistakes when preparing the model.

To circumvent this situation, a method that can be used to delineate the minimum modelling required (chapter 6) was proposed. The method uses information about the network layout and the wave speed in the lines to estimate the cable that should be included in the model and the cables that require a detail modelling of the respective cross-bonded sections.

The method has also the advantage of indicating the nodes that have to be present instead of just indicating the modelling depth, minimising the complexity of the model and the simulation running time.

To minimise possible inaccuracies part of the network can be designed using lumped-parameters models, at the expense of a relatively small increase in the simulation time.

In the event of inaccuracies, it can normally be detected as the peak overvoltage does not occur at the expected instant, but later. In such case the number of cables in the model should be increased.

A cable-based network has a frequency spectrum very different to the one of an equivalent OHL-based network, and possible resonances between a long HVAC cable and a transformer are more probable.

A precise representation of the frequency spectrum requires an extensive modelling of the area around the cable. It was shown that the use of a hybrid-system mixing FD-models and lumped-parameters models provides better results than those obtained using equivalent networks without a large difference in the simulation running time.

The strong correlation between the frequency spectrum at one node and the energisation transient of the cable connected to the same node was also demonstrated.

The influence of the cross-bonding sections in the spectrum was assessed, and it was demonstrated that the differences are only noticeable for frequencies higher than the one of the main resonance point.

9.2 New contributions

The main contributions of this research project are:

- A detailed description of some of the main electromagnetic transient phenomena in a cable-based network or a network with many cables
  - Demonstration of the phenomena by means of simulations using a real transmission-network model;
- A detailed description and demonstration of countermeasures for the different phenomena
  - New method for the calculation of the pre-insertion resistor when minimising the zero-missing phenomenon
  - Demonstration of which type of switching to use to minimize different phenomena;

- New equations for the calculation of the peak current and frequency during a transient when having cables in parallel
- Method to estimate in Matlab the maximum overvoltage associated with the de-energisation of a cable and shunt reactor together (with mutual coupling)
- New equations for the estimation of the resonance frequencies during the de-energisation of a cable and shunt reactor together (with mutual coupling)
- Measurements of a 100 km 150 kV land+submarine cable
    - Validated the single-core cable models and shunt reactor models (also done by several other authors before)
    - Demonstrated that the submarine cable model needs to be improved
- Guidelines for the digital simulation of electromagnetic cable transients
    - Method to estimate which cables should be included in the simulation model
    - Method to estimate which cables require a precise modelling of the cross-bonded sections
    - Guidelines for simplifications that can be made in the cable, shunt reactor and transformer models as a function of the type of energisation and phenomena
    - Matlab code that can be used to do a fast verification of the cable model and fitting;
- Harmonic analysis of a cable-based network
    - Influence of deviations on the thickness of the cable layers in the frequency spectrum
    - Model for simulating the frequency spectrum

9.3 Future work

- The interaction between HVAC cables and power electronic devices during a electromagnetic transients was not addressed in this thesis;
- The study of a mixed network where neither cables nor OHLs are dominant may result in different transients. This was briefly addressed in this thesis, but may a be topic for deeper analysis;
- The thesis provided countermeasures for some of the phenomena. However, more can be applied depending on the system layout and characteristics;
- Optimising the location of the shunt reactor as a function of the network layout;
- Implementation/automation of the chapter 6 method in an EMTP software;
- Improvements in the submarine cable models are necessary

10. References:

[1] CIGRE Joint Working Group 21/22.01, "Comparison of High Voltage Overhead Lines and Underground Cables - Report and Guidelines", 1996

[2] R. Bartnikas, K. D. Srivastava "Power and Communication Cables: Theory and Applications", IEEE Press: Power Engineering Series, 2000

[3] Kabelhandlingsplan 132-150kV, Energinet.dk, 2009 (in Danish)

[4] ELINFRASTRUKTURUDVALGET, Technical report on the future expansion and undergrounding of the electricity transmission grid, 2008

[5] CIGRE Working Group B1.07, "Statistics of AC Underground Cables in Power Networks", 2007

[6] CIGRE Joint Working Group 21/33, "Insulation Co-ordination for HV AC Underground Cable System", 2001

[7] SIEMENS, "Wind farm Horns Rev: Insulation co-ordination of system connection", 2009

[8] EnerNex Corporation, "Rødsand 2 Insulation Co-ordination Study", 2009

[9] Tokyo Electric Power Company, "Joint Feasibility Study on the 400kV Cable Line Endrup-Idomlund", 2008

[10] IEC 60071-2, "Insulation Co-ordination - Part 2: Application guide", 1996

[11] CIGRE Working Group C4-502, "Power System Technical Performance Issues Related to the Application of Long HVAC Cables", (to be published)

[12] IEC TR 60071-4, "Insulation Co-ordination - Part 4: Computational guide of insulation co-ordination and modelling of electrical networks, 2004

[13] A. I. Ibrahim, H. W. Dommel, "A Knowledge Base for Switching Surge Transients", International Conference on Power Systems Transients (IPST), Canada, Paper No. 50, 2005

[14] Ping-Heng Ho, Chi-Jui Wu, "Transient analysis of the 161 kU Taywan-PengHu submarine power cable system", European Transactions on Electrical Power, 2009

[15] Ivo Uglesic, Sandra Hutter, Miroslav Krepela, Bozidar Filipovic-Grcic, Franc Jakl, "Transients Due to Switching of 400 kV Shunt Reactor", International Conference in Power Systems Transients (IPST), Brazil, Paper No. 045, 2001

[16] Alan Greenwood, "Electric Transients in Power Systems, John Wiley & Sons, 1st Edition, 1978

[17] Lou van der Sluis, "Transients in Power Systems", John Wiley & Sons, 2001

[18] W. Wiechowski, P. Børre Eriksen, "Selected Studies on Offshore Wind Farm Cable Connections - Challenges and Experience of the Danish TSO", IEEE-PES General Meeting, 2008

[19] Lars Liljestrand, Ambra Sannino, Henrik Breder, Stefan Thorburn, "Transients in Collection Grids of Large Offshore Wind Parks", Wind Energy, 2008

[20] R. A. Turner, K. S. Smith, "Resonance Excited by Transformer Inrush Current in Inter-connected Offshore Power Systems", 43rd IEEE Industry Applications Conference 2008

[21] F. Anan, S. Ikumi, S. Shimada, S. Nishiwaki, Y. Noro, T. Yokota, K. Yamamoto, "Countermeasures for Substation Equipment Against Various Special Phenomena in Japan's Longest (54 km) 66 kV AC Cable Transmission System", IEEE-PES General Meeting, 2004

[22] F. F. da Silva, C. L: Bak, U. S. Gudmunsdottir, W. Wiechowski, M. R. Knardrupgard, "Methods to Minimize Zero-Missing Phenomenon", IEEE Transactions on Power Delivery, Vol. 25, No. 5, October 2010

[23] IEEE Standard Rating Structure for AC High-Voltage Circuit Breakers, IEEE Std. C37.04-1999, 1999

[24] Steffan G. Johanson, Lars Liljestrand, Flemming Krogh, Johan Karlstrand, Jutta Hanson, "AC Cable solutions for Offshore Wind Energy", Copenhagen Offshore Wind Conference, 2005

[25] I. B. Johnson, A. J. Schultz, N. R. Schultz, R. B. Shores, "Some Fundamentals on Capacitance Switching", Power Apparatus and Systems, Part III. Transactions of the American Institute of Electrical Engineers, Vol. 74, Issue 3, 1955

[26] IEEE Application Guide for Transient Recovery Voltage for AC High-Voltage Circuit Breakers, IEEE Std. C37.011-2005, 2005

[27] IEEE Application Guide for Capacitance Current Switching for AC High-Voltage Circuit Breakers, IEEE Std. C37.012-2005, 2005

[28] IEEE Guide for the Protection of Shunt Capacitor Banks, IEEE Std. C37.99-2000, 2000

[29] IEC 62271-100, "High-voltage switchgear and controlgear - Part 100: High-voltage alternating-current circuit-breakers", Edition 1.1, 2003

[30] F. Ritcher, "Switching of capacitive currents - back-to-back cables", Siemens Energy Sector, 2009 (presentation)

[31] CIGRE Working Group B1.05, "Transient Voltages Affecting Long Cables", 2005

[32] E. W. Greenfield, W. A. Pullman "Transient Behavior of Short and Long Cables", IEEE Transaction on Power Apparatus and Systems, Vol. PAS-103, No. 11, 1984

[33] Claus Leth bak, Wojciech Wiechowski, Kim Søgaard, Søren Damsgaar Mikkelsen, "Analysis and simulation of switching surge generation when disconnecting a combined 400 kV cable/overhead line with shunt reactor", International Conference in Power Systems Transients (IPST), France, Paper No. 24, 2007

[34] A. Morched, B. Gustavsen, M. Tartibi, "A universal model for accurate calculation of electromagnetic transients on overhead lines and underground cables," *IEEE Transactions on Power Delivery,* 14(3), p.1032–1038, July 1999

[35] Manitoba HVDC Research Centre Inc, "PSCAD Online Help - Frequency Dependent (Phase) Models", 2006

[36] B. Gustavsen, J. A. Martinez, D. Durbak, "Parameter Determination for Modeling System Transients - Part II: Insulated Cables"; IEEE Transactions on Power Delivery, Vol. 30, No. 3, July 2005

[37] A. Ametani, Y. Miyamoti, N. Nagaoka, "Semiconducting layer impedance and its effects on cable wave-propagation and transient characteristics", IEEE Transactions on Power Delivery, Vol. 19, No.4, October 2004

[38] Johan H. R. Enslin, Yi Hu, Richard A. Wakefield, "System Considerations and Impacts of AC Cable Networks on Weak High Voltage Transmission Networks", IEEE PES Transmission and Distribution Conference and Exhibition 2005/2006, 2006

[39] E. Peschke, R. von Olshausen "Cable Systems for High and Extra-High Voltage – Development, Manufacture, Testing, Installation and Operation of Cables and their Accessories", Pirelli, 1999

[40] G. F. Moore, "Electric Cables Handbook", Blackwell Science, 3rd edition, 1997

[41] Demetrios A. Tziouvaras, "Protection of High-Voltage AC Cables", 59th Annual Conference for Protective Relay Engineers, 2006

[42] ICF Consulting, “Overview of the Potential for Undergrounding the Electricity Networks in Europe”, prepared for DG TREN/European Commission, 2003
[43] American Superconductor, "Superconductor Power Cables - Application Note", available at: http://www.amsc.com/products/htswire/HTSCables.html (in September 2010)
[44] 60-500 kV High Voltage Underground Power Cables: XLPE insulated cables, Nexans
[45] Jarot Setyawan, "Investigation of Partial Discharge Occurrence and Detectability in High Voltage Power Cable Accessories", Master Thesis, Delft University of Technology, 2009
[46] CIGRE Working Group B1.19, "General Guidelines for the Integration of a New Underground Cable System in the Network", 2004
[47] Gruppe vedr. Elektriske System Transient Analyser, "Transients studies of the Horns Rev 2 HVAC cable connection", Energinte.dk, 2008
[48] IEEE Std C57.21-1990, "IEEE Standard Requirements, Terminology, and Test Code for Shunt Reactors Rated Over 500 kVA", IEEE, 1990
[49] Surya Santoso, Roger C. Dugan, Thomas E. Grebe, Peter Nedwick, "Modeling Ferroresonance Phenomena in an Underground Distribution System", International Conference in Power Systems Transients (IPST), Brazil, 2001
[50] J. R. Marti, A. C: Soudack, "Ferroresonance in power systems: Fundamental solutions", IEE Proceeding-C. Vol. 138, No. 4, July 1991
[51] José Pedro Sucena Paiva, "Redes de Energia Eléctrica: uma análise sistémica", IST Press, 1st Edtion, 2005 (in Portuguese)
[52] Jos Arrilaga, Neville R. Watson, "Power System Harmonics", John Wiley & Sons, 2nd edition, 2003
[53] R. A. Turner, K. S. Smith, "Transformer Inrush Currents", IEEE Industry Applications Magazine, Vol. 16, Issue 5, 2010
[54] Neville Watson, Jos Arrilaga, "Power systems electromagnetic transients simulation", IET power and energy series, no. 39, 2003
[55] Manitoba HVDC Research Centre Inc, "PSCAD Online Help - Model Selection", 2006
[56] Unnur Stella Gudmundsdóttir, "Modelling of long High Voltage AC cables in Transmission Systems", PhD Thesis, Aalborg University, 2010
[57] Kim Søgaard, Claus L. Bak, "Analyse og modellering af dynamiske forhold for 400kV linjen FERSLEV-TRIGE", Institute of Energy Technology, Aalborg University, June 2005 (in Danish)
[58] ABB, "Blåbjerg Reaktor Instruktionsmanual", 2009 (Shunt reactor test report - in Swedish)
[59] C. D. Tsirekis, N. D. Hatziargyriou, "Control of Shunt Capacitors and Shunt Reactors Energization Transients", International Conference in Power Systems Transients (IPST), United States of America, 2003
[60] Danijela Palmgren, "Cable Systems-Handouts", ABB, November 2010
[61] CIGRE Brochure 39, "Guidelines for Representation of Network Elements when Calculating Transients", Working Group 02 (Internal overvoltages) Of Study Committee 33 (Overvoltages and Insulation Coordination), 1990
[62] Christian F. Jensen, "Switching studies for the Horns Rev 2 wind farm main cable", Thesis from Master Student, Aalborg University, 2009
[63] Alan Budner, "Introduction of Frequency-Dependent Line Parameters into an Electromagnetic Transients Program", IEEE Transactions on Power Apparatus and Systems, Vol. PAS-89, No. 1, January 1970
[64] H. M. J. De Silva, A. M. Gole, J. E. Nordstrom, L. M. Wedepohl, "Robust Passivity Enforcement Scheme for Time-Domain Simulation of Multi-Conductor Transmission Lines and Cables", IEEE Transactions on Power Delivery, Vol. 25, Issue 2, April 2010
[65] J. R. Marti, "Accurate Modelling of Frequency-dependent Transmission Lines in Electromagnetic Transient Simulations", IEEE Transactions on Power Apparatus and Systems, Vol. PAS-101, No. 1, January 1982
[66] European network of transmission system operators website: https://www.entsoe.eu/system-operations/regional-groups/ (in January 2011)
[67] E-TRAN V1.1 - Electrical Translation Program for Power Systems - User's Manual, Electranix Corporation, February, 2003
[68] Power Technologies, Inc., "PSS/E^{TM} 30- Volume I: Program Operation Manual", August 2004
[69] ABB, "XLPE Cable Systems - User's Guide", Rev. 2
[70] Daqing Hou, Jeff Roberts, "Capacitive Voltage Transformers: Transient Overreach Concerns and Solutions for Distance Relaying", Canadian Conference on Electrical and Computer Engineering, 1996
[71] Bogdan Kasztenny, Dave Sharples, Vince Asaro, Marzio Pozzuoli, "Distance Relays and Capacitive Voltage Transformers - Balancing Speed and Transient Overreach", 53rd Annual Conference for Protective Relay Engineers, 2000
[72] ABB, "Live Tank Circuit Breakers: Buyer's Guide", 4th edition, May 2008
[73] J. F. Borges da Silva, "Electrotecnia Teórica - 1ª Parte", 2nd Edition, AEIST, 1995 (in Portuguese)
[74] GE Power Systems Energy Consulting, "Connecticut Cable Transient and Harmonics Study for Phase 2: Final Report", November 2003
[75] D. Thukaram, H. P. Khincha, Sulabh Khandelwal, "Estimation of switching transient peak overvoltages during transmission line energisation using artificial neural network", Electric Power Systems Research, Vol. 76, Issue 4, January 2006
[76] Seyed Abbas Taher, Iman Sadeghkhani, "Estimation of magnitude and time duration of temporary overvoltages using ANN in transmission lines during power system restoration", Simulation Modelling Practice and Theory, Vol. 18, Issue 6, June 2010
[77] IEC 62271-100, "High-voltage switchgear and controlgear - Part 100: High-voltage alternating-current circuit-breakers", Edition 2.0, 2008
[78] IEC 60056 (1987-03), "High-voltage alternating-current circuit-breakers", 1987
[79] R.W. Alexander, D. Dufournet, "Transient Recoery Voltage (TRV) for High-Voltage Circuit Breakers", IEEE Tutorial: "Design and Application of Power Circuit Breakers", IEEE-PES GM 2008
[80] S. M. Wong, L. A. Snider, E. W. C. Lo, Overvoltages and reignition behaviour of vacuum circuit breaker", IPST 2003
[81] L. V. Bewley, "Travelling Waves on Transmission Systems", Wiley New York, 1951
[82] CIGRE Working Group B1.18, "Special Bonding of High Voltage Power Cables", October 2005
[83] ABB, "Technical Proposal N07 - 1185.Rev 4", 2007 (confidential)
[84] Nexans, "Horns Rev 2 Offshore Wind Farm - Technical Description of 170kV Submarine Cable", 2006 (confidential)
[85] IEC 60076-6, "Power Transformers - Part 6: Reactors", Edition 1.0, 2007
[86] Afshin Rezaei-Zare, Reza Iravani, "Impacts of Various Representations of Core Saturation Curve on Ferroresonance Behavior of Transformers", International Conference in Power Systems Transients (IPST), Japan, Paper No. 217, 2009
[87] A. Ametani, "Wave Propagation Characteristics of Cables", IEEE Transactions on Power Apparaasdastus and Systems, Vol. PAS-99, No. 2, March/April, 1980
[88] Nasser Tleis, "Power Systems Modelling and Fault Analysis", 1st Edition, Newnes, 2008
[89] Tarik Abdulahović, "Analysis of High-Frequency Electrical Transients in Offshore wind Parks", Thesis for the degree of Licentitate of Engineering, Chalmers University of Technology, 2009
[90] Mohamed Abdel-Rahman, "Frequency Dependent Hybrid Equivalents of Large Networks", PhD Thesis, University of Toronto, 2001
[91] A. A. Morched, V. Brandwajn, "Transmission Network Equivalents for Electromagnetic Transients Studies", IEEE Transactions on Power Apparatus and Systems, Vol. PAS-102, No. 9, September 1983

[92] PSCAD Application Notes, "Converting a Solved PSS/E Case to PSCAD for Transient Simulations", 2006

[93] IEEE Guide for the Application of Sheath-Bonding Methods for Single-Conductor Cables and Calculation of Induced Voltages and Currents in Cable Sheaths, IEEE Std. 575-1988

[94] IEC 62067, "Power cables with extruded insulation and their accessories for rated voltages above 30 kV (Um=36kV) up to 150 kV (Um=170 kV) - Test methods and requirements", Edition 3.0, 2004

[95] IEC 60840, " Power cables with extruded insulation and their accessories for rated voltages above 150 kV (Um=170kV) up to 500 kV (Um=550 kV) - Test methods and requirements", Edition 1.0, 2001

[96] Centre for Marine and Coastal Studies - University of Liverpool, "A Baseline Assessment of Electromagnetic Fields Generated by Offshore Windfarm Cables - Final Report", 2003

[97] Centre for Marine and Coastal Studies - University of Liverpool, "Electromagnetic Simulations of 135 kV Three-Phase Submarine Power Cables - Final Report", 2005

[98] A. M. O. Mohamed, "Impact of Soil Magnetic Permeability on Water Content Prediction Using TDR", The 12th International Conference of International Association for Computer Methods and Advances in Geomechanics (IACMAG), 2008

[99] A. Ametani, "A general formulation of impedance and admittance of cables", IEEE Transaction on Power Apparatus and Systems, Vol. PAS-99, No. 3, May/June 1980

[100] Steffen Schulz, "Four Lectures on Differential-Algebraic Equations", Humboldt Universität zu Berlin, 2003

[101] N. Nagaoka, A. Ametani, "Transient calculations on crossbonded cables", IEEE Transaction on Power Apparatus and Systems, Vol. PAS-102, No. 4, April 1983

[102] Y. Itho, N. Nagaoka, A. Ametani, "Transient Analysis of a crossbonded cable system underneath a bridge", IEEE Transaction on Power Delivery, Vol. 5, No. 2, Aprill 1990

11. Appendices

11.1 Appendix A - 2030 Western Denmark transmission grid

Figure 11.1 - 2030 Western Denmark transmission grid. Note Due to differences between the English and Danish names of some cities, the STSV-LEM link is named STS-LKR in the map

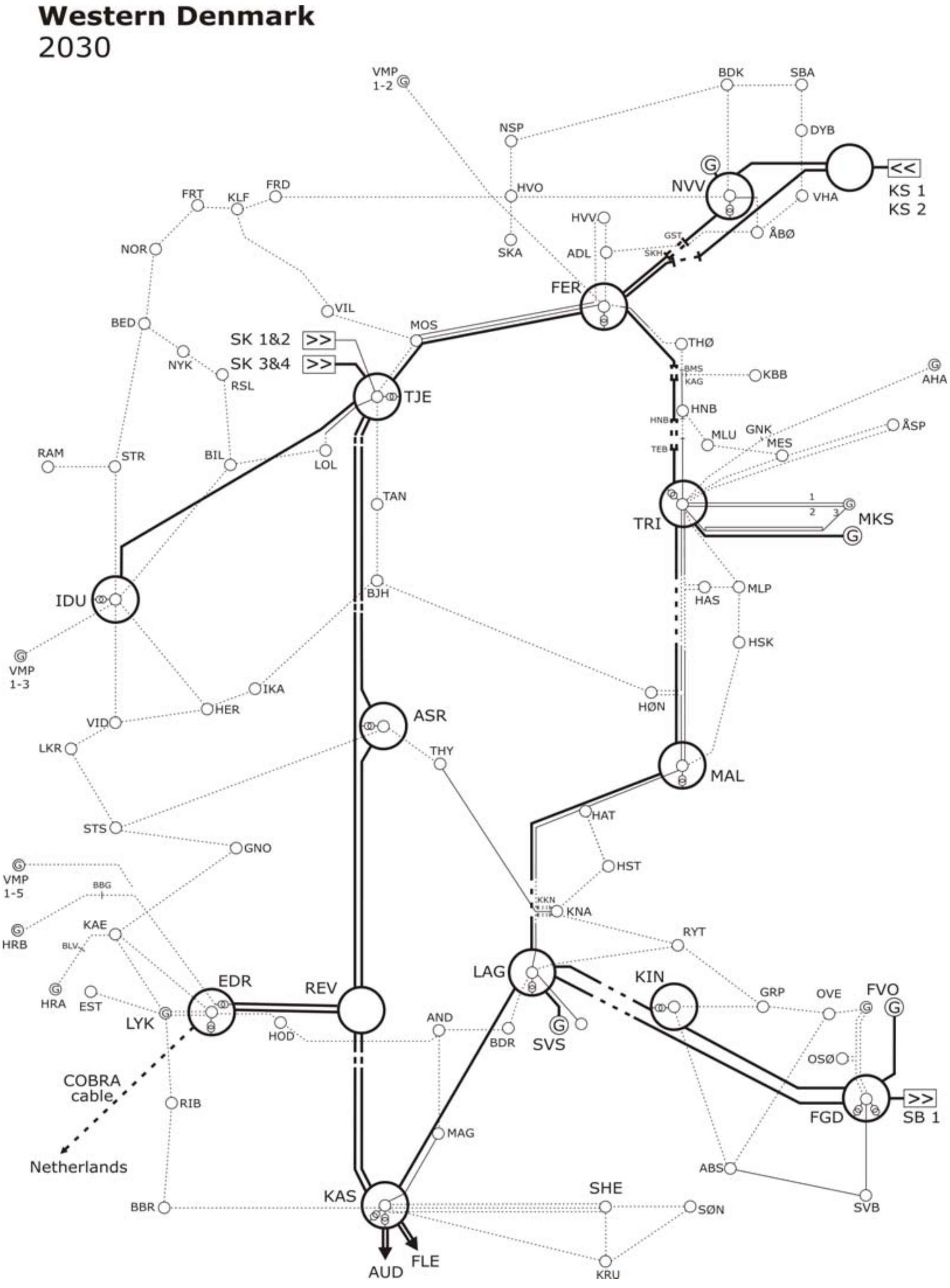

Figure 11.2 - Single-line diagram of the 2030 Western Denmark transmission grid. Note: Due to differences between the English and Danish names of some cities, the STSV-LEM link is named STS-LKR in the map

11.2 Appendix B - Frequency spectrums for the system conversation validation

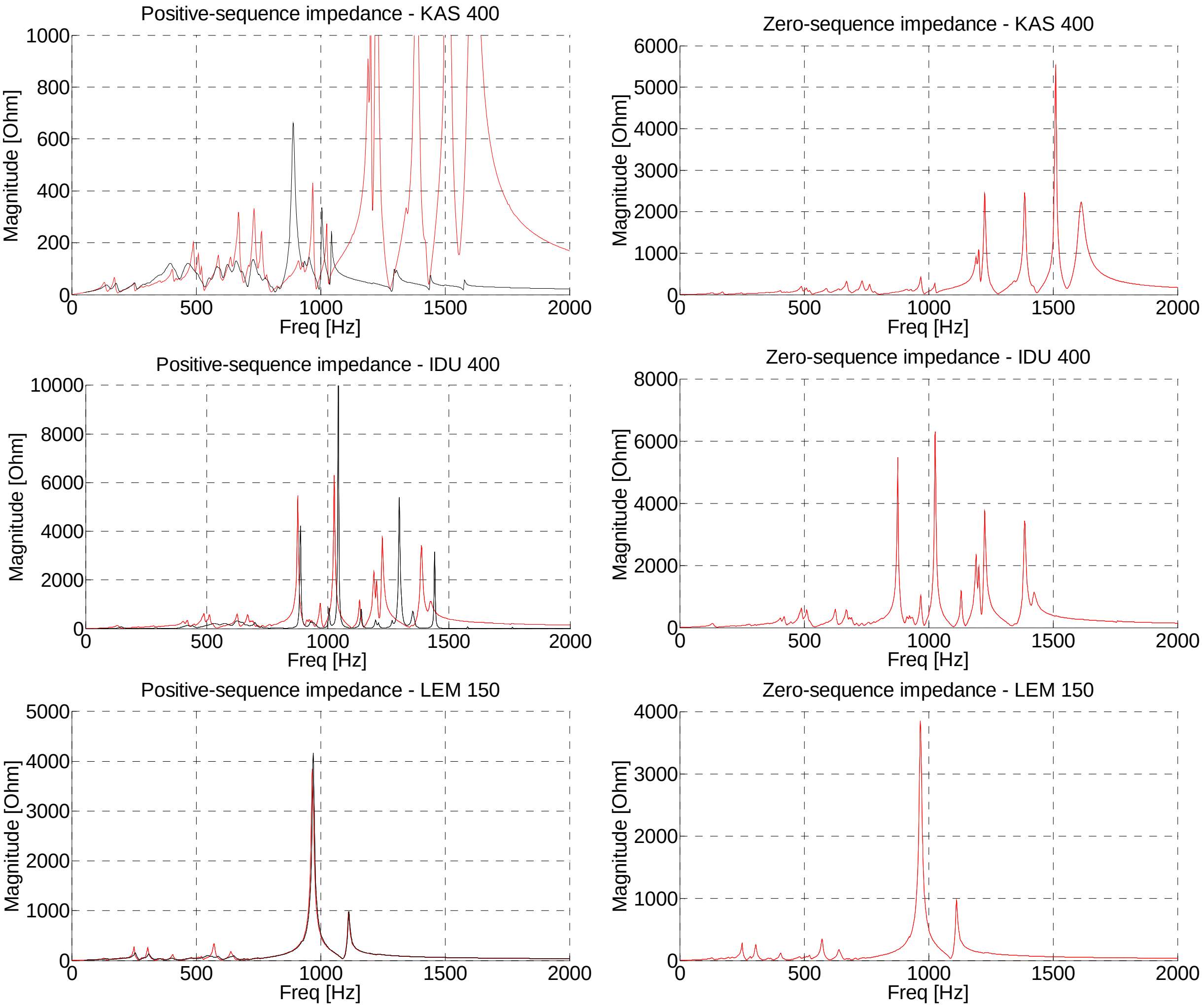

Figure 11.3 - Positive and zero sequence impedances for case 2 (Red: PSCAD; Black: Power Factory)

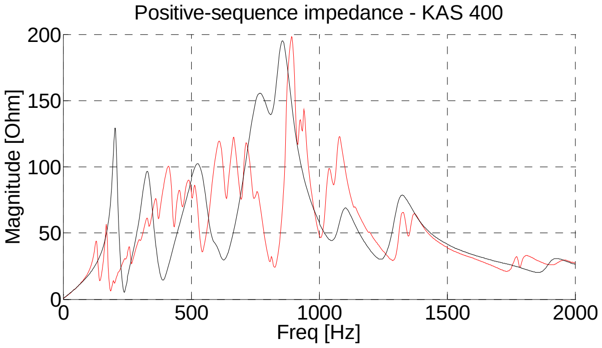

Figure 11.4 - Positive sequence impedance for case 3 (Black: Rest of system as equivalent grid; Red: Rest of the system using pi-models)

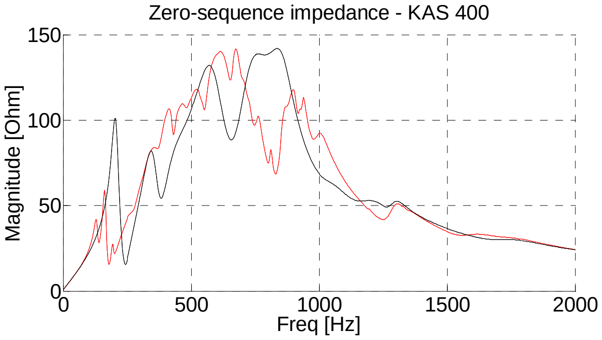

Figure 11.5 - Zero sequence impedance for case 3 (Black: Rest of system as equivalent grid; Red: Rest of the system using pi-models)

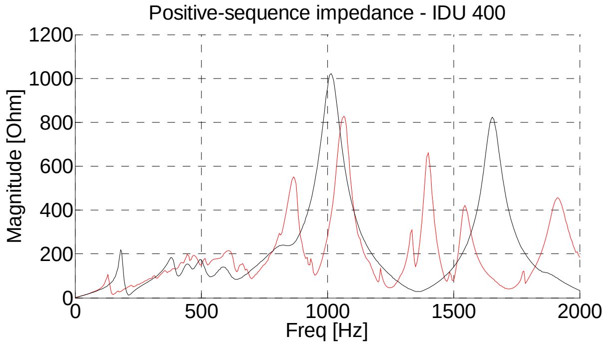

Figure 11.6 - Positive sequence impedance for case 4 (Black: Rest of system as equivalent grid; Red: Rest of the system using pi-models)

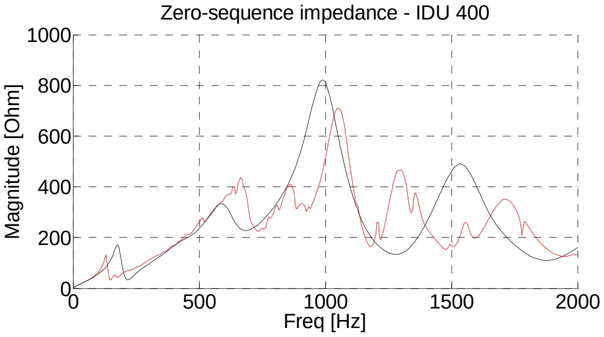

Figure 11.7 - Zero sequence impedance for case 4 (Black: Rest of system as equivalent grid; Red: Rest of the system using pi-models)

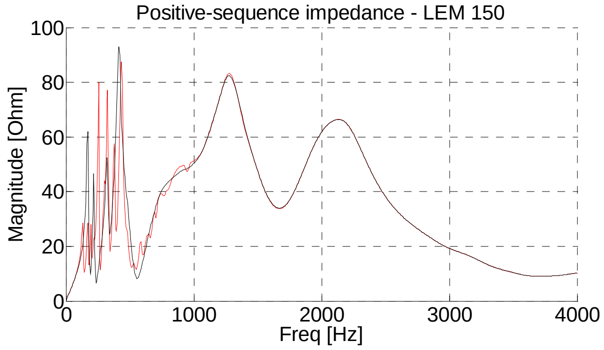

Figure 11.8 - Positive sequence impedance for case 5 (Black: Rest of system as equivalent grid; Red: Rest of the system using pi-models)

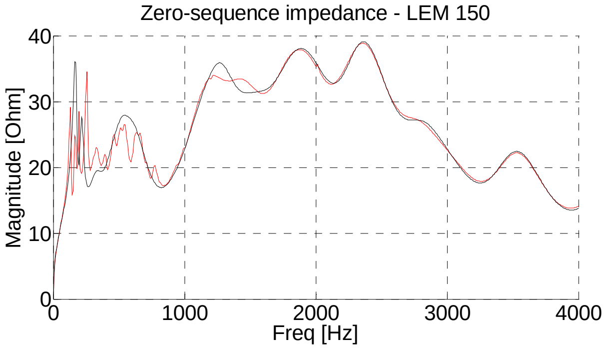

Figure 11.9 - Zero sequence impedance for case 5 (Black: Rest of system as equivalent grid; Red: Rest of the system using pi-models)

11.3 Appendix C - Calculation of the pre-insertion value to avoid zero-missing phenomenon

Considering V=V1cos(ωt):

$$V_2 = V_1\left(\frac{s}{s^2+\omega^2}\right) - R_p \cdot V_2\left(\frac{1}{s\cdot L_s + R_s} + sC + \frac{1}{R + sL + \dfrac{1}{sC}}\right) \Leftrightarrow$$

$$V_2\left(1 + R_p\left(\frac{1}{sL_s + R_s} + sC + \frac{sC}{R\cdot sC + s^2LC + 1}\right)\right) = V_1\left(\frac{s}{s^2+\omega^2}\right)$$

$$V_1 = V_2\left(\frac{s^2+\omega^2}{s} + R_p\left(\frac{s^2+\omega^2}{s\left(sL_s+R_s\right)} + C\left(s^2+\omega^2\right) + \frac{C\left(s^2+\omega^2\right)}{R\cdot sC + s^2LC + 1}\right)\right)$$

Making: $A = \dfrac{s^2+\omega^2}{s}$ and $B = \dfrac{s^2+\omega^2}{s\left(sL_s+R_s\right)} + C\left(s^2+\omega^2\right) + \dfrac{C\left(s^2+\omega^2\right)}{R\cdot sC + s^2LC + 1}$

Solving B:

$$\frac{s^2+\omega^2}{s\left(sL_s+R_s\right)} + C\left(s^2+\omega^2\right)\left(1 + \frac{1}{s^2LC + sRC + 1}\right) = \frac{s^2+\omega^2}{s^2L_s + sR_s} + C\left(s^2+\omega^2\right)\left(\frac{s^2LC + sRC + 1 + 1}{s^2LC + sRC + 1}\right) =$$

$$= \frac{\left(s^2+\omega^2\right)\left(s^2LC + sRC + 1\right) + C\left(s^2+\omega^2\right)\left(s^2L_s + sR_s\right)\left(s^2LC + sRC + 2\right)}{\left(s^2L_s + sR_s\right)\left(s^2LC + sRC + 1\right)} \quad \leftarrow \frac{(1)}{(2)}$$

Solving (2)

$$\left(s^2L_s + sR_s\right)\left(s^2LC + sRC + 1\right) = s^4L_sLC + s^3L_sRC + s^2L_s + s^3R_sLC + s^2R_sRC + sR_s =$$

$$= s^4L_sLC + s^3\left(L_sRC + R_sLC\right) + s^2\left(L_s + R_sRC\right) + sR_s$$

Solving (1)

$$\left(s^2+\omega^2\right)\left(s^2LC + sRC + 1\right) + C\left(s^2+\omega^2\right)\left(s^2L_s + sR_s\right)\left(s^2LC + sRC + 2\right)$$

Making: $1(A) = \left(s^2+\omega^2\right)\left(s^2LC + sRC + 1\right)$ and $1(B) = C\left(s^2+\omega^2\right)\left(s^2L_s + sR_s\right)\left(s^2LC + sRC + 2\right)$

Solving 1(A)

$$s^4LC + s^3RC + s^2 + s^2LC\omega^2 + sRC\omega^2 + \omega^2 = s^4LC + s^3RC + s^2\left(LC\omega^2 + 1\right) + sRC\omega^2 + \omega^2$$

Solving 1(B)

$$\begin{aligned}
&\left(s^2C + \omega^2C\right)\left(s^2L_s + sR_s\right)\left(s^2LC + sRC + 2\right) = \left(s^4L_sC + s^3R_sC + s^2\omega^2CL_s + sR_s\omega^2C\right)\left(s^2LC + sRC + 2\right)\\
&= s^6L_sLC^2 + s^5L_sRC^2 + s^4L_s2C + s^5R_sLC^2 + s^4R_sRC^2 + s^3R_s2C + s^4L_sL\omega^2C^2 + s^3\omega^2L_sRC^2 + s^2\omega^2 2CL_s +\\
&+ s^3R_sL\omega^2C^2 + s^2R_sR\omega^2C^2 + sR_s\omega^2 2C =\\
&= s^6L_sLC^2 + s^5\left(L_sRC^2 + R_sLC^2\right) + s^4\left(L_s2C + R_sRC^2 + L_sL\omega^2C^2\right) + s^3\left(R_s2C + \omega^2L_sRC^2 + R_sL\omega^2C^2\right) +\\
&+ s^2\left(\omega^2 2CL_s + R_sR\omega^2C^2\right) + sR_s\omega^2 2C
\end{aligned}$$

So $B = \dfrac{(1A) + (1B)}{(2)}$

Solving A, putting already the numerator of B:

$$\begin{aligned}
A &= \frac{s^2 + \omega^2}{s}\cdot\frac{s^4L_sLC + s^3\left(L_sRC + R_sLC\right) + s^2\left(L_s + R_sRC\right) + sR_s}{s^4L_sLC + s^3\left(L_sRC + R_sLC\right) + s^2\left(L_s + R_sRC\right) + sR_s} =\\
&= \left(s^2 + \omega^2\right)\cdot\frac{s^3L_sLC + s^2\left(L_sRC + R_sLC\right) + s^1\left(L_s + R_sRC\right) + R_s}{s^4L_sLC + s^3\left(L_sRC + R_sLC\right) + s^2\left(L_s + R_sRC\right) + sR_s} =\\
&= \frac{s^5L_sLC + s^4\left(L_sRC + R_sLC\right) + s^3\left(L_s + R_sRC\right) + s^2R_s}{s^4L_sLC + s^3\left(L_sRC + R_sLC\right) + s^2\left(L_s + R_sRC\right) + sR_s} +\\
&\frac{s^3L_sLC\omega^2 + s^2\left(L_sRC\omega^2 + R_sLC\omega^2\right) + s^1\left(L_s\omega^2 + R_sRC\omega^2\right) + R_s\omega^2}{s^4L_sLC + s^3\left(L_sRC + R_sLC\right) + s^2\left(L_s + R_sRC\right) + sR_s} =\\
&= \frac{s^5L_sLC + s^4\left(L_sRC + R_sLC\right) + s^3\left(L_s + R_sRC + L_sLC\omega^2\right) + s^2\left(R_s + L_sRC\omega^2 + R_sLC\omega^2\right)}{s^4L_sLC + s^3\left(L_sRC + R_sLC\right) + s^2\left(L_s + R_sRC\right) + sR_s} +\\
&+ \frac{s^1\left(L_s\omega^2 + R_sRC\omega^2\right) + R_s\omega^2}{s^4L_sLC + s^3\left(L_sRC + R_sLC\right) + s^2\left(L_s + R_sRC\right) + sR_s}
\end{aligned}$$

Calculations assuming that is Vsin(ωt) instead of Vcos(ωt):

$$V_2 = V_1\left(\frac{\omega}{s^2+\omega^2}\right) - R_p \cdot V_2\left(\frac{1}{s \cdot L_s + R_s} + sC + \frac{1}{R + sL + \frac{1}{sC}}\right) \Leftrightarrow$$

$$V_2\left(1 + R_p\left(\frac{1}{sL_s + R_s} + sC + \frac{sC}{R \cdot sC + s^2 LC + 1}\right)\right) = V_1\left(\frac{\omega}{s^2+\omega^2}\right)$$

$$V_1 = V_2\left(\frac{s^2+\omega^2}{\omega} + R_p\left(\frac{s^2+\omega^2}{sL_s\omega + R_s\omega} + sC\left(\frac{s^2+\omega^2}{\omega}\right) + \frac{sC}{R \cdot sC + s^2 LC + 1} \cdot \left(\frac{s^2+\omega^2}{\omega}\right)\right)\right) \Leftrightarrow$$

$$\Leftrightarrow V_1 = V_2\left(\frac{s^2+\omega^2}{\omega} + R_p\left(\frac{s^2+\omega^2}{sL_s\omega + R_s\omega} + sC\left(s^2+\omega^2\right)\left(\frac{1}{\omega} + \frac{1}{s^2 LC\omega + sRC\omega + \omega}\right)\right)\right)$$

Making: $A = \frac{s^2+\omega^2}{\omega}$ and $B = \frac{s^2+\omega^2}{sL_s\omega + R_s\omega} + sC\left(s^2+\omega^2\right)\left(\frac{1}{\omega} + \frac{1}{s^2 LC\omega + sRC\omega + \omega}\right)$

Solving B:

$$\frac{s^2+\omega^2}{sL_s\omega + R_s\omega} + sC\left(s^2+\omega^2\right)\left(\frac{1}{\omega} + \frac{1}{s^2 LC\omega + sRC\omega + \omega}\right) =$$

$$= \frac{s^2+\omega^2}{sL_s\omega + R_s\omega} + \left(s^3 C + s\omega^2 C\right)\left(\frac{s^2 LC\omega + sRC\omega + 2\omega}{s^2 LC\omega^2 + sRC\omega^2 + \omega^2}\right)$$

Making:

$B(1) = \left(s^2+\omega^2\right)\left(s^2 LC\omega^2 + sRC\omega^2 + \omega^2\right)$ and $B(2) = \left(s^3 C + s\omega^2 C\right)\left(s^2 LC\omega + sRC\omega + 2\omega\right)\left(sL_s\omega + R_s\omega\right)$

Solving B(1):

$$\left(s^2+\omega^2\right)\left(s^2 LC\omega^2 + sRC\omega^2 + \omega^2\right) = s^4 LC\omega^2 + s^3 RC\omega^2 + s^2\left(\omega^2 + LC\omega^4\right) + sRC\omega^4 + \omega^4$$

Solving B(2):

$$
\begin{aligned}
&\left(s^3C+s\omega^2C\right)\left(s^2LC\omega+sRC\omega+2\omega\right)\left(sL_s\omega+R_s\omega\right)=\\
&=\left(s^5LC^2\omega+s^4RC^2\omega+s^3 2C\omega+s^3LC^2\omega^3+s^2RC^2\omega^3+s2C\omega^3\right)\left(sL_s\omega+R_s\omega\right)=\\
&=s^6LC^2L_s\omega^2+s^5LC^2R_s\omega^2+s^5RL_sC^2\omega^2+s^4RR_sC^2\omega^2+s^4 2CL_s\omega^2+s^4LL_sC^2\omega^4+s^3 2CR_s\omega^2+\\
&+s^3LR_sC^2\omega^4+s^3RL_sC^2\omega^4+s^2RR_sC^2\omega^4+s^2 2CL_s\omega^4+s2R_sC\omega^4=\\
&=s^6LC^2L_s\omega^2+s^5\left(LC^2R_s\omega^2+RL_sC^2\omega^2\right)+s^4\left(RR_sC^2\omega^2+2CL_s\omega^2+LL_sC^2\omega^4\right)+\\
&+s^3\left(2CR_s\omega^2+LR_sC^2\omega^4+RL_sC^2\omega^4\right)+s^2\left(RR_sC^2\omega^4+2CL_s\omega^4\right)+s2R_sC\omega^4
\end{aligned}
$$

Numerator (N):

$$
\begin{aligned}
&\left(sL_s\omega+R_s\omega\right)\left(s^2LC\omega^2+sRC\omega^2+\omega^2\right)=\\
&=s^3LL_sC\omega^3+s^2L_sRC\omega^3+sL_s\omega^3+s^2LCR_s\omega^3+sRCR_s\omega^3+R_s\omega^3=\\
&=s^3LL_sC\omega^3+s^2\left(L_sRC\omega^3+LCR_s\omega^3\right)+s\left(L_s\omega^3+RCR_s\omega^3\right)+R_s\omega^3
\end{aligned}
$$

Solving A:

$$
\begin{aligned}
&\left(\frac{s^2+\omega^2}{\omega}\right)\left(\frac{s^3LL_sC\omega^3+s^2\left(L_sRC\omega^3+LCR_s\omega^3\right)+s\left(L_s\omega^3+RCR_s\omega^3\right)+R_s\omega^3}{s^3LL_sC\omega^3+s^2\left(L_sRC\omega^3+LCR_s\omega^3\right)+s\left(L_s\omega^3+RCR_s\omega^3\right)+R_s\omega^3}\right)=\\
&=\left(s^2+\omega^2\right)\left(\frac{s^3LL_sC\omega^2+s^2\left(L_sRC\omega^2+LCR_s\omega^2\right)+s\left(L_s\omega^2+RCR_s\omega^2\right)+R_s\omega^2}{s^3LL_sC\omega^3+s^2\left(L_sRC\omega^3+LCR_s\omega^3\right)+s\left(L_s\omega^3+RCR_s\omega^3\right)+R_s\omega^3}\right)
\end{aligned}
$$

Denominator of A:

$$
\begin{aligned}
&\left(s^2+\omega^2\right)\left(s^3LL_sC\omega^2+s^2\left(L_sRC\omega^2+LCR_s\omega^2\right)+s\left(L_s\omega^2+RCR_s\omega^2\right)+R_s\omega^2\right)=\\
&=s^5LL_sC\omega^2+s^4\left(L_sRC\omega^2+LCR_s\omega^2\right)+s^3\left(L_s\omega^2+RCR_s\omega^2\right)+s^2R_s\omega^2+\\
&+s^3LL_sC\omega^4+s^2\left(L_sRC\omega^4+LCR_s\omega^4\right)+s\left(L_s\omega^4+RCR_s\omega^4\right)+R_s\omega^4=\\
&=s^5LL_sC\omega^2+s^4\left(L_sRC\omega^2+LCR_s\omega^2\right)+s^3\left(L_s\omega^2+RCR_s\omega^2+LL_sC\omega^4\right)+\\
&+s^2\left(L_sRC\omega^4+LCR_s\omega^4+R_s\omega^2\right)+s\left(L_s\omega^4+RCR_s\omega^4\right)+R_s\omega^4
\end{aligned}
$$

Numerator is equal to the one of B.

The final solution is:

$$V_1(s)=V_2\left(\frac{A}{N}+\frac{B(1)+B(2)}{N}\right)$$

11.4 Appendix D - Matlab code for the calculation of the pre-insertion resistor

```
clear
clc

%system parameters
V=(2/3)^0.5*165e3;
w=2*pi*50;
length=47.49;
R=0.0442*length;
L=0.115/w*length;
C=(length*6.671945673e-5)/(2*w);
Ls=1.0062;
Rs=0.659;

%control variables
Rp=1;
control_variable=0;
num_nans=0;

%The closing condition is not to have DC component what means to have a
%peak value at 10ms that doesn't have almost any DC component.
%This means that the the value of Is at 10ms should be equal to the initial
%value of the DC component

%Initial DC component value
Isa=-V/(Rs^2+(w*Ls)^2)^0.5*cos(w*0-atan(w*Ls/Rs)-pi/2);

%Is this case the control variable has a tolerance of 10A

while (control_variable>Isa+3 || control_variable<Isa-3)

    total=0;
    Cur=0;

        if  num_nans==0
    componente_DC(Rp)=control_variable;
    else
        componente_DC(Rp)=componente_DC(Rp-3);
    end


    %Rp is the value of the pre-insertion resistance, the step of its value
    %depends of the precision wanted and the time that the user is willing to wait

    Rp=Rp+1

    %denominator is 1(a)=b + 1(B)=c + (A)=a

    a=[0 L*C*Ls*w^2 Ls*R*C*w^2+L*C*Rs*w^2 Ls*w^2+R*C*Rs*w^2+L*Ls*C*w^4 Rs*w^2+Ls*R*C*w^4+L*C*Rs*w^4
Ls*w^4+R*C*Rs*w^4 Rs*w^4];
    b=[0 0 L*C*w^2 R*C*w^2 w^2+L*C*w^4 R*C*w^4 w^4];
    c=[L*Ls*C^2*w^2 L*C^2*Rs*w^2+R*Ls*C^2*w^2 R*Rs*C^2*w^2+2*C*Ls*w^2+L*Ls*C^2*w^4
2*C*Rs*w^2+L*Rs*C^2*w^4+R*Ls*C^2*w^4 R*Rs*C^2*w^4+2*C*Ls*w^4 2*Rs*C*w^4 0];

    d=a+b*Rp+c*Rp;

    %numerator will be n

    n=[L*Ls*C*w^3 Ls*R*C*w^3+L*C*Rs*w^3 Ls*w^3+R*C*Rs*w^3 Rs*w^3];

    %method of partial fraction in order to make easier the convertion to
    %time domain

    [r,p,k]=residue(n,d);

    %invocation of symbolic mathematic toolbox
    %without it, would be necessary to do the inverse laplace transform by hand
```

```
    syms s

    %it was noticed that the method of partial fraction origins always 6
    %elements

    for i=1:size(r)
        time(i)=r(i)/(s-p(i));
    end

    total=sum(time);

    %total is the voltage after the pre-insertion resistance
    %Current_Is is the current in the shunt

    Current_Is=total/(s*Ls+Rs);
    Current_t=ilaplace(Current_Is);

    %control variable will be the value of the current Is at 10ms

    t=10e-3;
    control_variable=subs(V*Current_t);

    teste(Rp)=control_variable;

    %because of the numeric precision of matlab some times the control
    %variable will have a non-defined value. when that happens the program
    %increases the value of the pre-insertion resistance and try again

    num_nans=isnan(control_variable);
    if num_nans~=0;
        control_variable=100;
    end

    %carefull with value below, it works for this situation but for other
    %cases can be too small

    if(Rp>700)
        break
    end
end
```

11.5 Appendix E - De-energisation of a cable and a shunt reactor together (without mutual coupling)

To show the influence of a shunt reactor in a de-energisation, the equations for the system shown in Figure 11.10 will be written.

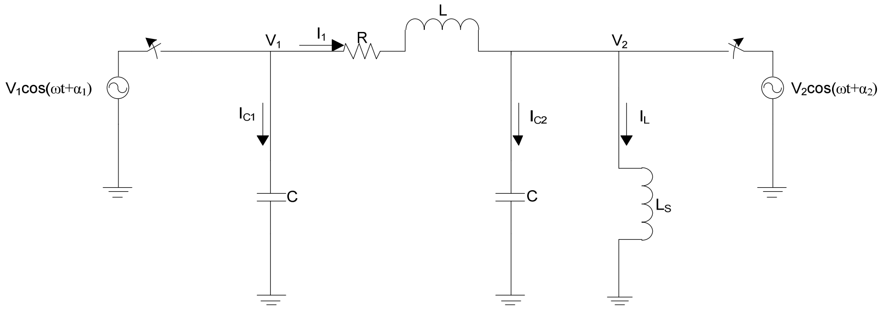

Figure 11.10 – Single-line diagram for the disconnection of the system cable+shunt reactor

$$\begin{cases} V_1 - V_2 = I_1\left(sL - R\right) - LI_1\left(0\right) \\ I_{C1} = sCV_1 - CV_1\left(0\right) \\ I_{C2} = sCV_2 - CV_2\left(0\right) \\ V_2 = sL_sI_L - L_SI_L\left(0\right) \\ I_L = I_1 - I_{C2} \end{cases} \tag{70}$$

Solving the system is obtained the following voltage for V$_2$.

$$V_2 = \frac{A \cdot N_1}{N_2\left(N_1 - B\right)} + \frac{C}{N_1 - B} \tag{71}$$

Where:

$$A = sL_SC\left(V_1\left(0\right) + V_2\left(0\right)\right) - L_SI_S\left(0\right) \tag{72}$$

$$B = -s^2L_SC \tag{73}$$

$$C = s^2L_SC\left(I_1\left(0\right)L - sLCV_1\left(0\right) - RCV_1\left(0\right)\right) \tag{74}$$

$$N_1 = \left(s^2CL_s + 1\right) \cdot \left(s^2LC + sCR + 1\right) \tag{75}$$

$$N_2 = s^2CL_S + 1 \tag{76}$$

The equation (71) will be numerically solved using Matlab. If the cable inductance (L) is not considered and the following values are used, (77) is obtained:

C=1μF
R=1Ω
L_shunt=1H
V1(0)=150kV
V2(0)=130kV

$$V = 140\frac{(\cos(707.1t) - 1.5157\times10^{-4}\times\sin(707.1t)}{\exp\left(\frac{t}{8}\right)} - \frac{10}{\exp(2000000t)}kV \tag{77}$$

Observing (77) it is easy to see that it can be simplified without loss of accuracy to (78).

$$V = 140\frac{\cos(707.1t)}{\exp\left(\frac{t}{8}\right)}kV \tag{78}$$

By changing the parameters, it is possible to see how they influence the results.

- When the initial voltages V1(0) or V2(0), the only changes are in the amplitude of the voltage.

Example:

$V = 115\frac{\cos(707.1t)}{\exp\left(\frac{t}{8}\right)}$, if V1(0)=100kV and V2(0)=130kV

$V = 125\frac{\cos(707.1t)}{\exp\left(\frac{t}{8}\right)}$, if V1(0)=150kV and V2(0)=100kV

So it can be concluded that the amplitude is the average of the initial voltages at both cable ends.

- Changes in the resistance value only changes the decay time. The decaying time constant is directly proportional to R.

Example:

$$V = 140\frac{\cos(707.1t)}{\exp\left(\frac{5t}{8}\right)}kV, \quad \text{if R=5}\Omega$$

- Changes in the shunt reactor inductance influence the resonance frequency and the decay time. The decaying time constant is inversely proportional to L. The resonance frequency is inversely proportional to the square root of L.

Example:

$$V = 140\frac{\cos(316.2t)}{\exp\left(\frac{t}{40}\right)}kV, \quad \text{if Ls=5H}$$

- Changes in the cable capacitance influence the resonance frequency, which is inversely proportional to the square root of C.

$$V = 140\frac{\cos(316.2t)}{\exp\left(\frac{t}{8}\right)}kV, \quad \text{if C=5}\mu\text{F}$$

So the equation is:

$$V = \frac{V1(0)+V2(0)}{2}\cdot\frac{\cos\left(\frac{1}{\sqrt{2LsC}}t\right)}{\exp\left(\frac{Rt}{8Ls}\right)}kV$$

Note: The number 2 in the resonance frequency is because C is half of the cable capacitance

To verify the deduction made before, the following values will be used: R=0.513 Ω; Ls=0.6 5H; C=1.6811 µF, V1(0)=124 kV, V2(0)=87 kV.
The expected result is:

$$V = 105.5\cdot\frac{\cos(674.4t)}{\exp(0.099t)}kV$$

The equation obtained using Matlab was:

$$V = 105.5 \cdot \frac{\cos(674.4t) - 9.4692 \times 10^{-5} \sin(105.5)}{\exp(0.099t)} - 18.5 \exp(-2319000t)\, kV$$

Reference should be made to the amplitude of the second negative exponential. Its value is equal to half of the difference between V1(0) and V2(0), and this exponential is present in order to maintain the continuity in the voltage, which in $t=0^+$ is equal to V2(0), i.e. the voltage in the shunt reactor end. If the voltage in both ends is equal, this component will not be present.

In the previous equation, the cable inductance is not considered. Doing it would introduce a second sinusoidal with a very high damping.

$$V = 139.96 \frac{(\cos(707t) - 1.5157 \times 10^{-4} \times \sin(707.1t)}{\exp\left(\frac{t}{8}\right)} - 9.968 \frac{(\cos(44720t) - 1.11 \times 10^{-2} \times \sin(44720t)}{\exp(499.9t)} kV$$

The first part of the equation is equal to the previous, with the exception of the amplitude, which decreases by 0.0286%.

The amplitude of this high frequency component is proportional to the difference between the initial voltages at both cable ends. As this difference is usually very small, this component has almost no influence on the result, and it is not necessary to consider it. The exception is if there is a large difference between the voltage at both ends of the cable (example: clearing a fault).

Even if there is a large difference between the voltages, what will happen is that the amplitude of the first component is much reduced and there are no changes in the maximum peak value. As an example, (79) presents the equation and Figure 11.11 the plot for the disconnection when V2(0)=0. In this case the second component of the equation has an amplitude equal to the amplitude of the first component, which is half of V1(0). In this way, the peak value continues to be 150 kV, i.e. V1(0), but as the high frequency component is damped very fast, there is also a fast decrease in the voltage in the moments after the de-energisation, and only the first component remains, which is lower than it would be if the difference between the voltages were smaller.

$$V = 75 \frac{\cos(707t)}{\exp\left(\frac{t}{8}\right)} - 75 \frac{\cos(44720t)}{\exp(499.9t)} kV \qquad (79)$$

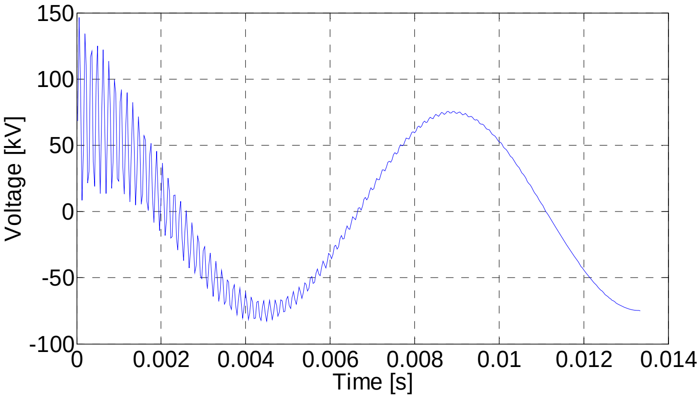

Figure 11.11 – Voltage during cable de-energisation if $V_1(0)=0$

11.6 Appendix F - De-energisation of a cable and a shunt reactor together (with mutual coupling)

The introduction of mutual coupling substantially increases the equations complexity, and it is no longer possible to use a single-phase system. In order to solve the equations, the cable is simplified to a capacitor, the system being the one presented in Figure 11.12, modelled by (80), whose matricial form is shown in (81).

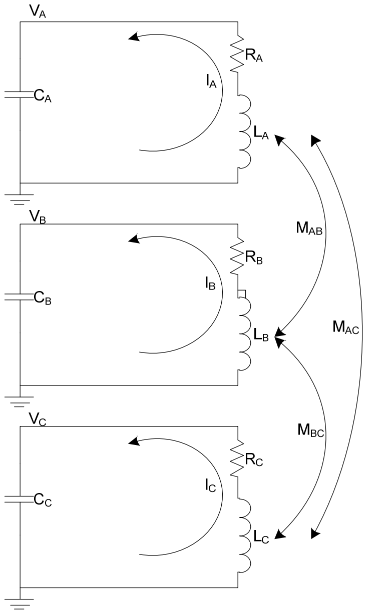

Figure 11.12 – System used to study the cable and shunt reactor de-energisation considering mutual coupling

$$\begin{cases} -V_A - R_A I_A = L_A \dfrac{dI_A}{dt} + M_{AB}\dfrac{dI_B}{dt} + M_{AC}\dfrac{dI_C}{dt} \\ C_A \dfrac{dV_A}{dt} = I_A \\ -V_B - R_B I_B = L_B \dfrac{dI_B}{dt} + M_{BA}\dfrac{dI_A}{dt} + M_{BC}\dfrac{dI_C}{dt} \\ C_B \dfrac{dV_B}{dt} = I_B \\ -V_C - R_C I_C = L_C \dfrac{dI_C}{dt} + M_{CA}\dfrac{dI_A}{dt} + M_{CB}\dfrac{dI_B}{dt} \\ C_C \dfrac{dV_C}{dt} = I_C \end{cases} \tag{80}$$

$$\frac{d}{dt}\begin{bmatrix} I_A \\ V_A \\ I_B \\ V_B \\ I_C \\ V_C \end{bmatrix} = \begin{bmatrix} L_A & 0 & M_{AB} & 0 & M_{AC} & 0 \\ 0 & C_A & 0 & 0 & 0 & 0 \\ M_{BA} & 0 & L_B & 0 & M_{BC} & 0 \\ 0 & 0 & 0 & C_B & 0 & 0 \\ M_{CA} & 0 & M_{CB} & 0 & L_C & 0 \\ 0 & 0 & 0 & 0 & 0 & C_C \end{bmatrix}^{-1} \begin{bmatrix} -R_A & -1 & 0 & 0 & 0 & 0 \\ 1 & 0 & 0 & 0 & 0 & 0 \\ 0 & 0 & R_B & -1 & 0 & 0 \\ 0 & 0 & 1 & 0 & 0 & 0 \\ 0 & 0 & 0 & 0 & -R_C & -1 \\ 0 & 0 & 0 & 0 & 1 & 0 \end{bmatrix} \begin{bmatrix} I_A \\ V_A \\ I_B \\ V_B \\ I_C \\ V_C \end{bmatrix} \tag{81}$$

The system can be solved by Matlab using the function ODE45, which uses the Dormand-Prince method, based on the Runge-Kutta algorithm.

To calculate the initial conditions, it is assumed that the voltage is at peak value at the disconnection instant, that no current chopping occurs, i.e. the current is zero when the CB opens, and that the phases open in the following sequence, A-C-B. The initial conditions are shown in (82) where V is the voltage amplitude.

$$\begin{cases} V_A(0) = V\cos\left(\omega_r 6.666\times10^{-3}\right) \\ I_A(0) = \dfrac{V\cos\left(\omega_r 6.666\times10^{-3} - \dfrac{\pi}{2}\right)}{\sqrt{R_A^2 + \left(\omega_r L_A\right)^2}} \\ V_B(0) = V \\ I_B(0) = 0 \\ V_C(0) = -V\cos\left(\omega_r 3.333\times10^{-3}\right) \\ I_C(0) = \dfrac{-V\cos\left(\omega_r 3.333\times10^{-3} - \dfrac{\pi}{2}\right)}{\sqrt{R_C^2 + \left(\omega_r L_C\right)^2}} \end{cases} \tag{82}$$

Equation (81) is simplified to (83).

$$\frac{d}{dt}A = B^1 CA \Leftrightarrow \frac{d}{dt}A = DA \tag{83}$$

The eigenvalues (λ) and eigenvectors (δ) of D are calculated. After knowing these values it can be calculated the auxiliary variable x (85) and k (86), which are 6x1 matrix. And obtain the currents and voltages using (87).

$$\lambda_i = a \pm jb \tag{84}$$

$$x = e^{at}\delta\left(\cos\left(bt\right) \pm j\sin\left(bt\right)\right) \tag{85}$$

$$\begin{bmatrix} k_1 \\ k_2 \\ k_3 \\ k_4 \\ k_5 \\ k_6 \end{bmatrix} = \begin{bmatrix} \delta_1 & \delta_2 & \delta_3 & \delta_4 & \delta_5 & \delta_6 \end{bmatrix}^{-1} \begin{bmatrix} I_A(0) \\ V_A(0) \\ I_B(0) \\ V_B(0) \\ I_C(0) \\ V_C(0) \end{bmatrix} \tag{86}$$

$$A = \sum_{i=1}^{6} k_i^T x_i \tag{87}$$

Example:

Considering the following data: V=134.7kV; R=0.34Ω; L=1.46H; C=10.09μF; all mutual inductances equal to -0.1H.

$$\begin{bmatrix} \lambda_1 \\ \lambda_2 \\ \lambda_3 \\ \lambda_4 \\ \lambda_5 \\ \lambda_6 \end{bmatrix} = \begin{bmatrix} -0.13 + j280.5 \\ -0.13 - j280.5 \\ -0.11 + j252.1 \\ -0.11 - j252.1 \\ -0.11 + j252.1 \\ -0.11 - j252.1 \end{bmatrix} \tag{88}$$

$$\delta_1 = \delta_2^* = \begin{bmatrix} j0.0016 \\ 0.5773 \\ j0.0016 \\ 0.5773 \\ j0.0016 \\ 0.5773 \end{bmatrix} \quad \delta_3 = \delta_4^* = \begin{bmatrix} j0.0020 \\ 0.8165 \\ -j0.0010 \\ -0.402 \\ -j0.0015 \\ -0.4136 \end{bmatrix} \quad \delta_5 = \delta_6^* = \begin{bmatrix} -j0.0002 \\ -0.0625 \\ +j0.0019 \\ 0.7363 \\ -j0.0017 \\ -0.6738 \end{bmatrix} \tag{89}$$

$$\begin{bmatrix} k_1 \\ k_2 \\ k_3 \\ k_4 \\ k_5 \\ k_6 \end{bmatrix} = \begin{bmatrix} 10.9939 - j12.0771 \\ 10.9939 + j12.0771 \\ -19.2322 - j120.9141 \\ -19.2322 + j120.9141 \\ 118.088 - j55.6764 \\ 118.088 + j55.6764 \end{bmatrix} \tag{90}$$

$$\begin{aligned} I_A(t) = {} & (10.9939 - j12.0771)(j0.0018)e^{-0.13}\left(\cos(280.5t) + j\sin(280.5t)\right) + \\ & + (10.9930 + j12.0771)(-j0.0018)e^{-0.13}\left(\cos(280.5t) - j\sin(280.5t)\right) + \\ & + k_3x_3 + k_4x_4 + k_5x_5 + k_6x_6 \end{aligned} \tag{91}$$

$$
\begin{aligned}
V_A(t) = {} & (10.9939 - j12.0771)(0.5773)e^{-0.13}\left(\cos(280.5t) + j\sin(280.5t)\right) + \\
& + (10.9939 - j12.0771)(0.5773)e^{-0.13}\left(\cos(280.5t) - j\sin(280.5t)\right) + \\
& + k_3x_3 + k_4x_4 + k_5x_5 + k_6x_6
\end{aligned}
\qquad (92)
$$

....

....

If the mutual inductances are all equal, it is possible to have an expression for the calculation of the frequencies, which is given by (93). Equation (93) can be simplified to (94) with a minimum loss of accuracy.

$$
\begin{aligned}
f_1 &= \frac{\sqrt{C\left(CR^2 - 4L + 4M\right)}}{2C(L-M)} \\
f_2 &= \frac{\sqrt{C\left(CR^2 - 4L + 4M\right)}}{2C(L-M)} \\
f_3 &= \frac{\sqrt{C\left(-CR^2 + 4L + 8M\right)}}{2C(L+2M)}
\end{aligned}
\qquad (93)
$$

$$
\begin{aligned}
f_1 &\approx \sqrt{\frac{1}{C(L-M)}} \\
f_2 &\approx \sqrt{\frac{1}{C(L-M)}} \\
f_3 &\approx \sqrt{\frac{1}{C(L+2M)}}
\end{aligned}
\qquad (94)
$$

Different mutual inductances

For different mutual inductances it is not so simple to obtain a direct expression. The analytical solving is very difficult, as the eigenvalues will go up to power six.

Instead of solving the equations deduction methods were tried. The thesis author varied the mutual inductance values and tried to find equations that would fit the numerical results obtained. Equation (94) is used as starting point for the deduced equations.

The author found that (95) fits the numerical results very closely, and that it can be used to calculate the resonance frequencies as long as the mutual inductance values are several times smaller than the self-inductance, which is the normal situation.

$$
\begin{aligned}
f_1 &\approx \sqrt{\frac{1}{C\left(L-M_{Max}\right)}} \\
f_2 &\approx \sqrt{\frac{1}{C\left(L-M_{Min}\right)}} \\
f_3 &\approx \sqrt{\frac{1}{C\left(L+2M_{avg}\right)}}
\end{aligned}
\qquad (95)
$$

Demonstration

The equations will first be demonstrated for: M_{AB}=-0.05 H; M_{BC}=-0.035 H; M_{AC} € [-0.1 -0.002] H. The simulated cable is the 47.49 km NVV-BDK cable, compensated at 45% (L=1.46H). Figure 11.13 shows the simulation results, comparing the frequencies calculated by (95) and through numerical resolution of (83). The maximum error is inferior to 0.35%.

If the mutual inductance increases too much for values close to the self-inductance, the error increases substantially.

Figure 11.14 repeats the results shown in Figure 11.13, but for M_{AC} € [-1 -0.002] H. The error increases when M_{AC} increases, up to approximately 21% for M_{AC}=-1H. If the self-inductance also increases, the error would be smaller. For a self-inductance 10 times larger, the maximum error would be less than 1%.

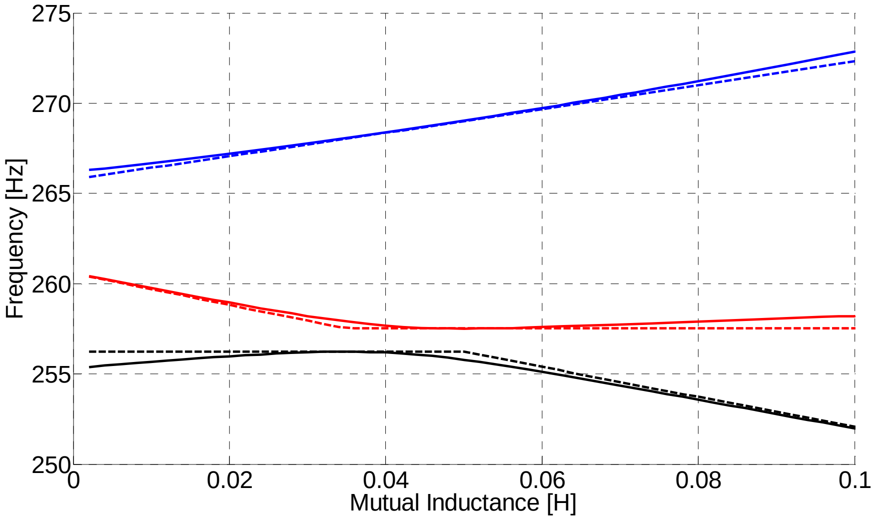

Figure 11.13 - Frequencies calculated according to (95) (dashed lines) and (83) (solid lines)

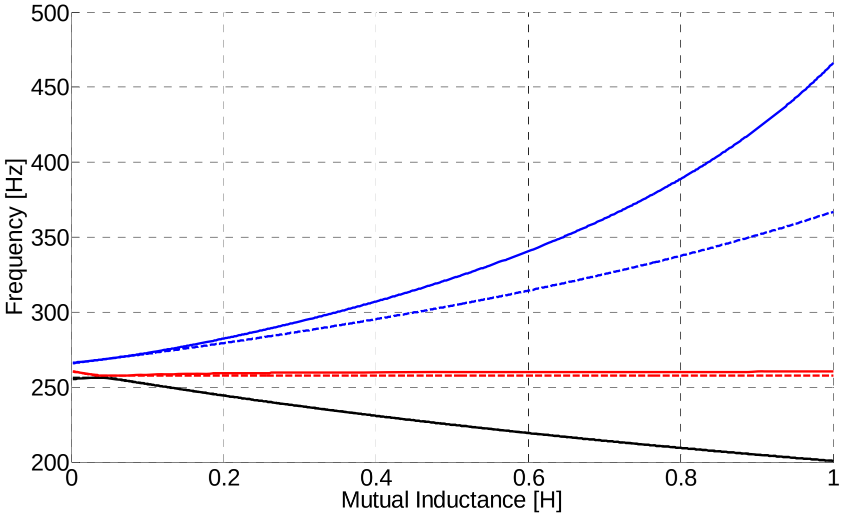

Figure 11.14 - Frequencies calculated according to (95) (dashed lines) and (83) (solid lines)

The equation verification was extended, and all mutual inductances were varied: M_{AB} € [-0.1 -0.002] H; M_{BC} € [-0.1 -0.002] H; M_{AC} € [-0.1 -0.002] H. The variation step was equal to 0.004 H, in a total of 15625 simulations (25x25x25).

The maximum error is lower than 3.5% for f_1 and 1% for f_2 and f_3, reinforcing the accuracy of (95).

The author of the thesis would like to emphasise that (95) was not demonstrated mathematically. Thus, the equation accuracy is not 100% guaranteed, but from the cased analysed it could be seen that the equation was accurate, and that from a logical point of view it makes sense.

11.7 Appendix G - De-energisation of a cable and a shunt reactor together after a single-phase-to-ground fault (with mutual coupling)

Equal to the example in Appendix F but without mutual coupling between phase C and the other two phases. It is equivalent to have a fault in phase C.

$$\begin{bmatrix} \lambda_1 \\ \lambda_2 \\ \lambda_3 \\ \lambda_4 \\ \lambda_5 \\ \lambda_6 \end{bmatrix} = \begin{bmatrix} -0.90 + j270 \\ -0.90 - j270 \\ -0.79 + j252 \\ -0.79 - j252 \\ -0.84 + j261 \\ -0.84 - j261 \end{bmatrix} \tag{96}$$

$$\delta_1 = \delta_2^* = \begin{bmatrix} j0.0019 \\ 0.7071 \\ j0.0019 \\ 0.7071 \\ 0 \\ 0 \end{bmatrix} \quad \delta_3 = \delta_4^* = \begin{bmatrix} j0.0018 \\ 0.7071 \\ -j0.0018 \\ -0.7071 \\ 0 \\ 0 \end{bmatrix} \quad \delta_5 = \delta_6^* = \begin{bmatrix} 0 \\ 0 \\ 0 \\ 0 \\ j0.0026 \\ 1 \end{bmatrix} \tag{97}$$

$$\begin{bmatrix} k_1 \\ k_2 \\ k_3 \\ k_4 \\ k_5 \\ k_6 \end{bmatrix} = \begin{bmatrix} 39.74 - j45.47 \\ 39.74 + j45.47 \\ -55.52 - j48.38 \\ -55.52 + j48.38 \\ -43.51 + j51.57 \\ -43.51 - j51.57 \end{bmatrix} \tag{98}$$

As it can be seen in (97), the voltages and currents of phase A and B are not influenced by phase C and the voltage and current in phase C is not influenced by phases A and B.

The imaginary parts of the eigenvalues (96) are different, meaning that the voltages and the currents in phases A and B will have a component whose frequency is equal to the difference between these imaginary parts, 2.58 Hz in this specific case. This low frequency component is also present in example 1.

The reason for the increase in the overvoltage when in the presence of a single-ground fault is found in (98), where $k_{1,2}$ absolute values are practically equal to the absolute value of $k_{3,4}$, something that does not happen in example 1. As these values are practically equal, the low-frequency component has an amplitude approximately equal to the amplitude of the resonance frequency component.

The peak voltage is the summation of the resonance frequency component and the low frequency component, and as the low-frequency component amplitude is larger in example 2, the overvoltage is also larger in example 2.

As an example, the voltage in the moments after the disconnection for both examples is shown in Figure 11.15, Figure 11.16 and Figure 11.17. It can be seen that in example 2 the maximum peak value and the minimum peak value are larger and smaller, respectively, because of the largest amplitude of the low frequency beating.

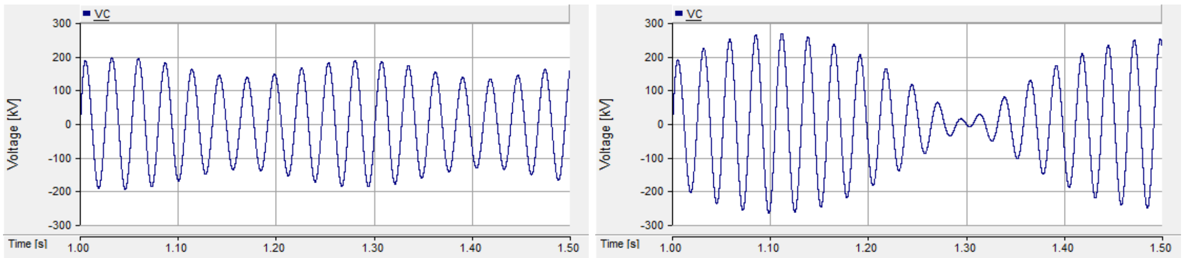

(a) (b)

Figure 11.15 – Voltage after disconnection in Phase A. a) Example 1; b) Example 2

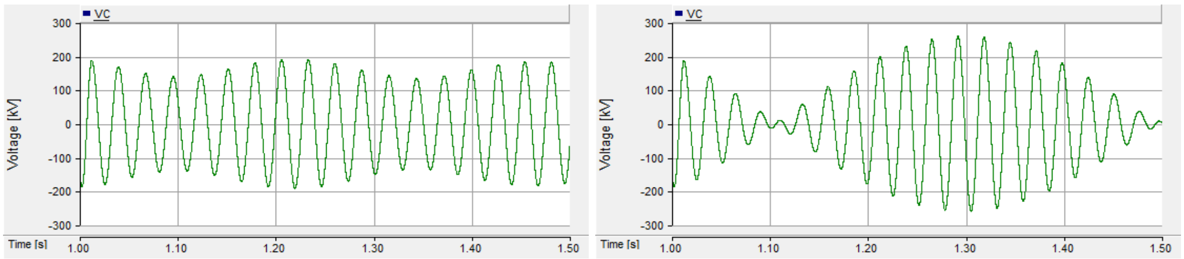

(a) (b)

Figure 11.16 - Voltage after disconnection in Phase B. a) Example 1; b) Example 2

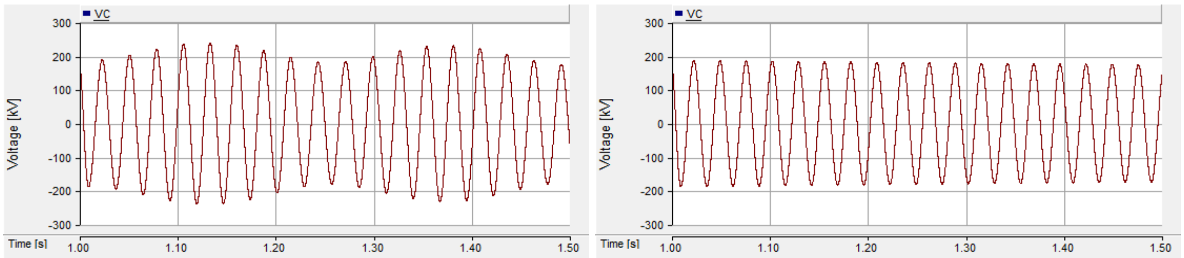

(a) (b)

Figure 11.17 - Voltage after disconnection in Phase C. a) Example 1; b) Example 2

An interesting aspect is that the increase in the overvoltage is only noticeable if there are 6.666 ms between the openings of the two non-faulted phases. If the time difference is only of 3.333ms, no increase is noticed. In this situation (no mutual inductance between phase B and the other two phases) the absolute values of $k_{1,2}$ and $k_{4,5}$ (see (99)) are no longer similar and therefore the amplitude of the low-frequency component is not as high.

Note that this does not mean that the larger overvoltage will only be present if there is 6.666 ms between the opening of the phases, as *k* depends on all parameters, e.g. capacitance, inductance, etc… .

$$\begin{bmatrix} k_1 \\ k_2 \\ k_3 \\ k_4 \\ k_5 \\ k_6 \end{bmatrix} = \begin{bmatrix} -33.6560 - j13.4605 \\ -33.6560 + j13.4605 \\ -33.7321 + j84.0529 \\ -33.7321 - j84.0529 \\ 67.3613 - j0.0333 \\ 67.3613 + j0.0333 \end{bmatrix} \tag{99}$$

11.8 Appendix H - Energisation of cables in parallel - Theoretical equations

For the calculations the system is seen as two lossless pi-models in parallel Figure 11.18.

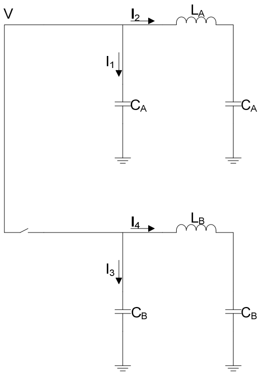

Figure 11.18 - System used to calculate the inrush current frequency

The currents are calculated as shown in (100). The second cable is considered as being unload; thus, all initial conditions are equal to zero.

$$\begin{cases} I_1 = sC_AV - C_AV(0) \\ I_2 = \dfrac{sC_AV - C_AV(0) + sL_AC_AI_2(0) - L_AC_A\dot{I}_2(0)}{s^2L_AC_A + 1} \\ I_3 = sC_BV \\ I_4 = \dfrac{sC_BV}{s^2L_BC_B + 1} \end{cases} \tag{100}$$

The value $V(0)$ should not be the same in I_1 and I_2 as the voltage is not constant in all of the cable. In a well-designed system, however, the difference should be minor, and thus the values are considered equal. The cable is mostly capacitive. Therefore, $V(0)$ is considered as equal to the peak voltage, $I_2(0)$ to zero and $\dot{I}_2(0)$ to the peak current.

Continuing to developing (100), (101) is obtained.

$$V\left(sC_A + \frac{sC_A}{s^2L_AC_A + 1} + sC_B + \frac{sC_B}{s^2L_BC_B + 1}\right) = C_AV(0) + \frac{L_AC_A\dot{I}_2(0)}{s^2L_AC_A + 1} \tag{101}$$

Equal cables

If the cables are equal, L_A is equal to L_B and C_A to C_B, and (101) is written as (102), where $C=C_A=C_B$ and $L=L_A=L_B$. The current into the cable is then given by (103)

$$V=\frac{s^2LC^2V(0)+CV(0)+LC\dot{i}_2(0)}{s\left(s^2 2LC^2+4C\right)} \tag{102}$$

$$I=\frac{LC\dot{i}_2(0)}{s^2 2CL+2}+\frac{CV(0)}{2} \tag{103}$$

By applying the inverse Laplace transform on (103), (104) is obtained, and the resonance frequency (105), where C is now the total cable capacitance.

$$I(t)=\frac{\sin\left(\sqrt{\frac{1}{LC}}t\right)\sqrt{LC}\dot{i}_2(0)}{2}+\frac{CV(0)\delta(t)}{2} \tag{104}$$

$$\omega_r=\sqrt{\frac{2}{LC}} \tag{105}$$

Different length cables

The relation between the capacitance and inductance of the two cables is given by (106) and (107).

$$C_B=xC_A \quad \wedge \quad C=C_A \tag{106}$$

$$L_B=yL_A \quad \wedge \quad \mathrm{L}=L_A \tag{107}$$

Equation (101) is written as (108), and the current is equal to (109).

$$V=\frac{s^4\left(yxL^2C^3V(0)\right)+s^2\left(yxLC^2V(0)+LC^2V(0)+yxL^2C^2\dot{i}_2(0)\right)+CV(0)+LC\dot{i}_2(0)}{s\left(s^4\left(yx^2L^2C^3+yxL^2C^3\right)+s^2\left(yx^2LC^2+2xLC^2+2yxLC^2+LC^2\right)+\left(2xC+2C\right)\right)} \tag{108}$$

$$\begin{aligned}I=&\frac{C\left(s^4\left(yxL^2C^3V(0)\right)+s^2\left(yxLC^2V(0)+LC^2V(0)+yxL^2C^2\dot{i}_2(0)\right)+CV(0)+LC\dot{i}_2(0)\right)}{s^4\left(yx^2L^2C^3+yxL^2C^3\right)+s^2\left(yx^2LC^2+2xLC^2+2yxLC^2+LC^2\right)+\left(2xC+2C\right)}+\\&\frac{C\left(s^4\left(yxL^2C^3V(0)\right)+s^2\left(yxLC^2V(0)+LC^2V(0)+yxL^2C^2\dot{i}_2(0)\right)+CV(0)+LC\dot{i}_2(0)\right)}{\left(s^2LC+1\right)\left(s^4\left(yx^2L^2C^3+yxL^2C^3\right)+s^2\left(yx^2LC^2+2xLC^2+2yxLC^2+LC^2\right)+\left(2xC+2C\right)\right)}\end{aligned} \tag{109}$$

The partial fractions method cannot be applied to (109), as the numerator and denominator of the first term have the same order of the magnitude (s^4). Applying the propriety of Linearity, (109) is separated into two terms. This first term represents (110) in the frequency domain. Therefore, the frequency of I_3 is equal to the frequency of V, which can be calculated from (108).

$$I_3 = C_B \frac{dV}{dt} \tag{110}$$

The partial fractions method is applied to the second part of the polynomial, which represents the current I_4, (111).

$$V = L_B \frac{dI_4}{dt} + \frac{1}{C_B}\int I_4 dt \tag{111}$$

The roots are conjugated complexes (112). Thus, the second part of (109) can be written as (113).

$$\begin{gathered}
\alpha_1 = \pm\sqrt{-\frac{1}{LC}} \\
\alpha_2 = \pm\sqrt{-\frac{yx^2 + 2yx + 2x + 1 - \sqrt{y^2x^4 + 4y^2x^3 - 4yx^3 + 4y^2x^2 - 6yx^2 + 4x^2 - 4yx + 4x + 1}}{2CL\left(yx^2 + yx\right)}} \\
\alpha_3 = \pm\sqrt{-\frac{yx^2 + 2yx + 2x + 1 + \sqrt{y^2x^4 + 4y^2x^3 - 4yx^3 + 4y^2x^2 - 6yx^2 + 4x^2 - 4yx + 4x + 1}}{2CL\left(yx^2 + yx\right)}}
\end{gathered} \tag{112}$$

$$I = \frac{A1s + A2}{\left(s-\alpha_1\right)\left(s-\alpha_1^*\right)} + \frac{A3s + A4}{\left(s-\alpha_2\right)\left(s-\alpha_2^*\right)} + \frac{A5s + A6}{\left(s-\alpha_3\right)\left(s-\alpha_3^*\right)} \tag{113}$$

Solving (113), (114) is obtained.

$$\begin{gathered}
A1 = 0 \\
A2 = yx^2L^3C^4\dot{I}_2(0) + yxL^3C^4\dot{I}_2(0) \\
A3 = 0 \\
A4 = yxL^2C^3\left[\frac{\sqrt{y^2x^4 + 4y^2x^3 - 4yx^3 + 4y^2x^2 - 6yx^2 + 4x^2 - 4yx + 4x + 1}\left(V(0) - L\dot{I}_2(0) - xL\dot{I}_2(0)\right) + yx^3L\dot{I}_2(0) + yx^2\left(3L\dot{I}_2(0) - V(0)\right) + 2yx\left(L\dot{I}_2(0) - V(0)\right) - 2x^2L\dot{I}_2(0) - 3xL\dot{I}_2(0) + V(0) - L\dot{I}_2(0)}{2\sqrt{y^2x^4 + 4y^2x^3 - 4yx^3 + 4y^2x^2 - 6yx^2 + 4x^2 - 4yx + 4x + 1}}\right] \\
A5 = 0 \\
A6 = -yxL^2C^3\left[\frac{\sqrt{y^2x^4 + 4y^2x^3 - 4yx^3 + 4y^2x^2 - 6yx^2 + 4x^2 - 4yx + 4x + 1}\left(-V(0) + L\dot{I}_2(0) + xL\dot{I}_2(0)\right) + yx^3L\dot{I}_2(0) + yx^2\left(3L\dot{I}_2(0) - V(0)\right) + 2yx\left(L\dot{I}_2(0) - V(0)\right) - 2x^2L\dot{I}_2(0) - 3xL\dot{I}_2(0) + V(0) - L\dot{I}_2(0)}{2\sqrt{y^2x^4 + 4y^2x^3 - 4yx^3 + 4y^2x^2 - 6yx^2 + 4x^2 - 4yx + 4x + 1}}\right]
\end{gathered}$$

(114)

Thus, the resonance frequencies are calculated by (115) (where C is now the total cable capacitance). The frequencies of (109) first term are equal to (115)

$$\omega_{r1,2}^{2}=\frac{\left(yx^{2}+2yx+2x+1\right)\pm\sqrt{y^{2}x^{4}+4y^{2}x^{3}-4yx^{3}+4y^{2}x^{2}-6yx^{2}+4x^{2}-4yx+4x+1}}{CL\left(yx^{2}+yx\right)}\qquad(115)$$

The resonance frequency corresponding to α_1 is not considered because the term A2 is, for normal values of capacitance and inductance, several thousands of times smaller than A4 and A6.

If the two cables are of the same type, y is equal to x and (115) is simplified to (116) (where C is now the total cable capacitance).

$$\omega_{r1,2}^{2}=\frac{\left(x^{3}+2x^{2}+2x+1\right)\pm\sqrt{x^{6}+4x^{5}-6x^{3}+4x+1}}{CL\left(x^{3}+x^{2}\right)}\qquad(116)$$

Validation

Equation (108) can be numerically solved by Matlab if all variables are known. Table 11.1 shows the frequencies calculated using (115) and by numerically solving (108).
The simulations parameters are those of the 47.49km NVV-BDK cable:
C=10.087μF
L=16.797mH
$V(0)$=202kV
$\dot{I}_2(0)$=532A

Table 11.1 - Comparison of the frequencies when using Matlab or (115)

	x=0.75;y=0.75	**x=0.5;y=0.5**	**x=0.75;y=0.25**	**x=0.65;y=0.35**	**x=0.1;y=0.9**
f_1 (Matalb)	608	656	638	643	738
f_1 (equation)	608	656	638	643	738
f_2 (Matlab)	927	1289	1530	1378	1911
f_2 (equation)	927	1289	1530	1378	1911

This first validation seems to confirm the accuracy of the equation, but it does not fully confirm the results as simplifications were made before (108), most notably the use of lossless cables and to consider the grid as being very weak. As a result, the results are compared with simulations made in PSCAD.
The comparison with PSCAD is more complicated for two reasons:

- The amplitude of the frequency components is not the same, and in some situations one of the frequencies is dominant;
- The frequency of the simulated inrush current is obtained through SFFT, which is not 100% accurate for transients;

As a result, it was decided to compare the dominant frequency only. Table 11.2 shows the frequencies obtained. The errors are acceptable, and the equations are considered validated.

Table 11.2 - Comparison of the frequencies when using PSCAD or (115)

	x=0.75;y=0.75	**x=0.5;y=0.5**
f_1 (equation)	952	1289
f_2 (PSCAD)	980	1155
Error (%)	-2.86	11.6%

Simplification

The equation can be simplified at the expense of accuracy. Instead of using a pi-model, the cable can be considered as an inductor in series with a capacitor, Figure 11.19.

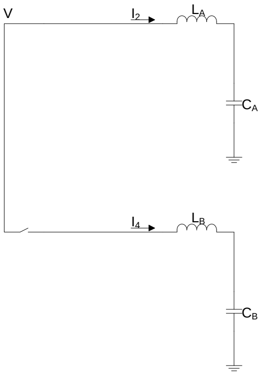

Figure 11.19 - Simplified system used to calculate the inrush current frequency

Equation (101) is written as (117), and the resonance frequency is equal to (118).

$$V(t)=\frac{V(0)+L\dot{I}_2}{x+1}+\frac{LC\cos\left(\sqrt{\frac{x+1}{LCx+LCxy}}t\right)\left(V(0)+L\dot{I}_2\right)(yx-1)}{(LCx+LCxy)(x+1)} \tag{117}$$

$$f_r=\frac{1}{2\pi}\sqrt{\frac{x+1}{LCx+LCxy}} \tag{118}$$

On the one hand (118) is much simpler than (115), but on the other hand it only provides one of the resonance frequencies and with a substantial error if the second cable being energised is much smaller, as shown in Table 11.3.

Table 11.3 - Comparison of the frequencies when using simple or complex formulas

	x=0.75;y=0.75	**x=0.5;y=0.5**	**x=0.75;y=0.25**	**x=0.65;y=0.35**	**x=0.1;y=0.9**
f_1 (simple)	631	773	747	750	1316
f_1 (complex)	608	656	638	643	738
f_2 (complex)	927	1289	1530	1378	1911
Error (%)	3.8	17.8	17.1	16.6	78.3

11.9 Appendix I - Matlab calculation of maximum overvoltage for a hybrid cable-OHL

The first step in the algorithm is to define the relation between the different reflection and refraction coefficients (119).

$$\begin{aligned} k_{bb} &= -k_{aa} \\ k_{ab} &= 1 + k_{aa} \\ k_{ba} &= 1 - k_{aa} \end{aligned} \tag{119}$$

Where, k_{aa} is the reflection coefficient between the first and second line, k_{bb} the reflection coefficient between the second and first line, k_{ab} the refraction coefficient between the first and second line and k_{ba} the refraction coefficient between the second and first line (see Figure 11.20).

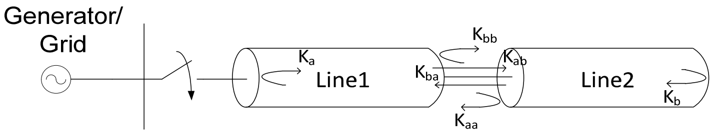

Figure 11.20 – Reflection and refraction coefficients for a hybrid line

Historically, the analysis of travelling waves and their reflection and refractions was made using lattice diagrams as originally proposed in [81]. Starting from a lattice diagram similar to the one shown in Figure 11.21, a binomial tree as shown in Figure 11.22 is designed.

Each of the tree's nodes represents the voltage in Line2 receiving end and has an equivalent travelling time and multiplication coefficient.

The node 1 represents the first wave reaching the end of Line2, having as travelling time *ta+tb* and multiplication coefficient $k_{ab}.k_b$. The following nodes are built in the following way (compare Figure 11.22 with Figure 11.21 to better understand the logic behind the algorithm):

- If going to the left, it is considered that the wave that was reflected/refracted in the joint point is now reaching the Line2 receiving end. Therefore *2ta* is added;
- If going to the right, it is considered that the wave that reached the receiving end in the father node is reflected back to the joint, from there reflecting back into the Line2 receiving end. Therefore *tb* is added two times;
- If going to the right, the multiplication coefficient of the father node is multiplied by $k_{bb}.k_b$. It is always the reflection in the joint of the wave that was previously reflected in Line2 receiving end;
- If going to the left two situations can happen:
  - If the father node is even, the multiplication coefficient of the father node is multiplied by $k_{aa}.k_a$. In this case the wave reaching the Line2 receiving end is the wave that was previously reflected back in the joint and it is not refracted to Line2.
  - If the father node is odd, the multiplication coefficient of the father node is multiplied by $k_{ba}.k_a.k_{ba}$ and divided by k_{bb}. In this case the wave reaching the Line2 receiving end is the

wave that after reaching Line2 receiving end is refracted to Line1 and refracted again to Line2;

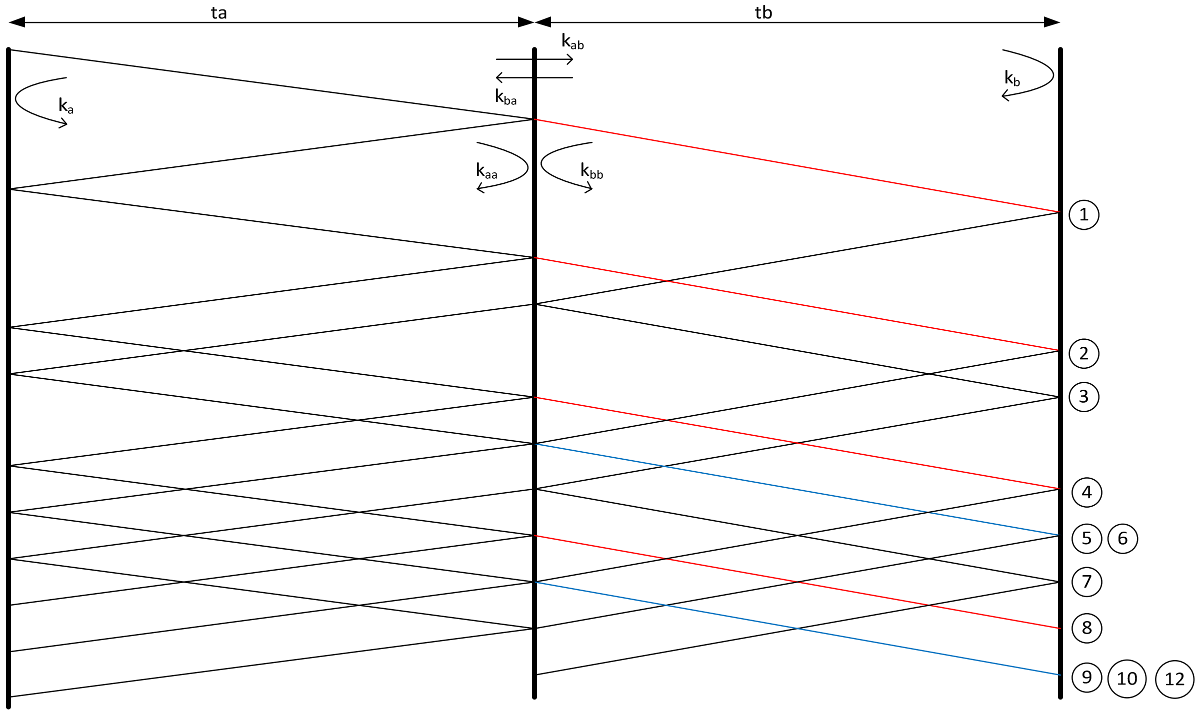

Figure 11.21 – General Lattice diagram. Black: Reflection; Red: Refraction; Blue: Superimpose reflection and refraction

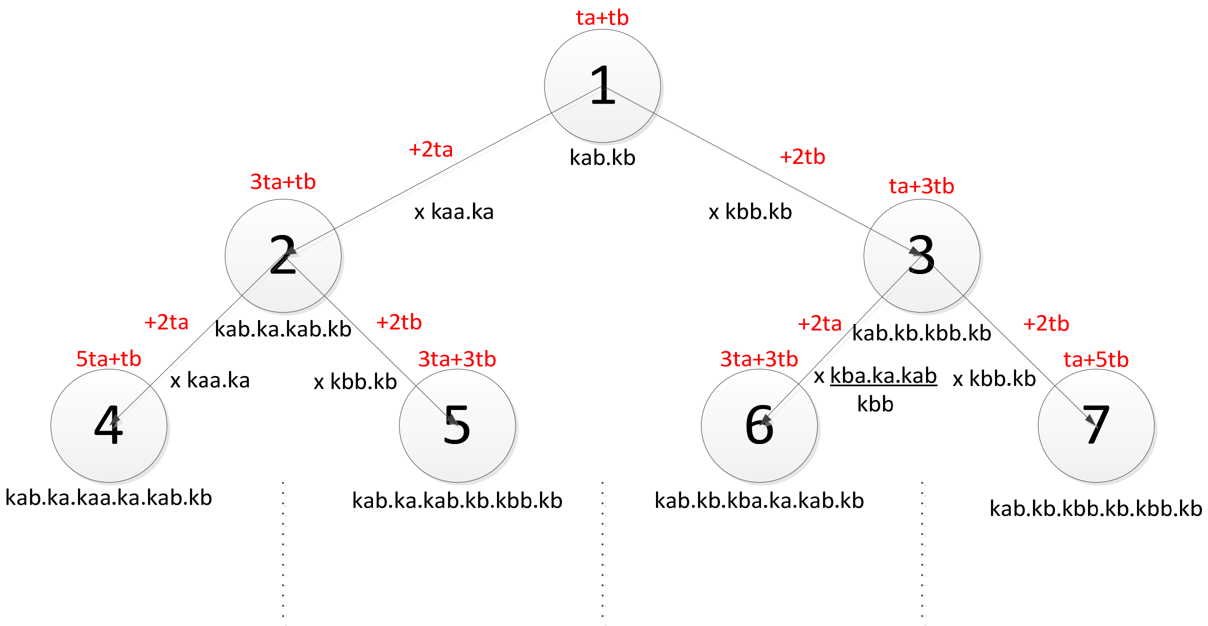

Figure 11.22 – Binomial tree used to calculate the maximum voltage

After all the nodes' travelling times and multiplication coefficients has been calculated, it is necessary to organise the nodes by crescent travelling times. At this point it is necessary to be careful so that some nodes are not erased since several nodes have equal travelling times (e.g. nodes 5 and 6).

The voltage in the receiving end for each node is equal to (120) where V_{send} is the original wave sending voltage (±2 pu in the worst-case scenario) and k the node multiplication coefficient.

$$V(n) = 2V_{send} \cdot k(n) \tag{120}$$

The voltage in the receiving end at a given time *t* is given by (121), where *n(t)* is the node in the time sorted list corresponding to *t* and $V_{initial}$ the line initial voltage value (typical ±1pu).

$$V(t) = \sum_{n=1}^{n(t)} V(n) + V_{initial} \tag{121}$$

Limitation

The big limitation of this method is associated with the tree length, as the algorithm is accurate only up to a time defined by (122), where *d* is the tree deepness:

$$t < d \cdot ta + tb, \quad \text{if } tb > ta \tag{122}$$

The maximum voltage depends on both refractions and reflections, it being impossible to predict the maximum overvoltage instant for a hybrid OHL-cable. For short cables, i.e. smaller *tb*, this is not a problem as the maximum will occur in the first instants, but as the length increases, this maximum will occur more later, thus making a larger tree necessary. As the algorithm is of the order $O(2^n)$, this method is too heavy to be used.

11.10 Appendix J - Code for the estimation of the required modelling distance

```
%open the PSS/E file and get the grid information
%the PSS/E file is separed in two, one containg the busbars and other
%containng the branchs. This division is made in order to allow Matlab to
%read the information

busbars=load('busbar.raw');
% branch=load('branch_with_ohl.raw');
branch=load('branch_long_cable.raw');

%the node being energised/re-energised
restriked_node=80301;
%The coaxial speed of the wave in a cable (not possible to calculate from
%the PSS/E file
speed1=179; % in m per microsecond
%The coaxial speed of the wave in an OHL
speed2=280;
 %the time required to the first cable peak
charg_time=518; %in microseconds
%all these values should be inseted by the user

%Desing connection and speed matrices
%x means a connection between the busbars, where x is the length. 0 means no connection

size_bus=length(busbars);

t=1;
for a=1:size_bus
    if (busbars(a,4)==80 && busbars(a,2)==165)
        tempora_bus(t)=busbars(a,1);
        t=t+1;
    end
end

num_busbars=length(tempora_bus);

matrix_connection=zeros(num_busbars,num_busbars);
matrix_speed=zeros(num_busbars,num_busbars);

size_branches=length(branch); %number of branches

for a=1:size_branches
    aux1=branch(a,1);
    aux2=branch(a,2);
    for b=1:num_busbars
        if aux1==tempora_bus(b)
            if tempora_bus(b)==restriked_node
                restriked_bus=b;
            end
            size_c(a)=branch(a,16)*1000;%the cable length is in m
            for c=1:num_busbars
                if aux2==tempora_bus(c)
                    matrix_connection(b,c)=size_c(a);
                    matrix_connection(c,b)=size_c(a);
                    if branch(a,15)==2
                        matrix_speed(b,c)=speed2;
                        matrix_speed(c,b)=speed2;
                    end
                    if branch(a,15)==1
                        matrix_speed(b,c)=speed1;
                        matrix_speed(c,b)=speed1;
                    end
                end
            end
        end
    end
end


%calculates all possible paths up to 8 busbars of distance
%calculates the time for each of the paths nodes
t=1;
for a=1:num_busbars
    if matrix_connection(restriked_bus,a)~=0;
        aux(1)=matrix_connection(restriked_bus,a)/matrix_speed(restriked_bus,a);
        for b=1:num_busbars
            if matrix_connection(a,b)~=0 && b~=restriked_bus;
                aux(2)=matrix_connection(a,b)/matrix_speed(a,b);
```

```
                for c=1:num_busbars
                    if matrix_connection(b,c)~=0 && c~=a;
                        aux(3)=matrix_connection(b,c)/matrix_speed(b,c);
                        for d=1:num_busbars
                            if matrix_connection(c,d)~=0 && d~=b;
                                aux(4)=matrix_connection(c,d)/matrix_speed(c,d);
                                for e=1:num_busbars
                                    if matrix_connection(d,e)~=0 && e~=c;
                                        aux(5)=matrix_connection(d,e)/matrix_speed(d,e);
                                        for f=1:num_busbars
                                            if matrix_connection(e,f)~=0 && f~=d;
                                                aux(6)=matrix_connection(e,f)/matrix_speed(e,f);
                                                for g=1:num_busbars
                                                    if matrix_connection(f,g)~=0 && g~=e;
                                                        aux(7)=matrix_connection(f,g)/matrix_speed(f,g);
                                                        for h=1:num_busbars
                                                            if matrix_connection(g,h)~=0 && h~=f;
                                                               aux(8)=matrix_connection(g,h)/matrix_speed(g,h);
                                                                times_total(t)=sum(aux);
                                                                times_aux(t,:)=cumsum(aux);
                                                                sequencia(t,1:8)=[a,b,c,d,e,f,g,h];
                                                                t=t+1;
                                                            end
                                                        end
                                                    end
                                                end
                                            end
                                        end
                                    end
                                end
                            end
                        end
                    end
                end
            end
        end
    end
end


%The node 8 in one of the sequences may be the node 2 in other of the
%sequences. In this case is not necessary to model so many nodes of
%distance
%this function calculates how many nodes of distance are necessary to model
%for each of the sequences
for a=1:length(sequencia)
    for c=1:8
        if charg_time<1.9*times_aux(a,c) %1,9 instead of 2 to give a security interval
            conta_levels(1:8)=10;
            for b=1:length(sequencia)
                if sequencia(a,c)==sequencia(b,1)
                    %                  'needs 1'
                    conta_levels(1)=1;
                end
                if sequencia(a,c)==sequencia(b,2)
                    %                  'needs 2'
                    conta_levels(2)=2;

                end
                if sequencia(a,c)==sequencia(b,3)
                    %                  'needs 3'
                    conta_levels(3)=3;
                end
                if sequencia(a,c)==sequencia(b,4)
                    %                  'needs 4'
                    conta_levels(4)=4;
                end
                if sequencia(a,c)==sequencia(b,5)
                    %                  'needs 5'
                    conta_levels(5)=5;
                end
                if sequencia(a,c)==sequencia(b,6)
                    %                  'needs 6'
                    conta_levels(6)=6;
                end
                if sequencia(a,c)==sequencia(b,7)
                    %                  'needs 7'
                    conta_levels(7)=7;
                end
            end
            conta_levels_aux(a)=min(conta_levels);
            caminho(a,1:c)=sequencia(a,1:c);
```

```
            break
        end
    end
end

num_levels=max(conta_levels_aux)


%select the paths and the busbars that have to be in the system
bus_memo(1)=restriked_node;
z=1;
control_var=0;
for a=1:length(sequencia)
    for b=1: b=1:length(caminho(1,:))
        control_var=0;
        if caminho(a,b)~=0
            caminho_names(a,b)=tempora_bus(caminho(a,b));
            for c=1:z
                if tempora_bus(caminho(a,b))==bus_memo(c)
                    control_var=1;
                end
            end
            if control_var==0
                bus_memo(z+1)=tempora_bus(caminho(a,b));
                z=z+1;
            end
        end
    end
end

%bus_memo has the the busbars that have to be in the system
%caminho_names has all the paths
%num_levels has the required modelling dep
```

11.11 Appendix K - Values for the sensitivity analysis

Table 11.4 - Thickness of the cable layers for a deviation in the thickness of the conductor

Cross-Section	Layer	Reference	1%	5%	10%	15%	20%
800mm2	Rc1	0.01685	0.0170185	0.0176925	0.018535	0.0193775	0.02022
	Ri1	**0.03505**	**0.0352185**	**0.0358925**	**0.036735**	**0.0375775**	**0.03842**
	Rc2	0.035479	0.0356475	0.0363215	0.037164	0.0380065	0.038849
	Ri2	0.0415	0.0416685	0.0423425	0.043185	0.0440275	0.04487
	y2	1.17231	1.172604972	1.173772374	1.175231627	1.17669088	1.178150132
	x2	0.04175	0.0419185	0.0425925	0.043435	0.0442775	0.04512
	Cond. res.	3.12189E-08	3.18464E-08	3.44188E-08	3.77748E-08	4.1287E-08	4.49552E-08
1200mm2	Rc1	0.022	0.02222	0.0231	0.0242	0.0253	0.0264
	Ri1	**0.042**	**0.04222**	**0.0431**	**0.0442**	**0.0453**	**0.0464**
	Rc2	0.042358	0.042578	0.043458	0.044558	0.045658	0.046758
	Ri2	0.047	0.04722	0.0481	0.0492	0.0503	0.0514
	y2	1.18184	1.182220452	1.183744657	1.185649912	1.187555168	1.189460424
	x2	0.04725	0.04747	0.04835	0.04945	0.05055	0.05165
	Cond. res.	3.5479E-08	3.61922E-08	3.91156E-08	4.29296E-08	4.6921E-08	5.10898E-08
2000mm2	Rc1	0.028	0.02828	0.0294	0.0308	0.0322	0.0336
	Ri1	**0.048**	**0.04828**	**0.0494**	**0.0508**	**0.0522**	**0.0536**
	Rc2	0.048314	0.048594	0.049714	0.051114	0.052514	0.053914
	Ri2	0.0545	0.05478	0.0559	0.0573	0.0587	0.0601
	y2	1.19483	1.195314756	1.197254653	1.199679524	1.202104395	1.204529266
	x2	0.05475	0.05503	0.05615	0.05755	0.05895	0.06035
	Cond. res.	3.44821E-08	3.51752E-08	3.80165E-08	4.17233E-08	4.56026E-08	4.96542E-08

Cross-Section	Layer	Reference	-1%	-5%	-10%	-15%	-20%
800mm2	Rc1	0.01685	0.0166815	0.0160075	0.015165	0.0143225	0.01348
	Ri1	**0.03505**	**0.0348815**	**0.0342075**	**0.033365**	**0.0325225**	**0.03168**
	Rc2	0.035479	0.0353105	0.0346365	0.033794	0.0329515	0.032109
	Ri2	0.0415	0.0413315	0.0406575	0.039815	0.0389725	0.03813
	y2	1.17231	1.172021271	1.170853868	1.169394616	1.167935363	1.16647611
	x2	0.04175	0.0415815	0.0409075	0.040065	0.0392225	0.03838
	Cond. res.	3.12189E-08	3.05976E-08	2.8175E-08	2.52873E-08	2.25556E-08	1.99801E-08
1200mm2	Rc1	0.022	0.02178	0.0209	0.0198	0.0187	0.0176
	Ri1	**0.042**	**0.04178**	**0.0409**	**0.0398**	**0.0387**	**0.0376**
	Rc2	0.042358	0.042138	0.041258	0.040158	0.039058	0.037958
	Ri2	0.047	0.04678	0.0459	0.0448	0.0437	0.0426
	y2	1.18184	1.181458349	1.179934145	1.178028889	1.176123633	1.174218377
	x2	0.04725	0.04703	0.04615	0.04505	0.04395	0.04285
	Cond. res.	3.5479E-08	3.4773E-08	3.20198E-08	2.8738E-08	2.56336E-08	2.27066E-08

2000mm2	Rc1	0.028	0.02772	0.0266	0.0252	0.0238	0.0224
	Ri1	**0.048**	**0.04772**	**0.0466**	**0.0452**	**0.0438**	**0.0424**
	Rc2	0.048314	0.048034	0.046914	0.045514	0.044114	0.042714
	Ri2	0.0545	0.05422	0.0531	0.0517	0.0503	0.0489
	y2	1.19483	1.194344807	1.192404911	1.189980039	1.187555168	1.185130297
	x2	0.05475	0.05447	0.05335	0.05195	0.05055	0.04915
	Cond. res.	3.44821E-08	3.37959E-08	3.11201E-08	2.79305E-08	2.49133E-08	2.20685E-08

Table 11.5 - Thickness of the cable layers for a deviation in the thickness of the insulation

Cross-Section	Layer	Reference	1%	5%	10%	15%	20%
800mm2	Rc1	0.01685	0.01685	0.01685	0.01685	0.01685	0.01685
	Ri1	**0.03505**	**0.035232**	**0.03596**	**0.03687**	**0.03778**	**0.03869**
	Rc2	0.035479	0.035661	0.036389	0.037299	0.038209	0.039119
	Ri2	0.0415	0.041682	0.04241	0.04332	0.04423	0.04514
	y2	1.17231	1.172628354	1.173889287	1.175465454	1.17704162	1.178617786
	x2	0.04175	0.041932	0.04266	0.04357	0.04448	0.04539
	Permittivity	2.796294498	2.793652982	2.783635591	2.772226015	2.761888769	2.752478752
1200mm2	Rc1	0.022	0.022	0.022	0.022	0.022	0.022
	Ri1	**0.042**	**0.0422**	**0.043**	**0.044**	**0.045**	**0.046**
	Rc2	0.042358	0.042558	0.043358	0.044358	0.045358	0.046358
	Ri2	0.047	0.0472	0.048	0.049	0.05	0.051
	y2	1.18184	1.182185811	1.183571451	1.185303502	1.187035553	1.188767604
	x2	0.04725	0.04745	0.04825	0.04925	0.05025	0.05125
	Permittivity	3.018698155	3.013492508	2.993829324	2.971583623	2.951566432	2.933458409
2000mm2	Rc1	0.028	0.028	0.028	0.028	0.028	0.028
	Ri1	**0.048**	**0.0482**	**0.049**	**0.05**	**0.051**	**0.052**
	Rc2	0.048314	0.048514	0.049314	0.050314	0.051314	0.052314
	Ri2	0.0545	0.0547	0.0555	0.0565	0.0575	0.0585
	y2	1.19483	1.195176192	1.196561833	1.198293883	1.200025934	1.201757985
	x2	0.05475	0.05495	0.05575	0.05675	0.05775	0.05875
	Permittivity	3.001426866	2.996241684	2.976656738	2.954501695	2.934568543	2.916539061

Cross-Section	Layer	Reference	-1%	-5%	-10%	-15%	-20%
800mm2	Rc1	0.01685	0.01685	0.01685	0.01685	0.01685	0.01685
	Ri1	**0.03505**	**0.034868**	**0.03414**	**0.03323**	**0.03232**	**0.03141**
	Rc2	0.035479	0.035297	0.034569	0.033659	0.032749	0.031839
	Ri2	0.0415	0.041318	0.04059	0.03968	0.03877	0.03786
	y2	1.17231	1.171997888	1.170736955	1.169160789	1.167584623	1.166008456
	x2	0.04175	0.041568	0.04084	0.03993	0.03902	0.03811
	Permittivity	2.796294498	2.798994545	2.810420899	2.826286809	2.844235778	2.864708035
1200mm2	Rc1	0.022	0.022	0.022	0.022	0.022	0.022
	Ri1	**0.042**	**0.0418**	**0.041**	**0.04**	**0.039**	**0.038**
	Rc2	0.042358	0.042158	0.041358	0.040358	0.039358	0.038358

	Ri2	0.047	0.0468	0.046	0.045	0.044	0.043
	y2	1.18184	1.1815	1.18010735	1.178375299	1.176643248	1.174911197
	x2	0.04725	0.04705	0.04625	0.04525	0.04425	0.04325
	Permittivity	3.018698155	3.02402805	3.046683567	3.078410797	3.114683974	3.15655496
2000mm2	Rc1	0.028	0.028	0.028	0.028	0.028	0.028
	Ri1	**0.048**	**0.0478**	**0.047**	**0.046**	**0.045**	**0.044**
	Rc2	0.048314	0.048114	0.047314	0.046314	0.045314	0.044314
	Ri2	0.0545	0.0543	0.0535	0.0525	0.0515	0.0505
	y2	1.19483	1.194483372	1.193097731	1.19136568	1.189633629	1.187901578
	x2	0.05475	0.05455	0.05375	0.05275	0.05175	0.05075
	Permittivity	3.001426866	3.006735901	3.029303684	3.060910029	3.097046851	3.138761744

Table 11.6 - Thickness of the cable layers for a deviation in the thickness of the screen

Cross-section	Layer	Reference	1%	5%	10%	15%	20%
800mm2	Rc1	0.01685	0.01685	0.01685	0.01685	0.01685	0.01685
	Ri1	0.03505	0.0305	0.0305	0.0305	0.0305	0.0305
	Rc2	**0.035479**	**0.035483**	**0.0355**	**0.0355219**	**0.035543**	**0.0355648**
	Ri2	0.0415	0.041504	0.041521	0.0415429	0.041564	0.0415858
	y2	1.17231	1.172321	1.17235	1.172387426	1.172425	1.172461731
	x2	0.04175	0.041754	0.041771	0.0417929	0.041814	0.0418358
1200mm2	Rc1	0.022	0.022	0.022	0.022	0.022	0.022
	Ri1	0.042	0.042	0.042	0.042	0.042	0.042
	Rc2	**0.042358**	**0.042362**	**0.042376**	**0.0423938**	**0.042412**	**0.0424296**
	Ri2	0.047	0.047004	0.047018	0.0470358	0.047054	0.0470716
	y2	1.18184	1.181846	1.18187	1.181901408	1.181932	1.181963415
	x2	0.04725	0.047254	0.047268	0.0472858	0.047304	0.0473216
2000mm2	Rc1	0.028	0.028	0.028	0.028	0.028	0.028
	Ri1	0.048	0.048	0.048	0.048	0.048	0.048
	Rc2	**0.048314**	**0.048317**	**0.04833**	**0.0483454**	**0.048361**	**0.0483768**
	Ri2	0.0545	0.054503	0.054516	0.0545314	0.054547	0.0545628
	y2	1.19483	1.194835	1.194857	1.194884168	1.194911	1.194938555
	x2	0.05475	0.054753	0.054766	0.0547814	0.054797	0.0548128

Cross-section	Layer	Reference	-1%	-5%	-10%	-15%	-20%
800mm2	Rc1	0.01685	0.01685	0.01685	0.01685	0.01685	0.01685
	Ri1	0.03505	0.0305	0.0305	0.0305	0.0305	0.0305
	Rc2	**0.035479**	**0.035475**	**0.035458**	**0.0354361**	**0.035415**	**0.0353932**
	Ri2	0.0415	0.041496	0.041479	0.0414571	0.041436	0.0414142
	y2	1.17231	1.172306	1.172276	1.172238816	1.172202	1.172164511
	x2	0.04175	0.041746	0.041729	0.0417071	0.041686	0.0416642

1200mm2	Rc1	0.022	0.022	0.022	0.022	0.022	0.022
	Ri1	0.042	0.042	0.042	0.042	0.042	0.042
	Rc2	**0.042358**	**0.042354**	**0.04234**	**0.0423222**	**0.042304**	**0.0422864**
	Ri2	0.047	0.046996	0.046982	0.0469642	0.046946	0.0469284
	y2	1.18184	1.181833	1.181808	1.181777393	1.181746	1.181715386
	x2	0.04725	0.047246	0.047232	0.0472142	0.047196	0.0471784
2000mm2	Rc1	0.028	0.028	0.028	0.028	0.028	0.028
	Ri1	0.048	0.048	0.048	0.048	0.048	0.048
	Rc2	**0.048314**	**0.048311**	**0.048298**	**0.0482826**	**0.048267**	**0.0482512**
	Ri2	0.0545	0.054497	0.054484	0.0544686	0.054453	0.0544372
	y2	1.19483	1.194824	1.194803	1.194775395	1.194748	1.194721009
	x2	0.05475	0.054747	0.054734	0.0547186	0.054703	0.0546872

Table 11.7 - Thickness of the cable layers for a deviation in the thickness of the outer insulation

Cross-section	**Layer**	**Reference**	**1%**	**5%**	**10%**	**15%**	**20%**
800mm2	Rc1	0.01685	0.01685	0.01685	0.01685	0.01685	0.01685
	Ri1	0.0305	0.0305	0.0305	0.0305	0.0305	0.0305
	Rc2	0.035479	0.035479	0.035479	0.035479	0.035479	0.035479
	Ri2	**0.0415**	**0.04156**	**0.041801**	**0.0421021**	**0.042403**	**0.0427042**
	y2	1.17231	1.172417	1.172835	1.173355989	1.173877	1.174398857
	x2	0.04175	0.04181	0.042051	0.0423521	0.042653	0.0429542
1200mm2	Rc1	0.022	0.022	0.022	0.022	0.022	0.022
	Ri1	0.042	0.042	0.042	0.042	0.042	0.042
	Rc2	0.042358	0.042358	0.042358	0.042358	0.042358	0.042358
	Ri2	**0.047**	**0.047046**	**0.047232**	**0.0474642**	**0.047696**	**0.0479284**
	y2	1.18184	1.18192	1.182241	1.182643419	1.183045	1.183447437
	x2	0.04725	0.047296	0.047482	0.0477142	0.047946	0.0481784
2000mm2	Rc1	0.028	0.028	0.028	0.028	0.028	0.028
	Ri1	0.048	0.048	0.048	0.048	0.048	0.048
	Rc2	0.048314	0.048314	0.048314	0.048314	0.048314	0.048314
	Ri2	**0.0545**	**0.054562**	**0.054809**	**0.0551186**	**0.055428**	**0.0557372**
	y2	1.19483	1.194937	1.195366	1.195901228	1.196437	1.196972675
	x2	0.05375	0.054812	0.055059	0.0553686	0.055678	0.0559872

Cross-section	**Layer**	**Reference**	**-1%**	**-5%**	**-10%**	**-15%**	**-20%**
800mm2	Rc1	0.01685	0.01685	0.01685	0.01685	0.01685	0.01685
	Ri1	0.0305	0.0305	0.0305	0.0305	0.0305	0.0305
	Rc2	0.035479	0.035479	0.035479	0.035479	0.035479	0.035479
	Ri2	**0.0415**	**0.04144**	**0.041199**	**0.0408979**	**0.040597**	**0.0402958**
	y2	1.17231	1.172209	1.171792	1.171270253	1.170749	1.170227386
	x2	0.04175	0.04169	0.041449	0.0411479	0.040847	0.0405458

1200mm2	Rc1	0.022	0.022	0.022	0.022	0.022	0.022
	Ri1	0.042	0.042	0.042	0.042	0.042	0.042
	Rc2	0.042358	0.042358	0.042358	0.042358	0.042358	0.042358
	Ri2	**0.047**	**0.046954**	**0.046768**	**0.0465358**	**0.046304**	**0.0460716**
	y2	1.18184	1.181759	1.181437	1.181035383	1.180633	1.180231365
	x2	0.04725	0.047204	0.047018	0.0467858	0.046554	0.0463216
2000mm2	Rc1	0.028	0.028	0.028	0.028	0.028	0.028
	Ri1	0.048	0.048	0.048	0.048	0.048	0.048
	Rc2	0.048314	0.048314	0.048314	0.048314	0.048314	0.048314
	Ri2	**0.0545**	**0.054438**	**0.054191**	**0.0538814**	**0.053572**	**0.0532628**
	y2	1.19483	1.194723	1.194294	1.193758335	1.193223	1.192686888
	x2	0.05375	0.054688	0.054441	0.0541314	0.053822	0.0535128

Table 11.8 - Deviations in the resistivity of the conductor, screen and permittivity of the insulation

	Cross-section	**Reference**	**1%**	**5%**	**10%**	**15%**	**20%**
Insulation Permittivity	**800**	2.796	2.82396	2.9358	3.0756	3.2154	3.3552
	1200	3.018	3.04818	3.1689	3.3198	3.4707	3.6216
	2000	3.001	3.03101	3.15105	3.3011	3.45115	3.6012

	Cross-section	**Reference**	**1%**	**5%**	**10%**	**15%**	**20%**
Conductor Resistivity	**800**	3.11E-08	3.14E-08	3.2676E-08	3.4232E-08	3.5788E-08	3.7344E-08
	1200	3.55E-08	3.58E-08	3.72435E-08	3.9017E-08	4.07905E-08	4.2564E-08
	2000	3.45E-08	3.48E-08	3.6204E-08	3.7928E-08	3.9652E-08	4.1376E-08

	Cross-section	**Reference**	**1%**	**5%**	**10%**	**15%**	**20%**
Screen Resistivity	**800**	1.72E-08	1.74E-08	1.806E-08	1.892E-08	1.978E-08	2.064E-08
	1200	1.72E-08	1.74E-08	1.806E-08	1.892E-08	1.978E-08	2.064E-08
	2000	1.72E-08	1.74E-08	1.806E-08	1.892E-08	1.978E-08	2.064E-08

	Cross-section	**Reference**	**-1%**	**-5%**	**-10%**	**-15%**	**-20%**
Insulation Permittivity	**800**	2.796	2.76804	2.6562	2.5164	2.3766	2.2368
	1200	3.018	2.98782	2.8671	2.7162	2.5653	2.4144
	2000	3.001	2.97099	2.85095	2.7009	2.55085	2.4008

	Cross-section	**Reference**	**-1%**	**-5%**	**-10%**	**-15%**	**-20%**
Conductor Resistivity	**800**	3.11E-08	3.08E-08	2.9564E-08	2.8008E-08	2.6452E-08	2.4896E-08
	1200	3.55E-08	3.51E-08	3.36965E-08	3.1923E-08	3.01495E-08	2.8376E-08
	2000	3.45E-08	3.41E-08	3.2756E-08	3.1032E-08	2.9308E-08	2.7584E-08

	Cross-section	**Reference**	**-1%**	**-5%**	**-10%**	**-15%**	**-20%**
Screen Resistivity	**800**	1.72E-08	1.7E-08	1.634E-08	1.548E-08	1.462E-08	1.376E-08
	1200	1.72E-08	1.7E-08	1.634E-08	1.548E-08	1.462E-08	1.376E-08
	2000	1.72E-08	1.7E-08	1.634E-08	1.548E-08	1.462E-08	1.376E-08

11.12 Appendix L - Cable parameter equations

The calculation of the frequency spectrums in PSCAD/EMTDC is a slow process. Thus, a code in Matlab was written, which can be used to calculate the cable frequency spectrum in a matter of seconds. The code can also be used, if necessary, to validate the PSCAD/EMTDC cable model.

11.12.1 Equations

This appendix presents equations without showing the respective theoretical background. The theory behind the equations used to calculate the impedance and admittance matrices is thoroughly explained in [56].

Admittance

The admittance matrix is given by (123), whose elements are given by (124).

$$Y_{shunt} = \begin{bmatrix} y_1 & -y_1 & 0 & 0 & 0 & 0 \\ -y_1 & y_1 + y_2 & 0 & 0 & 0 & 0 \\ 0 & 0 & y_1 & -y_1 & 0 & 0 \\ 0 & 0 & -y_1 & y_1 + y_2 & 0 & 0 \\ 0 & 0 & 0 & 0 & y_1 & -y_1 \\ 0 & 0 & 0 & 0 & -y_1 & y_1 + y_2 \end{bmatrix} \tag{123}$$

$$y_i = G_i + j\omega C_i \tag{124}$$

y_1 is the admittance between the core and the screen and y_2 the admittance between the screen and the earth.

Impedance

Conductor Series Impedance

$$Z_{Couter} = \frac{\rho_C m_C}{2\pi R_1} \cdot \frac{J_0(m_C R_1)}{J_1(m_C R_1)} \tag{125}$$

Where, ρ_c is the resistivity of the conductor

m_c is the reciprocal of the complex penetration depth for the conductor, and given by (126)

R_1 is the radius over the conductor

$J_n(x)$ is the Bessel function of *x,* of first kind and order *n*

$$m_C = \sqrt{\frac{j\omega\mu}{\rho_C}} \tag{126}$$

Insulation Series Impedance

$$Z_{CSinsul}\left(\omega\right) = \frac{j\omega\mu_{ins}}{2\pi}\ln\left(\frac{R_2}{R_1}\right) \tag{127}$$

Where, μ_{ins} is the permittivity of the insulation

R_2 the radius over the insulation

Screen Inner Series Impedance

$$Z_{Sinner}\left(\omega\right) = \frac{\rho_S m_S}{2\pi R_2}\coth\left(m_S\left(R_3 - R_2\right)\right) - \frac{\rho_S}{2\pi R_2\left(R_2 + R_3\right)} \tag{128}$$

Where, ρ_S is the resistivity of the screen

m_S is the reciprocal of the complex penetration depth for the screen

R_3 is the radius over the screen

Screen Outer Series Impedance

$$Z_{Souter}\left(\omega\right) = \frac{\rho_S m_S}{2\pi R_3}\coth\left(m_S\left(R_3 - R_2\right)\right) + \frac{\rho_S}{2\pi R_3\left(R_2 + R_3\right)} \tag{129}$$

Outer Insulation Series impedance

$$Z_{SGinsul}\left(\omega\right) = \frac{j\omega\mu_{out\_ins}}{2\pi}\ln\left(\frac{R_4}{R_3}\right) \tag{130}$$

Where, μ_{out_ins} is the permittivity of the outer insulation

R_4 the radius over the outer insulation

Mutual Series Impedance of two loops

$$Z_{mutual} = \frac{\rho_S m_S}{\pi\left(R_2 + R_3\right)}\operatorname{csch}\left(m_S\left(R_3 - R_2\right)\right) \tag{131}$$

Earth Series Self Impedance

Calculated according to the Saad, Gaba and Giroux theory.

$$Z_{earth}(\omega)=\frac{\rho_e m_e}{2\pi}\left[K_0\left(m_e R_4\right)+\frac{2}{4+m_e^2 R_4^2}e^{-2hm_e}\right] \tag{132}$$

Where, ρ_S is the resistivity of the earth

m_S is the reciprocal of the complex penetration depth for the earth

$K_n(x)$ is the Bessel function of *x,* of second kind and order *n*

h is the depth of the cable

Mutual Earth Impedance

$$Z_{earth\_mutual}(\omega)=\frac{\rho_e m_e^2}{2\pi}\left[K_0\left(m_e D\right)+\frac{2}{4+m_e^2 D^2}e^{-2hm_e}\right] \tag{133}$$

Where, D is the distance between the conductors

Matrix

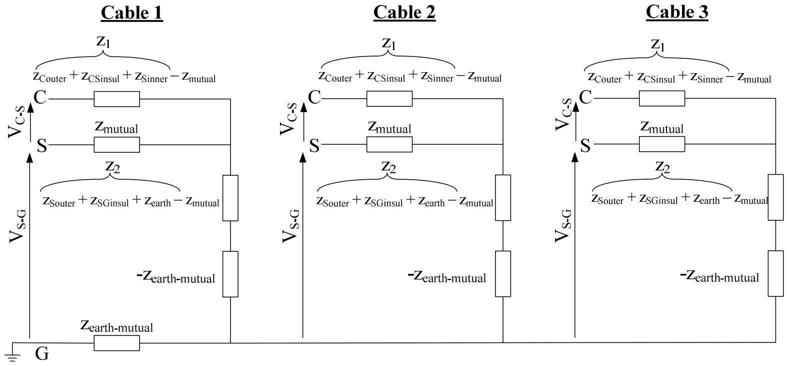

Figure 11.23 - Equivalent circuit for the design of the impedance matrix [56]

$$Z=\begin{bmatrix} z_{11}^{1} & -z_{12}^{1} & z_{gm12} & z_{gm12} & z_{gm13} & z_{gm13} \\ -z_{12}^{1} & z_{22}^{1} & z_{gm12} & z_{gm12} & z_{gm13} & z_{gm13} \\ z_{gm12} & z_{gm12} & z_{11}^{1} & -z_{12}^{1} & z_{gm23} & z_{gm23} \\ z_{gm12} & z_{gm12} & -z_{12}^{1} & z_{22}^{1} & z_{gm23} & z_{gm23} \\ z_{gm13} & z_{gm13} & z_{gm23} & z_{gm23} & z_{11}^{1} & -z_{12}^{1} \\ z_{gm13} & z_{gm13} & z_{gm23} & z_{gm23} & -z_{12}^{1} & z_{22}^{1} \end{bmatrix} \tag{134}$$

Where: $Z_{11}=Z_{Couter}+Z_{CSinsul}+Z_{Sinner}+Z_{Souter}+Z_{GSinsul}+Z_{earth}-2Z_{mutual}$

$Z_{12}=Z_{Souter}+Z_{GSinsul}+Z_{earth}-Z_{mutual}$

$Z_{22}= Z_{Souter}+Z_{GSinsul}+Z_{earth}$

$Z_{gm12}=Z_{earth\_mutual}$

Cross-bonded cable

The elements in the admittance and impedance matrix referent to the screen-conductor connection rotate for the new positions. For an example see the code below.

11.12.2 Matlab Code

The code below is for a cross-bonded cable. For a cable bonded in both ends, *Z=Z1*.

```
%%%%%%%%%%%%%%%%%%%%%%%%%%%%%%%%%%%%
%%%%%%%%%%%%%%%%%%%%%%%%%%%%%%%%%%%%
%--------------------------------------------------------------------------------%
% Cable data                                                                     %
%--------------------------------------------------------------------------------%
%%%%%%%%%%%%%%%%%%%%%%%%%%%%%%%%%%%%
%%%%%%%%%%%%%%%%%%%%%%%%%%%%%%%%%%%%
u_0=4*pi*1e-7; %Permeability of air
e0=8.854e-12; %Vacuum permittivity

%Depth of the three conductors
h1=1.18185;
h2=1.1;
h3=1.18185;

R1=22e-3; %Radius of conductor + inner radius of insulation 1
R2=42e-3; %Outer radius of insulation 1 + inner radius of sheath
R3=42.358e-3; %Outer radius of sheath + inner radius of insulation 2
R4=47e-3; %Outer radius of insulation 2

pc=3.55e-8; %Resistivity of conductor
u_rel_cond=1; %Relative permeability of the conductor

E_ins1=2.8; %Permittivity of inner insulation
u_ins1=1; %Permeability of inner insulation

p_sheath=1.72e-8; %Resistivity of the screen
u_rel_sheath=1;

E_ins2=2.3; %Permittivity of outer insulation
u_ins2=1;

p_earth=100; %Earth resistivity
u_rel_earth=1; %Relative permeability of the earth

%distance between the cable assuming a trefoil formation
d1=R4*2; %Distance between the two cables with an angle
x1=d1; %Distance between the two cables

d2=2*R4;
x2=R4;
pos3=sqrt(3)*R4;

d3=2*R4;
x3=R4;


l=21090;

% number of runs. In this example the frequency spectrum is from 1Hz to 1000Hz
for a=1:4000
```

```
   f=a*5;
   w=2*pi*f;
   %-----------------matrix Y-------------------------------------------------
   e_conductor=3.018; %corrected relative permittivity
   C_conductor=2*pi*e_conductor*e0/log(R2/R1); %capacitance for the conductor per m

   e_sheath=2.4;
   C_sheath=2*pi*e_sheath*e0/log(R4/R3); %capacitance for the sheath

   Y11=i*w*C_conductor; %result in mhos/m
   Y33=Y11;
   Y55=Y11;

   Y22=i*w*C_sheath;
   Y44=Y22;
   Y66=Y22;

   Y1=[Y11 -Y11 0 0 0 0
      -Y11 Y22+Y11 0 0 0 0
      0 0 Y33 -Y33 0 0
      0 0 -Y33 Y44+Y33 0 0
      0 0 0 0 Y55 -Y55
      0 0 0 0 -Y55 Y66+Y55];

   %cross of screens - position 2
   Y2=[Y1(1,1) Y1(1,4) Y1(1,3) Y1(1,6) Y1(1,5) Y1(1,2)
      Y1(1,4) Y1(4,4) Y1(3,4) Y1(4,6) Y1(4,5) Y1(4,2)
      Y1(1,3) Y1(3,4) Y1(3,3) Y1(3,6) Y1(3,5) Y1(3,2)
      Y1(1,6) Y1(4,6) Y1(6,3) Y1(6,6) Y1(6,5) Y1(6,2)
      Y1(1,5) Y1(4,5) Y1(3,5) Y1(6,5) Y1(5,5) Y1(5,2)
      Y1(1,2) Y1(2,4) Y1(3,2) Y1(6,2) Y1(5,2) Y1(2,2)];

   %cross of screens - position 3
   Y3=[Y2(1,1) Y2(1,4) Y2(1,3) Y2(1,6) Y2(1,5) Y2(1,2)
      Y2(1,4) Y2(4,4) Y2(3,4) Y2(4,6) Y2(4,5) Y2(4,2)
      Y2(1,3) Y2(3,4) Y2(3,3) Y2(3,6) Y2(3,5) Y2(3,2)
      Y2(1,6) Y2(4,6) Y2(6,3) Y2(6,6) Y2(6,5) Y2(6,2)
      Y2(1,5) Y2(4,5) Y2(3,5) Y2(6,5) Y2(5,5) Y2(5,2)
      Y2(1,2) Y2(2,4) Y2(3,2) Y2(6,2) Y2(5,2) Y2(2,2)];

   Y=0.3333333*(Y1+Y2+Y3); %normalisation of the shunt admittance

%%%%%%%%%%%%%%%%%%%%%%%%%%%%%%%%%%%%%%%%%%%%%%
%%%%%%%%%%%%%%%%%%%%%%%%%%%%%%%%%%%%%%%%%%%%%%
%Calculate theoretical values
%%%%%%%%%%%%%%%%%%%%%%%%%%%%%%%%%%%%%%%%%%%%%%
%%%%%%%%%%%%%%%%%%%%%%%%%%%%%%%%%%%%%%%%%%%%%%
 %------------------------------------------------------------------------------------%
 % Calculate parameters for impedance                                                 %
 %------------------------------------------------------------------------------------%

%%%%%%%%%%%%%%%%%%%%%%%%%%%%%%%%%%%%%%%%%%%%%%
%%%%%%%%%%%%%%%%%%%%%%%%%%%%%%%%%%%%%%%%%%%%%%
   m_cond=sqrtm(i*w*u_rel_cond*u_0/pc); %reciprocal of complex penetration depth for conductor
   m_sheath=sqrtm(i*w*u_rel_sheath*u_0/p_sheath); %reciprocal of complex penetration depth for sheath 1
   m_earth=sqrtm(i*w*u_rel_earth*u_0/p_earth); %reciprocal of complex penetration depth for conductor

%%%%%%%%%%%%%%%%%%%%%%%%%%%%%%%%%%%%%%%%%%%%%%
%%%%%%%%%%%%%%%%%%%%%%%%%%%%%%%%%%%%%%%%%%%%%%
%------------------------------------------------------------------------------------%
% Calculate impedances                                                               %
%------------------------------------------------------------------------------------%

%%%%%%%%%%%%%%%%%%%%%%%%%%%%%%%%%%%%%%%%%%%%%%
%%%%%%%%%%%%%%%%%%%%%%%%%%%%%%%%%%%%%%%%%%%%%%
   Z_insul=(i*w*u_ins1*u_0/(2*pi))*log(R2/R1);
   Z_insul2=(i*w*u_ins2*u_0/(2*pi))*log(R4/R3);

   %Calculate earth return from Gaba formulas
```

```
m_earth=sqrt(i*w*u_rel_earth*u_0/p_earth);
mR=m_earth*R4;
K0_mR=besselk(0,mR);
Zground1=((p_earth*m_earth^2)/(2*pi))*(K0_mR+2*exp(-2*h1*m_earth)/(4+m_earth^2*R4^2));
Zground2=((p_earth*m_earth^2)/(2*pi))*(K0_mR+2*exp(-2*h2*m_earth)/(4+m_earth^2*R4^2));
Zground3=((p_earth*m_earth^2)/(2*pi))*(K0_mR+2*exp(-2*h3*m_earth)/(4+m_earth^2*R4^2));

md1=m_earth*d1;
md2=m_earth*d2;
md3=m_earth*d3;
K0_md1=besselk(0,md1);
K0_md2=besselk(0,md2);
K0_md3=besselk(0,md3);
l_1=h1+h2;
l_2=h1+h3;
l_3=h2+h3;
Zg_mutual1=((p_earth*m_earth^2)/(2*pi))*(K0_md1+2*exp(-l_1*m_earth)/(4+m_earth^2*x1^2));
Zg_mutual2=((p_earth*m_earth^2)/(2*pi))*(K0_md2+2*exp(-l_2*m_earth)/(4+m_earth^2*x2^2));
Zg_mutual3=((p_earth*m_earth^2)/(2*pi))*(K0_md3+2*exp(-l_3*m_earth)/(4+m_earth^2*x3^2));

mr2=m_sheath*R2;
mr3=m_sheath*R3;

I0_mr1=besseli(0,m_cond*R1);
I1_mr1=besseli(1,m_cond*R1);
I0_mr2=besseli(0,mr2);
I1_mr2=besseli(1,mr2);
I0_mr3=besseli(0,mr3);
I1_mr3=besseli(1,mr3);

K0_mr2=besselk(0,mr2);
K1_mr2=besselk(1,mr2);
K0_mr3=besselk(0,mr3);
K1_mr3=besselk(1,mr3);

Z_cond=(pc*m_cond/(2*pi*R1))*I0_mr1/I1_mr1;

Z_shinner=(p_sheath*m_sheath/(2*pi*R2))*coth(m_sheath*(R3-R2))-p_sheath/(2*pi*R2*(R2+R3));

Z_shouter=(p_sheath*m_sheath/(2*pi*R3))*coth(m_sheath*(R3-R2))+p_sheath/(2*pi*R3*(R2+R3));

Z_mutual=(p_sheath*m_sheath/(pi*(R2+R3)))*csch(m_sheath*(R3-R2));

Z11=Z_cond+Z_insul+Z_shinner;
Zm=Z_mutual;
Z22_1=Z_shouter+Z_insul2+Zground1;
Z22_2=Z_shouter+Z_insul2+Zground2;
Z22_3=Z_shouter+Z_insul2+Zground3;

Z1=[Z11+Z22_1-2*Zm Z22_1-Zm    Zg_mutual1     Zg_mutual1 Zg_mutual2     Zg_mutual2
    Z22_1-Zm       Z22_1       Zg_mutual1     Zg_mutual1 Zg_mutual2     Zg_mutual2
    Zg_mutual1     Zg_mutual1  Z11+Z22_2-2*Zm Z22_2-Zm   Zg_mutual3     Zg_mutual3
    Zg_mutual1     Zg_mutual1  Z22_2-Zm       Z22_2      Zg_mutual3     Zg_mutual3
    Zg_mutual2     Zg_mutual2  Zg_mutual3     Zg_mutual3 Z11+Z22_3-2*Zm Z22_3-Zm
    Zg_mutual2     Zg_mutual2  Zg_mutual3     Zg_mutual3 Z22_3-Zm       Z22_3];

%cross of screens - position 2
Z2=[Z1(1,1) Z1(1,4) Z1(1,3) Z1(1,6) Z1(1,5) Z1(1,2)
    Z1(1,4) Z1(4,4) Z1(3,4) Z1(4,6) Z1(4,5) Z1(4,2)
    Z1(1,3) Z1(3,4) Z1(3,3) Z1(3,6) Z1(3,5) Z1(3,2)
    Z1(1,6) Z1(4,6) Z1(6,3) Z1(6,6) Z1(6,5) Z1(6,2)
    Z1(1,5) Z1(4,5) Z1(3,5) Z1(6,5) Z1(5,5) Z1(5,2)
    Z1(1,2) Z1(2,4) Z1(3,2) Z1(6,2) Z1(5,2) Z1(2,2)];

%cross of screens - position 3
Z3=[Z2(1,1) Z2(1,4) Z2(1,3) Z2(1,6) Z2(1,5) Z2(1,2)
    Z2(1,4) Z2(4,4) Z2(3,4) Z2(4,6) Z2(4,5) Z2(4,2)
    Z2(1,3) Z2(3,4) Z2(3,3) Z2(3,6) Z2(3,5) Z2(3,2)
    Z2(1,6) Z2(4,6) Z2(6,3) Z2(6,6) Z2(6,5) Z2(6,2)
    Z2(1,5) Z2(4,5) Z2(3,5) Z2(6,5) Z2(5,5) Z2(5,2)
```

```
   Z2(1,2) Z2(2,4) Z2(3,2) Z2(6,2) Z2(5,2) Z2(2,2)];

Z=0.33333333*(Z1+Z2+Z3);


%vector H ->sequences order is +-0
h=exp(j*2*pi/3);
H_seq=[1 1 1
   h^2 h 1
   h h^2 1];

%Change of the elements positions in order to decouple the conductors
%from the screens
Z_corrected=[Z(1,1) Z(1,3) Z(1,5) Z(1,2) Z(1,4) Z(1,6)
   Z(3,1) Z(3,3) Z(3,5) Z(3,2) Z(3,4) Z(3,6)
   Z(5,1) Z(5,3) Z(5,5) Z(5,2) Z(5,4) Z(5,6)
   Z(2,1) Z(2,3) Z(2,5) Z(2,2) Z(2,4) Z(2,6)
   Z(4,1) Z(4,3) Z(4,5) Z(4,2) Z(4,4) Z(4,6)
   Z(6,1) Z(6,3) Z(6,5) Z(6,2) Z(6,4) Z(6,6)];

Y_corrected=[Y(1,1) Y(1,3) Y(1,5) Y(1,2) Y(1,4) Y(1,6)
   Y(3,1) Y(3,3) Y(3,5) Y(3,2) Y(3,4) Y(3,6)
   Y(5,1) Y(5,3) Y(5,5) Y(5,2) Y(5,4) Y(5,6)
   Y(2,1) Y(2,3) Y(2,5) Y(2,2) Y(2,4) Y(2,6)
   Y(4,1) Y(4,3) Y(4,5) Y(4,2) Y(4,4) Y(4,6)
   Y(6,1) Y(6,3) Y(6,5) Y(6,2) Y(6,4) Y(6,6)];


ZAA=[Z_corrected(1,1) Z_corrected(1,2) Z_corrected(1,3)
   Z_corrected(2,1) Z_corrected(2,2) Z_corrected(2,3)
   Z_corrected(3,1) Z_corrected(3,2) Z_corrected(3,3)];
ZAB=[Z_corrected(1,4) Z_corrected(1,5) Z_corrected(1,6)
   Z_corrected(2,4) Z_corrected(2,5) Z_corrected(2,6)
   Z_corrected(3,4) Z_corrected(3,5) Z_corrected(3,6)];
ZBA=[Z_corrected(4,1) Z_corrected(4,2) Z_corrected(4,3)
   Z_corrected(5,1) Z_corrected(5,2) Z_corrected(5,3)
   Z_corrected(6,1) Z_corrected(6,2) Z_corrected(6,3)];
ZBB=[Z_corrected(4,4) Z_corrected(4,5) Z_corrected(4,6)
   Z_corrected(5,4) Z_corrected(5,5) Z_corrected(5,6)
   Z_corrected(6,4) Z_corrected(6,5) Z_corrected(6,6)];


YAA=[Y_corrected(1,1) Y_corrected(1,2) Y_corrected(1,3)
   Y_corrected(2,1) Y_corrected(2,2) Y_corrected(2,3)
   Y_corrected(3,1) Y_corrected(3,2) Y_corrected(3,3)];
YAB=[Y_corrected(1,4) Y_corrected(1,5) Y_corrected(1,6)
   Y_corrected(2,4) Y_corrected(2,5) Y_corrected(2,6)
   Y_corrected(3,4) Y_corrected(3,5) Y_corrected(3,6)];
YBA=[Y_corrected(4,1) Y_corrected(4,2) Y_corrected(4,3)
   Y_corrected(5,1) Y_corrected(5,2) Y_corrected(5,3)
   Y_corrected(6,1) Y_corrected(6,2) Y_corrected(6,3)];
YBB=[Y_corrected(4,4) Y_corrected(4,5) Y_corrected(4,6)
   Y_corrected(5,4) Y_corrected(5,5) Y_corrected(5,6)
   Y_corrected(6,4) Y_corrected(6,5) Y_corrected(6,6)];


Z_phase=ZAA-ZAB*inv(ZBB)*ZBA; %impedance of the conductor
Y_phase=YAA;

Z_seq=inv(H_seq)*Z_phase*H_seq;
Y_seq=Y_phase;

%conductor positive sequence
Z_pos=Z_seq(1,1);
Y_pos=Y_seq(1,1);

lambda=sqrtm(Y_pos*Z_pos);

%correction to use the exact pi-model
Z_pos=Z_pos*l*sinh(lambda*l)/(lambda*l);
```

```
    Y_pos=Y_pos*l*tanh(lambda*l/2)/(lambda*l/2);

    Z_positivo=Z_pos(1,1);
    Y_positivo=Y_pos(1,1);

    Y_imp=inv(Y_positivo/2);
    teste(a,:,:)=((Z_positivo+Y_imp)*Y_imp)/(Z_positivo+2*Y_imp);
end
```

11.13 Appendix M - Comparison of the resonance frequencies for different bonding configurations

The shunt admittance matrix is equal for both bonding configurations, but the series impedance matrix presents some differences.

In applying the method explained in the previous appendix, (135) and (136) for the positive-sequence series impedance of the conductor are obtained.

$$Z_{both}^{+} = Z_{CC} - Z_{CS2} + \frac{\left(Z_{CS1} - Z_{CS2}\right)^2}{Z_{CS2} - Z_{SS}} \tag{135}$$

$$Z_{cross}^{+} = Z_{CC} - Z_{CS2} \tag{136}$$

The resonance points have higher magnitudes and lower frequencies for the cross-bonded cable than for the both-end bonded cable. As the differences in the resonances are noticeable for the first resonance point, the nominal pi model instead of the equivalent pi model can be used, which results in a simple mathematical analysis.

The line impedance for the nominal pi model is given by (137).

$$Z = \frac{\left(1 - \omega^2 LC\right) + j\left(\omega RL\right)}{\left(-\omega^2 C^2 R\right) + j\left(2\omega C - \omega^3 C^2 L\right)} \tag{137}$$

The shunt admittance is equal for both bonding types and the differences in the impedance are a function of *L* and *R*.

Resonance Frequency

The resonance frequency is given by (138), which is obtained by developing (137). *L* is the imaginary part of the series impedance (135)-(136). Consequently, the imaginary part of $Z^{+}_{cross} > Z^{+}_{both}$. Subsequently, the imaginary part of the last element of (135) should be negative, i.e. (139).

$$\omega^2 = \frac{2}{LC} \tag{138}$$

$$imag\left(\frac{\left(Z_{CS1} - Z_{CS2}\right)^2}{Z_{CS2} - Z_{SS}}\right) < 0 \tag{139}$$

Both the real and imaginary parts of Z_{SS} are always larger than the equivalents in Z_{CS2}. Thus, the denominator of (139) has always a negative real and imaginary part (140).

$$Z_{CS2} - Z_{SS} = -a - jb \tag{140}$$

The development of the numerator of (139) results in (141).

$$\left(Z_{CS1}-Z_{CS2}\right)^2=\left(\left(c+jd\right)-\left(e+jf\right)\right)^2=\left(c^2-d^2+e^2-f^2-2ce+2df\right)+j\left(2cd+2ef-2cf-2de\right) \quad (141)$$

The magnetic field is stronger between the core and screen of the same cable than between the cores or core-screen of two different cables. Thus, $d>f$ while $c\approx e$, and so (141) can be simplified to (142).

$$\begin{aligned}&\left(Z_{CS1}-Z_{CS2}\right)^2=\left(-d^2-f^2+2df\right)+j0\Leftrightarrow\left(Z_{CS1}-Z_{CS2}\right)^2=\left(-d^2-\left(d-g\right)^2+2d\left(d-g\right)\right)\\&\Leftrightarrow\left(Z_{CS1}-Z_{CS2}\right)^2=-d^2-d^2-g^2+2dg+2d^2-2dg\Leftrightarrow\left(Z_{CS1}-Z_{CS2}\right)^2=-g^2\end{aligned} \quad (142)$$

It is concluded that the numerator of (139) has only a negative real part. Therefore, (139) can be written as (143).

$$\begin{aligned}&\frac{\left(Z_{CS1}-Z_{CS2}\right)^2}{Z_{CS2}-Z_{SS}}=\frac{-g^2}{-a-jb}=-g^2\cdot\left(-a'+jb'\right)\\&\Leftrightarrow\frac{\left(Z_{CS1}-Z_{CS2}\right)^2}{Z_{CS2}-Z_{SS}}=\left(a'g^2\right)+j\left(-b'g^2\right)\end{aligned} \quad (143)$$

The imaginary part of (139) is always negative and the resonance frequency of a cross-bonded cable is always lower than the resonance frequency if bonded at both-ends.

Magnitude

Parallel resonance

From (137) the magnitude is given by

$$\begin{aligned}&\|Z\|=\frac{\left(1-\omega^2LC\right)+j\omega RC}{-\omega^2RC^2}\Leftrightarrow\|Z\|=\frac{\left(1-\omega^2LC\right)}{-\omega^2RC^2}+\frac{j\omega RC}{-\omega^2RC^2}\\&\Leftrightarrow\|Z\|=\frac{L}{2RC}+j\frac{L}{C^2\sqrt{\frac{2}{LC}}}\Leftrightarrow\|Z\|=\sqrt{\frac{L^2}{4C^2R^2}+\frac{L^3}{2C^3}}\\&\Leftrightarrow\|Z\|=\sqrt{\left(\frac{L}{C}\right)^2\frac{1}{4R^2}+\left(\frac{L}{C}\right)^3\frac{1}{2}}\end{aligned} \quad (144)$$

The two variables that depend on the bonding are R and L, which are, respectively, the real and imaginary parts of the series impedance matrix (to be precise the imaginary part is XL, but for this analysis, this is not very relevant).

From the analysis of the resonance frequency and (135), (136) and (143) it is known that the both-end bonded cable has a higher resistance and a lower inductance. Doing the substitutions in (144), it is concluded that the magnitude of the parallel resonance points is lower in the both-end bonded cable.

Series resonance

For a series resonance the impedance magnitude is given by (145). The value of L is lower for a both-end bonded cable, resulting in lower magnitude at the series resonance points for this type of bonding.

$$Z = \frac{j(\omega RL)}{-\omega^2 C^2 R} \Leftrightarrow \|Z\| = \frac{L}{\omega C^2} \Leftrightarrow \|Z\| = \frac{L\sqrt{LC}}{2C^2} \tag{145}$$

11.14 Appendix N - Variation of the resonance frequency as a function of changes in cable capacitance

$$Z_{System} = \frac{\left(R + j\omega L\right)\frac{1}{j\omega C_1}}{R + j\omega L + \frac{1}{j\omega C_1}} \Leftrightarrow Z_{System} = \frac{R + j\omega L}{\left(1 - \omega^2 LC_1\right) + j\omega RC_1} \tag{146}$$

$$Z_T = \frac{\frac{R + j\omega L}{\left(1 - \omega^2 LC_1\right) + j\omega RC_1} \cdot \frac{1}{j\omega C_2}}{\frac{R + j\omega L}{\left(1 - \omega^2 LC_1\right) + j\omega RC_1} + \frac{1}{j\omega C_2}} \Leftrightarrow Z_T = \frac{R + j\omega L}{1 - \omega^2 LC_1 + j\omega RC_1 + j\omega RC_2 - \omega^2 LC_2}$$
$$\Leftrightarrow Z_T = \frac{R + j\omega L}{\left(1 - \omega^2 L\left(C_1 + C_2\right)\right) + j\omega R\left(C_1 + C_2\right)} \tag{147}$$

Frequency:

$$\omega = \frac{1}{\sqrt{L\left(C_1 + C_2\right)}} \tag{148}$$

Substituting:

$$Z_T = \frac{R + j\frac{L}{\sqrt{L\left(C_1 + C_2\right)}}}{j\frac{R}{\sqrt{L\left(C_1 + C_2\right)}}\left(C_1 + C_2\right)} \Leftrightarrow Z_T = \frac{R\sqrt{L\left(C_1 + C_2\right)} + jL}{jR\left(C_1 + C_2\right)} \Leftrightarrow Z_T = \frac{L}{R\left(C_1 + C_2\right)} - j\sqrt{\frac{L}{\left(C_1 + C_2\right)}} \tag{149}$$

The magnitude is calculated

$$\left\|Z_T\right\| = \sqrt{\left(\frac{L}{R\left(C_1 + C_2\right)}\right)^2 + \frac{L}{C_1 + C_2}} \tag{150}$$

In order for the magnitude to be larger in one of the models, R or C_1 must be smaller in that model or the L must be larger.
In (151) is derivated (148) in order to C_2.

$$\frac{d\omega}{dC_2} = -\frac{L}{2\left(L\left(C_1 + C_2\right)\right)\sqrt{L\left(C_1 + C_2\right)}} \tag{151}$$

The smaller the value of C_1, the larger the frequency variation. This explains why the frequency variation is larger in model D5-L than in models D1-L or D3-L.

11.15 Appendix O - List of publications

Note: The articles are not attached to the thesis, but they can all be obtained by contacting the thesis author.

Journals

F. F. da Silva, C. L. Bak, U. S. Gudmundsdottir, W. Wiechowski, M. R. Knardrupgard, “Methods to Minimize Zero-Missing Phenomenon”, IEEE Transactions in Power Delivery, Vol. 25, No. 5, October 2010

Unnur Stella Gudmundsdottir, Claus L. Bak, Wojciech Wiechowski and F. Faria da Silva, "Wave propagation and benchmark measurements for cable model validation", IEEE Transactions in Power Delivery (*under review*)

F. Faria da Silva, Claus L. Bak, Per B. Holst, "Estimation of the Required Modeling Depth for the Simulation of Cable Switching in a Cable based Network" ", IEEE Transactions in Power Delivery (*under review*)

F. Faria da Silva, Claus L. Bak, Per B. Holst, "Energization of Long HVAC Cables in Parallel - Analysis and Estimation Formulas" ", IEEE Transactions in Power Delivery (*under review*)

Conferences

F. Faria da Silva, C. L. Bak, U. S. Gudmundsdottir, W. Wiechowski, M.R.Knardrupgard, “Use of a pre-insertion resistor to minimize zero-missing phenomenon and switching overvoltages”, IEEE-PES General Meeting 2009

F. Faria da Silva, Claus L. Bak, W. Wiechowski, "Study of High Voltage AC Underground Cable Systems", PhD Seminar on Detailed Modelling and Validation of Electrical Components and Systems, 2010

F. Faria da Silva, Claus L. Bak, M. Lind Hansen, “Back-to-Back Energization of a 60kV Cable Network – Inrush Currents Phenomenon”, IEEE-PES General Meeting 2010

F. Faria da Silva,W. Wiechowski, C. L. Bak, U. S. Gudmundsdottir, “Full Scale Test on a 100km, 150kV AC Cable”, 43rd CIGRE Session, 2010

F. Faria da Silva, Claus L. Bak, Per B. Holst, "Switching Restrikes in HVAC Cable Lines and Hybrid HVAC Cable/OHL Lines", International Conference on Power Systems Transients (IPST), 2011

C.F. Jensen, F. Faria da Silva, Claus Leth Bak, W. Wiechowski, "Switching studies for the Horns Rev 2 wind farm main cable", International Conference on Power Systems Transients (IPST), 2011

F. Faria da Silva, Claus L. Bak, Per B. Holst, "Study of Harmonics in Cable-based Transmission Networks", 44th CIGRE Session, 2012 (*under review*)

Planned

These are papers currently being written or in planning stage. The final titles may be different.

Estimation of the Required Modeling Depth for the Simulation of Line Switching in an OHL-based or hybrid Cable-OHL Networks

Energisation of cables in weak grids

Comparison of simulation times - Frequency-dependent models and lumped-parameters models (*Note: This paper pretends to show that the use of a mix FD-models/lumped-parameters approach represents only a small increase in the simulation running time*)